From the Priority Research Area Infections
of the Research Center Borstel
Leibniz-Center for Medicine and Biosciences

Division of Biophysics
Prof. Dr. Thomas Gutsmann

Anti-inflammatory Regulation of Immune Cells by Membrane Active Host Defense Peptides

Dissertation

In Fulfillment of the Requirements
for the Doctoral Degree
of the University of Lübeck

from the Department of Natural Sciences

submitted by

Laura Paulowski

from Hamburg

Borstel 2016

First referee:	Prof. Thomas Gutsmann
Second referee:	Prof. Alfred X. Trautwein
Date of oral examination:	10th of February 2017
Approved for printing:	Lübeck, 16th of February 2017

The here present doctoral thesis was written
at the Research Center Borstel – Leibniz-Center for Medicine and Biosciences
in the Division of Biophysics
part of the Priority Area Infections
under supervision of PROF. DR. THOMAS GUTSMANN
in the space of time from June 2013 to October 2016.

Sic parvis magna – Thus great things from small things come

▪ *Sir Francis Drake* ▪

To my companions

ABSTRACT

Antimicrobial peptides (AMPs), also termed cationic host defense peptides (HDPs), comprise the ancient arm of innate immunity and are found among all multicellular organisms[11]. Members of this substance family work in concert and provide the non-specific first line of defense against colonization by pathogenic microorganisms[18]. This diverse collection of defense molecules is produced by the host organism in response to infection without the occurrence of any resistance to these multi-functional molecules[11a]. An understanding of the structure and function of these biologically active molecules is of high importance due to the widespread use of antibiotics leading to multi-drug resistant bacteria. The number of resistant pathogens is dramatically increasing during the last decade and raise the need for alternative agents with antibiotic function. In this thesis, the cationic antibiotic peptide polymyxin B (PMB) from *Paenibacillus polymyxa*, that serves as reserve antibiotic and has known resistance induction probability, is investigated together with the cationic α-helical peptide LL-32, an active variant of the human cathelicidin LL-37. HDPs, and thereunder LL-32, exhibit strong membrane permeabilizing activity, as well as lipopolysaccharide neutralizing function; therefore, this peptide family is supposed to play a major role in the regulation of inflammatory response of the immune system.

Defined model and native membrane systems were chosen, to study the mode of action and reveal potential points of interference. In general, three main model systems were considered: membranes reconstituted from (1) pure phospholipids, (2) ternary lipid mixtures with different fractions of cholesterol, and (3) ternary mixtures supplemented with 10mol% of negatively charged phospholipids. In addition, as biological host cell membrane system, human macrophages, and in further advances a HEK293-TLR4/MD2 cell line were used as mimicry for the host cell membrane. The activity of LL-32 and PMB was studied from membrane binding over insertion to membrane reorganization in combination with their immunomodulatory and anti-inflammatory function. Further, membrane permeabilization was investigated on reconstituted membranes

modelling the binary lipid system of the cytoplasmic membrane of Gram-negative bacteria and on the ternary lipid system of human immune cells. This should provide information on the antimicrobial activity and bacterial killing on the one hand, and cytotoxic effects, that can be induced in the host cell due to overexpression of HDPs in response to acute inflammation, on the other hand.

From an interpretation of these data, a two-step host defense mechanism for both, LL-32 and PMB, was proposed and the dual role of LL-32 was identified in the anti-inflammatory regulation of immune cells by interacting with the membrane as primary target and with the TLR4-receptor as secondary target.

DEUTSCHE ZUSAMMENFASSUNG

Antimikrobielle Peptide (AMPs), auch unter dem Namen kationische *host defense peptides* (HDPs) zusammengefasst, sind Bestandteil des angeborenen Immunsystems und stellen den wohl ältesten Teil dessen dar. Sie werden von nahezu allen multizellulären Organismen exprimiert[11a]. Vertreter dieser Substanzklasse weisen ein einzigartiges Zusammenspiel auf und bilden die erste, unspezifische Verteidigungslinie gegen bakterielle Besiedelung[18]. Diese diverse Sammlung von Abwehrmolekülen wird als Antwort auf Infektionen vom Wirtsorganismus exprimiert, ohne dass dieser Resistenzen gegen diese multifunktionalen Moleküle entwickeln konnte. Wie genau diese biologisch aktiven Substanzen strukturell aufgebaut sind und mit dem Wirtsorganismus interagieren, ist gerade heutzutage von großer Bedeutung, da die immerwährende Gabe von Antibiotika bei bakteriellen Infektionen zu immer mehr multiresistenten Strängen geführt hat, welche ein weltweites Gesundheitsrisiko der modernen Welt darstellen. Über die vergangenen Jahrzehnte hinweg, hat die Nummer resistenter Pathogene dramatisch zugenommen. Diese alarmierende Entwicklung verlangt zunehmend nach alternativen Wirkstoffen mit antibiotischer Wirkung, ohne dass dabei Resistenzen induziert werden.

In der vorliegenden Dissertation werden daher zum einen das kationische Polypeptid-Antibiotikum Polymyxin B aus *Paenibacillus polymyxa*, welchem Resistenz-Induktionspotential nachgesagt wird, und das α-helikale antimikrobielle Peptid LL-32, ein Fragment des humanen Kathelizidins LL-37, ausführlich untersucht. HDPs, darunter auch LL-32, weisen starke Membranpermeabilisierungsaktivität wie auch Lipopolysaccharid-neutralisierende Wirkung auf. Diese Charakteristika verdeutlichen, dass diese Peptidfamilie eine große Rolle in der Regulierung der inflammatorischen Antwort und damit einen wichtigen Bestandteil des Immunsystems einnehmen.

Definierte Modell- und native Membransystem wurden ausgewählt um den Wirkmechanismus sowie potentielle Wirkstellen auf der

Membranebene zu identifizieren. Hierzu wurden folgende drei Hauptmodelle berücksichtigt: (1) pure Lipid-Doppelschichten, (2) ternäre Lipidsysteme mit variablen Anteil an Cholesterol und (3) Zusatz dieser ternären Systeme mit 10mol% negativ geladener Phospholipid-Spezies. Zusätzlich zu diesen Modellsystemen wurden auch humane Makrophagen und im weiteren Verlauf eine TLR4/MD2-exprimierende HEK293-Zelllinie als biologisches Mimikry für die Wirtszellmembran untersucht.

Die Aktivität von LL-32 und PMB wurden hinsichtlich jeden Schrittes – von Membranbindung über -insertion bis hin zur Reorganisation der Membran – in Kombination mit der nachgesagten immunmodulatorischen und anti-inflammatorischen Funktion untersucht. Des Weiteren wurde die membranpermeabilisierende Wirkung an rekonstituierten Membranen, in einem binären Lipidsystem zur Modellierung der Zytoplasmamembran Gram-negativer Bakterien und im ternären Lipidsystem zur Mimese humaner Immunzellen, näher charakterisiert. Dadurch konnten einerseits Informationen über die antimikrobielle Aktivität und die damit verbundene bakterielle Abtötung und andererseits über zytotoxische Effekte, die sich auf der Wirtszelle durch Überexpression der HDPs als Antwort auf akute Inflammation äußern können, gewonnen werden.

Letztendlich war es möglich auf Grundlage all dieser Daten für beide Substanzen einen fundierten zweistufigen Wirkmechanismus zu erstellen. Zudem konnte für das Peptid LL-32 eine bivalente Rolle in der anti-inflammatorischen Regulation von Immunzellen identifiziert werden, wobei die Membran als Primärtarget und der TLR4-Rezeptor als sekundäres Target fungiert.

TABLE OF CONTENTS

1. INTRODUCTION

1.1 MEMBRANE COMPONENTS AND ARCHITECTURE

Every cell is confined by a cellular envelope composed of an outer membrane as permeability barrier, preventing the cell *inter alia* from leakage[19]. The cellular boundary called plasma membrane has been called the attention of many research groups throughout the world trying to understand its structure and function. Among that, the separation of the intracellular compartments together with ensuring the flow of substances and communication between the cells and their intracellular compartments belong to the main functions of biological membranes. In general, membranes are comprised of a lipid bilayer of which the major building blocks are phospho- and glycolipids and sterols. Dependent on the membrane function, the protein-lipid mass ratio can vary between 1:4 and 4:1[20]. Membranes with low metabolic activity, thereunder plasma membranes, are composed of a higher lipid fraction compared to e.g. mitochondrial membranes harboring all the enzymes involved in the respiratory chain and oxidative phosphorylation. In this specific case, the protein fraction represents 80% and is beyond the lipid fraction[21]. The membrane compound consists among transmembrane and peripheral proteins local accumulations of cholesterol and sphingolipids, building very versatile microdomains (~10^{-8} cm^{-2}/sec)[22], also termed as "lipid rafts". Two different types of raft domains are characterized: planar lipid or non-*caveolar* rafts and flask-shaped *caveolae*. These cholesterol-rich domains provide the ability for cytoskeletal interaction and enable a highly dynamic structure. The membrane architecture valid for almost all natural membranes along with their thermodynamic properties were described in 1972 by S.J. SINGER and G.L. NICHOLSON as "protein icebergs floating in a sea of lipid bilayer" and centralized in the *Fluid Mosaic Model* (Figure 1)[20, 23].

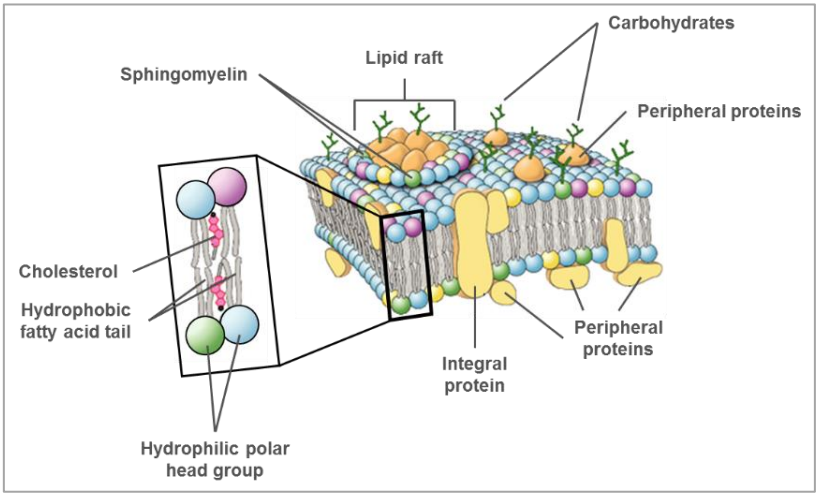

Figure 1 | Detail of an illustration of the membrane architecture according to the *Fluid Mosaic Model* by SINGER and NICHOLSON (adapted)[5]. Main membrane components are labeled.

1.1.1 CHOLESTEROL AND LIPID RAFT FORMATION

In 1815, CHEVREUL discovered cholesterol as a component of human gallstones and defined the term *cholesterine* (*chole* for bile and *stereos* for solid)[24]. REINITZER succeeded in identifying the empirical formula ($C_{27}H_{46}O$) for this molecule[24]. The exact structure, that is known today, was published in 1932 by WIELAND and DANE[24]. Cholesterol represents a unique membrane compound, since this molecule was found to be essential in laterally segregated domains or "lipid rafts". There exist a multitude of established synonyms, the most prominent ones for these specific regions among raft domains are detergent resistant membranes (DRMs), glycosylphosphatidylinositol (GPI) domains, glycosphingolipid signaling domains, *Caveolae*-like domains, (cholesterol-rich) microdomains, and liquid-ordered domains[25]. As currently understood, these membrane regions span in average 50 nm in diameter and are considered to comprise relatively small (micrometer scale and below) domains that are depleted in unsaturated phospholipids and a multitude of transmembrane proteins but enriched in cholesterol together with sphingolipids and certain lipid-anchored proteins (e.g. GM1)[22].

The raft builder is a predominantly hydrophobic molecule composed of an *iso*-octyl hydrocarbon tail, exhibiting high flexibility followed by a rigid tetracyclic non-aromatic ring skeleton of nearly planar arrangement that defines its chemical classification[25]: Cholesterol belongs to the class of sterols (Figure 2). Its polar 3*β*-hydroxyl group located at the **A**-ring of the molecule is responsible for the amphiphilic character and facilitates the orientation and anchoring of cholesterol in the membrane[25-26]. This group is found to be next to the ester bond of the phospholipid headgroup. With an approximately length of 20 Å, cholesterol is only able to span one leaflet of a lipid bilayer[27]. The *α*-face of the molecule feature a flat and smooth side with only axial oriented hydrogen atoms and without any substituents, whereas the rough side (β-face) carry the protruding methyl substituents (C18- and C19-position) and the *iso*-octyl chain (C17-position), giving the molecule an uneven molecular design[28]. Studies have shown, that the smooth face is oriented towards the saturated chains, whereas the rough β-face is in proximity to the unsaturated chain of the phospholipid or to membrane standing protein domains[28-29].

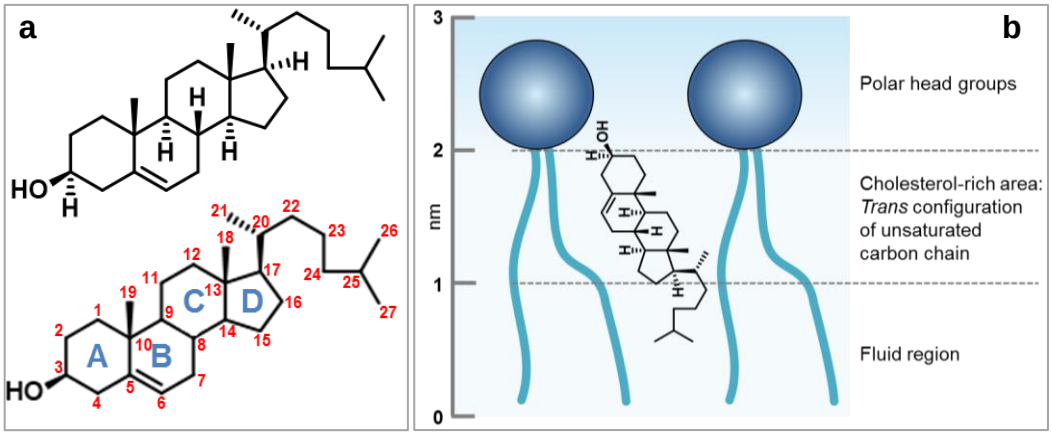

Figure 2 | Scheme of the orientation of the sterol molecule cholesterol within the membrane compound (adapted)[7]. (a) Chemical structure of cholesterol with stereochemistry; bold wedge: front/up, dashed wedge: back/down (upper panel) and labeling of the ring system with consecutive numbering of the carbon atoms (lower panel). (b) Illustration of the sterol-lipid interaction with two phospholipid molecules in one leaflet of a lipid bilayer. Cholesterol forces the unsaturated hydrocarbon chain to adopt its *trans* configuration. Only cholesterol as central molecule in this drawing is depicted in its chemical structure.

The human body contains around 140 g of cholesterol, whereof 95% is present in intracellular spaces and the cellular membranes[30]. With around 90%, plasma membranes expose the highest degree of cholesterol (45mol%) within the membrane compound[28, 31]. Interestingly, the lowest level of cholesterol (10-12mol%) within the membrane was found directly at the site of cholesterol biosynthesis, in the membrane of the endoplasmic reticulum (ER)[28, 31b]. Cholesterol-rich microdomains are supposed to have a sorting function of membrane molecules and play a major role in signal transduction processes. For over 40 years, researchers are challenged by revealing the exact function of cholesterol-lipid interaction and raft formation[32]. Cholesterol favors the formation of crystals over adopting a bilayer upon dispersion in aqueous media[32]. Phase transition studies have shown that data curves are strongly broadened due to a reduction of enthalpy from gel to liquid crystalline state upon mixing lipids with cholesterol[25]. Furthermore, phospholipid-cholesterol-mixtures can adopt complex patterns of lateral organization. IPSEN *et al.* introduced in the late 1980s with the formation of a "liquid-ordered" phase by saturated phospholipids and cholesterol an important conceptual tool for a deeper understanding of lipid-sterol interactions[33]. This phase coexists with the until then conventional liquid-disordered or fluid phase and gel phase, that are mainly constituted by pure phospholipids.

However, cells lacking cholesterol or having a malfunction in their cholesterol metabolism exhibit no normal growth[34]. This implies that cholesterol is also involved in cell growth and plays an important role for accurate function. Moreover, the passive permeability of phosphatidylcholine-composed bilayers is scaled down by raising levels of cholesterol within the membrane compound. Higher degrees of passive permeability are traced back to packing defects caused by non-cooperative isomerization of C—C single bonds in the lipid bilayer. Small molecules can use these transient packing defects for transcending through the membrane. In presence of cholesterol, the lipid ordering is increased and the packing density is optimized leading to a reduction of permeability: The annulated ring system of the sterol causes a decrease in conformational flexibility of the hydrocarbon chains of the membrane lipids with a simultaneous

increase in rigidity of the bilayer. This results in an almost *all-trans* configuration of the fatty acid chains and a depletion of membrane defects.

Studies at the membrane level, reveal that by varying the content of cholesterol, the whole cellular machinery is influenced: An increase in the level of cholesterol in the membrane leads to both, a proportionate in- and decrease in membrane protein function – For instance, cholesterol acts as negative modulator for the protein rhodopsin: All cellular processes, this receptor protein is involved in, are modulated, whereas the activity of the Na^+-K^+-ATPase together with the ATP-hydrolyzing activity is enhanced, and again other membrane functions (e.g. rabbit ATPase activity or the murine sucrase, lactase and maltase activity) seem to be insensitive to changes in cholesterol content[34]. However, membranes exhibiting a high degree of cholesterol and low anionic charge put eukaryotic cells out of the target range of many naturally occurring compounds among them AMPs (e.g. hBD-3-l)[35].

As described in *section 1.2.4 (page 30 et seqq.)* for the AMPs, even cholesterol uses a set of different routes for modulating the functions of biological membranes: This special membrane component exposes aside from inhibitory also stimulating function. Cholesterol alters the bulk biophysical properties of membranes by increasing the orientation order of the lipid hydrocarbon chains and concurrent reduction of the "free volume" resulting in a loss of accurate membrane protein function[25]. Membrane-standing proteins require the additional space of "free volume" to undergo conformational changes and remaining active. Regulatory and stimulating functions are induced by direct binding of cholesterol to membrane proteins.

These characteristics of cholesterol and respectively lipid rafts, show insistently the strong involvement in membrane modulation and therewith in recruiting and recognition mechanisms, providing the induction of major immune regulatory signaling cascades. Thereby, cholesterol-rich microdomains support the whole process of host defense.

1.1.2 The Bacterial Endotoxin Lipopolysaccharide

Lipopolysaccharide (LPS) is the major component (≥ 90%) of the outer membrane of the bacterial cell envelope and is ubiquitously expressed by almost all Gram-negative bacteria[36]. Exceptions are found in the Gram-negative bacterial strains *Treponema pallidum*, the two Borrelia genera *B. burgdorferi* and *B. hispanica*, the two Sphingomonas strains *S. capsulate* and *S. paucimobili*, the eubacterium *Thermus thermophilus*, and the Deinococcus-Thermus genus *Meiothermus taiwanensis*, that harbor glycophingolipids (GSLs) in their outer membrane leaflet[37]. LPS is the primary trigger of bacterial infections involving the release of pro-inflammatory mediators, alerting the host organism. Thus, LPS represents one of the central targets of the innate immune system.

The structure of LPS pursues a general scaffold: a polycarbohydrate attached to a lipid component (*lipid A*), whereof the polysaccharide is constituted of a core region and a polymeric oligosaccharide (*O-antigen*)[38]. This part is highly variable and specific to each bacterial strain. The *lipid A* tail of this endotoxin is assumed to be linked to the expression of cytokines induced by LPS[39]. In 1980, Shiba *et al.* synthesized the first free *lipid A* and confirmed this moiety as the endotoxic center of LPS[40]. This specific bacterial lipid molecule comprises a phosphorylated β-1,6-linked glucosamine disaccharide, where long fatty acid chains are attached to with varying in length and degree of saturation. According to the composition of their *lipid A* region, LPS of different bacterial strains can adopt different three-dimensional conformations (*E. coli*: conical conformation vs. *lipid A* precursor *Ia*: cylindrical shape)[38]. The core domain is connected to the *lipid A* moiety by an (α2→6)-ketosidic bond of the 3-deoxy-D-mannooctulosonic acid, also referred to as 2-keto-3-deoxyoctulosonate (KDO).

The core domain is further divided into an inner and outer core: the inner core is composed of one to three KDO residues, whereof the last residue in this region is found to be modified with a phosphate or ethanolamine group. In some LPS, the inner core is furnished to a certain extent with D-glycero-D-talo-oct-2-ulosonic acid (KO), replacing the common KDO residues[37]. The KDO residues are followed by two to three phosphorylated heptoses. In the outer core, hexoses (D-glucose,

D-mannose, D-galactose) are prevalently present. The hexoses are bound via β1→3 glycosylated linkages. Typically, the *O-antigen* is ligated to the third hexose (Figure 3). The different hexoses comprised in the outer core give the LPS its characteristic branched structure in this domain.

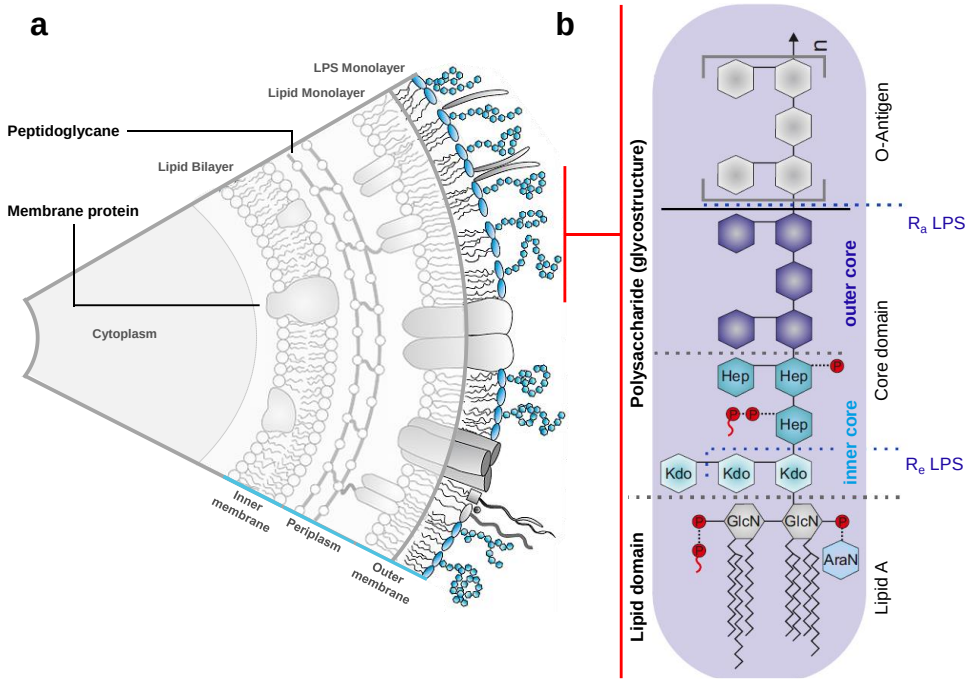

Figure 3 | General structural scaffold of the cell envelope of Gram-negative bacteria (modified)[9]. (a) Only the LPS-containing outer leaflet of the outer bacterial membrane is highlighted. (b) A simplified molecular structure of the endotoxin is depicted. The major regions are labeled: the highly variable O-polysaccharide chain or *O-antigen* is responsible for serological specificity of LPS variants. It comprises the main target for antibody responses against LPS. Lipooligosaccharide (LOS) expressing bacteria or rough mutant strains are lacking this part of the molecule; the outer core is constituted of several sugar groups such as hexoses and hexosamines; the inner core is highly conserved and contains unusual carbohydrate residues (KDO and heptoses); the *lipid A* moiety is formed by a highly conserved di-glucosamine backbone with variations in acyl chain length and substitution pattern giving the glycolipid its toxic entity.

LPS molecules that are constituted only of *lipid A* together with the inner core region are expressed by *deep-rough* bacterial strains, giving the smallest form of LPS: R_e LPS. Whereas the LPS scaffold with inclusion of the outer core region is mainly expressed by *rough* bacterial strains. LPS molecules exhibiting the whole core domain are classified as R_a LPS mutants.

1.2 Antimicrobial Peptides And Host Defense

The discovery of antimicrobial peptides (AMPs) dates back to 1939, were Dubos *et al.* identified the first substance, exhibiting antimicrobial activity in prokaryotic cells by isolation from *Bacillus brevis*[15, 41]. One year later, Hotchkiss and Dubos extracted an AMP which was termed gramicidin[3b, 42]. The group of gramicidins were found to exhibit activity against a wide range of Gram-positive bacteria *in vitro* and *in vivo*. The therapeutic potential of these compounds were confirmed in guinea-pigs by showing successful healing of infected skin traumata[3b, 43]. Gramicidins became first candidates for commercially manufactured antibiotics[3b, 44].

With the discovery of penicillin in 1928 by A. Fleming[45] and streptomycin in 1943 by A. Schatz[46] the "Golden Age of antibiotics" started and the interest in the therapeutic potential of natural host antibiotics and the importance of their immune defense strategy has taken a back seat in research for the upcoming 20 years. With the end of the "Golden Age of antibiotics" in the early 1960s, the need for alternative agents with antibiotic function became urgent by raising number of multidrug-resistant microbial pathogens. This hinge in history reawakened the interest in host defense molecules. This time point is to be considered as the true origin of research into AMPs[47]. In the same decade, the first animal AMP, bombinin[48], was found in the orange speckled frog *Bombina variegate* and the antimicrobial protein, lactoferrin[49], was isolated from cow milk. Antimicrobial peptides from leukocytes[50], today known as α-defensins, were isolated in the late 1970s and 1980s from rabbit and human cells[51]. Together with the group of purothionins, these defensins were found to be the first cysteine-stabilized AMPs. In 1981, Boman *et al.* performed essential studies for the isolation and characterization of cecropins; the very first α-helical AMP-family[52]. In 1987, a landmark study by Zasloff *et al.* revolves around the isolation and characterization of cationic AMPs from the African clawed frog, *Xenopus laevis*; he and his coworkers demonstrated the important role of these peptides, named magainins (*Hebrew:* shield) in host defense[53]. A couple of years later, another group of AMPs was identified: β- and θ-defensins were isolated from bovine granulocytes[54] and leukocytes of the rhesus monkey[55] and characterized. Up to now, over 5,000 antimicrobial substances,

thereunder more than 3,500 natural and 1,500 synthetic sequences, have been discovered or synthesized and were categorized as AMPs[15, 56].

This short review in history of AMPs shows insistently that these small effector molecules play a major role in the mammalian immune system and in host defense, including humans[11a]. A closer look on these very diverse studies established the evidence that AMPs are present all over the phylogenetic tree, from pro- (e.g. bacteria) and eukaryotes (e.g. protozoan, fungi, plants, insects, and animals) to the existence in virtually all multicellular organisms[15]. These evolutionarily ancient molecules represent the weapons to combat bacteria, fungi and viruses that have the potential to develop resistance to any conceivable agent used by default when it comes to infection[11a]. How these small effector molecules of the innate immune system have shaped up as major building block in immunity is remarkable. To put these unique features of AMPs in a nutshell, common postulated interaction sites on the host cell level for this peptide family are depicted in the illustration stated below (Figure 4).

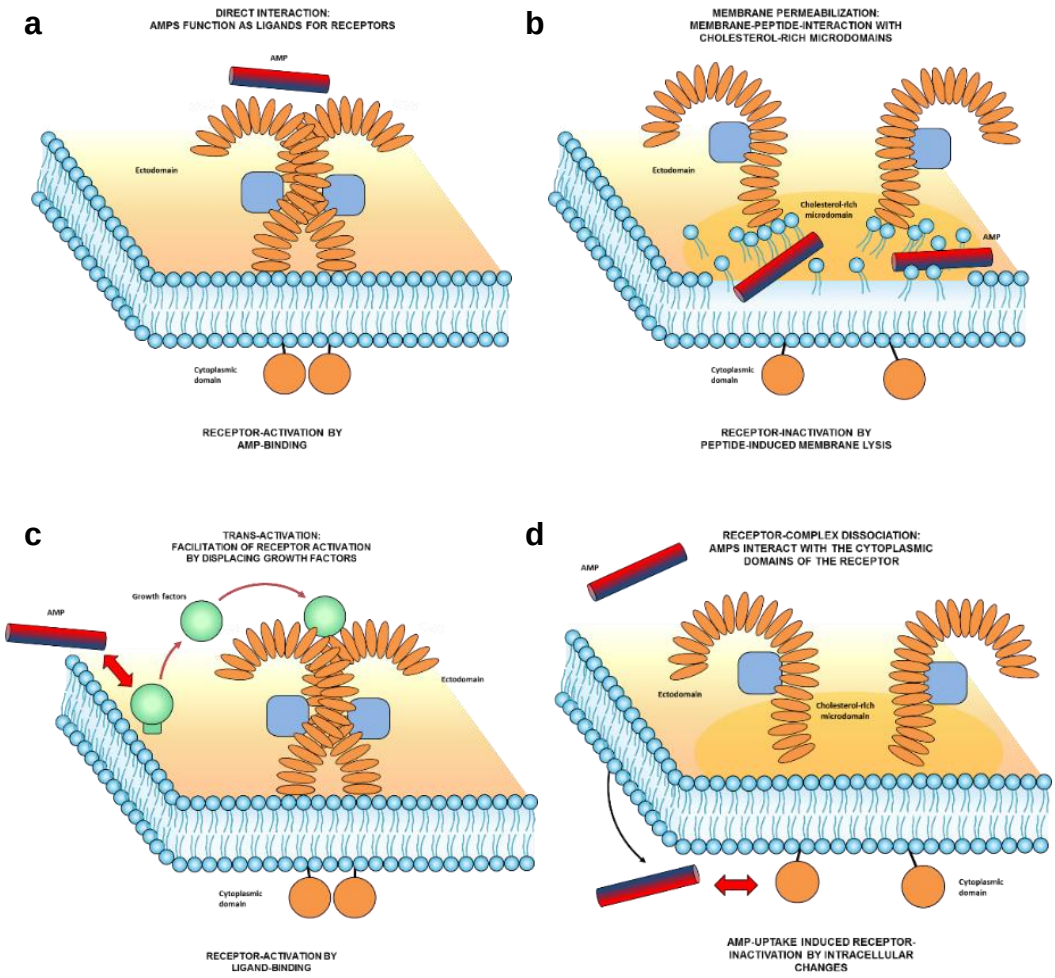

Figure 4 | Potential models for the interaction of AMPs with the host cell membrane (modified)[3]. (a) Direct binding of AMPs to the receptor complex initiating signaling. AMPs function in this model as specific ligands for the receptor. (b) AMPs induce structural changes in the cholesterol-rich microdomains associated with the receptor. This mediates a change in receptor function or dissociation with allowing the receptor to signal without a ligand or turning insensitive for ligand binding. The regular signaling cascade is switched off. (c) Trans-activation model: AMPs stimulate the release of membrane-bound growth factors which in turn binds to its high-affinity receptor facilitating receptor activation. (d) Receptor dissociation due to intracellular interactions. AMPs bind to the cytoplasmic receptor domains, inactivating the signaling cascade.

1.2.1 Immunomodulatory Properties of AMPs

AMPs comprise the ancient innate arm of the mammalian immune defense[57]. Due to their immunomodulatory function and thereby the impact on infections and inflammation, AMPs are also often referred to as host defense peptides (HDPs)[58]. These small molecules have an outstanding role in the process of immunity, supported by a multitude of factors: negligible

resistance induction potential, sequence and structural diversity, wide distribution in immune cells (e.g. leukocytes, Paneth cells) and alerting phase tissues, thereunder gut and trachea, sensing bacterial infections[58]. Patients found to have a deficiency in certain HDPs (cathelicidins and defensins) are more prone to infections than patients with accurate function of AMP expression[58-59]. A correlation between the expression of HDPs and the states of infection and inflammation is confirmed, emphasizing the necessity of this peptide family not only in host defense but also in clearance, prevention and protection against bacterial assault.

HDPs can expose both direct antimicrobial activity by interaction with the hostile membrane, resulting in direct killing of the invading pathogen and by immune modulating activity (Figure 5)[58]. Latter demonstrates, that HDPs exhibit stimulating activity towards a wide set of biological effector molecules relevant for putting the host cell on alert and triggering the innate and adaptive immune system. HDPs were found to stimulate neutrophils and epithelial cells (innate immune system) and monocytes, macrophages and dendritic cells (linking innate and adaptive immune system)[58]. HDPs of higher organisms modify several cellular functions and participate in every facet of it, by boosting, inhibiting or complementing the immune response, whereof the suppression of pathogen-induced cytokine release, confirms the anti-inflammatory role of these molecules[60].

All in all, HDPs have a two-condition identity[60]: They can protect the host and at the same time the organism. In host defense, the peptides direct their antimicrobial activity against harmful pathogens and stimulate immune functions. Simultaneously, the organism is protected from detrimental effects of an excessive inflammatory response.

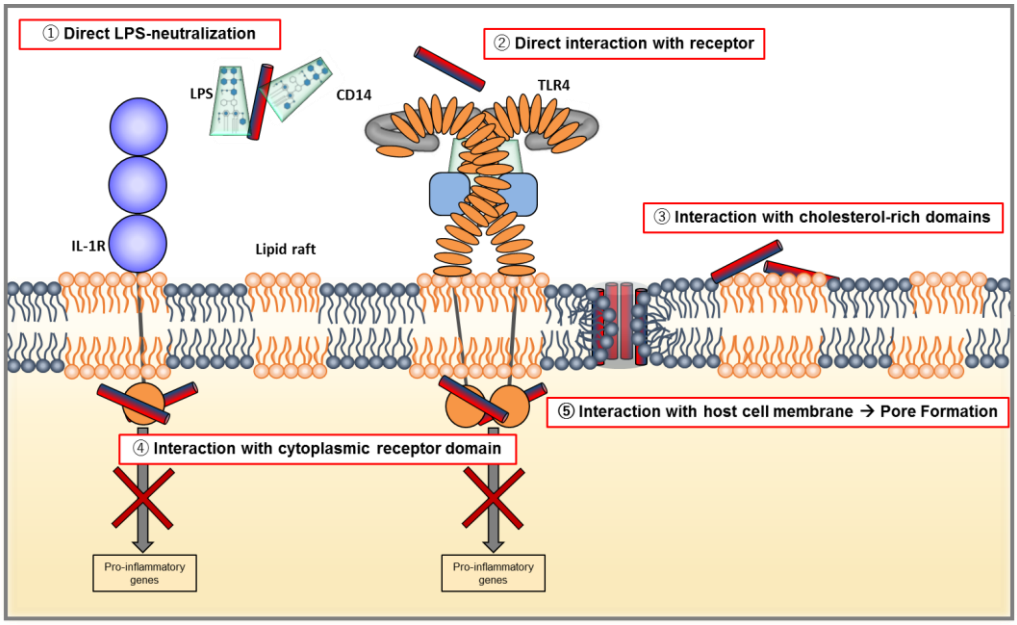

Figure 5 | Possible points of interference for peptide-induced modification of the immune system. ① Host defense by direct neutralization of LPS. ② Receptor mediated interaction: HDPs can alter the ligand-binding site or function as ligands by themselves. ③ Immunomodulatory function through receptor inactivation by interaction with the cytoplasmic TIR-domains of the signaling receptor complex. ④ Modulation of cholesterol-rich microdomains inhibit receptor dimerization, resulting in inactivation of the signaling cascade. ⑤ Membrane-directed antimicrobial activity leading to severe changes in membrane structure and composition with membrane disintegration through pore formation.

1.2.2 Peptide Scaffold and Characteristics

In general, AMPs are oligopeptides consisting of 12 to 50 amino acid residues of which two to nine are positively charged and up to 50% are hydrophobic amino acids[60]. Hancock *et al.* defined the term (cationic) host defense peptides due to their immune regulatory and modulatory role and their broad spectrum of target organisms[58]. Further entries of AMPs are anionic antimicrobial peptides/proteins (AAMPs), cationic amphipathic peptides, cationic AMPs (CAMPs), host defense peptides (HDPs), and α-helical antimicrobial peptides (α-AMPs)[15]. All of these enumerated peptide factions refer to the same substance family exposing a high degree of heterogeneity regarding their primary and secondary structures, their antimicrobial activity, their effects on host cells, and the regulation of their expression. In a broad view, this peptide family is composed of a high

amount of Arg and Lys residues giving the peptide its characteristic overall positive surface charge. Due to their amphipathic structure, AMPs are able to directly interact with bacterial membranes. The typical defined secondary structural motifs are shaped upon membrane insertion.

The fundamental folding principle underlying all classes of AMPs is the ability to adopt a shape, where patches of charged and polar, and hydrophobic residues are formed. Linear members of AMPs, e.g. cecropins and magainins, reorganize their structure to an amphipathic α-helix only upon entering a membrane[11a]. Some peptides use a modified α-helical design by C-terminal disulfide bonding, adding a single loop to the original structure. The defensing-subfamily e.g. arranges in relatively rigid anti-parallel β-sheets where the disulfide bond fixes the β-sheets and allows the formation of cationic and hydrophobic patches around this scaffold[11a]. Figure 6 provides an overview of the most common structural motif found in this diverse peptide family.

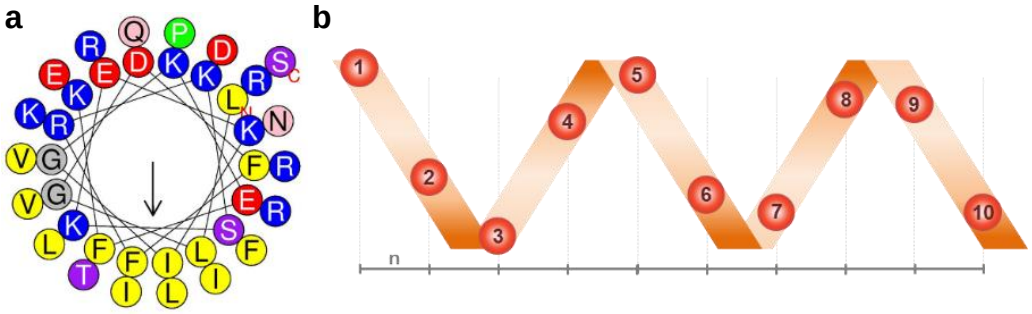

Figure 6 | Schematic representation of the α-helical peptide LL-37. (a) Helical wheel projection of the human cathelicidin (top view). The angle between two consecutive amino acid residues is 100°. C- and N-termini are marked. Color code: yellow: non-polar residues; blue: polar charged residues/basic; red: acidic residues; magenta: asparagine and glutamine; purple: serine and threonine; grey: polar uncharged residues; green: neutral residues. The arrow corresponds to the hydrophobic moment. (b) Cartoon of the lateral view of an α-helical AMP where two amino acids are located at intervals of n (n = 0.15 nm), adapted from BAHAR *et al.*[15].

In an α-helical peptide scaffold, two adjacent amino acids are arranged in 0.15 nm distance (denoted by n)[15]. Consecutive amino acids are stacked with a helical step size of 100° viewed from the peptide's central axis. Peptides exposing a β-sheet secondary structure are composed of at least two individual strands connected by disulfide bonds.

1.2.3 Possible Classification of AMPs

All the AMPs discovered up to now expose structural and functional diversity which makes it difficult to categorize them. Most of the AMPs identified up to date, can be broadly classified in four subgroups according to the peptide's secondary structure: β-sheet, α-helix, extended, and loop[15]. As a rule, cathelicidins favor an α-helical structure whereas the defensins form β-sheets. Moreover, these two groups belong to the most extensively studied ones.

Another categorization can be made according to Bahar and Ren taking the different targets of the AMPs and their mode of action for further differentiation.

1.2.3.1 Antiviral Activity of AMPs

Antiviral AMPs are able to target both enveloped RNA and DNA viruses[15, 61]. This class of AMPs neutralize viruses by interaction with the viral envelope or the threatened host cell membrane by several mechanisms: These peptides can either reduce the binding affinity of the virus to the host cell[62] or inserts into the viral envelope, leading to membrane disintegration and instability[63]. Both potential routes result in massive changes, whereby the virus is no longer able to infect the host cell. Besides these processes, a number of antiviral AMPs bind to specific receptors on the host cell membrane responsible for viruses to get access to the cytoplasmic space[64]. Some other AMPs of this category cross the cell membrane and localize in the cytoplasm and organelles, causing e.g. changes in the gene expression profile of the host cell[15]. This leads to a modification of the host cell by which blocking of the viral gene expression is induced or a stronger activation of the host defense system allows the cell to combat the invading virus. AMPs with known antiviral activity belong *inter alia* to the defensin-family[65], but peptides beyond this subgroup can exhibit broad and diverse activity against enveloped and non-enveloped viruses as well, thereunder the human cathelicidin LL-37[65]. This human derived AMP and its mouse homologue CRAMP act as inhibitors in vaccinia virus replication[66]. Thus it appears that LL-37 induces alterations

in morphology of vaccinia virus by evidence, indicating a direct effect on the virion[65]. The bovine cathelicidin indolicidin exhibits inhibitory function on HIV *in vitro*[63a], whereas other candidates isolated from amphibian skin interfere at an earlier stage with the virus and block infection during viral entry[67].

1.2.3.2 Antibacterial Activity of AMPs

AMPs classified in this category are extensively studied. These peptides can perfectly interact with the bacterial cell membrane due to their cationic nature. Antibacterial AMPs cause membrane disintegration by direct interaction with or insertion into the lipid bilayer structure. Some representatives of this peptide class leads to bacterial killing at already low concentrations without any change in membrane integrity[15]. This leads to the assumption, that these AMPs take a different route to kill bacteria: It was shown that some AMPs, exhibiting antibacterial function, can bind to RNA and DNA causing the inhibition of intracellular pathways necessary for DNA replication and protein synthesis[68]. AMPs involved in the blocking of cell wall synthesis are even able to kill antibiotic resistant bacteria[15].

1.2.3.3 Antifungal Activity of AMPs

This category of antimicrobial peptides results, as the name already implies, to the killing of fungi. The majority of this subfamily is composed of polar and neutral amino acids without any obvious correlation between peptide structure and target cell type. The antifungal peptides help the host cell to overcome mycosis by interacting directly with the cell wall of the fungus or by targeting intracellular components[69]. In contrast to antibacterial AMPs, antifungal peptides are able to bind chitin, one of the main building blocks of fungal cell walls[70]. These peptides kill the target cells by pore formation, by increasing permeabilization of the plasma membrane, or by disintegration of the fungal membrane[15].

1.2.3.4 Antiparasitic Activity of AMPs

The smallest group of AMPs is constituted by the antiparasitic peptides[15]. Representatives belonging to this category are e.g. magainin – which is also the first reported antiparasitic AMP – and cathelicidin. The latter is able to kill *Caernohabditis elegans* by the induction of pores in the cell membrane[71]. In general, antiparasitic AMPs uses the same modes of actions for killing (direct membrane interaction) as AMPs of the other categories presented and described in more detail in the upcoming sections.

1.2.4 Membrane Activity And Mode of Actions

AMPs use various modes of action to interact with the host cell and bacterial membrane to fight effectively invading pathogens: Besides pore formation and complete membrane disintegration via a detergent-like carpet mechanism it is believed that AMPs can disturb the integrity of the membrane by induction of a non-lamellar lipid phase[72]. When added to a bacterial cell suspension, AMPs are able to undergo "self-promoted uptake" to translocate the outer membrane or cell wall, followed by lysis of the cytoplasmic membrane[73]. Thus, a first association of the AMP to the negatively charged, LPS-containing bacterial cell surface is said to cause displacement of divalent cations, leading to an initial destabilization of this membrane type[73b]. All modes of action for AMPs share some common characteristics: Both major, carpet- and channel-forming, models show association of peptide monomers oriented parallel to the membrane surface, followed by accumulation of the monomers until a critical concentration is reached[73b].

Recent studies showed that AMPs work in concert and expose a synergistic effect[60], this furnishes the evidence that AMPs are able to translocate or massively change the membrane organization by using not only a single but several of the mechanisms presented in the following. Further, each of the processes described below can represent an initial, an intermediate, or a consequent step in the modes of action of AMPs.

1.2.4.1 Aggregation

For peptide aggregation, either monomers or oligomers are bound in parallel orientation onto the membrane surface. The peptides bound in monomers form oligomeric structures upon binding (Figure 7). Reorientation of the AMP-clusters lead to self-insertion into the membrane vertically to form sphere-like structures.

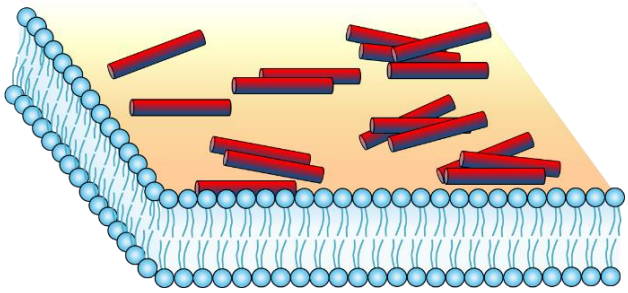

Figure 7 | Illustration of AMP self-aggregation on the membrane surface. Peptide monomers bind and accumulate parallel to the membrane surface. Recruiting of further membrane-bound peptides to form larger peptide clusters. Upon reaching the threshold concentration, peptide oligomers start self-insertion into the membrane.

1.2.4.2 Membrane Thinning

Huang *et al.* performed X-ray diffraction studies, elucidating a concentration dependent effect of AMP-induced membrane thinning[74]. In the initial state the amphipathic α-helical AMPs associate with the membrane surfaces leading to a membrane thickening in the first instance. The mismatch between increasing volume and surface area of the outer leaflet with no to only little effects of the inner leaflet may facilitate peptide self-insertion/aggregation[75]. Self-insertion of the AMPs into one leaflet of the lipid bilayer leads to the formation of a gap between the lipid molecules at the chain region (Figure 8). In reverse, the force induced by this mismatch pulls the neighboring lipid molecules to fill it.

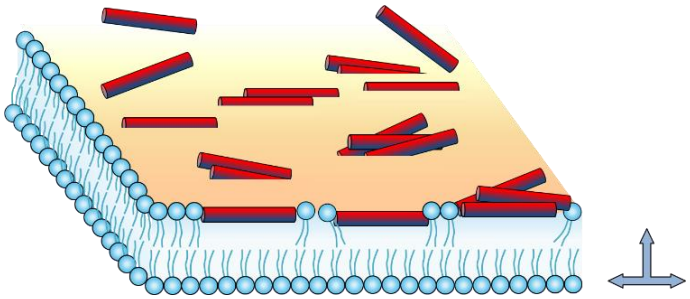

Figure 8 | Illustration of AMP-induced membrane thinning. Peptide monomers bind and accumulate parallel to the membrane surface. Recruiting of further membrane-bound peptides to form larger peptide clusters. Upon reaching the threshold concentration, peptide oligomers are immersed in the membrane outer leaflet inducing membrane thinning. The surface area of the membrane expands by simultaneous increase in strain (depicted by the three-way arrow: left/right for membrane thinning, surface expansion; arrow pointing upward stands for increase in strain.

1.2.4.3 Detergent-like Carpet Mechanism

The carpet mechanism depicts a conceptually complete different mode of action AMPs use for membrane disintegration. This permeabilization process was first described in 1988 by Steiner *et al.*[76]. In this model, peptides bind to the phospholipid headgroups and accumulate with their hydrophilic regions on the membrane surface, as the name indicates, like a carpet until a threshold concentration is reached. Above this concentration, the membrane is permeated and disintegrated in a detergent-like manner (Figure 9): The membrane composite is taken apart by reorientation of the hydrophobic residues induced by rotation of the peptide. The hydrophobic site is oriented in this way facing the hydrophobic core of the membrane. The natural curvature of the bilayer is perturbed by micellization. AMPs acting via the detergent-like carpet route have no distinct structural requirements, only a certain level of hydrophobicity and cationic charges along the peptide chain together with low binding affinity foster membrane permeation.

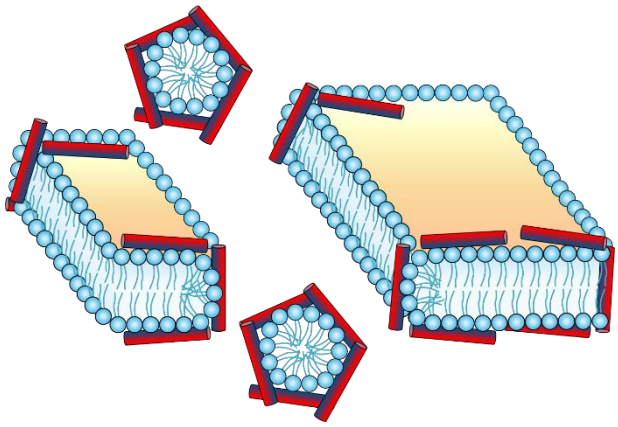

Figure 9 | Illustration of membrane disruption in accordance with the detergent-like carpet mechanism. Peptide monomers bind and accumulate parallel to the membrane surface. Progressive accumulation of membrane-bound peptide associated with the phospholipid head-groups. Leading to a "carpeting" or covering of the lipid bilayer with subsequent micellization ending in complete membrane disintegration as observed for detergents. Color code: blue, hydrophobic surface; red: hydrophilic surface.

Peptides exhibiting an overall positive charge are neither inserted into the hydrophobic core of the membrane nor self-assembly occur, where the hydrophilic regions of the peptide monomers facing each other. This model describes a situation in which the AMPs interact with the phospholipid headgroups throughout the entire membrane permeation process.

1.2.4.4 Transient-Pore Model

Despite a precise channel structure, as described in the upcoming sections for the toroidal-pore and barrel-stave model, transient pore formation across the membrane can already induce osmotic gradients that promote cell swelling and thus progressive thinning of the lipid bilayer. AMPs forming transient pores, disturb the membrane potential and pH gradients dramatically, leading to an uncoupling of ATP synthesis and thereby osmotic shock. Studies by Lafleur *et al.* revealed an increase in lipid alkyl chain disorder traced back to an increased surface area induced by osmotic swelling[73b, 77].

1.2.4.5 TOROIDAL-PORE MODEL

In the toroidal-pore model, AMPs align perpendicularly into the bilayer structure by expansion of the lipid headgroup regions. This induces a bending of the bilayer and fusion of the outer and inner leaflet (Figure 10). To transverse a membrane with a typical width of 32-38 Å[78], an α-helix with at least 22 amino acid residues is required. Most of the AMPs are too small to fulfill this structural prerequisite[73b]. Toroidal pores are constituted by a mixture of peptides and phospholipids[73b]; this compensates the prerequisite of the peptide to span the complete bilayer. The formation of these structural unique pores is accompanied by positive membrane curvature induced by AMP-accumulation at the membrane interface. Furthermore, peptide-insertion is energetically favorable and contributes positively to the pore forming process[79]. Pores with pore sizes ranging from 20 to 50 Å have been described. Beyond that, studies showed that toroidal pores are formed subsequent to peptide-induced membrane thinning allowing even shorter peptides to design a peptide/lipid pore. For LL-37 it is still highly controversially discussed whether this peptide is acting in accordance with the toroidal-pore model or if it is taking a carpet-like mechanism for membrane permeation[80].

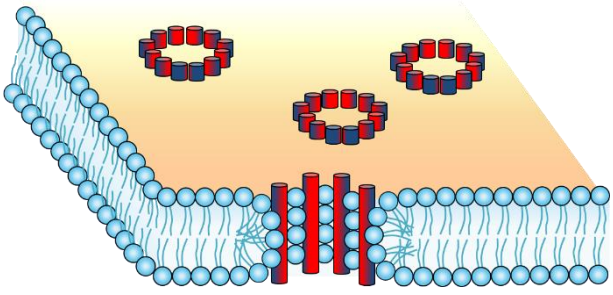

Figure 10 | Illustration of transmembrane pore formation in accordance with the toroidal-pore model. AMPs align perpendicularly into the bilayer structure by expansion of the lipid headgroup regions inducing a bending of the bilayer with fusion of the inner and outer leaflet. In this model, a mixture of AMPs and lipids comprise the scaffold of the pore. Color code: blue, hydrophobic surface; red: hydrophilic surface.

1.2.4.6 Barrel-Stave Model

The barrel-stave model depicts the second of the two described channel architectures induced by AMPs. In this case, AMPs self-associate upon membrane binding to form a transmembrane pore. These pores act as conductance channels, disturbing the transmembrane potential and ion gradients[73b]. In the biological system, this perturbance in charge distribution results in the leakage of cell components and as a last resort to cell death. Bacterial cells are no longer able to function properly and ATP-synthesis is uncoupled. In the early stages, water and ion flow are increasing, followed by total loss of the permeability barrier, which leads in the final stages to cell swelling and osmolysis. In the barrel-stave model, the amphipathic peptides are long enough to span through the hydrophobic core of the membrane. The peptides orient their hydrophobic regions towards the acyl chains of the phospholipids of the bilayer whereas the hydrophilic surfaces constitute a water-filled channel, much like staves are arranged to form a barrel. Peptides, penetrating the membrane in a barrel-stave like mechanism, need to insert into the hydrophobic core of the membrane (Figure 11). The implementation of barrel-stave transmembrane pores is mainly driven by two important properties: First, the interaction between AMPs and the target membrane is predominantly chosen by hydrophobic interactions. Second, peptides arranging in an amphipathic α-helix, need to be either composed of hydrophobic amino acids in majority or exhibit a net charge along the peptide backbone virtually neutral.

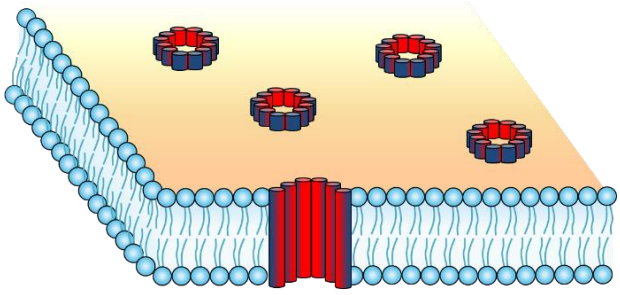

Figure 11 | Illustration of transmembrane pore formation in accordance with the barrel-stave model. Peptides reach the membrane either as monomers or oligomers and assemble parallel to the membrane surface as “staves”. Peptides insert into the lipid core of the membrane followed by recognizing additional monomers and oligomerization (barrel formation). The transmembrane pore is formed by reorganization and peptide insertion into the lipid bilayer. Color code: blue, hydrophobic surface; red: hydrophilic surface.

The fungal peptide, alamethicin is the most prominent candidate for which a barrel-stave-like mode of action was proposed. Alamethicin builds a pore comprised of eight to nine monomers with an approximately pore diameter of 18 to 26 Å[81].

1.2.4.7 SHAI-MATSUZAKI-HUANG (SMH) MODEL

This model introduced by Y. SHAI, K. MATSUZAKI, and H.W. HUANG and coworkers in the late 90s fits most of the antimicrobial peptides and comprises a combination of the long-established models described recently[82]. This model acts on the assumption, that AMPs follow a major three step mechanism, involving membrane-peptide interaction as initial step with subsequent lipid displacement and alterations of the membrane structure leading only in certain cases to peptide uptake into the target cell[11a].

A closer look reveals, that the model proposes a mode of action related on a combination of the long-established models: In the first step, AMPs bind to the membrane surface and cover it in a carpet-like manner (Figure 12, ①). Next, the peptides self-insert into the membrane, leading to membrane thinning of the outer leaflet together with an expansion of the membrane and an increase in strain all over the bilayer (Figure 12, ②). Increasing membrane stress, promotes phase transition and the formation of "wormholes". At this stage, the membrane is furnished with peptide-induced transient pores of no discrete structure (Figure 12, ③). These pores facilitate the uptake of lipid molecules and peptides (Figure 12, ④). At this stage either diffusion of the peptides onto intracellular targets (Figure 12, ⑤) or complete disintegration of the target cell membrane (Figure 12, ⑥) is induced.

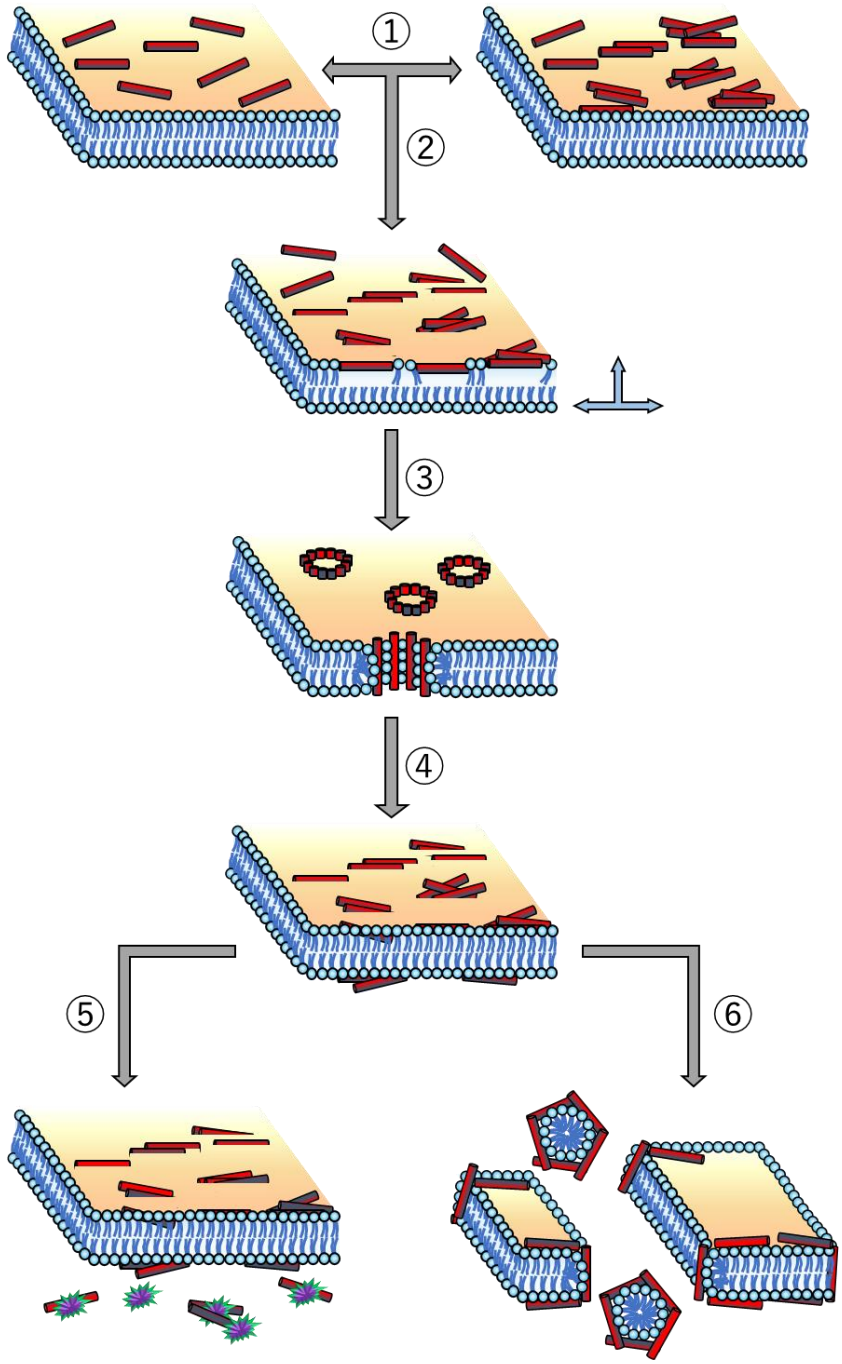

Figure 12 | The Shai-Matsuzaki-Huang model of the mode of action for an α-helical AMP (modified)[11a]. ① Peptide monomers bind to and oligomerize/aggregate on the membrane surface leaving local peptide clusters behind. ② After reaching a threshold concentration on the membrane surface, the peptide oligomers start self-insertion into the outer leaflet of the membrane. This results in membrane thinning and in turn in an expansion of the surface together with an overall increasing in strain of the bilayer (depicted by the three-way arrow where left and right resembles the membrane thinning process and the arrow pointing upward stands for the increase in strain). ③ Transient pore formation is facilitated by phase transition and "wormhole" formation. ④ Peptide-uptake and lipid-transport to the inner leaflet of the membrane. At this stage, peptides can either act ⑤ on the cytoplasmic side of the membrane and diffuse onto intracellular targets or ⑥ via complete disintegration of the target cell membrane.

1.3 Antimicrobial Peptides and Resistance

During the last decades and the ever-widening use of antibiotics, pathogens exhibiting antibiotic resistance proliferate dramatically making most of the commonly used therapeutic approaches ineffective. For a long time, antibiotics represented the choice treatment when it came to bacterial infections. The history showed, that exhibiting resistance may be a matter of months or it could take years: The advent of penicillin and streptomycin in 1943, herald the beginning of the "Golden Age of antibiotics" (*q.v. section 1.2, page 22*)[3b]. In 1945, first cases of penicillin resistances emerged from overuse. In contrast, for vancomycin it took decades after clinical introduction until first cases of vancomycin-resistant pathogens (1987) were reported.

The short replication times (20-30 min) for bacterial division together with the typical error frequency of one error per 10^7 bases forward the emergence of resistance patterns[13]. Mutations leading to antibiotic resistances can be developed in short time lags. For antibiotic resistance three main intrinsic mechanisms are discussed: (1) inactivation of the antibiotic, (2) efflux of the antibiotic, and (3) modification of the susceptible molecular target (Figure 13)[13].

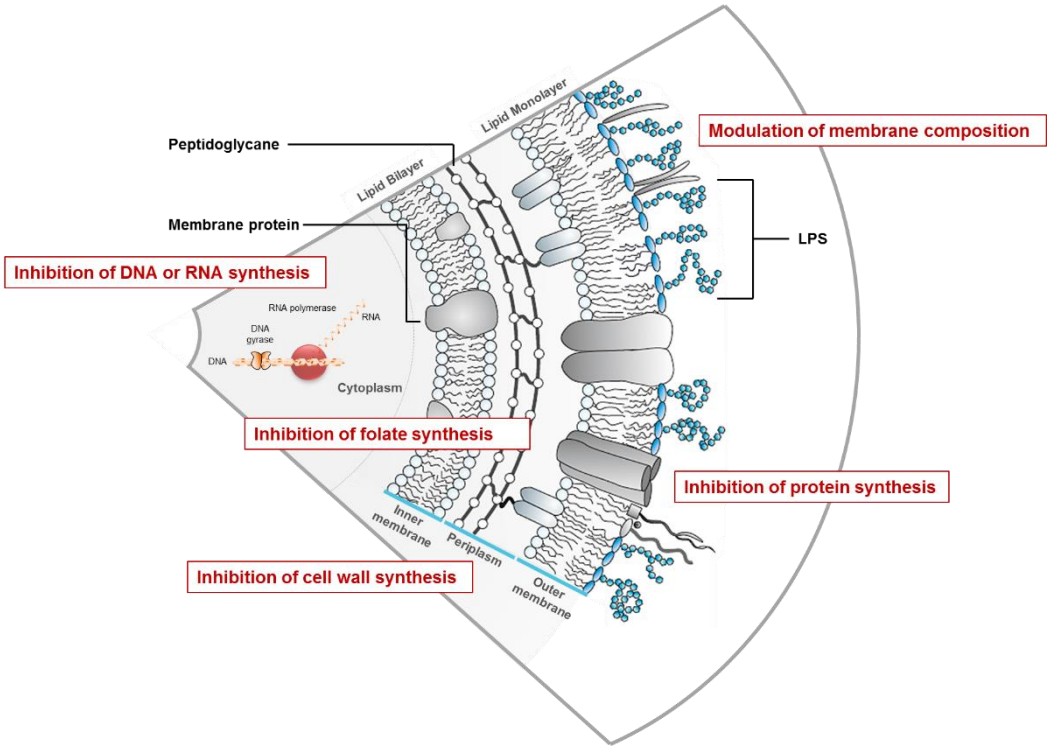

Figure 13 | Major targets for antibacterial action for Gram-positive and Gram-negative bacteria together with points of interference for acquiring resistance against common antibiotics and AMPs (modified)[9, 13]. Only a cut out of the two membranes of the Gram-negative bacterial cell envelope is illustrated.

In contrary to conventional antibiotics (e.g. penicillin or vancomycin), microbial resistance against AMPs is negligible small. AMPs manifest a unique bacterial killing strategy by exhibiting toxicity via non-specific processes rather than by an interaction with a specific protein-target[83]. As much as the modes of actions of AMPs and traditional antibiotics differ, the same is obvious for the selection pressures for developing resistance. A closer look on the resistance mechanisms described for the majority of AMPs, reveal that the pathogen is not entirely protected and thus the susceptibility to AMPs is only diminished. For bacterial strains bearing antibiotic resistance determinants it is a different matter: In this case no susceptibility to the corresponding therapeutic is detected and the antibiotic effect is completely defied[84]. Nonetheless, there exists parallels in how microorganisms can resist both HDPs and conventional antibiotics. Therein the major discussed mechanisms of antimicrobials include hydrolytic inactivation, extracellular trapping,

extrusion via drug exporters, bacterial cell envelope modifications, and bacterial exopolymer synthesis together with metabolic changes. All of the listed routes, induce resistance propensity towards both, cationic antimicrobial peptides (CAMPs) and therapeutic antibiotics. Resistance towards e.g. CAMPs can evoke from cleavage through bacterial proteases, whereas in case of antibiotics the bacterial β-lactamases manifest a similar effect and cleave β-lactam derived antibiotics. Further, secretory bacterial proteins are able to capture certain peptides. The glycopeptide intermediate resistant *Staphylococcus aureus* strains induce cell wall thickening trapping vancomycin and bar the therapeutic hence from cellular access. Furthermore, *Neisseria* genera express specific pumps, e.g. MtrCDE pump, that expel antimicrobials such as protegrins and LL-37. For antibiotics, this specific route of resistance induction is more broadly defined, because of the expression of a multitude of bacterial multi-drug exporters expelling all antibiotics with a hydrophobic nature. Antimicrobial peptides can exhibit a diminished binding affinity towards the pathogen's membrane when the bacterial cell envelope is furnished with more positively charged groups. This modification puts most of the CAMPs out of the target range and allows the invading pathogen to survive. By antibiotic treatment, especially with vancomycin, resistance is induced by exchanging D-alanine with D-lactate which leads to a lowered affinity of the antibiotic towards enterococcal cell walls. At latest, the synthesis of exopolymers together with changes in metabolic activity of the bacterium abrogates antimicrobial and antibiotic function of both HDPs and antibiotics. The corresponding formation of biofilms reduces the effect of these substances and is therefore added to the resistance potentials.

To date, AMP-resistant strains of the *enterobacteriaceae*-family, thereunder *Morganella* and *Serratia*, are known: These bacteria genera express a modulated outer membrane[11a]. These species are encased by an outer membrane lacking an appropriate density of acidic lipids to provide peptide binding sites. Another example for antimicrobial resistance is the bacteroidetes *Porphyromonas gingivalis*, that is responsible for periodontal diseases and is linked to rheumatoid arthritis. This strain exhibits strong antimicrobial resistance by secreting digestive proteases that cleave the peptides and making them inactive[11a].

Beyond that, studies on acquired resistances against AMPs have been published. In the framework of these studies, researchers have identified genes that are actually involved in virulence, but upon mutation or knocking out, these genes reprogram an already sensitive organism to be even more susceptible to a particular AMP[85].

But resistance induction with pexiganan, a synthetic AMP of the magainin-class, by chemical mutagenesis in *E. coli* and *Staphylococcus aureus* remained unsuccessful, leaving the AMPs still the best alternative to the default antibiotics.

1.4 Structure and Functions of LL-32 and PMB

1.4.1 The Human Cathelicidin Derivative LL-32

LL-32 belongs to the family of AMPs and represents a shortened fragment of the human cathelicidin LL-37 lacking the last five C-terminal amino acid residues. This cleavage resulted in an enhancement of the antimicrobial activity by exhibiting constant low cytotoxicity. LL-32 is constituted, as the name already indicates, of 32 amino acids in total with a hydrophobic face of the structural motif LIILFIF (Figure 14b) and an overall α-helical structure (Figure 14a). At low concentrations, LL-32 exists as unfolded random-coiled peptide monomer in solution. Upon increasing the concentration and the electrostatic interactions, the peptide rearranges to its active helical structure. For fluorescence studies, LL-32 is N-terminal labeled: In case of confocal laser scanning microscopy on model membranes the traditional Lissamine rhodamine B-labeled peptide ($Ex_{(max)}$: λ = 560 nm; $Em_{(max)}$: λ = 580 nm) was used, whereas for co-localization experiments together with receptor staining the more sensitive fluorescent dye Atto488-carboxy ($Ex_{(max)}$: λ = 480 nm; $Em_{(max)}$: λ = 515 nm) was introduced at the peptide's N-terminus according to the standardized solid phase Fmoc peptide synthesis performed by R. Bartels (*q.v. section 3.1.1, page 60*).

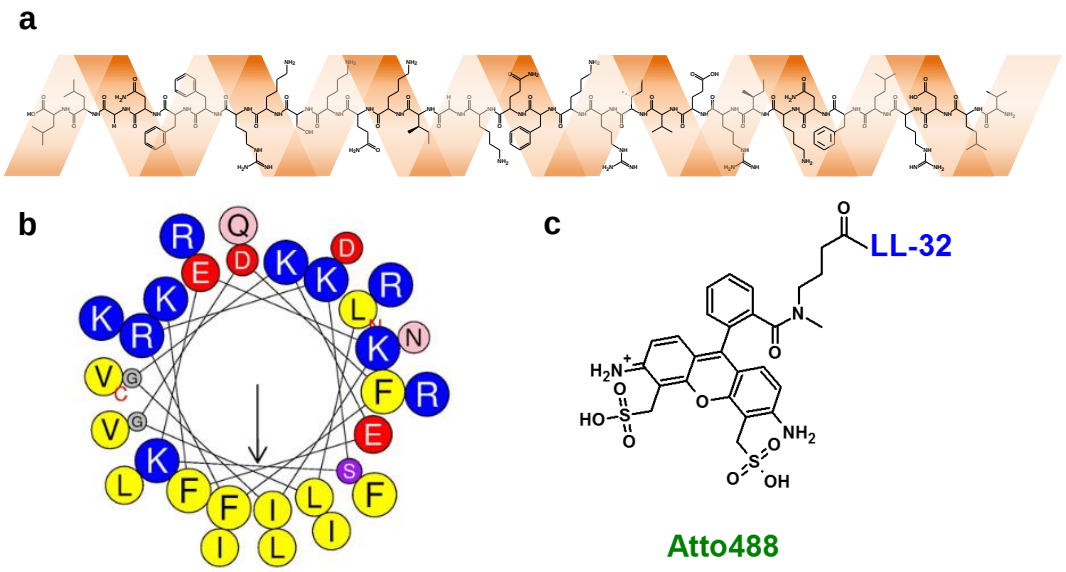

Figure 14 | Structural illustration of the AMP LL-32. (a) Molecular structure of LL-32 with an adumbrated α-helical scaffold. In average, four amino acid residues are needed for one turn. (b) α-helical wheel projection of the amino acid sequence of LL-32. The hydrophobic face is given by the amino acids LIILFIF. (c) Molecular structure of the Atto488-fluorescent label attached to the N-terminus of LL-32. (Other specific fluorescent labels are attached to the same region of LL-32, e.g. Lissamine rhodamine B).

1.4.2 The Peptide-antibiotic Polymyxin B

The lipopeptide polymyxin B (PMB) belongs to the class of bacterial non-ribosomal peptides[86] and is isolated from the bacterium *Paenibacillus polymyxa* as a mixture of isomers (B1, B1-I, B2, B3, and B6), whereof polymyxin B1 (R = *iso*-pentyl) and B2 (R = *iso*-butyl) are considered as the two major components (Figure 15).

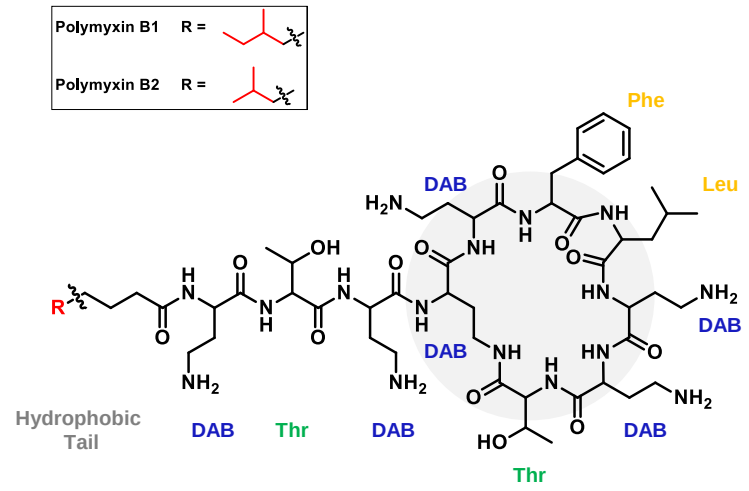

Figure 15 | Chemical structure of polymyxin B. The structure is formed by a positively charged cycloheptapeptide headgroup and a hydrophobic tail constituted of 8 or 9 carbon atoms. The headgroup charges result from the three L-α,γ-diaminobutyric acid (DAB) residues. Phenylalanine and leucine residues compose the hydrophobic locus of the peptide. The N-terminal region is furnished with two more positive charges (conferred by DAB residues at the tail group).

The group of polymyxins are constituted by cyclization of ten amino acid residues. These small peptide antibiotics exhibit a polar character in a similar vein to cell membranes with a net charge of +5 comprised by the amino acid composition and their terminal hydrophobic fatty acid chain[13]. PMB, in specific, is build up by a cycloheptapeptide ring with a C-8 (B2) or C-9 (B1) long fatty acid chain. This hydrophobic tail is linked by an amide bond to the peptide body (Figure 15). These structural characteristics facilitate the incorporation of the peptide into the bilayer of both, outer and inner membranes, of Gram-negative bacteria. Once absorbed in the membrane, PMB induces structural changes combined with a disturbing of the permeability barrier. Antibiotics belonging to this subclass, exhibit antibacterial activity against almost all Gram-negative bacilli except *Proteus* and *Neisseria* genera. Against *E. coli* and *Salmonella typhimurium* a minimal inhibitory concentration (MIC) less than 1 µg/mL was determined for PMB[86]. This high selectivity for the exertion of antibiotic activity against Gram-negative bacteria results from its high affinity for LPS[86]. The detailed mode of action on the bacterial membrane, as well as the mechanism of LPS-neutralization remain still unclear. In the literature, two major

molecular mechanisms of action are discussed, both at the membrane level: One route is related to membrane permeabilization with a detergent-like mechanism[87], whereas a second route is based on the consideration of lipid exchange of bacterial inner and outer membranes allowing the lipopeptide to undergo "self-promoted uptake"[87-88]. The membrane permeabilization model of PMB is rejected due to occurrence at concentration levels only above the determined MIC[86].

PMB is highly active against multi-drug resistant (MDR) Gram-negative pathogens present in the extracellular space. Antibiotic resistance to PMB is traced back to mutations involved in outer membrane LPS metabolism[87]. These modifications comprise the majority of mechanisms of resistance and distract the initial interaction of polymyxins in general dramatically. The anionic *lipid A* moiety of these mutated glycolipids incorporates the 4-aminoarabinose groups reducing its net charge and thereby the electrostatic attraction to PMB[89].

1.4.2.1 Labeling of PMB

The synthesis of a fluorescently labeled polymyxin species (Figure 16) was adapted from an US patent (#6,051,395) by R.M. Rocco[90]. Polymyxin B (Gibco™, ThermoFisher Scientific, Waltham, MA, USA) and the fluorescenct label (BODIPY® FL NHS Ester, Molecular Probes™, ThermoFisher Scientific, Waltham, MA, USA) are available on a commercial scale.

In the beginning of the synthesis PMB was solved in 0.1 M sodium hydrogen carbonate ($NaHCO_3$) buffer to obtain a 10 mg/mL concentrated solution. The BODIPY succinimidyl ester (5 mg) was solved in 500 µL dimethylformamide (DMF). The aqueous PMB solution (500 µL) was mixed with the organic BODIPY ester solution (100 µL) in a volumetric ratio of 5:1. To the reaction mixture, additional 500 µL of DMF were given. The obtained solution was stirred for 1.5 h at room temperature (rt). Afterwards, the solution was diluted with ultrapure water in a volumetric ratio of 1:2. The product was separated from the reactants by HPLC at λ = 214 nm.

Under alkaline (pH ≥ 9) conditions the succinimidyl ester group of the BODIPY compound will conjugate to the free primary amino groups of the polymyxin. The amino acid residues on the hydrophilic headgroup constitute a cone-like three-dimensional structure. A labeling of the amino groups at the hydrophilic region is unfavored due to the specific architecture of the peptide associated with steric hindrance. According to literature, a labeling at the L-α,γ-diaminobutyric acid (DAB) residues, DAB1 and DAB3, of the hydrophobic tail of the peptide is favored, whereof labeling at the DAB1-position is fostered[90b, 91].

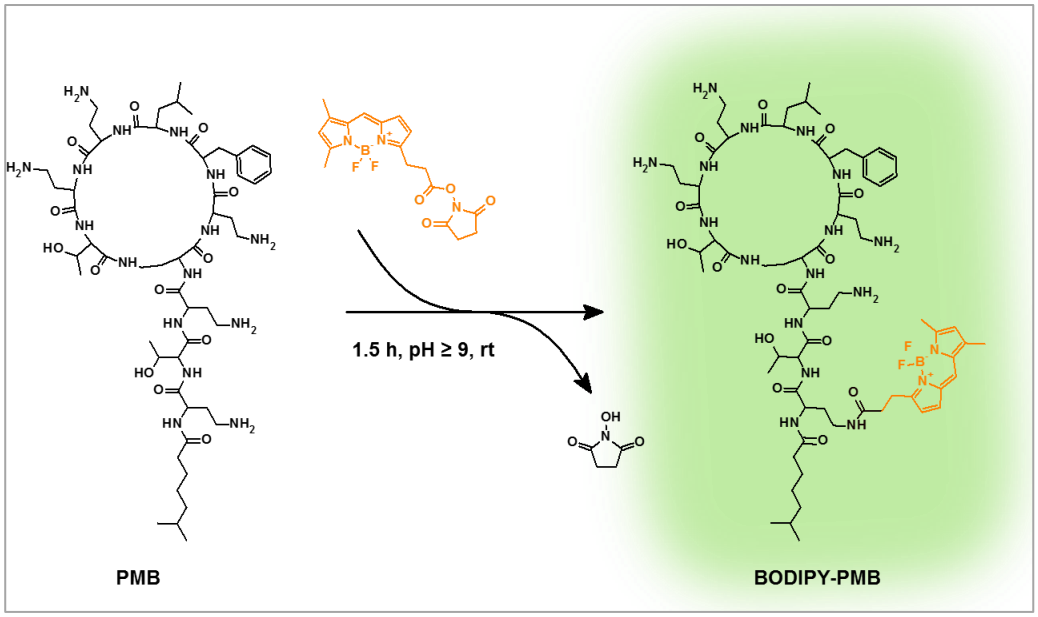

Figure 16 | Synthetic route for the labeling of peptide antibiotics. PMB is labeled with a BODIPY-species by succinimidyl ester coupling to the primary amino groups of the peptide under alkaline reaction conditions. The cycloheptapeptide headgroup is drawn as circle for clarity reasons. Color code: orange: BODIPY FL NHS ester; green: fluorescent product. The product with the labeling at the DAB1-position as primary position is depicted only.

We assume that a mixture of the product with the BODIPY-label linked at the DAB1- and DAB3-position is obtained. Peptide quality was analyzed by mass spectrometry giving the mono-substituted BODIPY-PMB compound with a molecular weight of 1477.6 g/mol. According to literature, the DAB residues located at the hydrophobic tail are responsible for LPS-interaction, therefore this compound was only used for FRAP, HEK293-TLR4/MD2-staining and membrane distribution experiments on

model and cellular membranes (*q.v. section 4.1.7, page 153; section 4.1.9, page 158; and section 4.2.2, page 204 et seqq.*)[91].

1.5 Cellular Signaling Pathways

1.5.1 The Pathogen Recognition Pathway of Toll-Like Receptors

A wide variety of pathogen components are recognized by signaling receptors. These so-called pattern-recognition receptors (PRRs) were originally reported as sensors for pathogen-associated molecular patterns (PAMPs)[4a, 92]. This receptor superfamily has the ability to recognize endogenous molecules released in response to e.g. stress or tissue damage. These molecules, often referred to as *alarmins*, together with the PAMPs, represent the damage-associated molecular patterns (DAMPs)[4a, 93]. Sensing of DAMPs results in the activation of the innate and adaptive immune response. The Toll-like receptor (TLR) family is part of the PRR-superfamily and represents an evolutionary host defense system by recognizing precisely these pathogen-derived macromolecules, ranging from bacterial and yeast cell wall components to viral and bacterial nucleic acids. This detection mechanism leads to the activation of a signaling cascade and therewith to the production of pro-inflammatory cytokines and type I interferons[4a].

The first Toll receptor protein was identified in the fruit fly *Drosophila melanogaster*[94]. In the middle of the 90s, studies of the adult insect revealed the expression of several host defense mechanisms induced by Toll signaling. These findings gave the basis for the identification of the antimicrobial peptide (AMP) *drosomycin*, considering that AMPs may play a major role in host defense of organisms lacking an adaptive immune system[94]. Because AMPs represent one of the most ancient forms of defense, pathogen-recognizing receptors sending signals for the production of AMPs are on good grounds for being the earliest receptors dedicated to defense against infections in multicellular organisms.

Up to now, ten functional TLRs (TLR1 to TLR10) have been described in humans[10a]. Mice are lacking the TLR10 receptor, but feature three additional TLRs (TLR11, TLR12, and TLR13) that are not found in the human organism[4a]. TLRs are sensors for microbes present in extracellular spaces; mammalian TLRs are not solely expressed on the cell-surface of the plasma membrane but also located intracellularly in the endosomal membrane (e.g. TLR3, TLR7, TLR8, and TLR9) where they are crucial for imparting recognition of nucleic acids[4a]. To build an active signaling unit, this receptor type has to undergo dimerization, whereof TLR2, TLR4, and TLR5 fuse as homodimers and TLR1—TLR2, TLR2—TLR6, TLR4—TLR6 build heterodimers. This enumeration shows the exceptional position of TLR4, as it can arrange in its functional unit by both, hetero- (TLR4—TLR6) and homodimerization (TLR4—TLR4). In the following, the focus will be put on the LPS-recognition pathway and the signaling through TLR4.

1.5.1.1 The TLR4-Receptor Complex and LPS-Binding

In general, the TLR-family belongs to the class of type I transmembrane proteins. They all share an ectodomain containing 19 to 25 tandem copies of a leucine-rich repeat (LRR) with a consensus sequence of LxxLxLxxN[2, 4a, 10b], forming the concave part of the receptor structure, a single-pass transmembrane domain, and a 150 to 200 residue cytoplasmic *Toll/IL-1 receptor* homology (TIR) domain[95], in which sequence conservation is primarily confined to three short motifs (box 1 to box 3)[2]. The multiple LRR-domains create a horseshoe-shaped protein scaffold and is involved in the recognition and ligand binding on either surface sides of the receptor[2, 4a, 10a]. Different amino acid compositions within the consensus sequence are responsible for variations in structural conformation of these regions and ligand specificity is reached[10b]. The recruitment of signaling adaptor molecules are mediated by the receptor's endodomain: Box 1 (FDAFISY, located at amino acid residue position 10) and box 2 (GYKLC-RD-PG, located at amino acid residue position 60) are involved in the binding of these adaptor molecules. Whereas box 3 (located at amino acid residue position 170) is predominantly involved in the directing of

receptor-localization, e.g. through interactions with cytoskeletal elements (Figure 17).

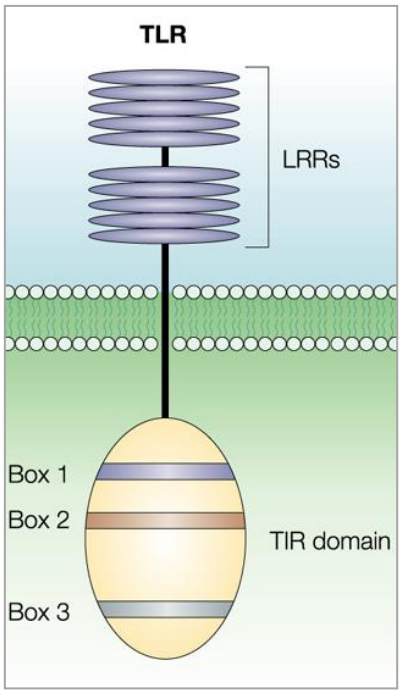

Figure 17 | Illustration of the general scaffold of the TLR receptor family[2]. Receptors belonging to the TLR-family feature an ectodomain containing 20 to 30 copies of a leucine-rich repeat (LRR) with amino acid variations in the consensus sequence of LxxLxLxxN, a single-pass transmembrane domain, and a 200 residues cytoplasmic *Toll/IL-1 receptor* (TIR) domain, in which sequence conservation is primarily confined to three short motifs (box 1 to box 3).

The TLR4 receptor complex is expressed by several types of immune cells, thereunder dendritic cells and macrophages[92, 96]. This receptor recognizes the cell wall component lipopolysaccharide (LPS) of invading Gram-negative bacteria (e.g. *Salmonella*) by a mechanism divided in both direct and indirect sensing of LPS. Systemic injection of LPS leads in minute amounts to an early sign of infections and prepare the immune system to counteract progressing infection. If the inflammatory response is amplified an uncontrolled, complete collapse of the circulatory and respiratory system can be induced[97]. This condition is termed as endotoxic or septic shock or in medical terms referred to as fatal septic shock syndrome[98]. In this state of health, the glycolipid LPS has induced an overwhelming cytokine release (e.g. TNF-α)[97].

In detail, LPS-mediated signaling requires the binding of the glycolipid to the *LPS-binding protein* (LBP). This results in a break-down of LPS-aggregates. The protein CD14 is recruited to the LRR-domains of the TLR4, building a complex. It was shown by S. D. WRIGHT and coworkers

that CD14 enhances LPS-induced inflammatory response, but that this cofactor is not mandatory for TLR4 function[99]. The receptor complex formation is completed by association of the small receptor protein MD2 to the extracellular domains of TLR4, where the sensitivity of MD2 to the acylation pattern of the *lipid A* moiety of LPS is responsible for the irreversible binding of one LPS monomer (Figure 18b). For proper LPS-recognition of the TLR4 receptor an accessory protein called *myeloid differentiation 2* receptor (MD2, also known as LY96) is needed. This protein has a size of 160 amino acids (~14 kDa) and is expressed as glycosylated soluble protein. The TLR4-cofactor MD2 cannot transmit signals on its own, because its lacking a transmembrane or intracellular domain. The protein is arranged in a β-cup fold structure, that is assembled of two anti-parallel β-sheets forming a large hydrophobic pocket. This hydrophobic pocket is required for ligand binding. Binding of LPS to the hydrophobic pocket of MD2 initiates dimerization of the two TLR4-MD2 complexes forming a homodimer (Figure 18a). The major contact interface between TLR4 and MD2 consists of two chemically distinct regions and is formed, before LPS-binding is actually initiated (primary interface; Figure 18b). These two contact-regions are termed as A and B patches and are provided by the N-terminal domain of TLR4, exhibiting a predominantly negative charge, whereas the central domains of the receptor compose the second patch with mostly positive charges[10b]. MD2 has its dimerization interface on the opposite side of this primary binding site (Figure 18c). It directly interacts with the LRR modules located at the amino acid residues in position 15 to 17 of the C-terminus of TLR4. LPS is bound directly to the TLR4 receptor by formation of hydrophobic and hydrophilic interactions (e.g. hydrogen bonds and electrostatic interactions) between the ligand and the surrounding loops of the cofactor. In addition, MD2 associates with the ectodomain of the receptor and is required for cell surface expression of TLR4[4a, 100]. Beyond that, cells lacking MD2 show to exhibit LPS-hyporesponsiveness[4a]: The cofactor MD2 is mandatory for regular TLR4-dependent function of LPS-recognition processes and LPS-response *in vivo*[100b].

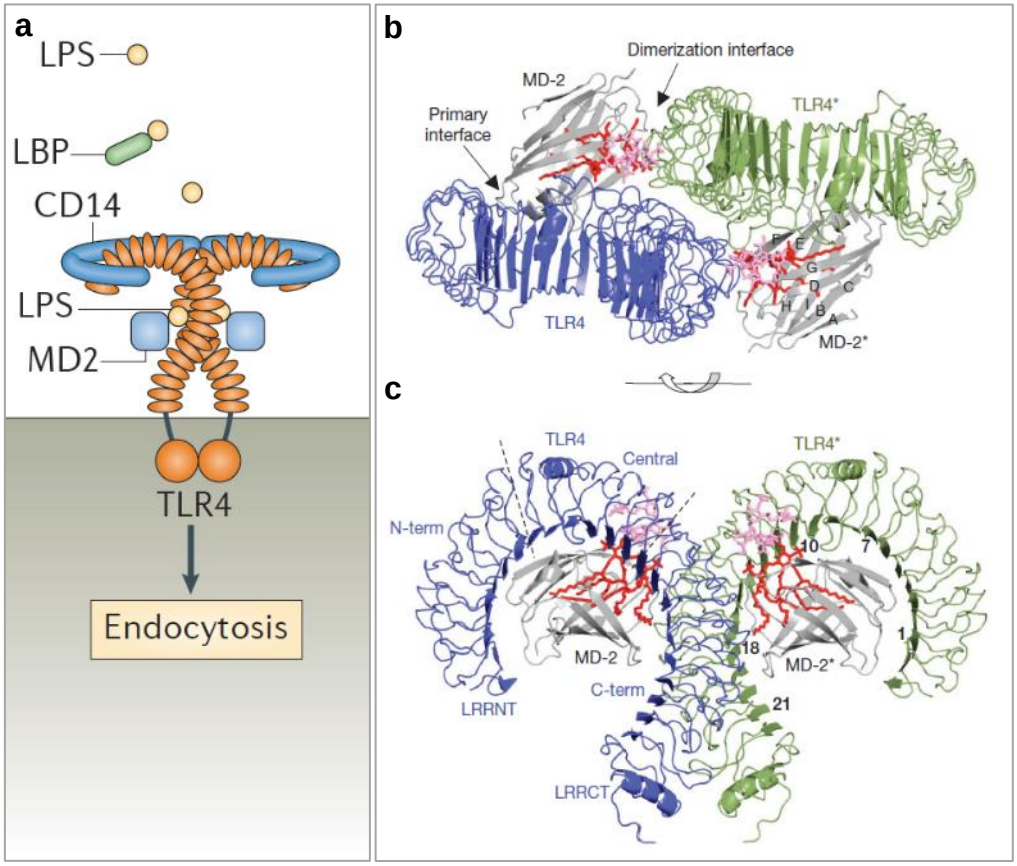

Figure 18 | Illustration of LPS-recognition and overview of the crystal structure of the TLR4/MD2-complex in the LPS-bound state. (a) Simplified mode of action of the LPS-recognition pathway[4]. (b) Bird's eye view of the homodimer of the TLR4/MD2-complex in its LPS-bound state. Prior to LPS-binding the primary receptor-cofactor interface between TLR4 and MD2 is formed. LPS-binding induces the formation of the dimerization interface. (c) Lateral view of the TLR4/MD2 complex with bound LPS. The *lipid A* moiety of LPS is highlighted in red, the carbohydrate inner core of LPS are colored magenta. LRRs module numbers of the TLR4 and the indications of the β-strands in MD2 are written in black. The first monomer of the receptor is depicted with TLR4 and highlighted in blue whereas the second monomer is designated to TLR4* and colored green. The receptor is divided in three parts: N-terminal domain, central domain and C-terminal domain. The N-terminus of the LRR-domains is occupied by a LRRNT module and the C-terminus is furnished with a LRRCT module[4b, 10].

1.5.1.2 The TLR4-Signaling Pathway And LPS

In 1997, Medzhitov, Preston-Hurlburt and Janeway established a milestone in immunology by identifying the first human homologue, the 95 kDa tall TLR4 receptor, of the *Drosophila Toll*[101].

Figure 19 shows the adaptor proteins relevant for TLR signaling. These proteins are involved in the downstream recruiting process of protein

kinases. Kinases are responsible for the activation of transcription factors e.g. *nuclear factor-κB* (NF-κB) and members of the *interferon* (IFN)-*regulatory factor* (IRF) family. Final association of the MD2-LPS hetero-complex to the ectodomains of TLR4 leads to signal transduction via the cytoplasmic TIR domains. Recruiting of adaptor proteins for further downstream triggering of the signaling cascade is induced. NF-κB, p38 and JNK/MAPK pathways are activated via TRAF6 by *myeloid differentiation primary-response gene 88* (MyD88)-dependent pathway. This signaling cascade involves the *myeloid differentiation primary-response gene 88 adaptor-like protein* (MAL, also referred to as TIRAP) as linking protein for the recruiting of MyD88. Whereas the MyD88-independent pathway signals via the *TRIF-related adaptor molecule* (TRAM) and *Toll/interleukin-1 receptor domain-containing adaptor protein* (TIRAP)[95]. The existing of these two signaling cascades give evidence for the assumption that TLR4 can function in several ways: One where CD14 is present and the full signaling potential is tapped (MyD88-independent pathway) and a second where the signaling is limited to the MyD88-dependent pathway (Figure 19)[102].

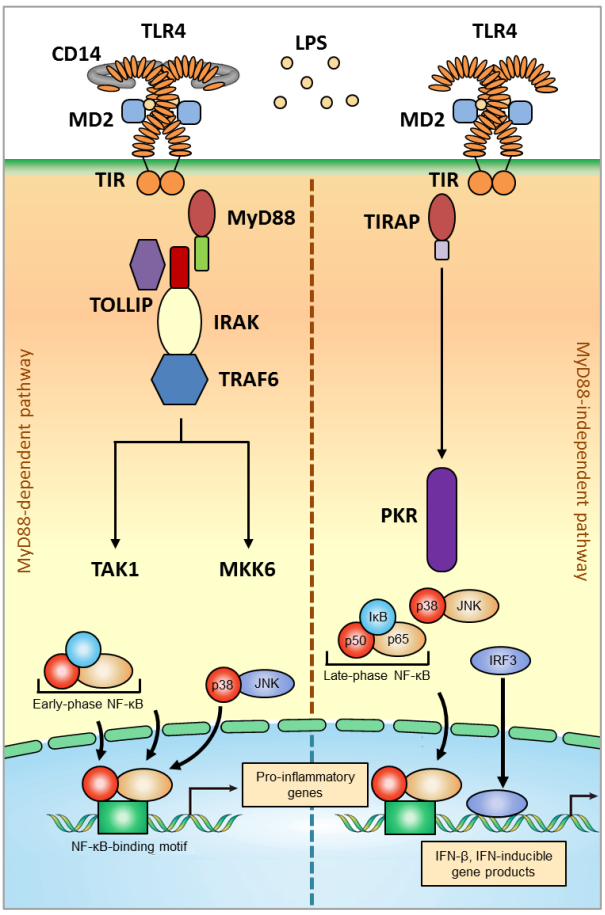

Figure 19 | Signaling pathway of TLR4 pursuant to MEDZHITOV (modified)[1]. Main components involved in signaling are illustrated: Adaptor protein MyD88, *Toll-interacting protein* (TOLLIP), *IL-1R-associated protein kinase* (IRAK), *TNF-receptor-associated factor 6* (TRAF6). TRAF6 triggers the production of pro-inflammatory genes by activation of NF-κB through *TGF-β-activated kinase* (TAK1) or by activating *c-Jun N-terminal kinase* (JNK) and p38 MAP kinases via the *mitogen-activated protein kinase kinase 6* (MKK6). TLR4 can also signal through the MyD88-independent pathway via the *Toll/Interleukin-1 receptor domain-containing adaptor protein* (TIRAP or MAL) and the downstream functioning protein kinase PKR.

1.5.2 THE PATHOGEN RECOGNITION PATHWAY OF INTERLEUKIN-1 RECEPTORS

Both, the TLR4 and Interleukin-1 receptors (IL-1Rs) have a conserved cytoplasmic TIR domain featuring three highly homologous regions (box motifs). Receptors as TLR4 and related signal transduction proteins, defined by sharing this IL-1 receptor homology domain, are all involved in host defense against pathogens. The ectodomains of TLR4 and IL-1R differ markedly in size and structure: The IL-1Rs are composed of three immunoglobulin (Ig)-like domains (Figure 20).

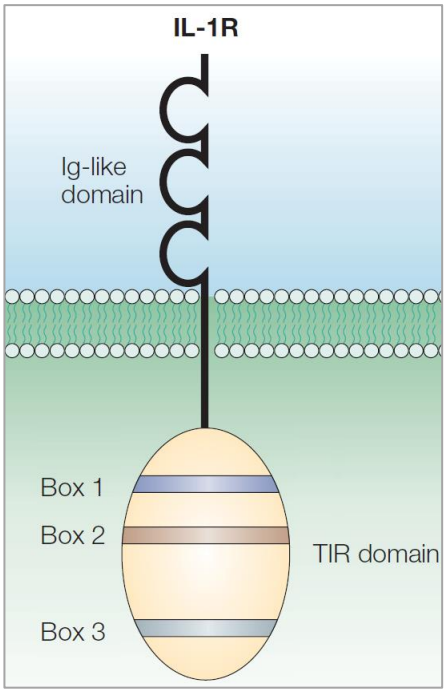

Figure 20 | Illustration of the general scaffold of the IL-1 receptor family[2]. Receptors belonging to the IL-1R-family feature an Ig-like ecto-domain composed of three Ig-units, a single-pass transmembrane domain, and a 200 residues cytoplasmic *Toll/IL-1 receptor* (TIR) domain, in which sequence conservation is primarily confined to three short motifs (box 1 to box 3).

Both, TLR and IL-1Rs signaling, rely on TIR domains and the activation of NF-κB and MAP kinases. The two receptors induce a shared signaling pathway resulting in expression of the same set of target genes. Four essential components are found to be equal in signaling via TLR and via IL-1R: the adaptor proteins MyD88 and TOLLIP; the protein kinase IRAK, and the adaptor TRAF6 (Figure 21).

MyD88 is furnished with two protein-interaction-domains: an amino-terminal death domain and a carboxy-terminal TIR domain. The adaptor protein's TIR domain associates with the cytoplasmic TIR domain of the IL-1R. The death domain of MyD88 is involved in the recruiting process of IRAK to the receptor complex by interacting with the N-terminal death domain of IRAK. Lacking the TIR domain, but bearing a C2 domain, as it is characterized for TOLLIP, offers the ability to direct interaction with the membrane lipids. Furthermore, TOLLIP can participate with different kinetics in the recruiting process of IRAK to the receptor complex by association with IRAK and the IL-1R-standing TIR domain. The functional differences between MyD88 and TOLLIP in directing the IRAK-recruiting process are not yet clearly understood. During the translocation of the receptor complex, IRAK undergoes auto-phosphorylation allowing the

association with TRAF6. TRAF6 in turn, functions downstream of IRAK and activates TAK1 and MKK6. These two kinases induce the expression of pro-inflammatory cytokines through activation of NF-κB, JNK, and p38.

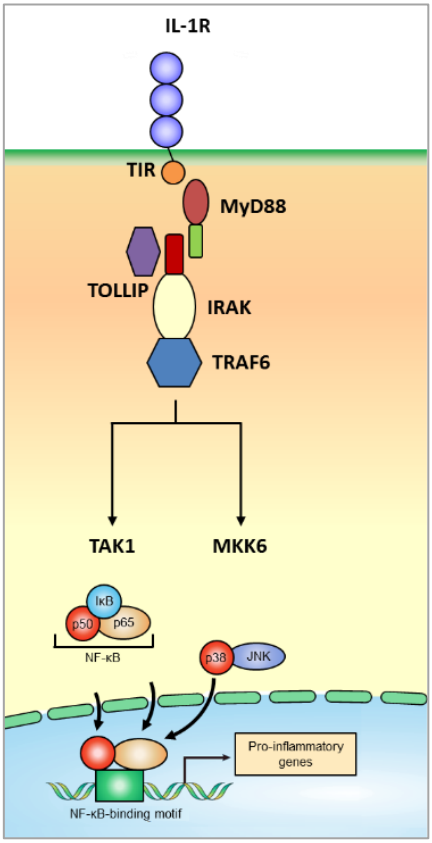

Figure 21 | Signaling pathway of IL-1R pursuant to MEDZHITOV (modified)[1]. Main components involved in signaling are illustrated: Adaptor protein MyD88, *Toll-interacting protein* (TOLLIP), *IL-1R-associated protein kinase* (IRAK), *TNF-receptor-associated factor 6* (TRAF6). TRAF6 triggers the production of pro-inflammatory genes by activation of NF-κB through *TGF-β-activated kinase* (TAK1) or by activating *c-Jun N-terminal kinase* (JNK) and p38 MAP kinases via the *mitogen-activated protein kinase kinase 6* (MKK6). Other than TLR4, IL-1R is not in the position to signal through the MyD88-independent pathway via the *Toll/Interleukin-1 receptor domain-containing adaptor protein* (TIRAP).

The IL-1 receptor fails to induce signaling in the absence of MyD88, indicating that this receptor is not in the position for signaling in a MyD88-independent pathway as it is available for TLR4. The IL-1 receptor complex only uses MyD88, which foster the evidence of differences in signal transduction by IL-1R and TLR4 even they exhibit homology of the cytoplasmic TIR-domains and feature the same signaling proteins and activate the same set of pro-inflammatory genes.

2. WORKING CONCEPT & AIMS

Host defense peptides (HDPs), as defined by GANZ and LEHRER, include only gene-encoded, ribosomal synthesized polypeptide antimicrobial substances with a length less than 100 amino acid residues and are counted as part of the very diverse peptide family of antimicrobial peptides (AMPs)[103]. These polypeptides do not expose solely antimicrobial activity against a variety of pathogens, they are also known to be involved in both the innate and adaptive immune responses by playing multifunctional roles. The ability of acting as natural antibiotic and shaping a fundamental part of the innate immune system lead to the implementation of the term HDPs. In general, it is of high importance to identify the role of HDPs in each step of inflammation and how this peptide family is involved in the whole process of host defense from pathogen sensing to immune regulation. The multifaceted action of HDPs and how these antimicrobial effector molecules manage to help the organism to neutralize invading pathogens and their pathogenicity factors, thereunder the bacterial lipopolysaccharide (LPS), is an essential component of the research work presented in this doctoral thesis. The understanding of the structural design principle of these molecules and their modes of action can represent the laying of the cornerstone for the design of new anti-infective drugs.

It is known, when it comes to bacterial infections an overexpression of an orchestra of AMPs is induced as a first line of defense, helping the organism to overcome the acute inflammatory response. Other components of innate immunity complementing this first line of defense to prevent bacterial colonization, including the barrier function of the skin, progressing acidification of the stomach, the sweeping motion of the cilia in the airway, and chemical defenses that cover host defense peptides (HDPs)[18]. This multi-faceted peptide family, initially known as AMPs, exhibit membrane and immune modulatory functions. The exact mechanism how this group of compounds interacts with the membrane is yet not clearly understood, even though various models for the interaction

of this peptide family with microbial and host cell membranes exist. As promising HDP-candidate, the α-helical peptide LL-32, a derivative of the naturally occurring human cathelicidin LL-37, was chosen for this thesis. This variant exhibits higher antibacterial activity compared to its initial structure and resembles an endogenous defense strategy, whereas the lipopeptide polymyxin B (PMB) represents an exogenous peptide antibiotic and the gold standard in terms of LPS-neutralization. The mode of action HDPs take for counter-regulating inflammatory response has been neglected for a long time. Since bacterial infections are still a worldwide health threat and drug-resistances are no isolated incidents, alternative therapeutic approaches are necessary to replace the medication of choice for bacterial infections: the prominent β-lactam- and tetracycline-based antibiotics, that are known for their high induction potential of antibiotic resistance. Therefore, the results collected on the basis of LL-32 and PMB in this thesis, represent a relevant basis for the design of anti-inflammatory therapeutic peptides by understanding the detailed mechanism of host defense during each step of inflammation. The working concept of this thesis can be divided into five major approaches combing the two strategies AMPs teach us – membrane and immune modulatory activity. This five-step working model covers the essential sites of interference for analyzing the mode of action of HDPs on the membrane and cellular level. Figure 22 summarizes the five strategic routes as stated below:

① Direct LPS-neutralization

② Direct interaction with the TLR4 receptor complex

③ Interaction with the cholesterol-enriched microdomains

④ Interaction with the cytoplasmic TIR domains of the receptor

⑤ Interaction with the host cell membrane and pore formation

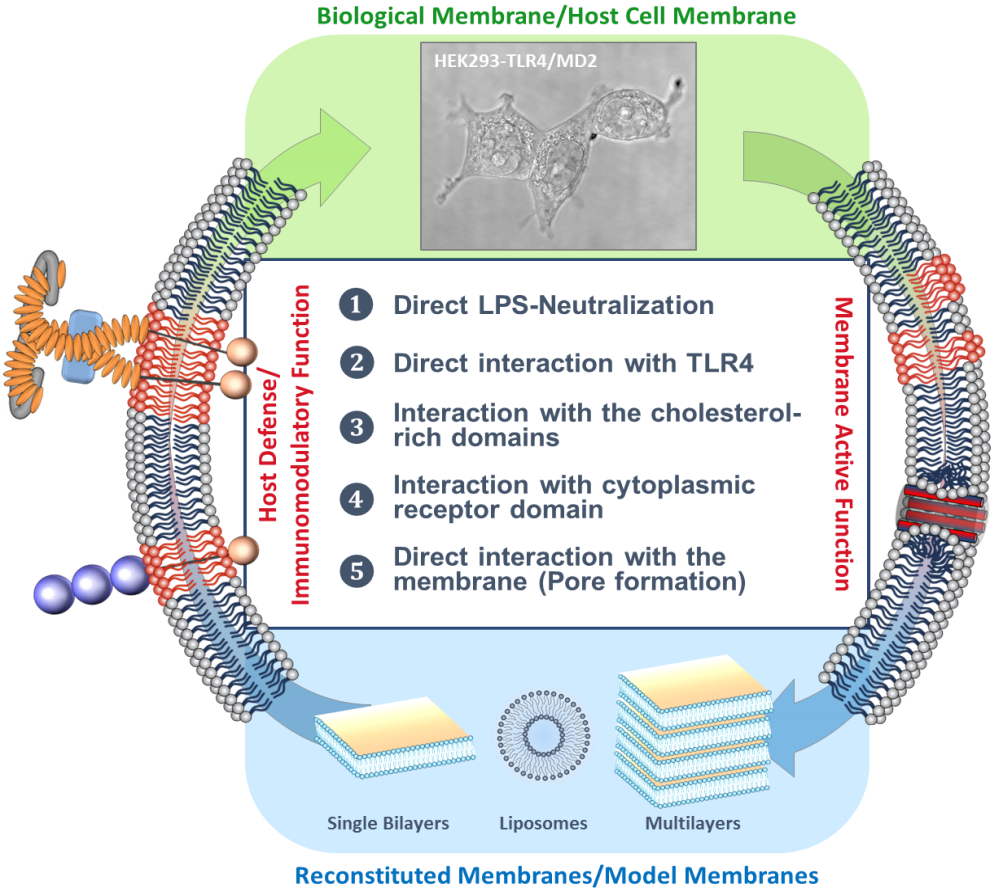

Figure 22 | Working concept for the characterization of host defense mechanisms on the membrane and cellular level taken by HDPs. ① Immune regulation by direct neutralization of LPS; ② Decrease of pro-inflammatory cytokines by receptor inactivation through direct interaction with the ectodomains; ③ Inhibition of receptor complex recruiting through interaction with cholesterol-rich microdomains; ④ Peptide-uptake allows the interaction with cytoplasmic receptor domains leading to an inactivation of the signaling complex; ⑤ Peptide-induced pore formation leads to a destabilization of the cell membrane and to leakage of intracellular components.

This concept pools results obtained from natural biological membranes and reconstituted model membranes to monitor processes, from membrane binding and insertion over pore formation to membrane lysis, of LL-32 and PMB localized on the membrane surface. As mimicry for the host cell membrane, macrophages isolated from human blood were used in the first instance. Cellular processes are rapidly transduced on this cell type. Therefore, with experimental progress, the focus was changed to a specific mutation of a HEK293 cell line, wherein the IL-1 receptor and the TLR4/MD2 receptor complex are expressed by lacking the accessory protein CD14. This defined immune cell homologue facilitated the monitoring of

cellular processes located on the membrane surface due to its specific membrane morphology and the slowed down course of membrane-associated processes. Thus, the HEK293-TLR4/MD2 cell line replaced the human macrophages as host cell membrane mimicry. The differentiation between direct LPS-neutralization (①) and receptor-mediated processes by interaction with the receptor's ecto- (②) or cytoplasmic domains (④) was realized by a complex series of stimulation experiments. The cytokine release induced by LPS- (①), TNF-α (②), and IL-1β (④) and the related regulatory function induced by LL-32 and PMB was studied (*q.v. section 3.7, page 118*).

Together with the cellular system, a wide experimental set of biophysical techniques was used to approach membrane-peptide interactions: The integration of LL-32 and PMB into the membrane was studied by FRET-intercalation assay (*q.v. section 3.5.2, page 105*). This assay provided information about the degree and ability of these compounds for membrane insertion. The interaction with cholesterol-rich membrane regions (③) could be monitored in this assay by the successful introduction of a FRET-pair, that allowed the differentiation between cholesterol-rich and -poor areas and therewith the influence on the intercalation process. The process of peptide-induced pore-formation (⑤) was investigated by various techniques, thereunder the potassium iodide quenching assay (*q.v. section 3.4.2, page 88*). This method facilitated the monitoring of small lesions by collisional fluorescence quenching. Pore-spanning (*q.v. section 3.4.3, page 91*) and tethered membranes (*q.v. section 3.4.4, page 93*) complemented the liposome-based assays and provided information on a planar system. The entire range of membrane-mediated processes can be demonstrated from early (intercalation) to late phase (membrane lysis) by this array of assays. Immobilization of giant vesicles (iGUVs) by avidin-biotin chemistry enabled the analysis of fluorescence distribution of membrane- and peptide-bound fluorophores (*q.v. section 3.5.1.3, page 103*), revealing that LL-32 and PMB bind to contrary membrane domains. X-ray studies of membrane stacks (*q.v. section 3.6.1, page 110*) and oriented circular dichroism (*q.v. section 3.6.4, page 115*) confirmed the in-lab results and showed that LL-32 exhibits, in contrast to PMB, a lipid raft stabilizing function under inflammatory conditions.

From an interpretation of the collected data, a two-step host defense mechanism for both, LL-32 and PMB, is proposed and it was possible to identify the dual role of LL-32 by its interaction via membrane- and receptor-mediated pathways in the process of anti-inflammatory regulation of immune cells.

3. MATERIAL & METHODS

3.1 SET OF SUBSTANCES

3.1.1 PEPTIDE SYNTHESIS AND LABELING

All natural and labeled peptide species used throughout this experimental research work were synthesized in-house at the *Research Center Borstel* by R. BARTELS in accordance with a standardized solid-phase Fmoc-synthesis protocol. The peptide synthesis is run out in an automated experimental lapse either on the peptide synthesizer ASP 222 (Intavis, Bioanalytical Instruments, Cologne, Germany) or 433A (Applied Biosystems, Carlsbad, CA, USA). Peptide quality was first proofed by RP-HPLC at 214 nm followed by additional mass spectrometry. Labeled peptides were coupled to carboxy-functionalized Atto488-fluorophores (Atto488 carboxy, Atto-Tec GmbH, Siegen, Germany) at the peptides' N-terminus. Polymyxin B (PMB) sulfate purified from *Paenibacillus Polymyxa* (Gibco™, ThermoFisher Scientific, Waltham, MA, USA) was coupled to succinimidyl ester functionalized 4,4-difluoro-5,7-dimethyl-4-bora-3a,4a-diaza-s-indacene-3-propionic acid (BODIPY® FL NHS Ester, Molecular Probes™, ThermoFisher Scientific, Waltham, MA, USA).

Peptides were dissolved, unless otherwise noted in 0.01% trifluoroacetic acid (TFA) to yield final stock concentrations of either 1 mM for cell culture experiments and 1.5 mM for model membrane assays. Further dilutions were prepared in 0.01% TFA or 5 mM HEPES (4-(2-hydroxyethyl)-1-piperazineethanesulfonic acid; Merck, Darmstadt, Germany) adjusted to pH 7.0 – depending on the particular experimental requirements – giving final peptide concentrations of 1, 3 and 10 µM. Labeled peptides were dissolved in ultrapure water to 1 mM stock concentrations. Stock-solutions were stored at −20 °C; for ongoing experiments peptides were kept at 4 °C to minimize freeze/thawing.

3.1.2 Antimicrobial and Membrane Active Agents

3.1.2.1 Human Cathelicidin LL-37

The 37 amino acids long peptide LL-37 belongs to the class of cathelicidin-related antimicrobial peptides. This class of polypeptides are expressed by diverse cell types (e.g. lysosomes, polymorphonuclear leukocytes, and keratinocytes) and therefore is found all over the human body. In common, all cathelicidins feature one highly conserved region (cathelin domain) followed by a highly variable cathelicidin (C-terminal) antimicrobial domain[104]. This is the reason why members of this peptide family are structurally heterogeneous. The human cathelicidin LL-37 plays a crucial role in innate immune defense against invasive bacterial infections and exhibits an α-helical structure, an amphipathic character, and an overall cationic net charge. The used cathelicidins and fragments feature all the same peptide scaffold and properties. The α-helical wheels (*q.v. Appendix II, page 282*) were plotted and the physicochemical properties (Table 1) were determined by *HeliQuest Analysis*[105].

TABLE 1. AMINO ACID SEQUENCE OF THE HUMAN CATHELICIDIN LL-37 AND SELECTED CHARACTERISTICS[105]

H-LLGDFFRKSKEKIGKEFKRIVQRIKDFLRNLVPRTES-NH_2	
Chemical formula	$C_{205}H_{341}N_{61}O_{52}$
Molecular weight (MW) in Da	4492.3
Hydrophobic moment (µH)	0.521
Hydrophobic face	LIILFI
Net charge z	6
Polar/Nonpolar-residues ratio in %	62.2:37.8
(number of residues)	(23:14)

3.1.2.2 Cathelicidin Representatives

3.1.2.2.1 LL-32

The antimicrobial peptide LL-32 is derived from the human cathelicidin LL-37 by cutting off the last five amino acids (Table 2). This shortening resulted in an increased antimicrobial and biological activity compared to the natural occurring LL-37[106].

TABLE 2. AMINO ACID SEQUENCE OF LL-32 AND SELECTED CHARACTERISTICS[105]

H-LLGDFFRKSKEKIGKEFKRIVQRIKDFLRNLV-NH_2	
Chemical formula	$C_{182}H_{303}N_{53}O_{43}$
Molecular weight (MW) in Da	3921.7
Hydrophobic moment (µH)	0.615
Hydrophobic face	LIILFIF
Net charge z	6
Polar/Nonpolar-residues ratio in %	59.4:40.6
(number of residues)	(19:13)

3.1.2.2.2 CAP18

The rabbit protein CAP18 has a weight of 18 kDa and a 37 amino acids long lipopolysaccharide-binding domain at its C-terminus (Table 3)[107]. CAP18 was first isolated from rabbit granulocytes[107]. Invasive Gram-positive and Gram-negative bacteria, thereunder *Staphylococcus aureus*, *Streptococcus pneumonia*, *Escherichia coli* (*E. coli*), *Pseudomonas aeruginosa*, and *Salmonella typhimurium*, are neutralized by CAP18 on the strength of its broad antimicrobial activity[107].

TABLE 3. AMINO ACID SEQUENCE OF THE RABBIT AMP CAP18 AND SELECTED CHARACTERISTICS[105]

H-GLRKRLRKFRNKIKEKLKKIGQKIQGLLPKLAPRTDY-$CONH_2$	
Chemical formula	$C_{202}H_{357}N_{69}O_{46}$
Molecular weight (MW) in Da	4432.5
Hydrophobic moment (µH)	0.471
Hydrophobic face	FLLIILLI
Net charge z	12
Polar/Nonpolar-residues ratio in %	62.2:37.8
(number of residues)	(23:14)

3.1.2.2.3 CRAMP

The 33 amino acid long cathelicidin-related antimicrobial peptide (CRAMP) is the LL-37 homolog found in mice (Table 4) and has been first identified in murine bone marrow cells and neutrophils[108]. CD spectral analysis revealed similar structural behavior compared to other AMPs of

the cathelicidin family and confirmed the formation of an amphipathic α-helix[108].

TABLE 4. AMINO ACID SEQUENCE OF THE MURINE AMP CRAMP AND SELECTED CHARACTERISTICS[105]

H-GLLRKGGEKIGEKLKKIGQKIKNFFQKLVPQPE-$CONH_2$	
Chemical formula	$C_{173}H_{295}N_{49}O_{43}$
Molecular weight (MW) in Da	3749.5
Hydrophobic moment (µH)	0.540
Hydrophobic face	IILLILP
Net charge z	6
Polar/Nonpolar-residues ratio in %	63.6:36.6
(number of residues)	(21:12)

3.1.2.2.4 BMAP-27

The bovine myeloid antimicrobial peptide 27 (BMAP-27) is 27 amino acids long and widely distributed in the organisms of cattle (Table 5). The amino acid residues 1-18 can arrange as amphipathic α-helix[109]. This peptide exerts antimicrobial activity against Gram-positive and Gram-negative bacteria (including methicillin-resistant *Staphylococcus aureus*), fungi, and cancer cells. BMAP-27 is said to induce damage of plasma membrane integrity and cell death by apoptosis[109].

TABLE 5. AMINO ACID SEQUENCE OF THE BOVINE AMP BMAP-27 AND SELECTED CHARACTERISTICS[105]

H-GRFKRFRKKFKKLFKKLSPVIPLLHL-$CONH_2$	
Chemical formula	$C_{158}H_{263}N_{45}O_{27}$
Molecular weight (MW) in Da	3225.1
Hydrophobic moment (µH)	0.456
Hydrophobic face	LFLLFFIF
Net charge z	10
Polar/Nonpolar-residues ratio in %	51.9:48.2
(number of residues)	(14:13)

3.1.2.2.5 BMAP-28

The bovine myeloid antimicrobial peptide 28 (BMAP-28) is 28 amino acids long (Table 6) and helps the organism of cattle to overcome inflammation by clearance of unwanted cells. This member of the

cathelicidin family is known to induce apoptosis in transformed cell lines and activated lymphocytes at doses in the low micromolar and submicromolar range[104].

TABLE 6. AMINO ACID SEQUENCE OF THE BOVINE AMP BMAP-28 AND SELECTED CHARACTERISTICS[105]

H-GGLRSLGRKILRAWKKYGPIIVPIIRI-$CONH_2$	
Chemical formula	$C_{145}H_{250}N_{44}O_{29}$
Molecular weight (MW) in Da	3073.9
Hydrophobic moment (µH)	0.503
Hydrophobic face	ALIYIGLIWGIGL
Net charge z	7
Polar/Nonpolar-residues ratio in %	46.4:53.6
(number of residues)	(13:15)

3.1.2.3 HUMAN β-DEFENSIN 3

The synthetic variant of the natural occurring human β-defensin hBD-3 is composed out of 45 amino acids. The sixfold mutation of cysteine to serine led to a structural reorientation of the molecule. The missing three disulfide bridges yield in a linearization of the peptide (Table 7). The so-called hBD-3-l (or hBD-3-6S) was encountered to have an enhanced activity compared to its related origin[110].

TABLE 7. AMINO ACID SEQUENCE OF THE SYNTHETIC VARIANT OF THE β-DEFENSIN 3 AND SELECTED CHARACTERISTICS[105]

H-GIINTLQKYYSRVRGGRSAVLSSLPKEEQIGKSSTRGRKSSRRKK-$CONH_2$	
Chemical formula	$C_{216}H_{378}N_{76}O_{64}$
Molecular weight (MW) in Da	5063.9
Hydrophobic moment (µH)	n.a.
Hydrophobic face	n.a.
Net charge z	11
Polar/Nonpolar-residues ratio in %	73.3:26.7
(number of residues)	(33:12)

3.1.2.4 ARENICIN-1

The 21 amino acids long isoform 1 of arenicin (Arenicin-1) features a β-hairpin structure and contains one disulfide bond (Table 8). The disulfide bond between carboxy- (Cys3) and amino-terminal end (Cys20) forms a

unique ring-like structure comprised of 18 amino acids[111]. Arenicin-1 was discovered in the lugworm *Arenicola marina* and is known to exert significant broad-spectrum antimicrobial activity with a low salt-sensitivity[112].

TABLE 8. AMINO ACID SEQUENCE OF ARENICIN-1 AND SELECTED CHARACTERISTICS[105]

H-RWCVYAYVRVRGVLVRYRRCW-COOH	
Chemical formula	$C_{127}H_{193}N_{41}O_{25}S_2$
Molecular weight (MW) in Da	2758.3
Hydrophobic moment (µH)	n.a.
Hydrophobic face	n.a.
Net charge z	6
Polar/Nonpolar-residues ratio in %	33.3:66.7
(number of residues)	(7:14)

3.1.2.5 NK-2

The peptide NK-2 is derived from the cationic core region of the porcine NK-lysin protein. The peptide consists of 27 amino acid residues. Key features are an overall positive net charge (Table 9) and an amphipathic, α-helical secondary structure induced by membrane peptide interaction[113]. NK-2 exhibits strong cytotoxicity against Gram-negative and Gram-positive bacteria, but is harmless for human cell types.

TABLE 9. AMINO ACID SEQUENCE OF THE PROCINE NK-LYSIN DERIVATIVE NK-2 AND SELECTED CHARACTERISTICS[105]

H-KILRGVCKKIMRTFLRRISKDILTGKK-CONH$_2$	
Chemical formula	$C_{135}H_{187}N_{37}O_{22}S$
Molecular weight (MW) in Da	3202.0
Hydrophobic moment (µH)	0.377
Hydrophobic face	IM
Net charge z	9
Polar/Nonpolar-residues ratio in %	59.3:40.7
(number of residues)	(16:11)

3.1.2.6 LPEP19-2.5

The synthetic antimicrobial peptide was discovered by K. BRANDENBURG. The anti-lipopolysaccharide (anti-LPS) peptide was

originally derived from the *Limulus* anti-LPS factor (LALF). Further peptide mutations lead to the final structure called LPep19-2.5 (Table 10).

TABLE 10. AMINO ACID SEQUENCE OF THE SYNTHETIC ANTIMICROBIAL PEPTIDE LPEP19-2.5 (ASPIDASEPT®) AND SELECTED CHARACTERISTICS[105]

H-GCKKYRRFRWKFKGKFWFWG-NH_2	
Chemical formula	$C_{135}H_{187}N_{37}O_{22}S$
Molecular weight (MW) in Da	2712.2
Hydrophobic moment (µH)	0.258
Hydrophobic face	FGWFYF
Net charge z	8
Polar/Nonpolar-residues ratio in %	55:45
(number of residues)	(11:9)

3.1.2.7 POLYMYXIN B

Polymyxin B (PMB) is a cyclic lipopeptide isolated from the bacterium *Paenibacillus polymyxa*. This substance can be parenterally administered and act as the last resort treatment of infections caused by MDR Gram-negative pathogens, which exhibit resistance to all conventional antibiotics[87]. PMB is commercially available (Gibco™, ThermoFisher Scientific, Waltham, MA, USA) and was purchased as sulfate salt. This substance belongs to the class of peptide antibiotics.

3.1.2.8 α-HEMOLYSIN

Alpha-toxin (Sigma-Aldrich, St. Louis, MO, USA), also known as α-hemolysin, is the major cytotoxic agent released by the bacterium *Staphylococcus aureus*. This substance was identified as first member of the pore forming β-barrel toxin family. It forms pores of a distinct size as it oligomerizes in the membrane, building a ring-shaped heptamer, called *staphylococcal alpha-hemolysin pore*[114]. Transport processes through these pores, are highly concentration dependent: At low protein concentrations only monovalent ions can be exchanged leading to DNA fragmentation and apoptosis; at higher concentrations larger, divalent ions (e.g. Ca^{2+}) permissive pores are built resulting in uncontrolled calcium ion influx[115].

Influx of Ca^{2+}-ions can trigger secondary cellular reactions such as necrosis[115]. Hemolysin is shipped in a lyophilized, citric acid buffered state and is dissolved according to the instructions in the manufacturer's product sheet in ultrapure water to yield a stock solution of 0.5 mg/mL or 15 µM, respectively.

3.1.2.9 NONACTIN

Nonactin is isolated from the bacteria *Streptomyces griseus* (Sigma-Aldrich, St. Louis, MO, USA) and belongs to the group of natural macrotetrolides. It integrates into membrane systems building small pores. In presence of alkali cations (K^+), nonactin forms complexes and exerts antibiotic activity on Gram-positive bacteria. In common, this substance is used as neutral lipid soluble ammonium and potassium ionophore. A stock solution of 1.5 mM is prepared in methanol (MeOH) due to insolubility in TFA and ultrapure water. Further dilutions were prepared out of the MeOH-stock in buffer to keep the amount of MeOH as small as possible.

3.1.3 LIPIDS

The lipids used for modelling membranes are stated in the table below (Table 11+12). All lipids were acquired by purchase from Avanti Polar Lipids (Avanti Polar Lipids Inc., Alabaster, AL, USA) and dissolved in chloroform ($CHCl_3$, p.a.) to a stock concentration of 10 mg/mL. Stocks were prepared in glass vials with solvent resistant snap-on lids (Macherey-Nagel, Dueren, Germany) and stored until further use at −20 °C. Lipid-stocks were diluted according to the requirements needed as stated in the individual method sections.

TABLE 11. LIPIDS USED FOR MEMBRANE RECONSTITUTION AND IMMOBILIZATION

Abbreviations	Chemical names	Specifications
DOPC	1,2-dioleoyl-*sn*-glycero-3-phosphocholine	synthetic
SM	*N*-(octadecanoyl)-sphing-4-enine-1-phosphocholine	Brain, porcine
Chol	Cholest-5-en-3ß-ol	Ovine wool
POPE	1-palmitoyl-2-oleoyl-*sn*-glycero-3-phosphoethanolamine	synthetic
POPG	1-palmitoyl-2-oleoyl-*sn*-glycero-3-phospho-(1'-rac-glycerol)	synthetic, sodium salt
PS	L-α-phosphatidylserine	Brain, porcine
Biotin-PE	1,2-dioleoyl-*sn*-glycero-3-phosphoethanolamine-*N*-(biotinyl)	synthetic, sodium salt

TABLE 12. LIPIDS USED FOR MEMBRANE LABELING

Abbreviations	Chemical names	Specifications
BODIPY-PC	β-BODIPY® FL C5-HPC (2-(4,4-difluoro-5,7-dimethyl-4-bora-3a,4a-diaza-s-indacene-3-pentanoyl)-1-hexadecanoyl-sn-glycero-3-phosphocholine)	Headgroup labeled
Atto633-DOPE	1,2-Dioleoyl-*sn*-glycero-3-phosphoethanolamine	Headgroup labeled
NBD-12-Chol	5-cholesten-3ß-ol 12-[(7-nitro-2-1,3-benzoxadiazol-4-yl)amino]dodecanoate	Headgroup labeled
NBE-PE	1,2-dioleoyl-*sn*-glycero-3-phosphoethanolamine-*N*-(7-nitro-2-1,3-benzoxadiazol-4-yl)	Headgroup labeled, Ammonium salt
Rh-DHPE	Lissamine™ Rhodamine B 1,2-dihexadecanoyl-*sn*-glycero-3-phosphoethanolamine	Headgroup labeled, Triethyl-ammonium salt
Rh-PE	1,2-dioleoyl-*sn*-glycero-3-phosphoethanolamine-*N*-(lissamine rhodamine B sulfonyl)	Headgroup labeled, Ammonium salt

3.1.4 STIMULANTS

3.1.4.1 LPS

In this thesis, the well-defined deep-rough mutant lipopolysaccharide (LPS) WBB01 was used as major stimulant for HEK293-TLR4/MD2 cells. This cell wall component of Gram-negative bacteria, is known to have strong TLR4-activating function and was isolated and purified in its R*e*-form from *E. coli*. This membrane compound was extracted in-house according to a protocol by GALANOS and co-workers where they used a monophasic mixture, consisting aqueous phenol, chloroform and petroleum ether for the isolation of LPS from R-form bacteria[116]. The WBB01-strain, in specific, expresses LPS without any substitutions at the *lipid A* region of this molecule[117]. All rough LPS-mutants share one characteristic structural feature: lacking *O-antigen*, but possessing *lipid A* and progressively shorter core oligosaccharides[118]. For cell culture experiments, LPS WBB01 was applied in final concentrations of 1, 5, 10, 50 and 100 nM diluted from a 1 mM stock solution. The stock solution was prepared under sterile conditions in ultrapure water and all further dilutions were prepared in 20 mM HEPES (pH 7.0). Aqueous LPS (stock)-solutions were handled sterile and stored in 1.5 mL Eppendorf tubes at −20 °C until further use.

3.1.4.2 IL-1β

Recombinant human Interleukin-1β (IL-1β; PeproTech, Rocky Hill, NJ, USA) is a 17.3 kDa protein containing 153 amino acid residues. IL-1β is mainly produced by blood monocytes and resembles an inflammatory mediator. This cytokine functions as central second messenger when it comes to host response induced e.g. by LPS as exogenous pyrogens. IL-1β is a highly active secreted cytokine and interacts on the cellular level with two IL-1-receptors: Interleukin 1 receptor type 1 (IL-1R1) and type 2 (IL-1R2). IL-1β was handled under sterile conditions and diluted in ultrapure water to yield a 50 μg/mL stock solution. The stimulant was further diluted in DMEM complete media and applied in final concentrations from 1 ng/mL up to 300 ng/mL.

3.1.4.3 TNF-α

The recombinant human tumor necrosis factor alpha (TNF-α; PeproTech, Rocky Hill, NJ, USA) has a weight of around 17 kDa and forms a triangular pyramidal structure. Each protomer is 185 amino acids long. The composition of two antiparallel β-pleated sheets and β-strands giving the TNF-family its characteristic "jelly roll" β-structure. TNF-α is mainly produced by activated macrophages and is involved in systemic inflammation[119]. It is one of the cytokines that make up the acute phase reaction and has immune regulating functions. The recombinant TNF-α is used as immunostimulant and was diluted in ultrapure water to yield a 100 µg/mL stock solution. The stimulant was handled under sterile conditions. Further dilutions were prepared in DMEM complete media TNF-α was applied in final concentrations ranging from 1 ng/mL up to 100 ng/mL.

3.1.4.4 TLR4-Ligands

When it comes to the study of TLR4-pathway activation, LPS-induced activation is the first matter of choice. To distinguish between TLR4-specificity and LPS-neutralization by AMPs, other ligands for the activation of the TLR4-receptor complex were taken into account, thereunder transition metals (Ni^{2+}) and proteins (MRP8, HMGB1, Taxol).

3.1.4.4.1 Transition Metals

Transition metals are elements with a partially filled *d* sub-shell or they can give rise to cations with an incomplete *d* sub-shell. Certain members of the *d*-block are known to function as TLR4-ligand[11b, 17, 120], e.g. Co^{2+}, Ni^{2+}, Cu^{2+}, Pd^{2+}, and Pt^{2+}. In this thesis, the focus was set on the divalent cation Ni^{2+} as candidate for TLR4-ligand functioning. Ni^{2+} was applied in its hexahydrate state (Sigma-Aldrich, St. Louis, MO, USA) and diluted in ultrapure water to a stock-concentration of 30 mM. Further dilutions of the transition metal were prepared in ultrapure water and final doses of 1, 3, 10, 30, 100, 300 µM and 1 and 3 mM were administered to the cells.

3.1.4.4.2 MYELOID-RELATED PROTEIN 8

The myeloid-related protein 8 (MRP8, S100A8) was kindly provided by T. VOGL (Institute of Experimental Dermatology, University of Münster, Münster, Germany). MRP8 is a cytoplasmic protein derived from phagocytes. This protein was shown to function as endogenous TLR4-ligand in presence of CD14[121]. MRP8 was delivered under dry ice as 1.11 mg/mL stock-solution in HEPES buffered saline (HBS). To guarantee active protein, the stock-solution was thawed once and divided into user-optimized aliquots, that were stored until usage at −20 °C. According to the experimental conditions, further dilutions were prepared in PBS. MRP8 was applied in 1, 3 and 5 μg/mL.

3.1.5 BUFFERS AND SOLUTIONS

Different buffer systems were applied and adjusted to the requirements for the assays, presented during the course of this thesis (Table 13). All membrane systems were reconstituted in one of three major buffer categories: one without any alkali-ions present, a second containing 100 mM KCl (potassium chloride; Sigma-Aldrich, St. Louis, MO, USA), and a third where the potassium chloride is replaced by NaCl (sodium chloride; Merck, Darmstadt, Germany). The simplest buffer system is comprised of 5 mM HEPES (4-(2-hydroxyethyl)-1-piperazineethanesulfonic acid; Merck, Darmstadt, Germany) and can be supplemented with 0.5 mM $CaCl_2$ x $2H_2O$ ($\sigma = 0.26 \cdot 10^3$ μS/cm, pH 7.4, 37 °C) if necessary. For mimicking physiological salt concentrations of the extracellular space, the base buffer composition was expanded to 100 mM NaCl, 5 mM HEPES supplemented with 0.5 mM $CaCl_2$ x $2H_2O$ if required. For cytoplasm mimicry, a buffer system composed of 100 mM KCl, 5 mM HEPES supplemented with 0.5 mM $CaCl_2$ x $2H_2O$ ($\sigma = 11.96 \cdot 10^3$ μS/cm, pH 7.4, 37 °C), if required, was used. Unless otherwise stated, the used buffer systems were prepared with ultrapure water (0.055 μS/cm at 25 °C; Milli-Q Advantage A10, Millipore, Billerica, MA, USA), sterile filtered over a 0.22 μm pore size filter (ExpressTM PLUS, Millipore, Billerica, MA, USA) and adjusted to pH 7.4 with a pH-meter (SI Analytics Lab 860, SI Analytics GmbH, Mainz,

Germany) with base of the corresponding counterion (1 N KOH TitriPUR; Merck, Darmstadt, Germany or 1N NaOH Titrinorm, respectively; VWR International, Darmstadt, Germany). Stock-buffers (10x) were stored at −20 °C in 50 mL aliquots, buffers in use were stored at 4 °C. The pH-value of the aliquoted stock-buffers was double-checked right after filling up to the final 1x buffer volume and sterile filtered once more. All buffer conditions used and their fields of application are listed in the table below to simplify clear arrangement (Table 13).

In the sequel, buffer conditions with the composition of 5 mM HEPES, 0.5 mM $CaCl_2$ x $2H_2O$ will be denoted as low-salt (w/o KCl) and the composition of 100 mM KCl, 5 mM HEPES, 0.5 mM $CaCl_2$ x $2H_2O$ as high-salt (100 mM KCl). Unless otherwise noted in the separate method sections, no modifications of the buffer conditions were applied.

TABLE 13. BUFFERS AND THEIR COMPOSITIONS APPLIED WITH RESPECT TO THE FIELDS OF APPLICATION

Buffer compositions	Fields of Application
5 mM HEPES	FRET-Intercalation, FCS, OCD
5 mM HEPES, 0.5 mM $CaCl_2$ x $2H_2O$	FRET-Intercalation, Calcein Release, FCS, KI-Quenching, Pore-spanning membranes, tethered membranes, MONTAL-MUELLER, GUV-Immobilization
100 mM KCl, 5 mM HEPES	FRET-Intercalation, SAXS
100 mM KCl, 5 mM HEPES, 0.5 mM $CaCl_2$ x $2H_2O$	FRET-Intercalation, Calcein Release, KI-Quenching, tethaPod, MONTAL-MUELLER
100 mM NaCl, 5 mM HEPES	FRET-Intercalation
100 mM NaCl, 5 mM HEPES, 0.5 mM $CaCl_2$ x $2H_2O$	FRET-Intercalation
20 mM HEPES, pH 7.0	Peptide Dilutions for Cell Culture Experiments
10 mM Sucrose	GUV-Preparation

3.1.5.1 TFA

Trifluoroacetic acid (TFA, Riedel-De Haën, Sigma Aldrich, St. Louis, MO, USA) was prevalently used as solvent for peptides. It was diluted with ultrapure water and sterile filtered. The TFA solution was stored in brown glass screw top bottles (Carl Roth GmbH & Co. KG, Karlsruhe, Germany)

at 4 °C. For application as solvent, TFA was used in a concentration of 0.01% (v/v).

3.1.5.2 PBS

Dulbecco's Phosphate Buffered Saline (PBS, Biochrom GmbH, Merck Millipore, Darmstadt, Germany) consists of 137 mM NaCl, 2.7 mM KCl, 8.1 mM Na_2HPO_4, and 1.5 mM KH_2PO_4[122]. The phosphate ions buffer the solution to a stable pH-value of 7.4. The alkali ion ratio (Na^+:K^+) in the PBS-buffer resemble the conditions of an isotonic saline solution inducing comparable osmotic pressure as present in the human organism.

3.1.5.3 RPMI

Very Low Endotoxin Roswell Park Memorial Institute (VLE RPMI) 1640 medium (Biochrom GmbH, Merck Millipore, Darmstadt, Germany) without stable L-Glutamine uses, as most of the cell culture mediums, a hydrogen carbonate-based buffer system ($NaHCO_3$, 2.0 g/L). The reducing agent glutathione sets this nutrient solution apart. Above all, RPMI consists of a mixture of glucose, saline, amino acids, biotins and vitamins, thereunder vitamin B_{12}, inositol, choline and *para*-aminobenzoic acid (PABA) (Table 14). This cell culture media maintains physiological pH at CO_2-atmospheres of ≥ 5% and is supplemented with phenol red as pH-indicator.

TABLE 14. DETAILED LISTING OF THE COMPONENTS OF THE CELL CULTURE MEDIUM VLE RPMI 1640[123]*

Saline (in mM)		L-Amino acids (in µM)			
NaCl	102.7	Arginine	1200	Hydroxyproline	150
KCl	5.4	Asparagine	400	Proline	170
$Na_2HPO_4x7H_2O$	5.6	Cysteine	400	Threonine	170
$MgSO_4x7H_2O$	0.4	Isoleucine	400	Tyrosine	110
$Ca(NO_3)_2x4H_2O$	0.4	Leucine	400	Valine	170
$NaHCO_3$	23.8	Serine	300	Histidine	100
Choline chloride	0.02	Lysine**	219	Methionine	100
		Aspartic acid	150	Phenylalanine	100
D-Glucose	11.1	Glutamic acid	140	Tryptophan	24.5

TABLE 14. – CONTINUED FROM PREVIOUS PAGE

Vitamins (in µM)	
Vitamin B_3 (Nicotinamide)	8.2
Vitamin B_x (PABA)	7.3
Vitamin B_6 (Pyridoxine**)	4.9
Vitamin B_1 (Thiamine)**	3.0
Vitamin B_5 (Pantothenic acid)	1.1
Vitamin B_2 (Riboflavin)	0.5
Vitamin B_{12} (Cyanocobalamin)	3.7 (nM)
Other ingredients (in µM)	
myo-Inositol	194.3
Glutathione	3.25
Folic acid	2.3
Biotin	0.8

*VLE RPMI 1640 (1x) is supplemented with 28 µM phenol red as indicator; **supplemented as its hydrochloride salt

3.1.5.4 DMEM

Dulbecco's Modified Eagle Medium (DMEM, Biochrom GmbH, Merck Millipore, Darmstadt, Germany) was developed in the late 50s to culture *Polyomaviruses* in primary and secondary murine cells. Compared to standard MEM medium, vitamins and amino acids are fourfold higher concentrated and supplemented with non-essential amino acids, micronutrients, and bicarbonate. For culturing HEK293-TLR4/MD2 cells high glucose DMEM (4.5 mg/L) supplemented with 10% fetal calf serum (FCS) is used.

TABLE 15. DETAILED LISTING OF THE COMPONENTS OF THE HIGH GLUCOSE CELL CULTURE MEDIUM DMEM[124]*

Saline (in mM)		L-Amino acids (in µM)			
NaCl	110.0	Valine	802	Cysteine	400
KCl	5.4	Isoleucine	800	Glycine	400
Na_2HPO_4	1.0	Leucine	800	Phenylalanine	400
$MgSO_4x7H_2O$	0.8	Lysine**	800	Tyrosine	397
$Fe(NO_3)_3x9H_2O$	45.6 (nM)	Threonine	798	Histidine**	200
$NaHCO_3$	44.0	Serine	400	Methionine	201
Choline chloride	0.03	Arginine**	400	Tryptophan	78.3
D-Glucose	25.0				

TABLE 15. – CONTINUED FROM PREVIOUS PAGE

Vitamins (in µM)	
Vitamin B_5 (Pantothenic acid)	16.8
Vitamin B_2 (Riboflavin)	1.1
Vitamin B_3 (Nicotinamide)	32.75
Vitamin B_1 (Thiamine)**	12.0
Other ingredients (in µM)	
myo-Inositol	40.0
Pyridoxal**	20.0
Folic acid	9.1

*DMEM (high glucose variant) is supplemented with 42.3 µM phenol red as indicator; **supplemented as its hydrochloride

3.1.5.5 OPTI-MEM

Opti-MEM® medium (Gibco™, Thermo Fisher Scientific, Rochester, NY, USA) is an optimized Minimal Essential Medium (Opti-MEM), buffered with HEPES and sodium bicarbonate ($NaHCO_3$, 2.4 g/L). Supplemented serum concentrations can be decreased by 50% without any change in cell growth rate or morphology due to its composition containing insulin, transferrin, hypoxanthine, thymidine, and trace elements, which make up for lesser serum. This makes Opti-MEM the ideal candidate for e.g. cationic transfection reagents (Lipofectamine 2000; *q.v. section 3.7.5.1, page 124*). Stable physiological pH is maintained at CO_2-atmospheres of ≥ 5%. The exact media formulation is kept under lock and key by manufacturer and can't be listed here because of that.

3.2 General Procedures

3.2.1 Membrane Composition and Properties

In this thesis, the focus is set on mainly three membrane compositions (Table 16): One reconstituted from the pure, zwitterionic 1,2-dioleoyl-*sn*-glycero-3-phosphocholine (DOPC) for mimicking uncharged lipid bilayers showing no domain formation at room temperature (rt) and 37 °C, a second composed of 1,2-dioleoyl-*sn*-glycero-3-phosphocholine (DOPC), *N*-(octadecanoyl)-sphing-4-enine-1-phosphocholine (SM), cholest-5-en-3β-ol (Chol) in a lipid ratio of 9:9:2 forming small cholesterol-rich microdomains and 2:2:1 forming larger cholesterol-enriched domains at rt mimicking immune cells, and a third reconstituted from 1-palmitoyl-2-oleoyl-*sn*-glycero-3-phospho-ethanolamine (POPE) and 1-palmitoyl-2-oleoyl-*sn*-glycero-3-phospho-(1'-rac-glycerol) (sodium salt) (POPG) in a lipid ratio of 4:1 to mimic the inner leaflet of the bacterial cell envelope of Gram-negative bacteria with an overall negatively charged surface. Lipid solutions were prepared as stated in *section 3.1.3 (page 67)* at stock concentrations of 10 mg/mL in $CHCl_3$.

TABLE 16. MODEL MEMBRANE SYSTEM AND THEIR COMPOSITIONS INCLUDING LIPID AND MOLAR RATIOS.

Model Membrane System	Lipid Ratio	Molar Ratio
DOPC		100
DOPC/SM/Chol	9:9:2	45:45:10
DOPC/SM/Chol+PS	9:9:2+10%	40.5:40.5:9:10
DOPC/SM/Chol	2:2:1	40:40:20
DOPC/SM/Chol+PS	2:2:1+10%	36:36:18:10
POPE/POPG	4:1	80:20

3.2.2 Membrane reconstitution systems

For mimicking cell like structures a set of membrane reconstitution systems are used (Figure 23-25), based on liposome or planar membrane formation. This wide choice of systems is introduced herein briefly and enlarged upon in *section 3.4* (*page 83*) and the referring subchapters. Pure small unilamellar vesicles (SUVs) spread on a solid support are utilized for

synchrotron experiments. SUVs embedding calcein allow the study of membrane permeabilization in an "all-or-none" or "graded" mode[125]. In this connection, pore formations have to exceed the approximated critical diameter of 1.3 nm which is the estimated diameter of calcein[126]. For studying permeabilization events at pore diameters below the critical diameter of this fluorescein-derivative, SUVs with an incorporated lipid-dye conjugate (NBD-PE) are used. In this approach, the conjugate is quenched by iodide ions, a typical chemical quencher, enabling the detection of already small membrane lesions. Introducing lipid-dye conjugates in SUVs, building e.g. a FRET-pair, allows the monitoring of peptide-intercalation processes.

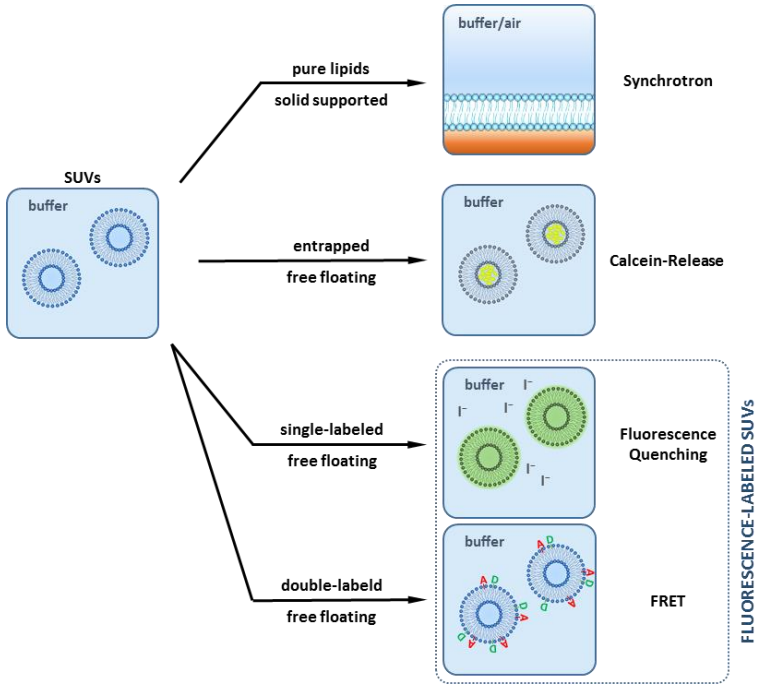

Figure 23 | Small unilamellar vesicles as membrane reconstitution system and their fields of application. By allowing SUVs to spread, solid supported bilayers are generated either on silicon wafers for X-ray reflectivity measurements or quartz glass crystals for oriented circular dichroism at a synchrotron source. Membrane permeabilization events are investigated either with SUVs filled with calcein by release assay or NBD-labeled SUVs by fluorescence quenching. Peptide-intercalation is studied using SUVs with an incorporated FRET-pair.

Fluorescently labeled giant unilamellar vesicles (GUVs) were used for analyzing the bulk lateral membrane organization by conventional fluorescence microscopy. Due to the very dynamic nature of the vesicles an

anchorage is essential for quantification of different fluorophores on the membrane surface. Introduction of a biotinylated lipid species (biotinylated PE) into these GUVs lead to immobilization via avidin-biotin-chemistry by non-covalent interaction enabling the distribution analysis of membrane-bound and peptide-bound fluorescent-dyes of one z-slice. This facilitates the capturing of correlation or anti-correlation of the two dyes. Further, GUVs without any incorporated fluorescence label are applied in nano-pore spanning bilayer experiments, where these vesicles were allowed to spread and thereby realized both, sealing of small buffer filled cavities and entrapping a fluorescent dye.

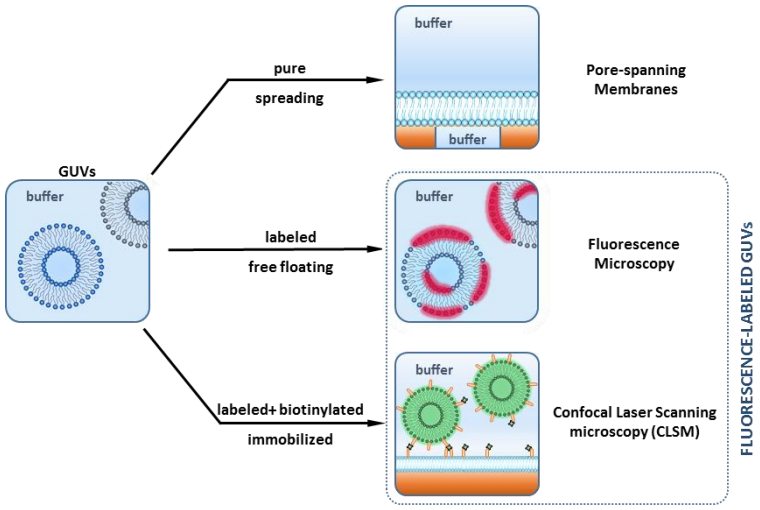

Figure 24 | Giant unilamellar vesicles (GUVs) as membrane reconstitution system and their fields of application. GUVs composed of pure lipids without incorporation of any fluorescence label or anchor molecules are used for the formation of pore-spanning membranes. Introducing a lipid-dye conjugate in the membrane compounds enables fluorescence microscopy and therewith the lateral organization of the giant vesicle. Extending this approach by supplementation with an anchor molecule during GUV-preparation enables immobilization of the otherwise very dynamic GUVs and the study of membrane-peptide-interaction by analyzing the distribution of membrane-and peptide-bound fluorophores in one z-slice.

Membrane stacks, tethered lipid bilayer membranes (tBLMs) as well as free standing bilayer lipid membranes (BLMs), in accordance with the MONTAL-MUELLER technique, were reconstituted by simple evaporation of the corresponding organic solvent. In the latter, the lipid bilayer is formed from two monolayers folding up against each other at an air-water interface by the hydrophobic apposition of their hydrocarbon chains. These

MONTAL-MUELLER membranes aid in the incorporation of membrane active compounds (e.g. ionophores, channel-forming peptides, and AMPs) and transmembrane proteins (e.g. ion channels, molecular pumps, and carrier) into the lipid bilayer and the analysis of single pores at an electrical capacity that matches that of biological membranes[127]. Further, this methodical approach facilitates asymmetric membrane formation and enables accurate protein reconstitution[127]. Tethered membranes depict one of the most robust methods for lipid bilayer reconstitution. The impedance spectroscopic approach of tBLMs employs real time modeling of the lipid bilayers and comprises a rapid test for membrane insertion and aggregation processes to pore formation and permeabilization.

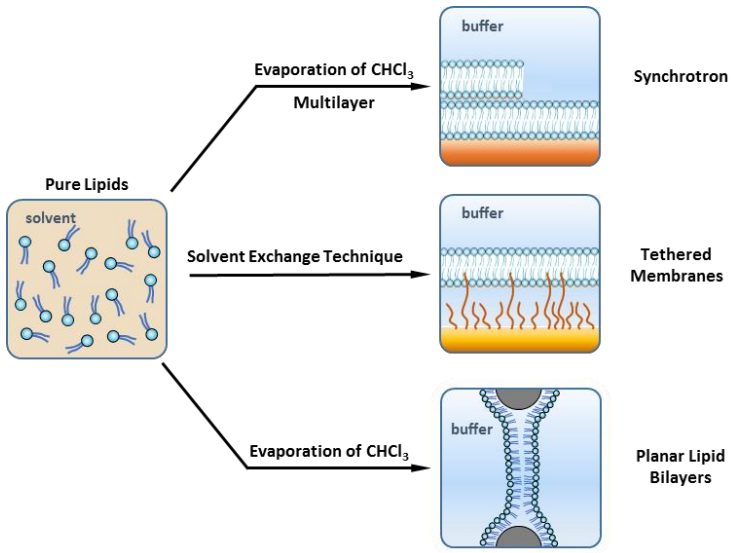

Figure 25 | Planar oriented membrane reconstitution systems and their fields of application. Membrane stacks or multilayer formation is realized by evaporation of $CHCl_3$ on a hydrophobized silicon wafer. These multilayers are used in synchrotron experiments and are analyzed regarding reflectivity and scattering behavior. Tethered membranes are formed by displacing the solvent EtOH with aqueous buffer onto a gold surface. These membranes are analyzed with an impedance reader where the conductivity is detected and integrated over a large membrane area. Free standing lipid bilayers are prepared pursuant to MONTAL-MUELLER. This method enables single-pore analysis under applied membrane voltages of -50 mV.

Figures 23-25 gave a short overview of the different membrane reconstitution systems used throughout this doctoral research work. Their preparation and final fields of application are described in detail in the

upcoming method sections. Beforehand, a general introduction of the procedures of liposome formation are given.

3.3 Liposome Preparation Techniques

3.3.1 Preparation of Small Unilamellar Vesicles

Vesicles within a size range below 100 nm are considered as small unilamellar vesicles (SUVs). These liposomes can be used for a wide set of experiments as mentioned recently (*q.v. section 3.2.2, page 76 et seqq.*). Only little adjustments have to be made according to their final field of application, such as introduction of lipid-dye conjugates into the membrane leaflets or vesicle loading with self-quenching dyes. Most commonly, SUVs are prepared by sonication in continuous mode[128]. According to the stability needed, the sonication mode and intensity can be adjusted. In the following, the used standard procedure for SUV preparation will be described. Beforehand, all lipids for SUV preparation were dissolved in $CHCl_3$ (p.a.) to a final concentration of 10 mg/mL and mixed according to the membrane composition of interest. Afterwards, the solvent was evaporated under nitrogen exposure. For proofing, complete $CHCl_3$ evaporation, the glass vials were placed on a block heater at 60 °C. Remaining solvent in the lipid film led to popping under the conditions applied. After total solvent removal, the lipid film was rehydrated in buffer to a final concentration of 1 mg/mL and sonicated (Sonifier Cell Disruptor B15, Branson Ultrasonics Corporation, Danbury, CT, USA; amplitude set to 30%, mode: continuous, time: 2 min/500 µL). For obtaining maximum homogeneity and stability, SUV-solutions underwent temperature cycling of 30 min at 4 °C and 30 min at 60 °C repeated for three times. SUVs were stored at 4 °C at least overnight or until usage.

3.3.2 Preparation of Multilamellar Vesicles

The preparation method of multilamellar vesicles (MLVs) is similar to the one of SUVs. The main difference lies in the way of sonication. For obtaining MLVs, a common ultrasound bath (Sonorex RK100 ultrasonic bath, BANDELIN electronic GmbH & Co. KG, Berlin, Germany) for sonication is used and the sonication steps are included in the temperature cycling. Lipids were handled as described in the section before. The glass vials containing the aqueous lipid solutions were placed in a floater and maintained in a 60 °C preheated ultrasound bath for 1 h. Afterwards, the glass vials were stored for 1 h at 4 °C. The MLV-solutions underwent this type of temperature cycling for three times in total. MLVs were stored at 4 °C overnight or until usage.

3.3.3 Preparation of Giant Unilamellar Vesicles

Giant unilamellar vesicles (GUVs) are approximately two to three orders of magnitude larger compared to SUVs or generally speaking, liposomes that are generated by sonication[129]. Giant vesicle formation by applying a static (DC) electrical field, was first reported in 1986 by Angelova and Dimitrov[130]. But only certain lipid types tend to form GUVs under these conditions; in all likelihood, the static electrical field induces only an ordering of the lipid molecules. Applying an alternating (AC) instead of a static electrical field circumvented the narrow lipid spectrum. GUVs - as presented here – are prepared by electroformation (Figure 26) reaching up to 100 μm in diameter. The dimensions of this model allow direct optical microscopic observation of the membrane organization. Free floating GUVs are highly dynamic. For long-term studies and membrane-peptide interaction, a confocal microscopic approach was established. Therefore, GUVs incorporate additionally to the fluorescent dye a biotinylated lipid species as anchor molecule. By avidin-biotin-chemistry GUVs are immobilized enabling the distribution analysis of membrane- and peptide-bound fluorophores along z-slices.

For this technique a modified version by M. KOISTINEN of the protocol by VEATCH *et al.* was used and optimized[131]. All lipids for the preparation of GUVs were first dissolved in $CHCl_3$ (p.a.) to a final concentration of 2 mg/mL. Fluorescently labeled and biotinylated lipids were dissolved directly in ethanol (EtOH, p.a.) to a final concentration of 0.5 mg/mL for the lipid-dye conjugates and 2 mg/mL for the biotinylated lipid species. All fluorescently labeled lipids as well as the biotinylated compound were labeled at the hydrophilic headgroup. The chloroformic lipid solutions were mixed in a lipid ratio of 2:2:1 (40:40:20) and the solvent was evaporated under nitrogen exposure. Afterwards the lipid film was resolved in 100 µL EtOH (p.a.) and the fluorescent and biotinylated lipids were added in a final concentration of 0.5 mol%. The mixture was applied on indium tin oxide (ITO) coated object slides (sheet resistance of <20 Ω; PGO, Iserlohn Germany). The slides were preheated to 60 °C on a heating plate and the lipid mixture was added dropwise and wiped out gently on both object slides equally to obtain a homogenous lipid film on the ITO-coated surface. Remaining solvent was evaporated for 90 min at 0.1 mbar. Thereafter, a silicon spacer (3.5x2.5x0.5 cm external dimensions, Sylgard 184, ratio 10:1 (v/v)) was placed in between the two object slides and fixed with brackets resulting in a chamber. The chamber was flooded with 10 mM sucrose (pH 7.4) solution (Sigma-Aldrich, St. Louis, MO, USA) and applied in the electroformation chamber. GUVs were formed at 55 °C for 5 h (10 Hz, 3 V, AC-field, sinus) and cooled down slowly to room temperature overnight.

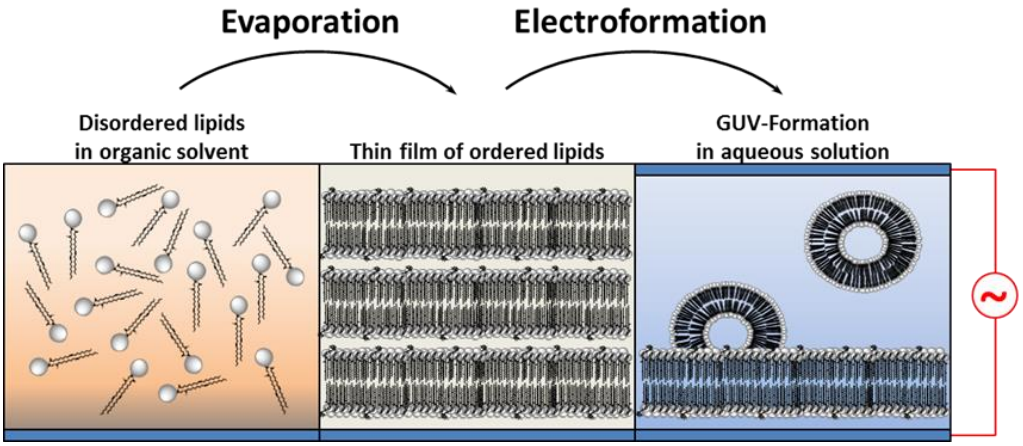

Figure 26 | Schematic illustration of the preparation of giant unilamellar vesicles (GUVs) in accordance with the electroformation method. Lipids are first dissolved in $CHCl_3$. Next, the solvent is evaporated in an N_2 atmosphere and the lipid film is resuspended in EtOH. The desired concentration of fluorescent dye or anchoring molecule (0.3-0.5mol%) is added to the lipid solution. The solution is carefully applied at 60 °C onto ITO-coated object slides and the solvent is removed at 0.1 mbar for 90 min. GUVs in an average size range from 1 to 50 µM are generated by electroformation for 5 h.

3.4 Membrane Permeabilization Techniques

Biological membranes exhibit a high variability in their lipid composition and therefore feature unique physicochemical properties of the lipids they are composed of. This characteristic allows AMPs to discriminate between bacterial and mammalian cell membranes[132]. On bacterial membranes, AMPs interact via nonspecific modes of action which keeps the resistance-induction potential of these molecules on a very low level. Within minutes, AMPs can kill bacteria by disrupting the target membrane. All of the methodical approaches for the determination of lipid bilayer permeabilization utilize the key characteristics of AMPs: The positive net charge of the peptides, that is essential for initial binding to the negatively charged bacterial membrane surface whereas the hydrophobic nature facilitates membrane insertion and promotes the process of membrane disintegration[133]. AMPs dramatically influence the integrity of bacterial membranes by interacting not only via a single pathway but taking

multiple routes and exhibiting a synergistic effect. As presented earlier, the most frequently discussed modes of action include pore formation and the coverage of the membrane surface by peptides. Although a number of AMPs, thereunder α-helical and β-sheet-type peptides, have been shown to induce toroidal pores[134]; to date, these models only agree upon the lethal physical interference of AMPs with the barrier function of bacterial membranes[133]. On mammalian cells, the membrane building block cholesterol puts most of the AMPs out of the target range of these membranes. To obtain *inter alia* information if AMPs can act *in vivo* via transmembrane pores, different membrane mimicries were used. The diverse set of permeabilization assays based on different reconstitution systems should help to discriminate, whether a certain AMP induce large-scale membrane failures or small defects that e.g. dissipate the transmembrane potential[135]. Both scenarios would result in cell death. Furthermore, the quantitative correlation between the potency of antimicrobial activity and the degree of membrane permeabilization induced by a specific peptide may be evidenced.

3.4.1 Calcein Release Assay

All liposome-based assays presented in the following were run out on a SPEX Fluorolog or on a Fluorolog-III fluorescence spectrometer (Horiba Jobin Yvon, Edison, NJ, USA). Both spectrometers were equipped with a single-grating excitation monochromator and two single-grating emission monochromators. As light source, a 450 W xenon short-arc gas discharge bulb (UXL-450S-O, Ushio, Steinhöring, Germany) was mounted. The T-shaped setup of the sample compartment allowed simultaneous fluorescence emission detection of two different wavelengths as required e.g. for FRET and the associated peptide-intercalation assay. Experiments were carried out in 10 mm wide standard cuvettes (Suprasil® quartz cuvette, Type 101-QS, Hellma Analytics, Muellheim, Germany) with a maximum liquid capacity of 3.5 mL at 37 °C unless otherwise specified. SUVs were prepared as described in *section 3.3.1* (*page 80*) and diluted to a final concentration of 10 µM in the buffer of interest. Samples were

preheated to 37 °C in a block heater, whereas peptide stocks in 0.01% TFA were stored on ice until usage.

To date, the calcein release assay still remains a sure method for studying membrane leakage. This prominent assay was developed in 1977 by BLUMENTHAL and WEINSTEIN and since then it is one of the standard techniques to study membrane permeabilization[136]. The general principle behind this assay includes the formation of liposomes loaded with a fluorescent dye at self-quenching concentrations. For large unilamellar vesicles (LUVs), concentrations of 50 mM calcein and above result in self-quenching of the fluorophore[136b, 137]. Due to osmotic inactivity of SUVs even higher concentrations of the dye (70-100 mM) can be applied in this case[138]. After removal of non-entrapped dye from the aqueous medium, leakage induced by membrane active compounds can be monitored by dye release. The calcein released from the vesicles is greatly diluted by the surrounding medium; thus, the self-quenching effect is overcome and the molecule starts to fluoresce.

This liposome-based assay uses SUVs in accordance with the general protocol as described in *section 3.3.1 (page 80)*. After evaporating the solvent, the dried lipid film was rehydrated in 268 µL buffer supplemented with 5 mg calcein (28 mM; Molecular Probes™, ThermoFisher Scientific, Roskilde, Denmark). To facilitate complete dissolving of the calcein, 20 µL NaOH (1 M) were added. The solution was protected from light and vortexed for 1 min. Vesicle formation by sonication (2 min, amplitude set to 30%) lead to incorporation of calcein. The calcein-filled SUVs were purified by size exclusion chromatography (SEC) via PD10-columns (Sigma-Aldrich, St. Louis, MO, USA). The PD10-columns were equilibrated first with double distilled pyrogen-free water. (10 mL, Aqua B. Braun) and afterwards with the buffer of interest (25 mL) before sample loading (500 µL). The sample was passed into the column matrix by addition of 2 mL buffer. The liposomes with entrapped calcein were eluted by addition of buffer (25 mL) as a well-separated, iridescent yellow, single fraction of approximately 500 µL. Non-entrapped calcein is detected as glaring yellow flow-through, whereupon the fractionation was stopped. For fluorescence spectroscopic analysis, the excitation wavelength was set to the absorption maxima of calcein (λ_{Ex} = 490 nm) and the emission wavelength λ_{Em} was set

to 520 nm. Experiments were carried out in standard cuvettes capturing a total volume of 3.5 mL. Liposomes were diluted 1:100 (v/v) in the buffer of interest, whereof a volume of 1980 µL were pipetted into the cuvette. The prepared calcein-filled SUVs were applied at a final concentration of 10 µM. At the outset, background and base fluorescence intensities were recorded (Figure 27, ①). The entrapped calcein molecules in the inside of the vesicles were resting in a non-fluorescence state, therefore only low fluorescence intensities were measured. Peptide stock solutions (1 mM in 0.01% TFA) were prepared as described in *section 3.2.1 (page 76)*. Peptide additions of 2 µL (1 µM), 4 µL (3 µM) and 14 µL (10 µM) resulted in an increase of fluorescence intensity in case of pore formation or membrane permeabilization. The self-quenching effect of the calcein is repealed by loss of the spatial proximity of the molecules to each other (Figure 27, ②). After the last peptide addition, progressing increase of fluorescence intensity is monitored until reaching its maximum level (Figure 27, ③). Total liposome disintegration is reached by addition of 10% Triton X-100 (200 µL; Merck Chemicals GmbH, Darmstadt, Germany) at the end of each measurement. If intact liposomes were remaining in solution a further increase in fluorescence intensity could be observed. In any other case, only dilution effects were detectable with no further increase in the fluorescence signal (Figure 27, ④).

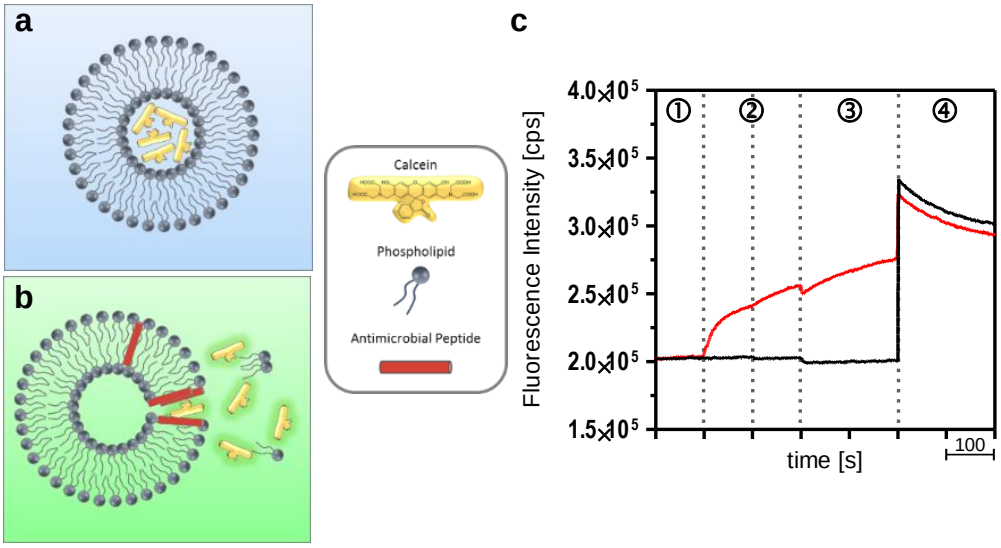

Figure 27 | Scheme of the calcein release assay. (a) Initial fluorescence intensity of calcein entrapped in liposomes before peptide addition. Liposomes reside in a non-fluorescent state due to self-quenching of the tightly packed calcein molecules. (b) Calcein release after peptide addition: peptide intercalation leads to an increase in diameter of the liposome before pore formation and membrane lysis. The self-quenching effect of calcein is repealed. (c) Raw data exemplarily depicted: ① Background fluorescence; ② Peptide addition period; ③ Fluorescence stabilization period after last peptide addition, ④ TX-100 addition for complete liposome permeabilization.

The percentage of membrane lysis caused by peptides was calculated pursuant to equation 1.

EQUATION 1:

$$Membrane\ permeabilization\ [\%] = \frac{(I_{Peptide} - I_{0\%})}{(I_{100\%} - I_{0\%})} \times 100\%$$

Where $I_{0\%}$ is the mean fluorescence intensity of SUVs before peptide addition (self-fluorescence of solution), and $I_{Peptide}$ stands for the mean fluorescence intensity in presence of peptide. $I_{100\%}$ resembles maximum membrane lysis 100 s after final peptide addition of the nonionic surfactant Triton X-100 (in the following stated as TX-100).

Obtained data were evaluated by spreadsheet analysis with GraphPad Prism 5 (Version 5.04, GraphPad Software, Inc., San Diego, CA, USA). The fluorescence signal recorded after TX-100 addition was handled as 100% calcein release and therefore put in direct context with the grade of membrane permeabilization measured. Calcein release assay data (*q.v. section 4.1.1, page 131*) were plotted as mean +SD of five independent experiments (n = 5; $p \leq 0.05$ = *; $p \leq 0.01$ = **; $p \leq 0.001$ = ***; $p \leq 0.0001$ = ****). All data were evaluated respectively to control measurements.

3.4.2 Potassium Iodide Quenching Assay

Another way to decrease the fluorescence intensity or induce quenching can be realized by dynamic or collisional quenching; but a multitude of quenching mechanisms exist: Fluorescence quenching processes can be induced e.g. in cases of complex building, when excited states are reacting, through spin-orbit coupling and intersystem crossing, or when internal conversion takes place, just to name a few[139]. Whereof the most common type of quenching effects is the collisional or dynamic quenching. During this process, energy is transferred from the excited-state fluorophore to other molecules (quencher) by collision.

Typical quencher substances include halogens, such as iodide (I^-), amines, oxygen, and electron-deficient molecules, e.g. acrylamide[139b]. This assay uses potassium iodide as quenching molecule due to its good solubility in aqueous solutions. To prevent the oxidization of iodide and the formation of polyiodides (I^- and I_3^-, oxidization state –I) to iodine (I_2, oxidization state 0), 0.4 mM $Na_2S_2O_3$ (sodium thiosulfate; Merck, Darmstadt, Germany) was added in a molar ratio of 1:2000 (KI:$Na_2S_2O_3$) to the 800 mM concentrated KI-solution[140].

$$I^- + I_2 \rightleftharpoons I_3^-$$

$$2S_2O_3^{2-} + I_2 \rightleftharpoons 2I^- + S_4O_6^{2-}$$

Fluorescence intensity can be regained by removal of the quencher molecules. For the experimental setup NBD-labeled liposomes were prepared as described in *section 3.3.1 (page 80)*. After injection of 1751 µL into a 10 mm wide standard quartz cuvette the fluorescence intensity was recorded (Figure 28, ①). As soon as stable background fluorescence was reached, 229 µL of an aqueous KI solution supplemented with $Na_2S_2O_3$ were added and a decrease in fluorescence intensity was detected (Figure 28, ②). This first decrease resulted from the fluorescence quenching of the fraction of lipid-dye conjugate incorporated in the outer leaflet of the liposomes. Only the fluorophores located in the inner leaflet were untroubled by quenching. Hence, the inner core of the SUVs remained fluorescent, but the intensity was distinctly decreased compared to the initial state (Figure 28, ③). Injections of 2 µL, (1 µM), 4 µL (3 µM) and 14 µL (10 µM) of membrane active compounds, such as antimicrobial peptides, result in pore formation and permeabilization as well as in certain cases to complete collapse of the liposomes. In this case, the inner core of the liposome is accessible for the quencher molecules due to peptide-induced permeabilization, resulting in liposome failure and destabilization with total fluorescence quenching (Figure 28, ④). A final addition of TX-100 was accomplished to verify complete membrane disintegration and maximal quenching (Figure 28, ⑤).

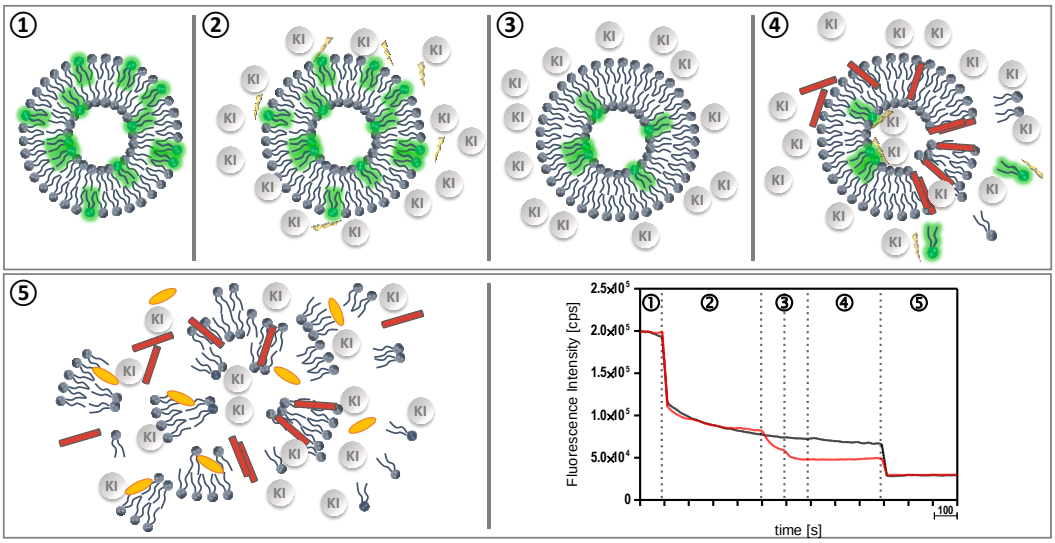

Figure 28 | Schematic representation of the potassium iodide quenching assay. ① Detection of total fluorescence. ② Addition of KI quenches the fluorescence on the outer leaflet of the liposome. ③ The quencher has no access to the inner leaflet of the liposome, giving the remaining fluorescence intensity of the inner leaflet. ④ Addition of membrane active substances lead to an intercalation and the induction of small pores. After reaching the critical concentration, the membrane stability is diminished to a degree where larger lesions are formed allowing the quencher to proceed to the inner leaflet. A drop in fluorescence at this stage resembles the fluorescence quenching of the inner leaflet. ⑤ For verification of complete membrane disintegration TX-100 is added. Remaining intact liposomes are solubilized and a further decrease in fluorescence intensity can be observed.

All data were evaluated as follows: The mean fluorescence intensity of the liposomes before peptide addition ($I_{0\%}$, self-fluorescence of solution) was subtracted from the mean fluorescence intensity after peptide addition ($I_{Peptide}$). The resulting value is divided by the difference of the mean maximum fluorescence intensity ($I_{100\%}$, after TX-100 addition) and $I_{0\%}$. The resulting quotient is multiplied by 100%. The same evaluation procedure is applied for the reference spectra giving the degree of influence of buffer and solvent used in the experiments. The resulting reference value in percentage is subtracted from the quenching value giving the effective quenching value. The degree of membrane lysis in % is obtained by equation 2.

EQUATION 2:

$$Membrane\ Lysis\ [\%] = \frac{(I_{0\%} - I_{Peptide})}{(I_{0\%} - I_{100\%})} \times 100\% - \frac{(I_{0\%} - I_{Buffer})}{(I_{0\%} - I_{100\%})} \times 100\%$$

Quenching assay data (*q.v. section 4.1.2, page 134*) were plotted as mean +SD of three independent experiments (n = 3; $p \leq 0.05$ = *; $p \leq 0.01$ = **; $p \leq 0.001$ = ***; $p \leq 0.0001$ = ****).

3.4.3 Pore-spanning Lipid Bilayers

To study peptide-induced permeabilization events in a system where the induction of positive or negative membrane curvature is decreased to a minimum, a novel fluorescent dye release assay, based on pore-spanning lipid bilayers, was successfully established. The chip-based assay is modified according to the former *NanoFAST E800* (Nanospot GmbH, Münster, Germany) biochip assay[141]. Modifications and optimization led to a fast, experimental setup with solid and reproducible results. The silicon wafer with pre-cut and pre-etched chips was commercially available (Micromotive GmbH, Mainz, Germany). The ready-to-use chip was assembled in-house. The silicon chips were glued with the Silastic® MDX4-4210 two-component adhesive (Dow Corning Inc., Midland; MI, USA) on cover glasses (ibidi GmbH, Martinsried, Germany) complemented with sticky-slide 8 well microscopy chambers (ibidi GmbH, Martinsried, Germany) on top to allow inverse microscopy. On the eve of use, all assembled slides were cleaned by air plasma (Diener electronics GmbH&Co.KG, PlasmaCleaner Zepto, Ebhausen, Germany; 0.5 min, intensity set to 6, air flow range between 0.4 to 0.6 mbar). Low-salt buffer (5 mM HEPES, 0.5 mM $CaCl_2 \times 2H_2O$) was used for mimicking the extracellular space. 250 µL of the buffer was applied onto the chip surface and the slide was sonicated for 2 min to replace the remaining air in the cavities by buffer. Thereafter, 5 µL of the fluorescent dye (Atto488 carboxy, Atto-Tec GmbH, Siegen, Germany) were added to one well, resulting in a final concentration of 5 nM. The fluorescent dye diffused into the cavities freely within a few minutes. Equal fluorescence distribution of the cavities was checked by microscopy (TILL Photonics, FEI, Graefelfing, Germany). Afterwards, 50 µL of freshly prepared GUVs were added and spread by centrifugation with a swing out rotor (10 min, 400 rpm, brake: off, 25 °C; Labofuge, Hereaus, Osterode, Germany). Thereafter, the chips were

washed five times with 200 µL buffer to remove free fluorescent dye from unsealed cavities and the surrounding media. Microscopy images showed fluorescent patches on the chip surface where the spread GUVs enclosed the Atto-dye in the inside of the cavities (Figure 29). Unsealed cavities appeared black.

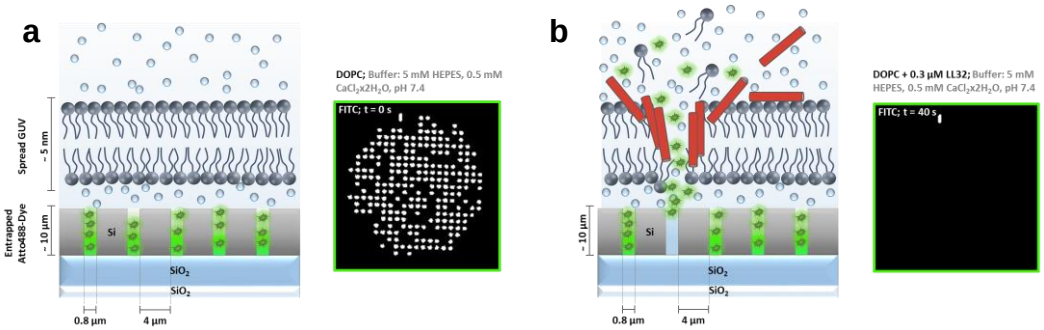

Figure 29 | Illustration of the nano-pore based fluorescence dye release assay of pore-spanning lipid bilayers. GUVs are spread onto the chip surface by centrifugation (400 rpm, 10 min, 25 °C). Free fluorophore is removed by five individual washing steps. (a) Before peptide addition, patch-sealed cavities can be observed. (b) After peptide addition the membrane patches are permeabilized and destroyed.

Time-scaled recording of the nano-pore-spanning membrane dye release assay was performed with a TILL Photonics microscope stage (FEI, Graefelfing, Germany). The microscope global temperature setting was adjusted and equilibrated to 37 °C. Subtotal equilibration could result in an optical drift while recording is running. After injections of the substances introduced within this doctoral thesis, the efflux of the entrapped fluorescent dye can be recorded over time, giving information of the time-resolved course of membrane permeabilization events. The dye-efflux can be studied quantitatively over time. An advanced protocol allows the determination of dye-efflux and peptide-influx over time as well as measuring the pore diameter by use of TexasRed®-labeled dextran molecules (Life technologies, Carlsbad, CA, USA) of a distinct size. Recorded data were pre-evaluated with ImageJ (Version 1.48v, Wayne Rasband, National Institutes of Health, Bethesda, MD, USA) with an integrated ROI mask threshold plugin (*Setting ROI mask threshold 100.ijm*; courtesy of Nanospot GmbH). This plugin detects the sealed cavities and measures the mean grey values over time (200 s). The read out is given in a Microsoft Excel table which is further analyzed with the Python-based user

procedure *test_py.py* written by J. WERNECKE (Python (x, y), Version 2.7.6.1). Out of the Excel spreadsheet the threshold-value can be determined and is set to 64.61% (±16.54%) of the highest mean grey value detected and filled into the input panel of the Python-tool. The defined threshold-value encounters which cavities are counted as "open" or "closed". The final data evaluation is performed and plotted in GraphPad Prism 5 where the 50% membrane permeabilization value (MP_{50}) can be determined if necessary for data interpretation.

3.4.4 TETHERED MEMBRANE TECHNOLOGY

This system is based on the principle of conventional solid supported membranes complemented by a polyethylene glycol (PEG) chain that functions as spacer between substrate and membrane. The tether is covalently bound to the gold substrate via disulfide bonding of its benzyl disulfide groups (tethaPlasm™; SDx Tethered Membranes Pty Ltd., Sydney, NSW, Australia) (Figure 30a). The benzene ring intensifies the disulfide bonding to the gold surface and functions at the same time as lateral spacer between the binding points on the substrate. In addition, shorter spacer molecules are attached to the substrate surface. These spacer molecules fill the area on the substrate and stabilize both the longer tether molecules as well as the reconstituted membrane. The spacer molecules consist of a shorter PEG-chain and a hydroxyl headgroup, and exhibit therefore a hydrophilic nature whereas the headgroups of the tether molecules have a hydrophobic domain (Figure 30b). After adding lipids, the hydrophobic domains of the tether molecules interact with the

hydrophobic part of the lipids. As soon as buffer is added, the lipid bilayer starts self-assembling onto the tethers.

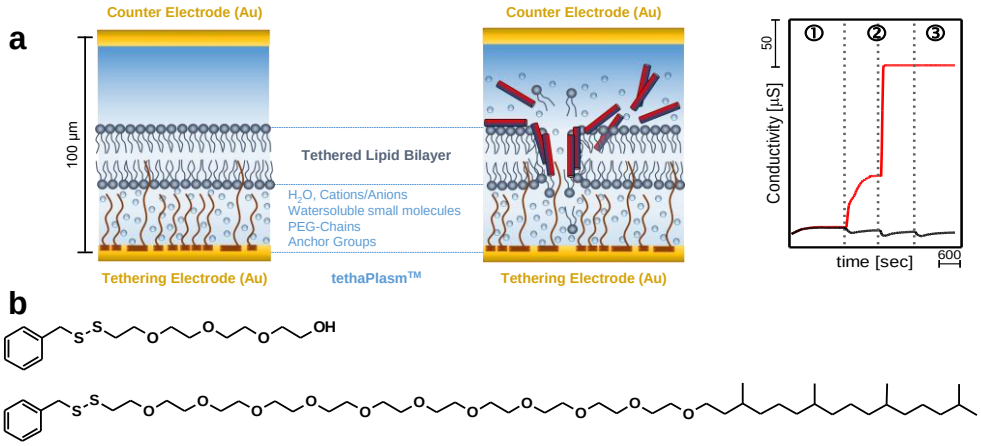

Figure 30 | Solid supported tethered membranes. (a) Schematic outline of the general surface structure assembled on the Au chip surface before membrane tethering. The substrate is partially covered by disulfide bridges with organodisulfides (anchor groups) containing PEG-chains. This layer is called tethaPlasm™. On top, the membrane is assembled and the background conductivity can be recorded. Representative raw data trend while recording: ① Membrane stabilization period; ② Injection period; ③ Total loss of membrane integrity short-circuits. (b) Chemical structure of the spacer and tether molecules of the pre-prepared tethered benzyl-disulfide tetra-ethylene glycol phytanyl (T10) coated gold electrode. The slide is furnished with four oxygen ethylene glycol linkers with a terminal OH-group (spacers) and with eight oxygen ethylene glycol linkers with a C20 phytanyl group (tethers). Tether and spacer molecules cover the electrode in a ratio of 10%:90%[16].

The distance between tethered membrane and the gold surface (tethering electrode) ranges approximately between 2.0 nm and 2.5 nm building a reservoir of adequate capacity. This reservoir tolerates a degree of ion mobility that is compatible to biological membranes, which is the basic requirement in the use of tBLMs as membrane mimicry: Ions crossing the membrane may be stored or returned to the external solution[16]. The electrode–electrode distance in total measures 100 µm whereof the size of the tethering electrode amounts to 2.1 mm^2 and is available for the reconstitution of tethered membranes[142]. The *tether to spacer ratio* influences the stability and fluidity of the reconstituted membrane. The shorter spacer molecules, induces membrane regions wherein the lipid molecules are highly dynamic. An increase of tether molecules up to 70% yield in membrane stiffening and poor reconstitution[143]. Only membrane active

compounds within a size range of maximum 1 kDa were able to incorporate into this type of tethered membrane. But a reduction of the density of tether molecules is virtually limitless: A *tether to spacer ratio* of 10%:90% increases the versatile membrane regions and enables to study membrane-protein-interaction of proteins with molecular weights up to 40 kDa. A further lowering giving a ratio of 1%:99% allows the analysis of even larger proteins (≤300 kDa)[16].

This chip-based system enables tethered membranes for impedance spectroscopic analysis via an impedance reader, the SDx-R1 tethaPod™ with the corresponding tethaPlate™ (SDx Tethered Membranes Pty Ltd., Sydney, NSW, Australia), that is furnished with six sample chambers onto one plate. The common principle of impedance spectroscopy is based on an electrochemical cell with a three-electrode-system composed of a working (*here:* tethering electrode), counter and reference electrode. All of the six chambers on the tethaPlate™ resemble a single electrochemical cell. For applying a constant potential onto the working electrode, a potentiostat is used. With the help of a frequency generator, the direct-current voltage (DC-field) is overlaid with a small alternating current voltage (AC-field) of known frequency ω and small amplitude i_0. As output parameters, the amplitude ν_0 and the phase difference ϕ of the concomitant electrical potential, that develops upon voltage application, are measured. The tethaPod™ runs at an AC-voltage of 20 mV within a frequency range from 1000 to 0.125 Hz[142].

Sample preparation were run out onto tethaPlates™ with T10 electrodes, whereat tether and spacer molecules furnish the gold electrode in a ratio of 1:10. Prefabricated parts were available on purchase and stored at 4 °C. Before each measurement, the thin functionalized slide (tether slide) were removed from the EtOH containing packaging and were dried upright for one minute at rt. The bottom side of the sample chamber slide was covered with a protection foil that was removed upon mounting onto the tether slide. For facilitating correct chip assembly, a clamping system was provided by manufacturer. Next, a silicon negative (spreader) of the sample chamber slide was applied onto the two-component system and covered with an aluminum plate. The equipped clamping system was compressed for one minute to allow uniform attachment of tether and sample chamber

slide. After removal of the spreader, the tethaPlate™ was fully assembled and ready-to-use. For preparation of a tethered membrane, ethanolic lipid stocks were used as stated in *section 3.1.3 (page 67)*. Lipid stocks were diluted in EtOH to yield a lipid concentration of 3 mM. Each chamber was furnished with 8 µL of the lipid solution and incubated for 2 min. Afterwards, the chambers were flooded by applying 93.4 µL of buffer. Three washing steps, each with 100 µL of buffer, were performed to remove remaining solvent and air. The tethaPlate™ was mounted in the impedance reader and the self-assembled tethered membranes were measured for 20 min (membrane stabilization period) before the first peptide addition. Peptides were diluted from 1 mM stocks in 0.01% TFA to yield 15 µM, 45 µM and 150 µM. Three peptide injections each of 6.7 µL were performed in time lags of 15 min resulting in final peptide concentrations of 1 µM, 3 µM and 10 µM in the sample chambers. Experiments were run out at 37 °C; to reduce evaporation of the buffer, the tethaPlate™ was covered with a standard coverslip.

All data were recorded with the software supplied by distributor and could be easily transferred to Microsoft Excel (Microsoft Office 365 Personal, Microsoft Corporation, Redmond, WA, USA). Final data evaluation and diagram generation (*q.v. section 4.1.4, page 143*) were performed with GraphPad Prism 5. Data curves were translated to column plots by determining the average over constant data points. For statistical analysis, a student's paired t-test (two-tailed) was applied to the data obtained. Data were plotted as mean +SD of five independent experiments ($n = 5$; $p \leq 0.05$ = *; $p \leq 0.01$ = **; $p \leq 0.001$ = ***; $p \leq 0.0001$ = ****). The tethered membrane technology offers a system where only small amounts of sample are required and the reconstituted membranes exhibit higher stability compared to conventional liquid-based black lipid membranes[144]. As add on for impedance spectroscopy this tool collects capacity and conductivity data of membranes enabling the integration over a relatively large membrane area. Peptide-induced membrane permeabilization is derived from this translation.

3.4.5 Planar Lipid Bilayers

Montal & Mueller developed in the early 70s a modified deposition technique to overcome the use of heavy non-volatile solvents[127] compared to the method developed by Mueller & Rudin in the early 60s. The Montal-Mueller technique for modelling lipid bilayers features a limited number of parameters which are controllable, due to the defined lipid environment of artificial membranes. This method enables the study of well-defined model systems together with the simulation of transport processes across (biological) membranes. The electrical properties of lipid bilayers can be exemplified by an equivalent circuit diagram wherein a capacitor and a resistance are arranged in a shunt circuit (Figure 31). The membrane capacitance (C_m) and the membrane resistance (R_m) both are depending on the area of the reconstituted membrane. Further, C_m is influenced by the nature of lipids and by the membrane thickness. Adam *et al.* measured a specific capacitance of $C_{m,s} = 0.4$ μF/cm² for organic solvent containing lipid bilayers[145], whereas Boheim *et al.* determined $C_{m,s} = 0.83$ μF/cm² for organic solvent-free bilayers[146]. The reconstituted planar lipid bilayer resembles an ideal electrical isolator and build up a high permeation barrier for ions. Ion-translocation through the hydrophobic part of the membrane is enabled when the high energy barrier is overcome. Membrane conductance increases, in case of pore formation due to protein or peptide insertion into the membrane. These pores build a favorable energetic way for ion-flux. Planar lipid bilayers are a well-established reconstitution system for the characterization of ion-translocation-processes and pore-formation induced by peptides and proteins.

Before setting up the first experiment, several preparations have to be made: At first, buffers were prepared (*q.v. section 3.1.5, page 71*). For this setup, all buffers were prepared and stored in autoclave treated glass bottles. Buffers were filtered sterile as described earlier and stored at 4 °C. Teflon compartments underwent a treatment train consisting of one-hour washing steps in bases, acids and organic solvents (① EtOH, 1 h, 60 °C; ② 1 M HNO_3, 1 h, 60 °C; ③ 0.1 M NaOH, 1 h, 60°C; ④ MilliQ, 1 h, rt; ⑤ $CHCl_3$/MeOH, volume ratio 2:1, 1 h, rt). Afterwards, Teflon compartments

were only handled with gloves and maximum dryness was reached by overnight incubation in a hot-air cabinet at 100 °C. Next, septa were prepared by die-cutting with a circular craft punch with a diameter of 1.6 cm. Therefore, an adhesive film was placed in-between two sheets of paper for obtaining better stability while die-cutting. The transfer foil was removed from the resulting "sticky frames". Two sticky frames were glued from both sides onto the Teflon foil without wrinkling. The stack of adhesive and Teflon foil was cut out round with an approximately diameter of 1.8 cm. For optimal positioning of the aperture, the cut-out foil stack was placed in-between two plastic holders with a spare area in the middle. The holder was mounted in a spark gap and apertures of circular type within a size range from 70 µm to 100 µm were obtained. For experimental setup, two Teflon compartments were carefully coated with silicone grease (Baysilone®, Bayer AG, Leverkusen, Germany) as sealing. The septum was shortly treated with a mixture of hexane/hexadecane (10:1, v/v) to increase its hydrophobicity. Afterwards, the septum was applied between the two Teflon compartments and the experimental chamber was tied together by a metal ring. The chamber was now ready to be installed in the experimental setup. The wire electrodes used, were made of Ag/AgCl (Science Products GmbH, Hofheim, Germany) with a surface area of 21.11 mm² (Ø = 0.8 mm, h = 8 mm). Each Teflon compartment was flooded with 1.5 mL buffer. All experiments were run out at 37 °C and executed with a membrane voltage of +50mV.

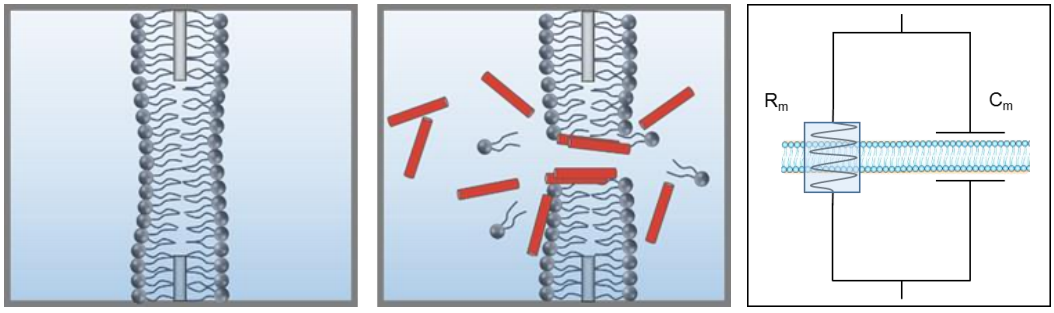

Figure 31 | Schematic drawing of the experimental setup in accordance with MONTAL-MUELLER. Left: Reconstituted free-standing lipid bilayer sealing the aperture. Middle: Peptide-induced pore formation along the bilayer resulting in an unsealing of the aperture and therewith to an increase in ion-flux. As a matter of form, electrodes are not depicted. Right: Equivalent circuit diagram of a lipid bilayer – shunt circuit of a capacitor and a resistance; where the membrane resistance is denoted as R_m and the membrane capacitance as C_m.

In the experimental setup pursuant to MONTAL-MUELLER, the septum is placed in between two Teflon compartments and the aperture starts out above the water surface. Both fluid chambers are completely separated by the aperture. By allowing 10 µL of a 1 mg/mL lipid solution to sit on the water surface, the volatile solvent is evaporated slowly by 10 min incubation and a monolayer is formed on the water surface on each compartment. Raising the buffer level carefully, leads to a coating of the aperture at the air-water interface where the two monolayers from the separate chambers start folding up against each other, forming a bilayer across the aperture (Figure 31).

This method allows the study of pore formation induced by membrane active compounds and their functional characterization at even small amounts of peptide. BLMs prepared according to MONTAL-MUELLER demonstrate a very sensitive tool for studying membrane permeabilization, since already single pores on a large lipid membrane area of approximately 1 mm² size as well as low ion currents down to 1 pA (1 pA = 6·106 e/s) can be detected[147]. Thus, even minor changes in membrane conductance are observed and make this electrophysiological approach the most suitable method for collecting information about single pores. Further, the experimental setup enables the study of pore formation in voltage-clamp mode, with applied transmembrane voltages from ±10, ±20, ±50 to maximum ±100 mV. The capacitance and current measurements of planar lipid bilayers were recorded with the tool *Biophysical Bilayer Analyse System 1.51* (LabVIEW 7.1, National Instruments Corporation, Austin, TX, USA). The resampled data file was loaded in Origin 6.0 for further evaluation. All experimental data of this method were adjusted by the device typical factor and smoothed with a moving average of 20 (*q.v. section 4.1.5, page 147*).

3.5 Membrane Intercalation, Organization & Dynamics

As mimicry for the outer leaflet of the plasma membrane of mammalian cells, mixtures are typically composed of cholesterol and either PC or SM or both. In this thesis, this membrane mimicry consists all three components, only the natural PC is displaced by the unsaturated fatty acid analog DOPC. Due to the individual properties of each component, such as structure, packing and chain order – just to name a few, saturated (SM) and unsaturated lipid species will phase separate. Cholesterol favors the interaction with saturated lipid species forcing the fatty acid chains to adopt an almost all-trans configuration. In these mixtures, the cholesterol-poor membrane regions or liquid-disordered phase (L_D) coexist with cholesterol-enriched membrane areas, that exhibit increased rigidity and a higher degree in lipid order, composing the liquid-ordered phase (L_O). For studying the influence of these distinct membrane regions, model membranes with an incorporated lipid-dye conjugate were used. All of the presented fluorophores are excluded from the liquid-ordered phase and therefore only the liquid-disordered membrane regions are fluorescently highlighted (Figure 32).

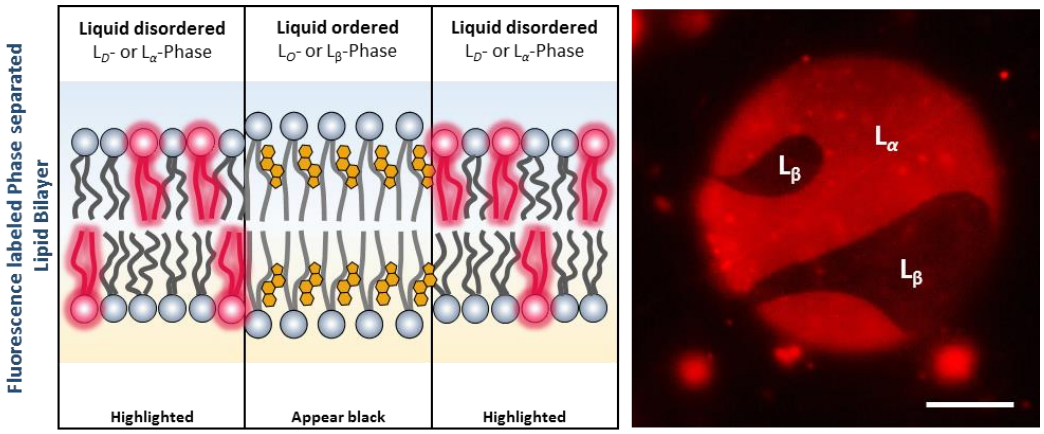

Figure 32 | Phase separation in cholesterol-rich lipid bilayers. Ternary lipid mixtures undergo phase separation at rt in presence of sphingolipids and sterols forming *lipid rafts*, defined regions exhibiting high order. The liquid-disordered or L_α-phase is mainly composed of phospholipids, whereas the liquid-ordered L_β-phase is enriched in cholesterol and sphingomyelin. Hemispherical view of phase separated, free-floating DOPC/SM/Chol-GUVs is depicted exemplary. Scale bar denotes 5 µm.

One exception is made in FRET-experiments for the determination of peptide-intercalation, wherein two different FRET-pairs are applied: one (NBD-PE/Rho-DHPE) labeling the cholesterol-poor membrane regions and a second (NBD-12-Chol/Rho-DHPE) labeling the cholesterol-rich membrane fractions. Figure 33 shows the chemical structures of the applied lipid-dye conjugates and their fields of application.

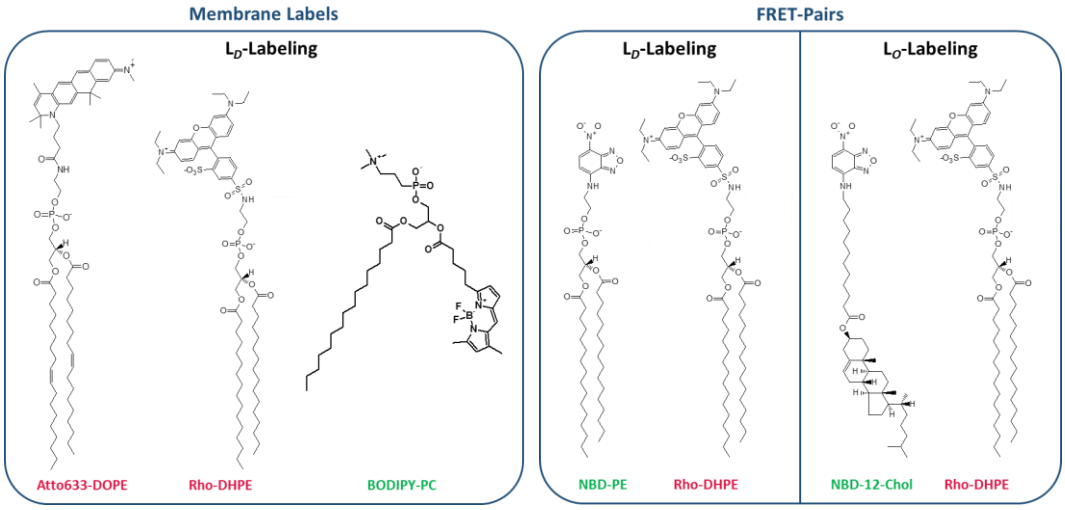

Figure 33 | Lipid-dye conjugates for labeling phase separated lipid membranes. Left: Lipid-dye conjugates for labeling (immobilized) GUVs. These dyes highlight the liquid-disordered or L_α-phase that is mainly composed of phospholipids. Due to the exclusion of these dyes from the liquid-ordered L_β-phase that is enriched in cholesterol and sphingomyelin, these areas appear black under a fluorescence microscope. Right: Used FRET-pairs for studying peptide intercalation and the influence of cholesterol-enriched domains.

3.5.1 Immobilization of Giant Unilamellar Vesicles

3.5.1.1 Preparation of Immobilization-Support

Solid supported bilayers generated from small unilamellar vesicles (SUVs) were used as support for immobilizing giant vesicles (*q.v. section 3.5.1.1, page 101*). The preparation stated in *section 3.3.1 (page 80)* was adjusted to the SUVs final application. Providing a base for the whole immobilization implementation, SUVs were prepared in the initial step. Therefore, DOPC was dissolved as described earlier in $CHCl_3$ to a final concentration of 2 mg/mL and mixed with biotinylated PE in a molar ratio of 99.5:0.5 mol%. The lipid mixture was evaporated under nitrogen exposure and the resulting lipid film was resolved in low-salt buffer (5 mM

HEPES, pH 7.4) to a final concentration of 1 mg/mL. SUVs were formed by applying a pulsed ultrasound (Ultrasonic-Homogenizer *HTU Soni130*, 2 min, pulse on/off: 2 s, amplitude set to 80%). Prepared SUVs (150 µL) were directly pipetted in four of the eight wells of the microscopy chamber (ThermoFisher, LabTekII®). The SUVs were allowed to spread by incubation overnight at 4 °C on a stirring plate (70 rpm). The other four wells were left empty for later cooling while imaging the immobilized GUVs.

3.5.1.2 Immobilization via Avidin-Biotin-Chemistry

Immobilization of GUVs was realized by avidin-biotin-chemistry linking the vesicles to a supported biotinylated bilayer (Figure 34)[148]. The support is built up of spread DOPC-SUVs (150 µL) as described in the section before and is separated from the coverslip by a 10-20 Å thick buffer film[149]. After overnight incubation on a stirring plate (70 rpm, 4 °C), GUVs (50 µL) were added in a *support to GUV ratio* of 3:1 (v/v). Thereafter, 15 µL avidin (1 mg/mL in MilliQ, Sigma-Aldrich, St. Louis, MO, USA) were added. The surrounding wells were furnished with ice for cooling. The solution was incubated in the dark at rt for at least 30 min allowing the linkage of the giant vesicles to the support. If required, the immobilization process can be imaged by confocal microscopy. After complete immobilization, fluorescently labeled peptides (e.g. Rho-LL-32, BODIPY-PMB, Rho-hBD-3-l) were added and their distribution on the vesicle's surface can be detected over time.

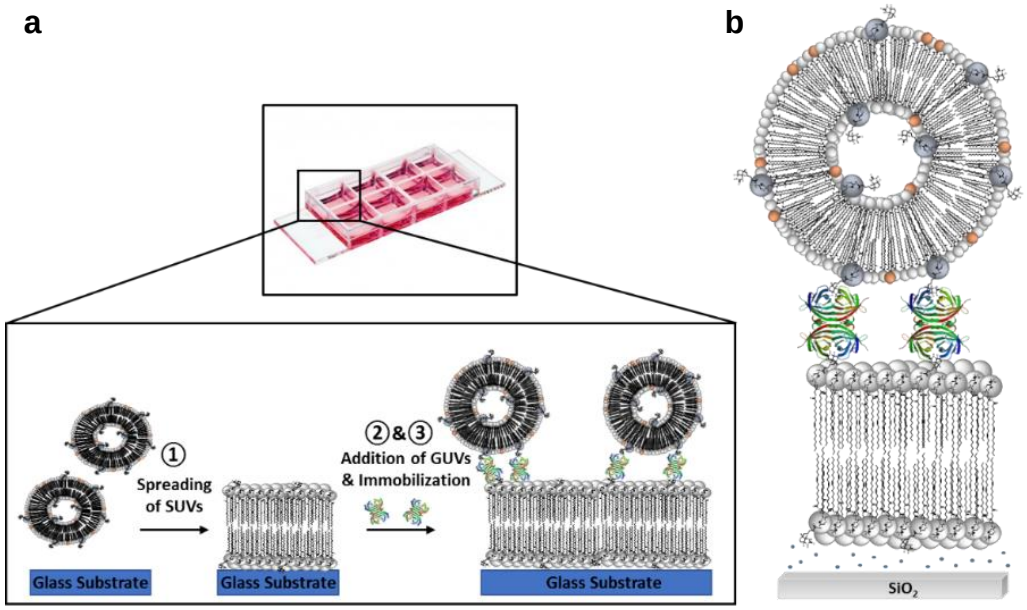

Figure 34 | Schematic presentation of the individual steps for the immobilization of giant vesicles. Each experimental set is scaled to LabTekII 8 well microscopy chambers. Biotinylated DOPC-SUVs (150 µL) are spread homogenously by overnight incubation on a stirring plate (70 rpm, 4 °C). Biotinylated and fluorescently labeled GUVs (50 µL) are added to the immobilization support followed by direct addition of avidin (15 µL, 1 mg/mL). GUVs are immobilized by incubation for at least 30 min (protected from light at rt).

3.5.1.3 Fluorescent-Dye-Distribution-Analysis (FDDA) of Immobilized GUVs

An in-lab developed software, based on Python (x, y) (Version 2.7.6.1), was established to analyze the fluorescence intensity along the circumference in one z-position. The user procedure *GUV-analysis.py* masks the membrane margins of the GUV (Figure 35). To function properly, the vesicles need to have a perfectly spherical shape, otherwise only fragments can be analyzed. The input panel of the software requires three main variables: The x- and y-coordinates of the center of the vesicle and the thickness of the fluorescent margin (*dr*) in pixel. With this information, the program is able to determine the radius. The dimensions (x- and y-position of the origin, radius) of the GUV of interest together with the *dr*-value defines the masking areas and the width between outer ($Mask_{out}$) and inner mask ($Mask_{in}$) in pixels.

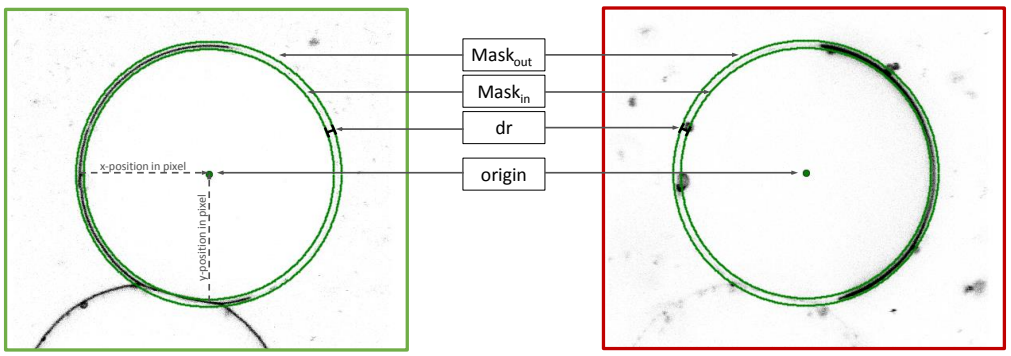

Figure 35 | Read-out of the masking areas defined in *GUV-analysis.py* for FDDA of giant vesicles reconstituted from DOPC/SM/Chol in a molar ratio of 2:2:1. GUVs were incubated with BODIPY-labeled PMB. Fluorescence data are transformed into grey-scale prior to progressive fluorescent dye distribution analysis (FDDA).

The embedded azimuthal tool of the user procedure then uses the starting angle (0°, three o'clock position) and an integration angle to specify the arc area between two concentric circles that are set as mask around the giant vesicles z-slice (*q.v. section 4.1.7, page 153*). Then, the tool divides the area from angle *deg1*, that is defined by starting angle minus integration angle, to angle *deg2*, that is defined by starting angle plus integration angle, into the specified number of bins. The average intensity is calculated for all pixel values in each bin. The pixel size of each bin is defined by the thickness parameter (*dr*) entered in the panel. Usually values of *dr* from 8 to 12 pixels are used, depending on the thickness of membrane margin. The azimuthal function works from zero to 360° counterclockwise and sums up all averaged values of all bins for each channel. As read out the summed intensities vs. the angle is plotted as profile for each channel. The distribution of both, peptide and vesicle, can be analyzed with respect to correlation or anti-correlation of the corresponding fluorescent dyes. The whole code can be accessed by request.

3.5.2 FÖRSTER RESONANCE ENERGY TRANSFER ASSAY

This liposome-based assay is built upon FÖRSTER Resonance Energy Transfer (FRET-) technique named after Theodor Förster. Today, this phenomenon is also referred to as fluorescence resonance energy transfer. This technique enables the determination of peptide-induced membrane intercalation. That is why small vesicles were prepared with incorporated lipid-dye conjugates, comprising a FRET-pair (*q.v. section 3.3.1, page 80*). As FRET-pairs either the ammonium salt of 1,2-dioleoyl-*sn*-glycero-3-phosphoethanolamine-*N*-(7-nitro-2-1,3-benzoxadiazol-4-yl) (NBD-labeled PE) and the triethylammonium salt of Lissamine™ rhodamine B 1,2-dihexadecanoyl-*sn*-glycero-3-phosphoethanolamine (Rhodamine B-labeled DHPE) are used for labeling the liquid-phase of the liposomes or 5-cholesten-3β-ol 12-[(7-nitro-2-1,3-benzoxadiazol-4-yl)amino]dodecanoate (NBD-labeled cholesterol) and Rhodamine B-labeled DHPE were used for highlighting the cholesterol-rich phase of the liposomes. The green fluorescent NBD-conjugates were first excited (donor dye) and taken to an excited state (S_1) due to an absorption maximum at higher frequency. To leave this promoted level back to its initial state (S_0), the donor dye is able to transfer its energy through singlet-singlet state transition (dipole-dipole interaction) to an acceptor dye, if both dyes are in spatial proximity. The distance wherein FRET can be observed ranges from 1 nm to 10 nm and thus resembles a molecular ruler (Figure 36)[9].

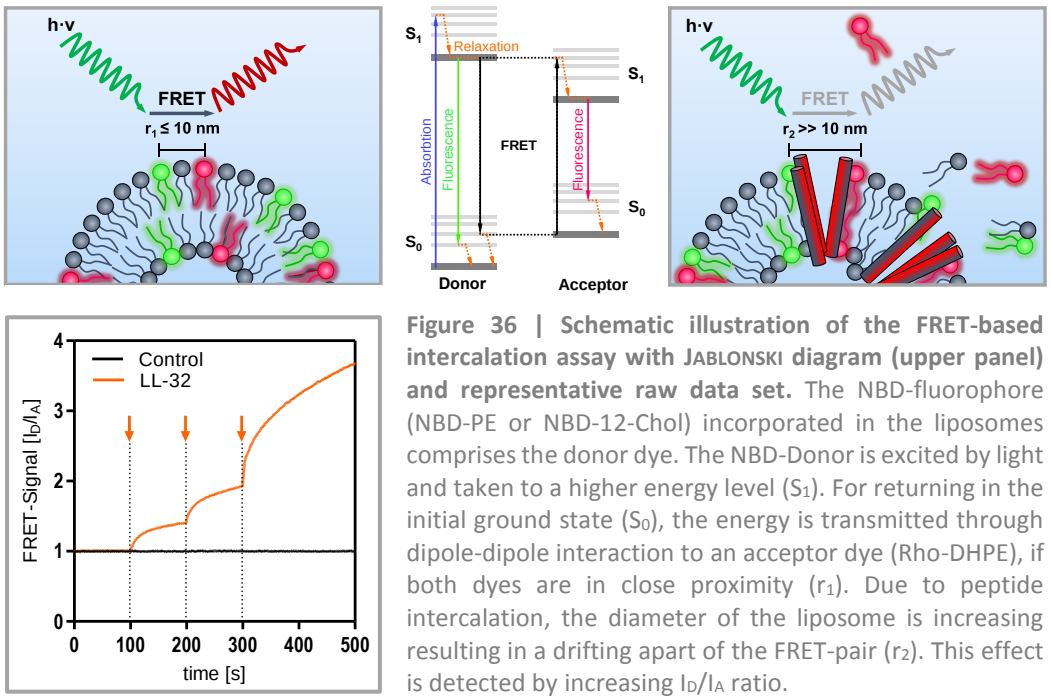

Figure 36 | Schematic illustration of the FRET-based intercalation assay with JABLONSKI diagram (upper panel) and representative raw data set. The NBD-fluorophore (NBD-PE or NBD-12-Chol) incorporated in the liposomes comprises the donor dye. The NBD-Donor is excited by light and taken to a higher energy level (S_1). For returning in the initial ground state (S_0), the energy is transmitted through dipole-dipole interaction to an acceptor dye (Rho-DHPE), if both dyes are in close proximity (r_1). Due to peptide intercalation, the diameter of the liposome is increasing resulting in a drifting apart of the FRET-pair (r_2). This effect is detected by increasing I_D/I_A ratio.

For the experimental setup liposomes with an incorporated FRET-pair were prepared as described in *section 3.3.1 (page 80)*. After injection of 1980 µL into a 10 mm wide standard quartz cuvette the initial fluorescence intensity was recorded on a SPEX Fluorolog or on a Fluorolog-III fluorescence spectrometer (Horiba Jobin Yvon, Edison, NJ, USA). As soon as stable background fluorescence was reached, three peptide injections within time lags of 10 min were performed: Injections of 2 µL (1 µM), 4 µL (3 µM) and 14 µL (10 µM) of LL-32 or PMB led to a step-like increase in I_D/I_A-ratio. This observation indicates diameter augmentation of the vesicles that is equipollent with a reorganization of the fluorescent probes to distances out of the range of FRET. Therefore, the I_D/I_A-ratio can be consulted for determining the degree of peptide-intercalation. All intercalation experiments were performed at 37 °C under the buffer conditions as stated in table 13 (*section 3.1.5, page 72*). Additionally, buffers supplemented with 100 mM NaCl instead of KCl as well as buffers without $CaCl_2$ x $2H_2O$ were used. All buffer systems were adjusted to pH 7.4 with 1 N base of the corresponding counterion. FRET-intercalation assay data (*q.v. section 4.1.6, page 150*) were plotted as

mean +SD of three independent experiments (n = 3; $p \leq 0.05$ = *; $p \leq 0.01$ = **; $p \leq 0.001$ = ***; $p \leq 0.0001$ = ****). Changes in the acceptor/donor ratio were evaluated respectively to control measurement.

3.5.3 Fluorescence Recovery after Photobleaching

Traditional fluorescence microscopy gives qualitative information of the bulk membrane organization; in other words, the localization of membrane-associated substances is merely detected in a "yes or no" state[150]. Photobleaching of specific membrane regions and the detection of fluorescence recovery enables the elucidation of protein dynamics associated with model or cellular membranes. This technique is called fluorescence recovery after photobleaching (FRAP). For FRAP-experiments, a fluorescent dye must be incorporated in the model membranes and/or linked to the compound of interest depending on the informative value of the experiments. The probed molecules localize in a region of interest (ROI) and are irreversibly bleached using a high-power laser illumination (Figure 37a+b). Over a fixed period, circumjacent fluorescent molecules diffuse into the ROI and the fluorescence intensity recovers gradually (Figure 37c). Consequently, information of the dynamic behavior of proteins and peptides as well as lipid molecules can be derived from the fluorescence recovery over time within the ROI (Figure 37d). The rate of fluorescence recovery is controlled by two major processes[150]: One fast process, in millisecond range, wherein the diffusion of circumjacent lipid-dye conjugates or fluorescently labeled peptides is predominant; and a second slower process, wherein thought has been given to the binding affinity between labeled compounds and potential binding partners present within the ROI. The latter is more pronounced for proteins on cellular surfaces, referring to the continuous turnover proteins undergo in cells. Thereby, the bleached area is repopulated with fluorescent proteins displacing the bleached molecules.

FRAP was performed in cooperation with the lab of C. Huebner (University of Lübeck, Institute of Physics, Lübeck, Germany). All preparations in advance were performed at the *Research Center Borstel*;

measurements were run out at the *University of Lübeck*. For studying membrane peptide interaction and dynamics, pure DOPC and DOPC/SM/Chol (2:2:1) liposomes as described in *section 3.3.1* (*page 80*) were prepared. The experimental setup was scaled to 8 well microscopy chambers (Nunc™ Lab-Tek™ II Chambered Coverglass, ThermoFisher Scientific, Roskilde, Denmark): 150 µL of SUVs were spread overnight on a plate shaker (70 rpm) at 4 °C. Fluorescently labeled peptides were diluted directly prior to use in protein low-bind tubes (Eppendorf AG, Hamburg, Germany) and kept in the dark while the experiment was running. Final concentrations of 1 nM or 10 nM (10 µL, 1:15, v/v) were applied. Fluorescence recovery after photobleaching (FRAP-) experiments were carried out on a home-built scanning confocal optical microscope (SCOM) stage at rt. This microscope stage was equipped with a water immersion objective N.A. 1.2 (Plan Apochromat VC, NIKON, Melville, NY)[151]. Figure 37 illustrates the principle behind this method together with an exemplary raw data set.

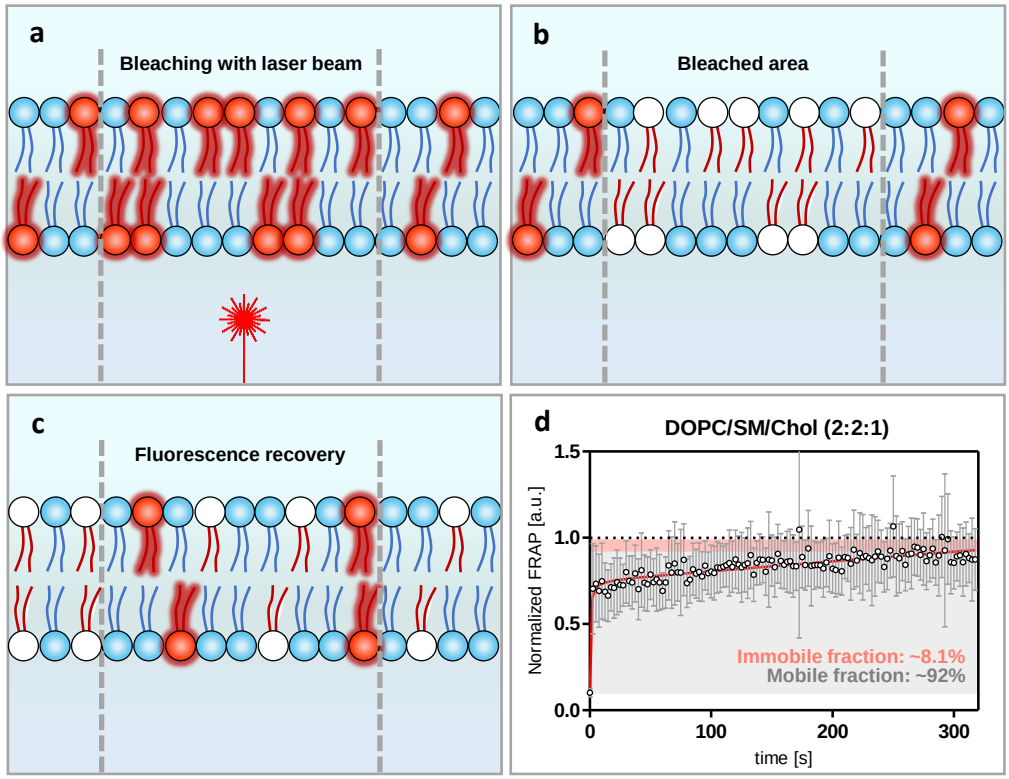

Figure 37 | Schematic illustration of the FRAP-technique. (a) The Fluorophores of membrane-bound dye of spread SUVs were bleached by exposure to maximum laser power for 10 min. (b) the bleached area is detected and (c) fluorescence recovery is recorded in linescan mode with an integration time of 8 ms. (d) shows normalized raw data of the ternary lipid system DOPC/SM/Chol in a lipid ratio of 2:2:1. The unbleached area is depicted by the dashed line colored in black. Red line gives the non-linear fit. The mobile and immobile fractions can be determined by calculating the areal fraction respectively to the reference line (unbleached area). The mobile fraction is highlighted in light grey and the immobile fraction is colored in light magenta.

For membrane labeling, the lipid-dye conjugate Atto633-DOPE (0.05mol%, 1:1000, v/v) was incorporated in the liposomes that were allowed to spread. The fluorescently labeled membrane was checked for homogenous distribution of the fluorophores, to ensure uniform spreading and all-over membrane coverage in the microscopy chamber. Labeled membranes were excited with a Coherent® high performance laser system (OBIS™ 685 nm LX 40 mW, Edmund Optics, Barrington, NJ, USA) set to 630 nm wavelength. This laser diode-based system exhibited an output power of 40 mW. FRAP-experiments were carried out at maximum power (110%, 44 mW) for 10 min. Fluorescence recovery was recorded in line scan

mode (256 pixels, 20x20 µm) with 2% laser power (1 mW) and an integration time set to 8 ms.

Peptide-bound fluorophores (BODIPY-, Atto488-) were excited with a solid-state continuum wave laser at 480 nm with an incoming power of 5 µW (Newport Spectra-Physics, Darmstadt, Germany). The blue laser features a maximum output power of 10 mW. For bleaching of the peptide-dye conjugate, the intensity was set to 40 µW. A piezo-driven *x-y* stage operating in closed loop facilitates sample scanning[151]. Scanning in z-direction is provided by combining the *x-y* stage with a piezo actuated objective stage (PIfoc, PI, Karlsruhe, Germany)[151]. Both fluorophores were excited and recorded simultaneously under the same conditions and software/experimental setup settings. Data were evaluated with IGOR Pro (Version 6.3.7.2, WaveMetrics, Inc., Lake Oswego, OR, USA) together with the integrated user procedure *Lade_List_Img.ipf* by courtesy of V. HIRSCHFELD (University of Lübeck, Institute of Physics, Lübeck, Germany).

3.6 SYNCHROTRON EXPERIMENTS

3.6.1 X-RAY REFLECTIVITY

X-ray reflectivity (XRR) measurements provide information about membrane structure in the sub-nanometer range and facilitates the resolution of elastic properties, thereunder bilayer bending and elastic deformation induced by membrane active compounds. Information of peptide-induced membrane thinning or thickening can be obtained as well as the electron density (ED) distribution can be calculated. For diffraction applications, short wavelength X-rays in the range of a few angstroms to 0.1 Å are used[152]. The typical photon energies of these so called hard X-rays range from 1 – 120 keV[152]. X-rays as well as atoms and molecules exhibit wavelength intervals of comparable magnitude. As a result, X-ray diffraction comprises an ideal tool for probing structural arrangements of

atoms and molecules (*here:* lipids) in a broad spectra of substrates. All data presented in this thesis were collected unless otherwise noted at the high resolution diffraction beamline P08 at PETRA III of the *Deutsches Elektronen-Synchrotron* (DESY) located in Hamburg, Germany.

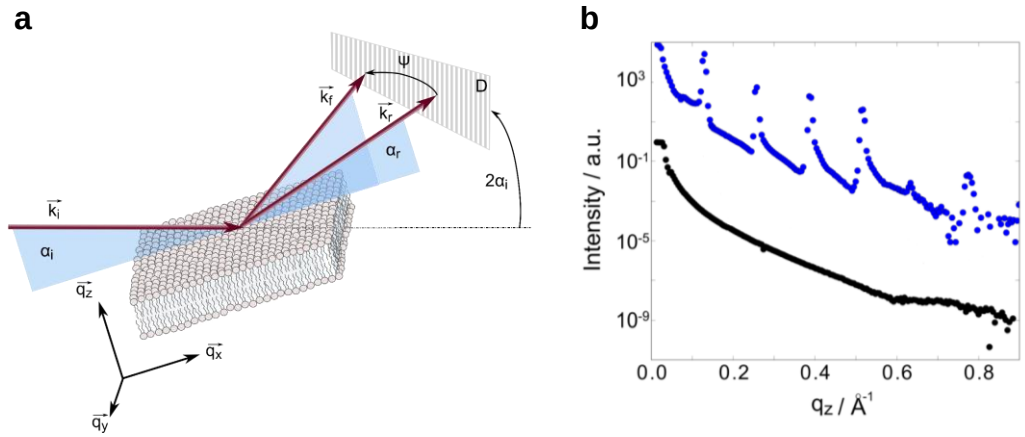

Figure 38 | X-ray reflectivity on aligned lipid membrane stacks. (a) Sample orientation for XRR-measurements. Cutline for the parameters: incident angle (α_i), reflected beam (α_r), detector (D), orientation in 3D ($\vec{q_x}$, $\vec{q_y}$, $\vec{q_z}$), radius of incoming ($\vec{k}_i$) and reflected beam ($\vec{k_r}$). (b) Representative reflectivity profile of a solid supported lipid multilayer (blue) and the pure Si-wafer (black). Courtesy of J. WERNECKE (modified)[12].

For reflectivity measurements, membrane stacks were prepared on a solid support. As solid support silicon wafers in the size of 1x1.5 cm were used. Before multilayer preparation, all silicon wafers underwent a treatment train in MeOH and ultrapure water (3x ultrasound 10-15 min) completed by plasma cleaning (PDC-002, Harrick Plasma, Ithaca, NY, USA). The wafers were placed on a balanced plate before sample preparation to maintain a precisely flat surface. For this method, lipids were dissolved in $CHCl_3$ to a concentration of 10 mg/mL. Pure DOPC, DOPC/SM/Chol in a lipid ratio of 2:2:1 and 9:9:2, and the lipid mixtures supplemented with 10mol% PS were investigated by XRR-measurements. All membrane systems were either prepared with the peptides LL-32 and PMB in a *lipid to peptide ratio* of 4:1 or without as control sample. The $CHCl_3$-stock solutions were directly pipetted together prior to application on the solid support. 100 µL of each sample were prepared, whereof 80 µL were spread on the silicon wafers. Slow evaporation of the solvent lead to

multilayer formation on the solid support. The wafers were lifted carefully with plastic tweezers and placed in gel packs for storage. The wafers in the gel packs were placed together with a water reservoir in a hot-air cabinet and remaining solvent was evaporated overnight.

For X-ray studies, the wafer was mounted in a Teflon chamber held together by screw-tied Kapton® polyimide film covered windows (Kapton® windows). For maximum humidity, 20 µL of ultrapure water were injected to the bottom of each side of the sample chamber.

After experimental setup and sample adjustment, a monochromatic X-ray beam hit the sample under a defined incident angle whereas the reflected beam was detected under a defined scattering angle. The intensity of the scattered beam was detected. In case the momentum transfer between incident and emergent wave of the scattering process is known, the structural amplitude of the sample can be deduced. The orbital electrons of the molecules have a shielding effect. The X-ray radiation is directly scattered at these electrons. With these information, the electron density distribution of the membrane can be determined.

XRR-data of solid supported membrane stacks were first evaluated with OriginPro® 8 (OriginLab Corporation, Northhampton, MA, USA) to obtain the electron density distribution. General proceedings include background and baseline corrections. Bragg peaks were fitted with a Gaussian or Lorentz fit. All SAXS profiles of multilamellar vesicles in solution and GISAXS-data of solid supported multilayers were evaluated by the Python (x, y) based tool developed by J. WERNECKE.

3.6.2 GRAZING INCIDENCE SMALL ANGLE X-RAY SCATTERING

Grazing incidence small angle X-ray scattering (GISAXS) data presented in this thesis were collected unless otherwise noted at the high resolution diffraction beamline P08 at PETRA III of the *Deutsches Elektronen-Synchrotron* (DESY) located in Hamburg, Germany. This technique is performed directly after XRR-data collection. With the help of this method, Bragg peaks are further analyzed by the samples' scattering

behavior to wide angles. Technically speaking, wide angle X-ray scattering (WAXS) is performed but termed as GISAXS. WAXS and SAXS are based on the same technique, the only difference lies in the shorter sample-detector distance. Therefore, with WAXS or GISAXS diffraction maxima at larger angles can be observed. The diffraction pattern of the Bragg peaks as well as the appearance of the C—C chain peak are analyzed by the Python-based evaluation program developed by J. WERNECKE. This program analyzes the distance between the fatty acid groups of the lipids within the membrane stack and their orientation. The packing density is obtained by the mean distance of the polar headgroups. Multilamellar model membrane systems were used due to stronger scattering signals compared to single bilayers.

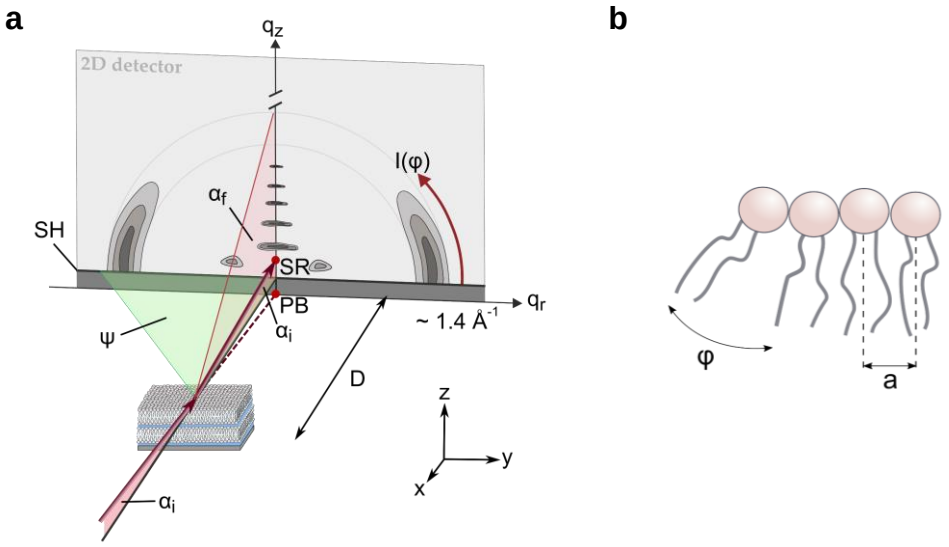

Figure 39 | Scattering geometry of GID experiments. (a) The sample surface of the membrane stack is arranged close-to-parallel to the X-ray beam. The two-dimensional detector is placed behind the sample at a certain distance D. The positions of primary beam and specular reflections are highlighted. Bragg peaks are detected at equidistant angles α_f. The chain correlation peak is detected as arc-shaped reflection around 1.4 Å^{-1}. Cutline for the parameters: incident angle (α_i), equidistant angles (α_f), primary beam position (PB), specular reflection (SR), distance (D), sample horizon (SH), orientation in 3D (x, y, z), incident beam ($\vec{k}_i$, red arrow). (b) Schematic illustration of the lipid ordering along the membrane normal. The chain tilt (φ) along the normal and the averaged chain-chain distance (a) are indicated. Courtesy of J. WERNECKE[12].

3.6.3 Small Angle X-Ray Scattering

Scattering experiments of multilamellar vesicles are used to study model membranes *in situ*. Moreover, in this method effects due to contact between sample and experimental setup are reduced to its minimum. Therefore, mechanical effects are absent. All small angle X-ray scattering (SAXS) experiments in solution were performed at the BioSAXS beamline P12 of the *European Molecular Biology Laboratory* (EMBL) at PETRA III located at the DESY in Hamburg, Germany.

SAXS provides a sophisticated tool to investigate scattering patterns of MLVs (*q.v. section 3.3.2, page 81*) in aqueous environment on the one hand. In this case, membrane structure shows no predominant orientation. Liposomes are distributed isotropically in all directions in space. On the other hand, orientated membranes can be prepared and studied: The orientation of the sample allows the capturing of reciprocal space in two dimensions. The separation of specular and diffuse scattering makes it possible to differentiate between lateral and vertical structures. Multilamellar model membrane systems result in a stronger scattering signal in comparison to single membranes.

For SAXS studies, an automated capillary sample station with controllable heating unit was used. MLVs were prepared as described in *section 3.3.2* in concentrations of 20 mg/mL at the *Research Center Borstel* one day prior to scheduled beamtime. MLVs were mixed with peptides (40 mg/mL in 0.01% TFA) directly before each measurement in a volumetric ratio of 2:1. For sample application, 80 mm long silica glass capillaries (Hilgenberg GmbH, Malsfeld, Germany) with a diameter of 1.5 mm and a wall thickness of 0.01 mm were used and filled with a total volume of 30 µL of the specimen via sterile injection needles (Ø = 0.8 x120 mm; B. Braun AG, Melsungen, Germany). Collected data were evaluated with the Python (x, y) user procedure *plot_temp_3D.py* provided by J. Wernecke.

The Bragg peak pattern with equal interpeak distances given in the SAXS profiles can be further evaluated by calculating the average repeat distance (Equation 3) and the average number of spatially correlated bilayers within the stack (Equation 4)[153].

EQUATION 3:

$$D_{av} = \frac{2\pi}{q_1}$$

q_1: position of the first-order Bragg peak

EQUATION 4:

$$N_{av} = \left(\frac{2\pi}{FWHM}\right) \cdot \frac{1}{D_{av}}$$

FWHM: full width at half maximum of the corresponding peak

3.6.4 Oriented Circular Dichroism

Conventional circular dichroism (CD) spectroscopy allows the structure determination of polypeptides and proteins. Thereby the differential absorption of left- and right-circularly polarized light by chiral substances at different wavelengths is measured. This spectroscopic technique not only complements high-resolution techniques such as X-ray crystallography or nuclear magnetic resonance (NMR) but also has become a *sine qua non* in structural biology. Even though the CD-technique features only low resolution, structural information of proteins and other chiral bio-macromolecules in their native environment can be gathered. In a spectral range from 260 nm to approximately 180 nm, secondary structural motifs can be analyzed, thereunder α-helix, parallel β-sheet, antiparallel β-sheet, turn and random coil.

Steady-state and time-resolved synchrotron radiation circular dichroism (SRCD) are used for collecting information of the secondary structure of e.g. proteins and other macromolecules. SRCD spectroscopy demonstrates an extension to the conventional CD spectroscopic measurements by enabling the detection of spectra with higher signal-to-noise levels and allowing data collection to lower wavelengths (280-160 nm). Further, samples can be measured in presence of strongly

absorbing non-chiral components, thereunder salts, buffers, lipids and detergents[154]. Oriented circular dichroism (OCD) data presented here were collected in the steady-state setup as mentioned recently[155]. This method helped identifying the membrane alignment of the α-helical peptide LL-32 on pure DOPC and cholesterol-rich membrane surfaces as mimics of cellular membranes and its degree of intercalation in these membrane systems (Figure 40). Extended information were obtained when OCD was combined with liquid circular dichroism (LCD) measurements[155]. All OCD-data were generated at the UV-CD12 beamline at the synchrotron radiation facility (ANKA) of the *Karlsruhe Institute of Technology* (KIT) under the guidance of J. BUERCK.

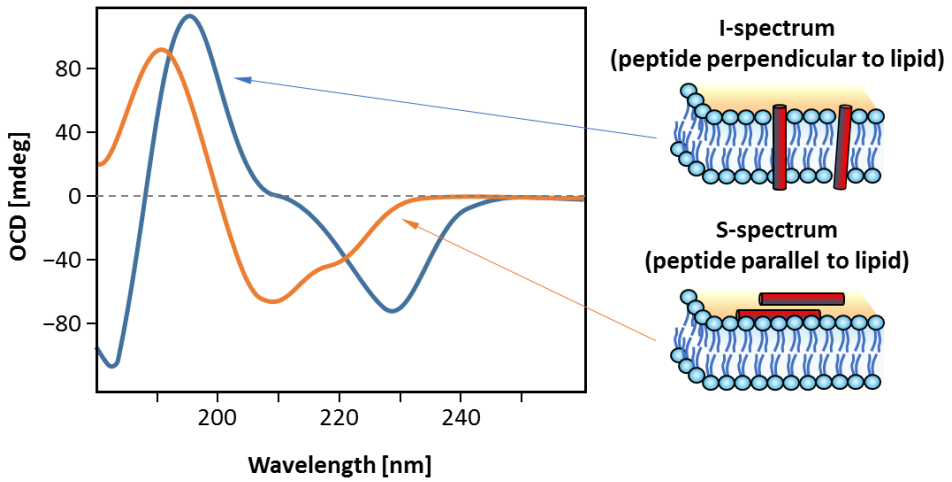

Figure 40 | Descriptive representation of an OCD-spectrum with I- and S-spectra and their corresponding bands (adapted)[8]. Parallel orientation of the peptide helix long with respect to the membrane normal is termed S-state (orange band) and a perpendicular orientation as I-state (blue band). Both states contribute for an α-helical peptide and give the characteristic minima at approximately 208 nm and 223 nm.

For steady-state OCD-experiments, SUVs were spread on cleaned quartz glass windows (Suprasil® QS, Hellma Optik GmbH, Müllheim, Germany). For this purpose, 50 µL of the 2 mg/mL prepared aqueous SUV-solutions (*as described in section 3.3.1, page 80*) with or without LL-32 (control) were added dropwise with a Hamilton syringe. The peptide was dissolved in 0.01% TFA to yield a stock concentration of 0.5 mg/mL. In the OCD-setup, final peptide amounts from 14 µg to a maximum of 28 µg could be applied. As membrane systems, pure DOPC, DOPC/SM/Chol in lipid

ratios of 2:2:1 and 9:9:2 and both ternary systems supplemented with 10mol% PS were investigated. The membrane systems just stated, were reconstituted in 5 mM HEPES at pH 7.4 to prevent scattering by alkali ions. All samples were measured at rt and equilibrated at least 8 h prior to measurement.

LCD-experiments were run out additionally to gain maximum amount of information about the orientation of LL-32 to the bilayer normal. For this method, a small flow-through cuvette was used capturing 100 µL sample volume. For liquid CD measurements, the same SUVs (2 mg/mL) as prepared for OCD-experiments were used. In this setup, the peptide stock solution is diluted 1:1 (v/v) yielding 0.25 mg/mL. The amount of peptide could be increased to a maximum of 56 µg. All LCD-measurements were carried out at rt.

All OCD-experiments were run out from 0° to 360° in intervals of 45° at 160 nm to 280 nm wavelength. In both setups peptide lipid ratios of P/L = 1/10; 1/20; 1/60 and 1/100 were applied. OCD- and LCD-data were evaluated with the software *CDtool* developed by LEES *et al.*[156] and plotted with GraphPad Prism 5. Therein, raw data were first averaged, baseline corrected between 258 nm and 270 nm, and smoothed with an integrated SAVITZKY-GOLAY filter[156]. LCD-experiments were run out in triplicates at constant angle of 90° (respectively to beampath). For data-analysis, LCD-data were proceeded analogous to OCD-data.

Both techniques, OCD- and LCD-measurements, gave maximum information of the alignment of the α-helical peptide LL-32 (Figure 40): Is the peptide aligned parallel to the membrane surface (S-state), the peptide adopts a S-state where the corresponding *fingerprint* CD band around 208 nm will exhibit maximum negative amplitude. Rearranges the peptide its helix alignment upon interaction with the membrane surface intercalating into the membrane, the peptide adopts a tilted (T-state) giving hints for transient pore formation or a fully inserted transmembrane orientation (I-state). These two states are detected by decreasing ellipticity at 208 nm[157].

3.7 Cell Culture Techniques

3.7.1 HEK293-TLR4/MD2 Cell culture Experiments

HEK293-TLR4/MD2 cells were always cultured in the presence of DMEM (Dulbecco's Modified Eagle Medium) which contains a selection antibiotic (G418; 1:1000, v/v) and an antimycotic (Hygromycin; 1:1000, v/v). The medium was supplemented with either 1% or 10% of fetal calf serum (FCS) as well as 2% of Penicillin-Streptomycin/L-Glutamine; stated in the following as DMEM complete media when 10% of FCS is present and as DMEM low media when only 1% of FCS was added. Cells were cultured at 37 °C and 5% CO_2 under the described medium conditions to confluence. The cells attained confluence and were harvested by addition of 1 mL Trypsin/EDTA (1x) under gentle shaking. The detaching reaction was stopped by adding 1 mL of DMEM complete media. Cell viability and total cell number were determined by Trypan blue staining (Merck Chemical GmbH, Darmstadt, Germany) mainly by manual counting in *Neubauer* chambers (C-Chip hemocytometer, NanoEnTek Inc., Seoul, Korea) or with an *EVE™ Automated Cell Counter* (NanoEnTek Inc., Seoul, Korea). The cell suspension was diluted according to the required number of cells in either DMEM complete media or DMEM low media. Cells were seeded into a 96 well flat bottom plate (200 µL, 50.000 cells/well) and incubated for 1 h at the environmental conditions stated above.

Thereafter, the antimicrobial peptides (PMB, LL-32, hBD-3-l, LPep19-2.5 and NK-2) were either added in final concentrations of 1 µM, 3 µM, and 10 µM or as a matter of clear arrangement only in 3 µM and 10 µM. Despite, variants of the human cathelicidin LL-37 (LL-37, LL-32, hCAP18, CRAMP, BMAP-27 and -28; *q.v. section 3.1.2.2, page 61 et seqq.*) were applied on HEK293-TLR4/MD2 cells in final concentrations of 3 µM and 10 µM in an extended stimulation protocol.

3.7.1.1 LPS-induced Stimulation

In the standard experimental protocol, after 30 min of incubation (37 °C, 5% CO_2) the bacterial cell wall component LPS was added in a final concentration of 10 nM. In a modified experimental setup, the peptides were pre-incubated first with LPS before addition onto the cells. Therefore, each peptide was mixed in a volume ratio of 1:1 (v/v) with LPS in an Eppendorf tube and incubated for 30 min. After 24 h the cells were centrifuged (5 min, 20 °C, 1400 rpm), supernatants were collected, and stored overnight at 4 °C. The IL-8 release was measured in the supernatant by human IL-8 ELISA.

In an extended LPS-induced stimulation protocol, the HEK293-TLR4/MD2 cells were first washed after the 30 min peptide-incubation period. Washing steps were first performed by centrifugation (5 min, 20 °C, 1400 rpm) followed by discarding of the supernatant and addition of 170 µL of fresh DMEM complete media. These steps were repeated for three times. Between each washing step, the degree of confluent grown cells was checked by microscopy. Afterwards, LPS was added in a final concentration of 10 nM for 24 h (37 °C, 5% CO_2). After lapse of time, the cells were centrifuged (5 min, 20 °C, 1400 rpm), supernatants were collected, and stored overnight at 4 °C. The cytokine release was measured in the supernatant by human IL-8 ELISA.

3.7.1.2 IL-1β-induced Stimulation

HEK293-TLR4/MD2 cells were further stimulated with the cytokine IL-1β. Concentrations from 1 ng/mL to 300 ng/mL were applied onto the cells. After 24 h stimulation, the cells were centrifuged (5 min, 20 °C, 1400 rpm) and the supernatants were processed as stated in the section above. The IL-8 release was measured in the supernatant by human IL-8 ELISA.

3.7.1.3 TNF-α-INDUCED STIMULATION

HEK293-TLR4/MD2 cells were further stimulated with the cytokine TNF-α. Concentrations from 1 ng/mL to 100 ng/mL were applied onto the cells. After 24 h stimulation, the cells were centrifuged (5 min, 20 °C, 1400 rpm) and the supernatants were processed as stated in the section above. The IL-8 release was measured in the supernatant by human IL-8 ELISA.

3.7.2 ENZYME-LINKED IMMUNOSORBENT ASSAY (ELISA).

Cell culture experiments were analyzed by conventional enzyme-linked immunosorbent assay (ELISA) where the release of the cytokine IL-8 (BD OptEIA, BD Biosciences, Franklin Lakes, NJ, USA) is detected. This biochemical technique enables the quantitative evaluation either based upon optical density or fluorescent units of the sample that is interpolated into a standard curve. ELISA analysis are scaled to 96 well immunosorbent plates (Nunc® Immuno plate MaxiSorp®, ThermoFisher Scientific Nunc A/S, Roskilde, Denmark). This immunoassay describes an antibody-based verification procedure. Due to the fact, that ELISAs are a basic principle *inter alia* for the detection of cytokines released from cells during exposure to different stimuli, the preparation steps this testing system is based on, are described briefly and accord with the manufacturer's protocol: At the outset, immunosorbent plates were coated with a first antibody, also called capture antibody (100 µL/well; 1:500, v/v), that exhibits high binding affinity to the solid surface. The plates were incubated overnight at 4 °C under gentle shaking on a stirring plate (70 rpm). On the next day, the coating solution was discarded and plates were washed three times with 200 µL per well of washing buffer (PBS+0.05% Tween-20, sterile). Afterwards, ELISA plates were blocked for at least 1 h with assay diluent (AD-buffer; PBS+10%FCS, sterile) on a stirring plate (140 rpm, rt). Next, the blocking solution was discarded and a dilution series in assay diluent of a standard solution (2.1 µL/1000 µL) that is based on recombinant human IL-8 was prepared, whereof 100 µL per well were applied. Blank wells were furnished with 100 µL and sample wells with

80 µL assay diluent each. Sample wells were loaded with 20 µL of the supernatants collected from stimulation experiments. For ELISA analysis, all samples were applied in double determinations unless otherwise noted. Plates were incubated on a stirring plate (140 rpm, rt) for two hours. Thereafter, the plate content was discarded one more time and plates were washed again for three times with washing buffer (200 µL/well). The cytokine content released from the cells during stimulation experiments bound to the capture antibody from the initial step and could now be detect with an enzyme conjugate together with a second antibody (detection antibody). Therefore, the enzyme conjugate (1:500, v/v) and the detection antibody (1:2000, v/v) were diluted in AD-buffer and 100 µL were pipetted into each well. For antibody coupling, plates were incubated 1 h (140 rpm, rt). At last, the content was discarded and plates were washed once more for three times (200 µL/well) with washing buffer. The final coloring reaction was induced by adding 100 µL of substrate buffer composed of potassium citrate (200 mM) and citric acid (250 mM) adjusted to pH 4.1, that is supplemented with an ethanolic tetramethylbenzidine (TMB) solution (20mM, 1:20, v/v) consisting small amount of hydrogen peroxide (H_2O_2, 1:167, v/v). High amounts of IL-8 resulted in a strong blue coloration from the former colorless solutions. This reaction was stopped by pipetting 50 µL of sulfuric acid (H_2SO_4, 1 M) in each well when reference wells of the first four dilutions of the standard turned blue. The addition of H_2SO_4 resulted in a color change from blue to yellow that absorbance was detected at 450 nm.

All ELISAs were run out on a microplate reader (Tecan Infinite 200P, TECAN, Crailsheim, Germany) and first evaluated with the software provided by manufacturer (Magellan V7.1, TECAN, Crailsheim, Germany). Further evaluations were performed by spreadsheet analysis with Microsoft Excel (Microsoft Office 365 Personal, Microsoft Corporation, Redmond, WA, USA). For plotting and statistical analysis, data was transferred from Excel to GraphPad Prism 5. Due to variabilities in stimulus response, raw cytokine data (in pg/mL) were recalculated to relative values (given in %), wherein the highest IL-8 release detected for the stimulus (LPS, IL-1β, TNF-α) was set to 100%, unless otherwise specified. All other relative values were given by use of the following formula: raw cytokine data (in

pg/mL) divided by highest raw cytokine data of stimulus applied (in pg/mL) multiplied by 100 (in %). All cell culture data were proceeded analogous. Experimental series were repeated at least three times ($n \geq 3$) and statistics were compiled in a student's paired t-test (two-tailed) and plotted as mean +SD ($p \leq 0.05$ = *; $p \leq 0.01$ = **; $p \leq 0.001$ = ***; $p \leq 0.0001$ = ****).

3.7.3 MTT Viability Assay

This colorimetric assay is based on the metabolic activity of the cells where the mitochondrial reductase converts the yellow tetrazole 3-(4,5-dimethylthiazol-2-yl)-2,5-diphenyltetrazolium bromide (MTT; Sigma-Aldrich, St. Louis, MO, USA) to the isomeric pair (*E, Z*)-5(4,5-dimethylthiazol-2-yl)-1,3-diphenylformazan (Formazan) exhibiting a characteristic purple color (Figure 41). Cellular oxidoreductase enzymes functions NAD(P)H-dependent. Under the defined conditions, as stated in the following, it is therefore possible to infer the number of viable cells from the reduction process. This assay gives information about the peptides cytotoxicity.

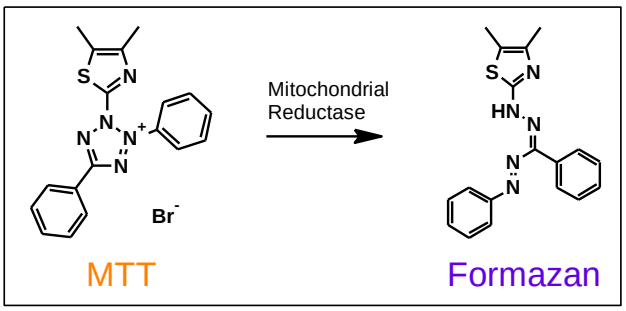

Figure 41 | Reaction mechanism of the reduction from the yellow tetrazole (MTT) to the purple Formazan. The metabolic activity of the cell is measured by means of mitochondrial reductase activity.

HEK293-TLR4/MD2 cells were harvested, seeded in a 96 well flat bottom plate (100 µL, 25.000 cells/well) in DMEM complete media, and incubated overnight (37 °C, 5% CO_2) to attain confluence. On the next day,

the cells were washed twice with 100 µL PBS supplemented with 10% of DMEM complete media. Meanwhile, the samples (*here:* LL-32 and PMB) were diluted according to the concentrations of interest (0.1 to 100 µM) and the controls were prepared. As positive control PBS supplemented with 10% DMEM complete media was used. The negative control comprises 20% TX-100 additionally. In the next step, the supernatants of the confluent cells were discarded and replaced by either 100 µL of sample, positive or negative control, followed by 24 h incubation (37 °C, 5% CO_2) for HEK293-TLR4/MD2 cells and by 4 h incubation (37 °C, 5% CO_2) for human macrophages. The MTT-solution (12 mM, 5 mg MTT diluted in 1 mL PBS) was always prepared on the day of assay read-out and directly before application. Cells were incubated for 2 h (37 °C, 5% CO_2) with 10 µL/well of the fresh MTT-solution. Afterwards, 100 µL of a stop-solution comprised of 54 mL isopropanol, 6 mL TX-100 and 480 µL HCl (37%) were pipetted into each well. The 96 well plate was analyzed colorimetrically at 570 nm (reference filter 690 nm) after resuspension of the formazan crystals. The MTT-cytotoxicity assay was run out in double determinations of four independent experiments (n = 4). All data were edited to Microsoft Excel, plotted and statistically evaluated with GraphPad Prism 5.

3.7.4 Cholesterol Depletion

To study the role of cholesterol in cellular processes and the influence on LPS-induced cytokine release, the cholesterol content in HEK293-TLR4/MD2 was depleted acutely by using chemical reagents (Figure 41). Cells were harvested and seeded in a 96 well flat bottom plate (200 µL, 50.000 cells/well) in DMEM complete media. The cells were allowed to adhere for 1 h (37 °C, 5% CO_2). Afterwards, the cells were centrifuged (5 min, 20 °C, 1400 rpm). The methyl-β-cyclodextrin (mβ-CD; Sigma-Aldrich, St. Louis, MO, USA) was diluted to final concentrations of 0.5 nM to 50 mM in DMEM low media while centrifugation was running. Next, the supernatants were discarded and replaced by DMEM low media (170 µL/well) supplemented with the depletion agent. The cells were incubated with cyclodextrin for 1 h (37 °C, 5% CO_2). After depletion, cells

were centrifuged again (5 min, 20 °C, 1400 rpm), the supernatants were collected for AmplexRed® Cholesterol Assay (Molecular Probes™, ThermoFisher Scientific, Waltham, MA, USA) and fresh DMEM complete media (170 µL/well) was added to the cells. The depleted cells were incubated for another 30 min (37 °C, 5% CO_2) before 10 nM LPS was added. After 24 h stimulation, the cells were centrifuged (5 min, 20 °C, 1400 rpm). The supernatants were collected and stored overnight at 4 °C for further ELISA read-out to quantify cytokine release.

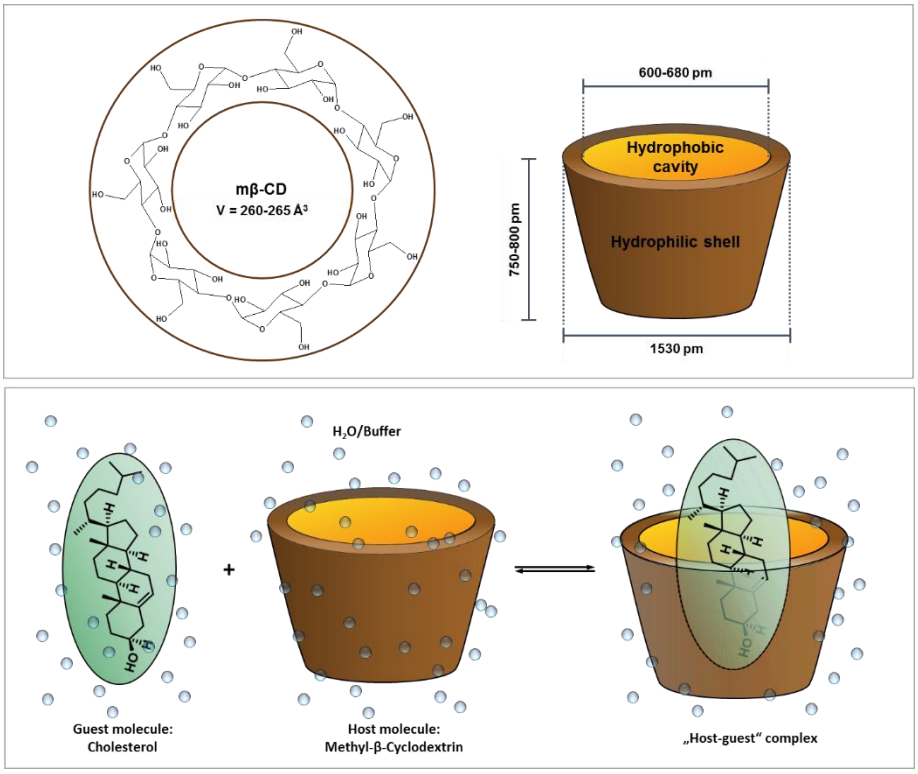

Figure 42 | Characteristics and schematic presentation of the host-guest mechanism of methyl-β-cyclodextrin and cholesterol[6]. Cyclodextrin allows the depletion of cholesterol from the membrane composite.

3.7.5 TLR4-Specificity of LL-32 and PMB

3.7.5.1 CD14-Transfection

With the help of transient transfection, genetic material can be introduced into a cellular organism, resulting in the expression of a naturally nonexistent gene encoding for a specific protein. In contrast to a

stable transfection, transiently transfected cells express the foreign gene without integration into their own genome and thus replication of this gene is switched off. After a distinct period of time, the ability for expression of the foreign genetic material is lost through e.g. cell division.

Transient transfection of CD14 to HEK293-TLR4/MD2 cells was performed in accordance with a protocol introduced by S. KEESE. The protocol was adapted to HEK293-TLR4/MD2 cells regarding incubation times and the total number of cells. HEK293-TLR4/MD2 cells were harvested as described before and seeded in a 96 well plate (200 µL, 30.000 cells/well). The cells were allowed to adhere for 4 h (37 °C, 5% CO_2). Before lapse of incubation time, the transfection agents were prepared in Opti-MEM (Gibco™, ThermoFisher Scientific, Waltham, MA, USA). For a single well 0.5 µL of the transfection agent Lipofectamine® 2000 CD (Invitrogen™, ThermoFisher Scientific, Waltham, MA, USA) and 0.2 µg hCD14-plasmid (c = 1.02 µg/µL) were diluted each in 25 µL Opti-MEM. The transfection agent was incubated for 5 min before both solutions were mixed. The resulting mixture was incubated for another 20 min at room temperature (rt) before application (50 µL/well) onto the cells. The transfection was run out in an incubator (37 °C, 5% CO_2) for 4 h. Afterwards, the media was replaced by either 200 µL/well fresh Opti-MEM for the CD14 transfected cells or by DMEM complete media for the untreated cells. The cells were incubated overnight (37 °C, 5% CO_2) and successfully transfected with CD14.

3.7.5.2 TLR4-LIGANDS-INDUCED STIMULATION

The CD14 transfected HEK293-TLR4/MD2 cells were further processed on the next day: 20 µL of either LL-32 or PMB in a final concentration of 10 µM were added to the transfected and non-transfected (control) cells. The cells were incubated for 30 min (37 °C, 5% CO_2) before TLR4-ligand addition (20 µL/well). As TLR4-ligands Ni^{2+}, MRP8, HMGB1, and Taxol were tested despite LPS. Table 17 shows the ligands and their final concentrations applied. After stimulation for 24 h, the supernatants were collected and stored overnight at 4 °C for further analysis by human IL-8 ELISA.

TABLE 17. EXOGENOUS AND PUTATIVE ENDOGENOUS TLR4-LIGANDS TESTED ON CD14 POSITIVE HEK293-TLR4/MD2 CELLS FOR IMMUNE REGULATORY FUNCTION.

Ligand Property	TLR4 Ligands	Concentration Range	Solvent
Exogenous	LPS	10 nM	20mM HEPES, pH 7.0
	Ni^{2+}	1, 3, 10, 30 µM and 0.1, 0.3, 1, 3 mM	MilliQ
	Taxol	0.3, 1, 3, 10 and 30 µM	DMSO
Endogenous	HMGB1	0.3, 1, 3 and 10 µg/mL	PBS
	MRP8	1, 3 and 5 µg/mL	HBS, pH 7.4

3.7.7 STAINING OF THE TLR4-RECEPTOR COMPLEX

For TLR4-receptor complex staining of HEK293-TLR4/MD2 cells, HEK293 cells were harvested as described earlier and seeded in cell numbers of 30.000 and 50.000 per 100 µL in DMEM complete culturing medium supplemented with Hygromycin and G418 (1:1000, v/v) in a six well µ-slide microscopy chamber (µ-Slide $VI^{0.4}$, ibidi GmbH, Martinsried, Germany). The microscopy slides are tissue culture treated, sterilized and furnished with a 180 µm thick polymer coverslip by distributor.

The medium was taken off the adherent cells and replaced by pre-heated (37 °C) serum-free DMEM medium. The cells were incubated for 20 min at 37 °C (5 % CO_2) before further proceedings. Meanwhile, the aqueous stock-solutions (1 mM in MilliQ) of BODIPY-labeled PMB and Atto488-labeled LL-32 and hBD-3-l were diluted in PBS to the desired final concentrations (3 µM and 10 µM). The DMEM medium was gently removed from the cells and replaced by 100 µL of the fluorescently labeled peptide diluted in PBS. The cells were exposed to the peptides for 5 min (BODIPY-PMB only 3 min) at 37 °C (5% CO_2). Afterwards, the HEK293-TLR4/MD2 cells were washed with 100 µL of ice-cold PBS solution before fixation with 100 µL PBS supplemented with 4% paraformaldehyde (PFA; rt, 10 min). Cells were washed two times with 100 µL PBS right after the ten-minute fixation period. Next, the anti-TLR4/MD2 antibody was added in a 1:20 dilution in PBS (25 µg/mL). As isotype control, a mouse IgG_{2a} antibody (Santa Cruz Biotechnology®, Inc. Dallas, TX, USA) was used

(1:100). For optimal staining, cells were incubated for 1 h at rt in the dark. After that, cells were washed another two times with 100 µL PBS before addition of the fluorescent conjugate binding to the isotype control: gαmIgG-Alexa Fluor® 647 was added in a 1:1000 dilution (2 µg/mL) in PBS. The secondary antibody was exposed to the fixed cells for 1 h at rt; the cells were protected from light. At last, the receptor stained cells were washed two times with 100 µL PBS to remove unbound antibody before staining of the nucleus was performed. For nucleic acid staining, Hoechst 34580 (Molecular Probes®, ThermoFisher Scientific, Waltham, MA, USA) was used in a dilution of 1:250 (4 µg/mL) in PBS. Cells were stained for 30 min at rt in the dark. Unbound dye was removed by three times washing with 100 µL PBS. Cell staining was accomplished by one more fixation step with PBS supplemented with 2% PFA (10 min, rt) followed by three times washing with 100 µL PBS.

The TLR4/MD2-receptor complex was stained with a monoclonal mouse IgG anti-TLR4 antibody (HTA 125, Imgenex, San Diego, CA, USA) Alexa Fluor® 647 conjugate (Molecular Probes®, ThermoFisher Scientific, Waltham, MA, USA). Staining-experiments were run out in cooperation with the division of *Immunobiophysics at the Research Center Borstel*. TLR4-staining was performed and analyzed via CLSM by A. SCHROMM (Division of Immunobiophysics, Research Center Borstel, Germany). The stained HEK293-TLR4/MD2 cells were stored at 4 °C submerged in PBS until analysis by confocal microscopy.

3.7.8 ISOLATION OF HUMAN MACROPHAGES

Human macrophages (hMΦ) were isolated from freshly peripheral blood samples of voluntary blood donors. For isolating distinct cell types, the blood samples were heparinized (20 IU/mL) directly after donation and further processed by mixing with equal volume ratio (1:1) of *Hanks Salt Solution* (HSS, Biochrom GmbH, Merck Millipore, Darmstadt, Germany). For density gradient centrifugation, Corning® 50 mL centrifuges tubes (Sigma-Aldrich, St. Louis, MO, USA) were furnished with 10 mL of Biocoll separating solution (Biochrom GmbH, Merck Millipore, Darmstadt,

Germany) and gently overlaid in a volume ratio of 1:3 (v/v) with the blood mixture. After centrifugation (30 min, 4 °C, 1800 rpm, brake: off) in a thermos centrifuge (Biofuge 17RS, Haereus-Sepatech, Osterode, Germany, rotor 3090), the supernatants were discarded and the interphase layers collected. The melded interphases were diluted to 50 mL with HSS and centrifuged (10 min, 4 °C, 1800 rpm) again. The supernatants were discarded one more time and the cell pellets were resuspended in 5 mL of RPMI 1640 media supplemented with 2 mM L-Glutamine, 100 U/mL Penicillin and 100 µg/mL Streptomycin (*abbr.* RPMI+PS/Glu 2%, Biochrom GmbH, Merck Millipore, Darmstadt, Germany). The cell suspensions were transferred to new Corning® tubes and diluted to 50 mL with RPMI. For macrophage maturation, MNCs (125-200·10^6 cells per Teflon bag) were stimulated with 0.1% of macrophage colony-stimulating factor (M-CSF, bio-techne, R&D System Inc., Minneapolis, MN, USA) diluted in RPMI+PS/Glu 2% supplemented with 4% of inactivated human AB-serum. Human macrophages were differentiated from mononuclear cells (MNCs) in Teflon bags within one week (37 °C, 5% CO_2).

4. RESULTS

4.1 MEMBRANE ACTIVE FUNCTION

Within the scope of this thesis, the presented antimicrobial peptides were characterized in detail respectively to their membrane active function, one of the key commonalities of this very diverse substance family (*q.v. section 1.2.4, page 30*). As simplest model membrane system, the pure zwitterionic lipid DOPC was used. With progress and gaining of insights of the mode of function of membrane activity, the set of model membranes was increased in degree of complexity and extended to the inner membrane model of the bacterial cell envelope composed mimicked by POPE/POPG as well as the imitation of human immune cells reconstituted from the lipid mixture with the composition DOPC/SM/Chol. The table stated below gives a concentrated overview of the chosen techniques, substances, and membrane systems used in this doctoral research work.

TABLE 18. OVERVIEW OF THE METHODICAL APPROACHES FOR THE CHARACTERIZATION OF MEMBRANE ACTIVE PROCESSES

Methods	Membrane System	AMPs
Calcein Release	DOPC	LL-32, hBD-3-l, arenicin-1
	POPE/POPG	LL-32, hBD-3-l, arenicin-1
KI Quenching	DOPC	LL-32, hBD-3-l, arenicin-1, PMB
	POPE/POPG	LL-32, hBD-3-l, arenicin-1
	DOPC/SM/Chol	LL-32, hBD-3-l, PMB
Pore-spanning Membranes	DOPC	LL-32, hBD-3-l, arenicin-1, PMB
	POPE/POPG	LL-32, hBD-3-l, arenicin-1
	DOPC/SM/Chol	LL-32, hBD-3-l, PMB
	DOPC/SM/Chol+PS	LL-32, hBD-3-l, PMB

TABLE 18. – CONTINUED FROM PREVIOUS PAGE

Tethered Membranes	DOPC	LL-32, hBD-3-l, arenicin-1, nonactin, α-hemolysin, PMB
	POPE/POPG	LL-32, hBD-3-l, arenicin-1, nonactin, α-hemolysin
	DOPC/Chol	LL-32, hBD-3-l, PMB
	DOPC/SM/Chol	LL-32, hBD-3-l, PMB
	DOPC/SM/Chol+PS	LL-32, hBD-3-l, PMB
MONTAL-MUELLER Membranes	DOPC	LL-32, hBD-3-l, arenicin-1, nonactin, α-hemolysin
	POPE/POPG	LL-32, hBD-3-l, arenicin-1, nonactin, α-hemolysin
FRET-Intercalation	DOPC/SM/Chol	LL-32, PMB

4.1.1 CALCEIN RELEASE ASSAY

For the antimicrobial peptide LL-32, 100% calcein release is already observed after the first peptide addition (1 μM, w/o KCl) to DOPC liposomes (Figure 43). Interestingly, a higher concentration of LL-32 (10 μM, w/o KCl) is needed to reach full membrane permeabilization on charged POPE/POPG (4:1) membranes, even the cationic surface charge of the peptide facilitates membrane insertion and therewith permeabilization processes for this membrane type. In presence of 100 mM KCl, the effect is significantly decreased for both membrane types: LL-32 showed a concentration dependent increase in lytic activity on DOPC membranes up to 75% at the highest dose (10 μM); whereas in case of POPE/POPG (4:1) no significant concentration dependency was observed. Low-salt vs. high-salt buffer conditions were significant for DOPC membranes. In case of an overall negative surface charge, only for the highest applied concentration of the peptide (10 μM) a significant difference was observed.

The linear version of the human β-defensin showed 60% membrane permeabilization on DOPC membranes at 1 μM (w/o KCl). In presence of 100 mM KCl, no membrane permeabilization activity was observed. On negatively charged lipid bilayers under low-salt conditions, a concentration dependent increase in calcein release was detected. When 100 mM KCl was present, the concentration dependent effect was diminished but the overall

detected calcein release was significantly increased (mean: 78%, 1 μM). Under high-salt conditions on POPE/POPG (4:1) membranes, hBD-3-l is 80-fold higher in activity compared to the uncharged membrane type.

Arenicin-1 showed under both buffer conditions a concentration dependent increase in membrane permeabilization for DOPC membranes. Low-salt conditions lead to a maximum of 60% (10 μM) membrane permeabilization. Under high-salt buffer conditions this effect is weakened (40%, 10 μM). The negatively charged POPE/POPG-membranes yield in a significant enhancement of membrane activity; the calcein release was increased with rising peptide concentrations. No permeabilization effect was observed at 1 μM arenicin-1 (w/o KCl), moderate calcein release was detected at 3 μM (18%, w/o KCl), and 90% liposome disintegration was reached at 10 μM. Whereas under high-salt conditions, 100% membrane permeabilization was already detected at low doses of arenicin-1 (1 μM).

The calcein release approach for the detection of membrane permeabilization is applicable for the small membrane active compounds (*here:* AMPs with an approximately size range between 3 to 6 kDa) but not for larger pore formers (e.g. α-hemolysin). A differentiation between intercalation and pore formation cannot be made; despite, the detected membrane lesions have to be large enough for the calcein to fit through. Smaller and transient pores aren't resolvable and are neglected by this method.

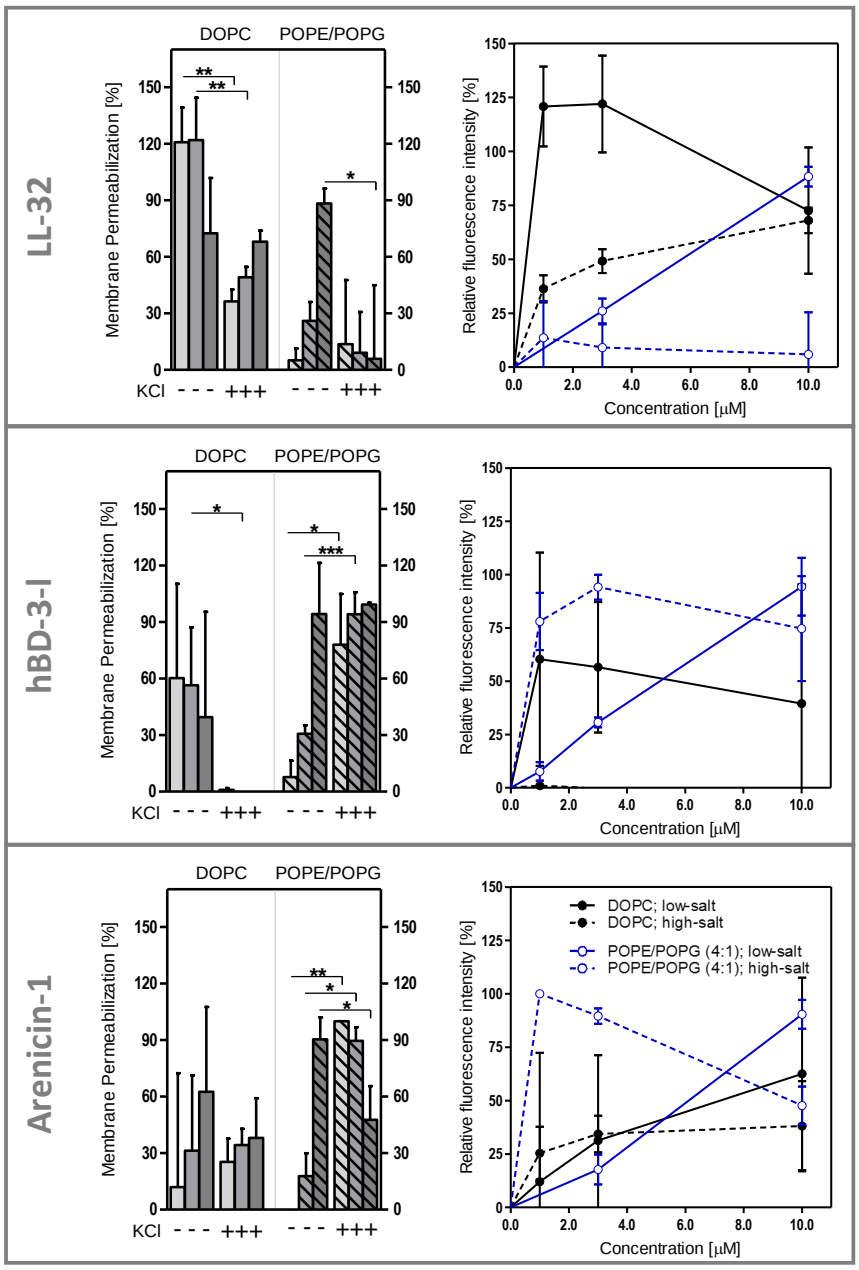

Figure 43 | Calcein release assay for testing the influence of membrane active compounds on charged and uncharged lipid bilayers. Antimicrobial peptides (LL-32, hBD-3-l, and arenicin-1) were tested on DOPC- and POPE/POPG-liposomes as membrane mimics entrapped with calcein. POPE/POPG-liposomes were prepared in a lipid ratio of 4:1. Permeabilization events were detected under low- (w/o KCl, −) and high-salt (100 mM KCl, +) buffer conditions. The increase in fluorescence intensity was detected over time at 37 °C. Peptide concentrations of 1, 3 and 10 µM were applied. TX-100 was added for total calcein release. Raw data were transformed into column diagrams by using equation 1. Curve charts are plotted for the sake of completeness. Cutline for the curve charts: DOPC-liposomes under low-salt (blue line) and under high-salt conditions (dashed blue line); POPE/POPG-liposomes under low-salt (black line) and under high-salt conditions (dashed black line). Statistical analysis was performed in a two-tailed student's paired t-test (non-significant: ns $p \geq 0.05$; significant: * $p \leq 0.05$; very significant: ** $p \leq 0.01$; extremely significant: *** $p \leq 0.001$). Data are plotted as mean of five (DOPC) or four (POPE/POPG) independent experiments +SD (n = 4-5).

4.1.2 Potassium Iodide Quenching Assay

On DOPC-membranes under low-salt conditions, LL-32 shows a concentration dependent permeabilization process starting with 8.8% fluorescence quenching at low concentrations (1 μM) increasing to a maximum of 51.5% (10 μM). Under high-salt conditions, this behavior is significantly diminished (30.5%, 10 μM). Whereas, LL-32 induces no distinct quenching effect on charged POPE/POPG-membrane systems under both conditions applied (top row; Figure 44).

However, the pore-forming ability of hBD-3-l, lies beyond the effective range of the quenching assay: On DOPC as well as on POPE/POPG membranes only weak quenching effects were detected under low-salt conditions. Whereas the effect on the charged membrane system is even less pronounced (5%, 10 μM). On DOPC membranes, a weak concentration dependent quenching effect is detected, resulting in a maximum quenching of 7.5%. These results are found under high-salt conditions in an analog manner only pronounced to lesser extent: On uncharged lipid bilayers, a maximum of 4.3% (10 μM) is obtained and on charged lipid bilayers the membrane activity is lost completely at the highest applied peptide concentration (second row; Figure 44).

Arenicin-1 exhibits a stronger permeabilizing effect on DOPC-membranes compared with the charged POPE/POPG-membrane type. Low concentrations (1 μM) of arenicin-1 already lead to a first quenching of the intra-liposome standing fluorophores. On DOPC lipid bilayers 6.8% (w/o KCl) and 4.7% (100 mM KCl) of the fluorescence are quenched; on POPE/POPG lipid bilayers 2.3% of the fluorescence is quenched by KI under both buffer conditions. With progressive concentration increase, the observed concentration dependent trend is more pronounced on the uncharged membranes (49%, w/o KCl and 31.6%, 100 mM KCl). On overall negatively charged membrane surfaces a maximum permeabilization activity of 11.6% (w/o KCl) respectively 9.3% (100 mM KCl) is reached (penultimate row; Figure 44).

Under low-salt conditions, nonactin integrates into the membrane building a functional carrier for K^+-ions on charged and uncharged lipid

bilayers. On liposomes reconstituted from pure DOPC, the ionophore shows no concentration dependent effect of KI-quenching. With increasing peptide concentrations no further decrease in fluorescence intensity was detected (36.2%, 1 μM; 47.4%, 3 μM; 42.3%, 10 μM). Only in presence of 100 mM KCl, the concentration dependent effect is resolvable on uncharged lipid bilayers with a maximum of 43.5% (10 μM, 100 mM KCl). Whereas, on the charged membrane type no measurable KI-quenching is detected in presence of alkali ions of high concentrations. For charged lipid bilayers, the observed effects are *vice versa*: In aqueous environments with low-salts, concentration dependency is resolvable with a maximum average of 30.3% quenching (last row; Figure 44).

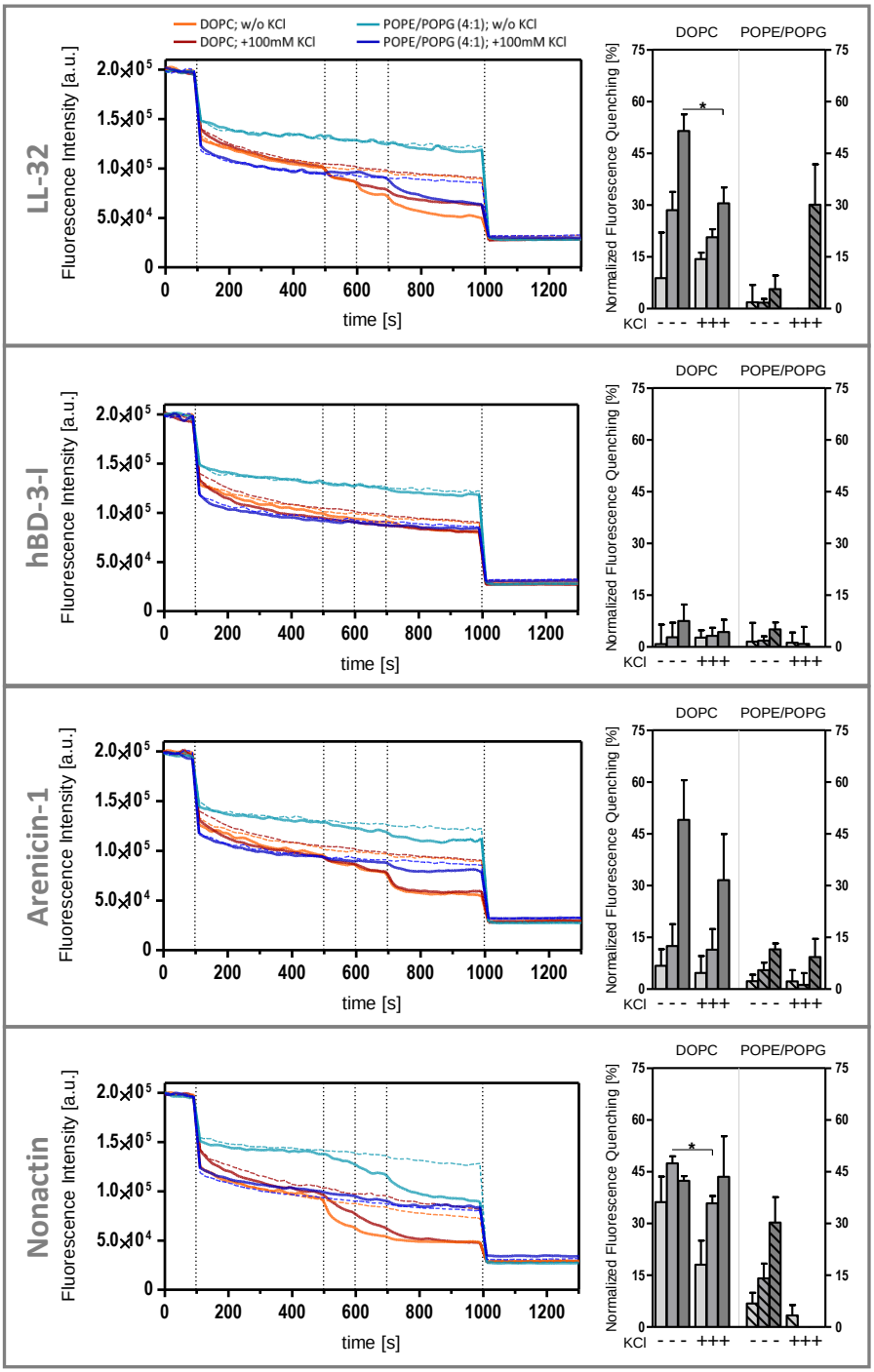

Figure 44 | Potassium iodide quenching assay for testing the influence of membrane active compounds on charged and uncharged lipid bilayers. Raw data (left) were transformed into column diagrams (right) by using equation 2. Control curves are depicted by the dashed lines of the respective color. All data are background corrected. Antimicrobial peptides (LL-32, hBD-3-l, and arenicin-1) were tested on DOPC- and POPE/POPG (4:1) liposomes labeled with NBD-PE. Membrane permeabilization was detected under low- (w/o KCl, −) and high-salt (100 mM KCl, +) buffer conditions. The decrease in fluorescence intensity was detected over time at 37 °C. Peptide concentrations of 1, 3 and 10 µM were applied. TX-100 was added for total fluorescence quenching. Statistical analysis was performed in a two-tailed student's paired t-test (non-significant: ns $p \geq 0.05$; significant: * $p \leq .0.05$). Data are plotted as mean of three independent experiments +SD (n = 3).

To link model membrane systems and biological membranes, the potassium iodide quenching assay was run out on the model analog to human immune cells studying the membrane activity of AMPs in presence of cholesterol. For this system, the same peptides were chosen as used on the cellular system (*q.v. section 3.2.1, page 76*).

Figure 45 shows the degree of fluorescence quenching induced by the membrane active antimicrobials LL-32 and hBD-3-l. The antibiotic peptide PMB as well as the AMPs were tested for pore formation in concentrations below cytotoxicity. On the human immune cells homologue DOPC/SM/Chol in a lipid ratio of 2:2:1, LL-32 showed strong induction of fluorescence quenching under low- (28.8%, 1 μM) and high-salt (21.4%, 1 μM) buffer conditions. Under both conditions applied, a concentration dependent trend was detected finding its maximum quenching at 38.5% (w/o KCl) and 32% (100 mM KCl). PMB and hBD-3-l expose only weak membrane activity: PMB induces lesions with a maximum in fluorescence quenching of 1.6% (1 μM; w/o KCl). For hBD-3-l, maximum fluorescence quenching is reached at 10 μM (1.6%; w/o KCl and 7.3%; 100 mM KCl).

These effects are more pronounced when the membrane system is supplemented with 10mol% PS: LL-32 already starts on an enhanced level with an average degree of 67.3% (w/o KCl) and 48.45% (100 mM KCl) fluorescence quenching at low concentrations (1 μM) leading to a maximum of 82.2% (w/o KCl) and 72.3% (100 mM KCl). The smaller peptide PMB shows its highest degree of fluorescence quenching under low-salt conditions (3.1%, 10 μM), whereas the larger linear peptide variant hBD-3-l exhibits a concentration dependent membrane activity with formation of lesions allowing the quencher molecule to fit through (8.1%, 10 μM; w/o KCl and 10.3%, 10 μM; 100 mM KCl).

The collisional fluorescence quenching induced by KI provides a liposome-based approach for the detection of even small membrane surface defects. With an approximately molar volume of 53.2 cm^3 the potassium iodide is about 7-times smaller in comparison to the calcein molecule (V_m = 372.1 ±5 cm^3) [1]. The quenching molecule can access the inner leaflet of the liposomes at an early stage in membrane permeabilization. This method enables broad spectrum detection of membrane permeabilization processes on cuvette-scale.

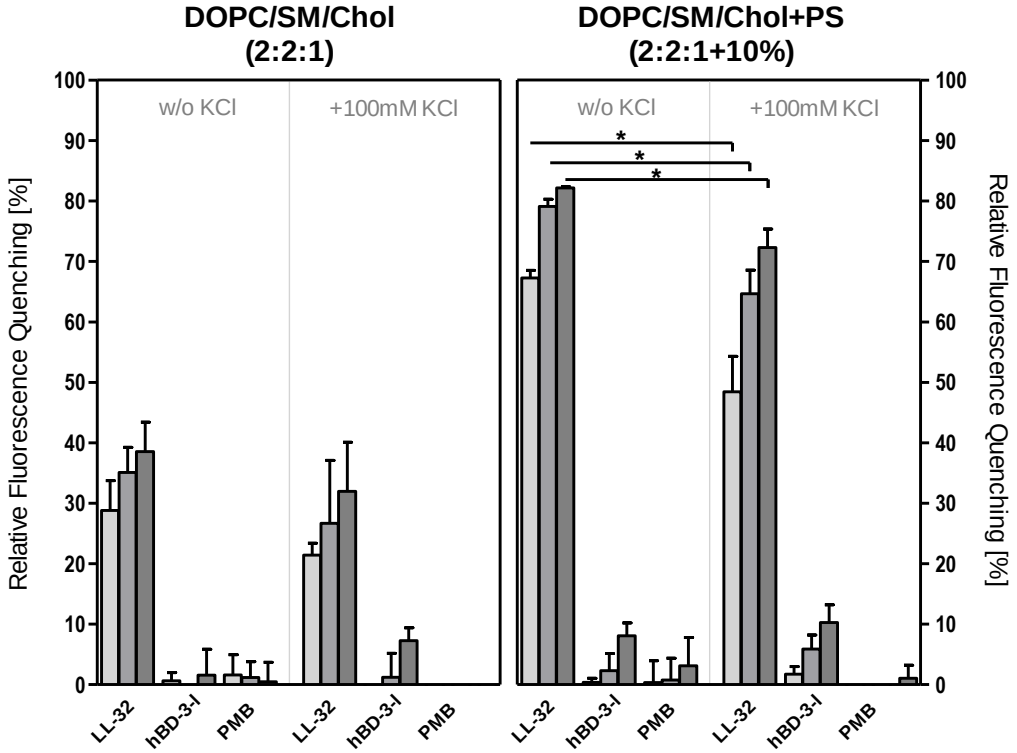

Figure 45 | Potassium iodide quenching assay for testing the influence of membrane active compounds on model immune cells. Raw data were transformed into column diagrams by using equation 2. All data are background corrected. Antimicrobial peptides (LL-32, hBD-3-l) were tested on DOPC/SM/Chol- (left) and DOPC/SM/Chol+PS-liposomes (right), both systems labeled with NBD-PE. Permeabilization was detected under low- (w/o KCl) and high-salt (100 mM KCl) buffer conditions. The decrease in fluorescence intensity was detected over time at 37 °C. Peptide concentrations of 1, 3 and 10 µM were applied. TX-100 was added for maximum fluorescence quenching. Statistical analysis was performed in a two-tailed student's paired t-test (non-significant: ns $p \geq 0.05$; significant: * $p \leq .0.05$). Data are plotted as mean of three independent experiments +SD (n = 3).

[1] Molar volumes were determined by using ChemSketch (ACD/Labs, Advanced Chemistry Development, Inc., Version 14.01)

4.1.3 Pore-Spanning Membranes

In this assay, a special type of membrane is used, that is derived by allowing GUVs to spread onto a silicon wafer. This wafer is equipped with approximately 250,000 cavities capturing 7.5 ±1 fL buffer each (*q.v. section 3.4.3, page 91*). By entrapping a fluorescent dye into these cavities, it is possible to detect pore formation within the size range of calcein and above on a planar system at low membrane curvatures.

For LL-32, it was possible to define a critical concentration of 0.1 μM on lipid bilayers reconstituted from pure DOPC. In this context, the term critical concentration stands for the minimal concentration at which peptide-induced dye-efflux is detected. The release of the entrapped fluorophore equates with membrane permeabilization. On membrane patches composed of pure DOPC, LL-32 shows at a final concentration of 0.1 μM the lowest (light blue line; Figure 46) to no effect (data not shown), whereas concentrations from 0.3 μM and above were leading to a strong and fast induced permeabilization effect (Figure 46). As expected, the ionophore nonactin shows on the same membrane system under low-salt conditions no effect, a similar effect was detected for the α-hemolysin (data not shown). However, the other members of the AMP-family, show similar permeabilizing behavior compared to LL-32. The linear version of the human β-defensin hBD-3 shows on DOPC membrane patches a sigmoidal membrane permeabilization process at a final concentration of 1 μM where the permeabilization rate is relatively constant over the whole process detected (burgundy line; Figure 46). No total lysis of the membrane patches was observed (approximately 10% intact cavities remaining) in this case, whereas at higher concentrations (10 μM) a faster and completed membrane disruption was reached (data not shown). Arenicin-1 lead to complete membrane disintegration at a final concentration of 1 μM on DOPC membranes (light grey line; Figure 46). However, for the small lipopeptide PMB (10 μM) a slow, sigmoidal dye-efflux was recorded on DOPC membranes leading to full lysis of the membrane patch (dark blue line; Figure 46).

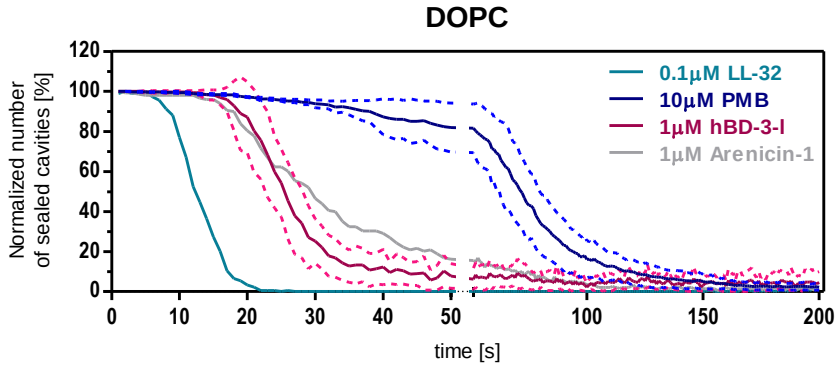

Figure 46 | Pore-spanning membranes reconstituted from pure DOPC. The peptide-induced dye-efflux of Atto488-carboxy after membrane permeabilization is plotted over time. Raw data were normalized to the number of cavities sealed by the membrane patch. Pore-spanning membranes were exposed to antimicrobial peptides (LL-32, hBD-3-l, PMB, and arenicin-1), nonactin (data not shown) and α-hemolysin (data not shown). Permeabilization was only detected under low-salt (w/o KCl) buffer conditions. The time resolved dye-efflux was recorded at 37 °C. One representative experiment for each peptide is plotted; ±SD (dashed lines) if integration over several membrane patches was applicable.

Making the system more complex, GUVs composed of domain-forming lipid-mixtures were prepared and spread onto the chip surface. For the formation of small cholesterol-rich microdomains, model membranes reconstituted from DOPC/SM/Chol in a lipid ratio of 9:9:2 (45:45:10) were used (Figure 47). The AMPs LL-32, hBD-3-l and PMB were exposed to this membrane system and evaluated regarding their permeabilization kinetics. For membrane lysis and simultaneous dye-release, higher concentrations (10 µM) were needed for each substance of interest. LL-32 showed an analog sigmoidal-shaped process with 80 s time delay before membrane permeabilization was induced (light blue line; Figure 47). For hBD-3-l, a time delay of 20 s was observed before start of dye-efflux. The permeabilization kinetics follow an exponential-decay-like trend for the first half of recording merging in a linear trend after 100 s. No total dye-release was detected, 20% of the cavities remain closed (burgundy line; Figure 47). Polymyxin B showed a linear, continuous but slow dye-release. After 200 s, 75% of the cavities remain sealed (dark blue line; Figure 47).

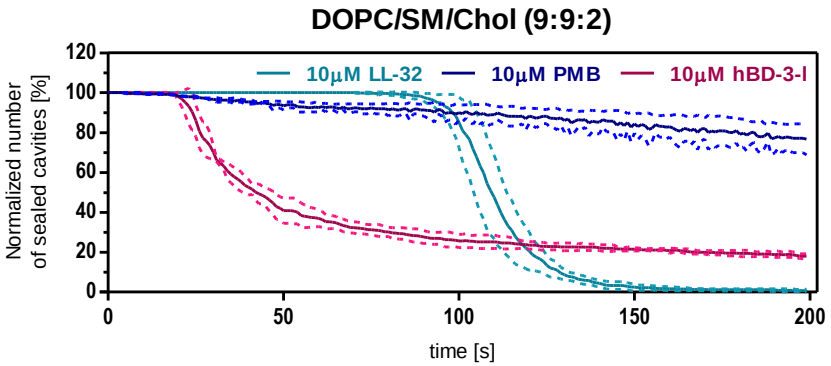

Figure 47 | Pore-spanning membranes reconstituted from DOPC/SM/Chol in a lipid ratio of 9:9:2. The peptide-induced dye-efflux of Atto488-carboxy after membrane permeabilization is plotted over time. Raw data were normalized to the number of cavities sealed by the membrane patch. Pore-spanning membranes were exposed to antimicrobial peptides (LL-32, hBD-3-l, and PMB. Permeabilization was only detected under low-salt (w/o KCl) buffer conditions. The time resolved dye-efflux was recorded at 37 °C. One representative experiment for each peptide is plotted; ±SD (dashed lines) if integration over several membrane patches was applicable.

The influence of negatively charged domain-forming lipid bilayers was tested on the system stated above supplemented with 10mol% PS within the membrane compound (Figure 48). The time delay as described recently, was diminished (20 s for LL-32 and 10 s for hBD-3-l). LL-32 interacts with PS-supplemented DOPC/SM/Chol membrane patches four times faster compared to DOPC/SM/Chol without negatively surface charges. The permeabilizing process stays sigmoidal-shaped with an increased decline (light blue line; Figure 48). The human defensin, however, shows in presence of PS a permeabilizing process with an overall exponential decay (burgundy line; Figure 48). For PMB, the linear trend on DOPC/SM/Chol membrane patches moved to a sigmoidal-shaped permeabilization event with a time delay of 120 s before the first dye-release was detected (dark blue line; Figure 48).

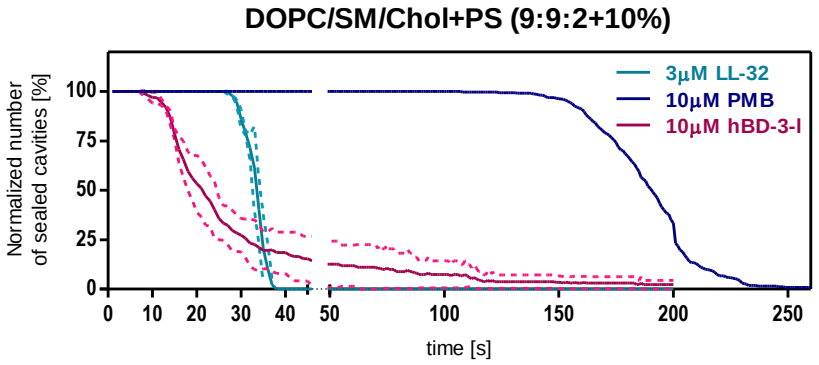

Figure 48 | Pore-spanning membranes reconstituted from DOPC/SM/Chol with 10mol% of negatively charged lipid. The lipid ratio is specified in brackets. The peptide-induced dye-efflux of Atto488-carboxy after membrane permeabilization is plotted over time. Raw data were normalized to the number of cavities sealed by the membrane patch. Pore-spanning membranes were exposed to antimicrobial peptides (LL-32, hBD-3-l, and PMB. Permeabilization was only detected under low-salt (w/o KCl) buffer conditions. The time resolved dye-efflux was recorded at 37 °C. One representative experiment for each peptide is plotted; ±SD (dashed lines) if integration over several membrane patches was applicable.

On the bacterial inner membrane mimicry (Figure 49), reconstituted from POPE/POPG (4:1) exhibiting overall negative surface charge, again no effect neither for nonactin nor α-hemolysin was observed (data not shown); in case of the peptides LL-32, hBD-3-l, and arenicin-1, higher concentrations were needed in all experiments compared to the uncharged DOPC membrane system. For LL-32, the fast sigmoidal-shaped permeabilization dynamic changed to a more linear trend, detected at a final concentration of 1 µM LL-32 (light blue line; Figure 49). Total dye-efflux was reached at a final concentration of 3 µM (data not shown). The whole process was slowed down even the membrane patches were relatively small.

For the induction of membrane permeabilization, arenicin-1, required increased concentrations as well. At a final concentration of 10 µM a slow and constant permeabilization process was detected, finding its origin in the middle of the membrane patch, whereof the dye was released only from 20% of the sealed cavities (light grey line; Figure 49). Interestingly, for hBD-3-l a similar phenomenon was observed: Herein, no membrane permeabilization was induced at 3 µM, but in the surrounding area of the small membrane patch, cavities started to regain their fluorescence (data not shown). This leads to the hypothesis that the

uncharged and higher concentrated POPE moiety of the membrane better sticks to the chip surface, sealing the cavities and the fluorescent dye tightly whereas the charged POPG-part is not able to stick to the chip surface in the same manner. This specific membrane region, maintains a sealing of the cavity in a way where no removal of the fluorescence dye after washing can occur on the one hand; but on the other hand, the membrane is not able to sit as close on the chip surface as needed for visible sealed cavities. Only due to the accumulation of hBD-3-l on the negatively charged membrane area, the electrostatic effect is circumvented and the cavities are sealed properly exhibiting their fluorescence. Only from concentrations of 10 µM, hBD-3-l was able to induce rapid and total dye release within the first 50 s following a steep linear decrease which is synonymous to membrane permeabilization (burgundy line; Figure 49).

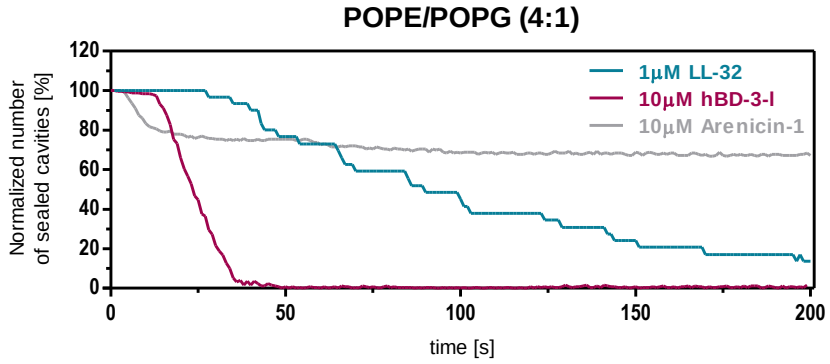

Figure 49 | Pore-spanning membranes reconstituted from POPE/POPG in a lipid ratio of 4:1 as mimicry for the inner leaflet of the bacterial cell envelope. The peptide-induced dye-efflux of Atto488-carboxy after membrane permeabilization is plotted over time. Raw data were normalized to the number of cavities sealed by the membrane patch. Pore-spanning membranes were exposed to antimicrobial peptides (LL-32, hBD-3-l, and arenicin-1), nonactin (data not shown) and α-hemolysin (data not shown). Permeabilization was only detected under low-salt (w/o KCl) buffer conditions. The time resolved dye-efflux was recorded at 37 °C. One representative experiment for each peptide is plotted.

4.1.4 Tethered Membranes

TethaPod-measurements were carried out in low-salt and high-salt buffer (100 mM KCl) at pH 7.4 and 37 °C. Low-salt data were adjusted according to the measured buffer conductivity as stated in *section 3.1.5*

(page 71). Figure 50 shows the obtained results for POPE/POPG (4:1) and DOPC membranes.

The antimicrobial peptides LL-32, hBD-3-l and arenicin-1 showed strong permeabilization events on both reconstituted membranes types with only low influences of the membrane systems chosen: Under low-salt conditions, LL-32 already induces strong permeabilization on DOPC membranes at low peptide concentrations (1 μM), whereas membrane disintegration with a compatible degree is reached at 3 μM under high-salt conditions (top row; Figure 50). The synthetic variant of the human β-defensin showed no permeabilization effect under high-salt conditions. However, under low-salt conditions hBD-3-l is highly active (second row; Figure 50). The same results were found for arenicin-1: High membrane activity under low-salt conditions, but almost no induction of permeabilization in presence of 100 mM KCl. Absence of high concentrations of alkali metal ions lead to a more pronounced membrane activity (penultimate row; Figure 50). Data shown for DOPC-membranes are highly significant compared to POPE/POPG-membranes, due to a better reconstitution of uncharged lipid bilayers on the chip surface.

The small ammonium ionophore nonactin is known to form complexes in presence of potassium. Under low-salt conditions, no effect was detected, neither on charged nor uncharged tethered lipid bilayers. The effects observed for nonactin within the progressing experimental course, could be traced back to the solvent MeOH (data not shown). Other solvents, e.g. ultra-purified water (data not shown) or 0.01% TFA exhibit no influence on tBLMs (top row; Figure 50). Large proteins as the tested α-hemolysin by *Staphylococcus aureus* that are known to have a membrane active function, show as strong effects on tethered membranes as the antimicrobial peptides. The permeabilization effect on DOPC-containing membranes is inferior at lower concentrations (1 μM and 3 μM) compared to the effect on charged membranes. Under high-salt conditions, it is the other way around. The stronger binding affinity towards uncharged phospholipid bilayer in the model, leads to an irreversible binding of the protein so that the integrity of the membrane barrier is lost and leakage ensues. The same effect is observed in a strongly weakened manner for negatively charged bilayers under high-salt conditions (last row; Figure 50).

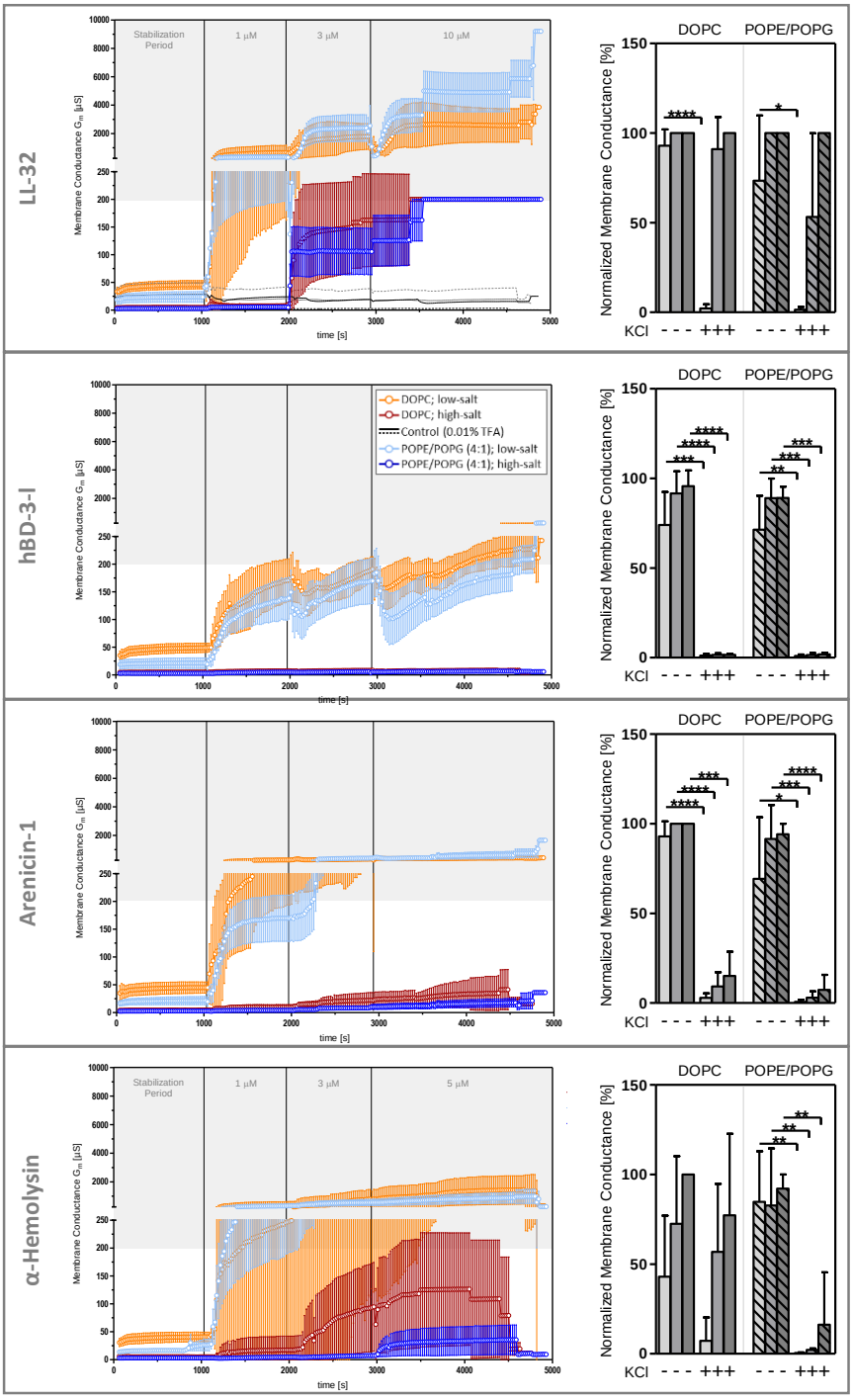

Figure 50 | Permeabilization effect of membrane active compounds on charged and uncharged tethered membranes. Raw data (left) were transformed into column diagrams (right) by using a variant of equation 1. Antimicrobial peptides (LL-32, hBD-3-l, and arenicin-1), nonactin and α-hemolysin were tested on planar tBLMs reconstituted from DOPC and POPE/POPG (4:1). Permeabilization was detected under low- (w/o KCl, −) and high-salt (100 mM KCl, +) buffer conditions. The increase in membrane conductance was detected over time at 37 °C. Peptide concentrations of 1, 3 and 10 µM (α-hemolysin: 1, 3 and 5 µM) were applied. Data was normalized to the maximum conductance (200 µS); values above this limit (grey shaded area) were set to 100%. Statistical analysis was performed in a two-tailed student's paired t-test (non-significant: ns ≥ 0.05; significant: * p ≤. 0.05; very significant: ** p ≤ 0.01; highly significant: *** p ≤ 0.001; extremely significant: **** p ≤ 0.0001). Data are plotted as mean of five independent experiments +SD (n = 5).

The data collected for tethered cholesterol-rich membranes composed of DOPC/SM/Chol were run out on an updated *tethaPod*-device which had the result that these measurements had no defined infinity value as the measurements performed on the old device (infinity reached at 200 µS conductivity). Therefore, for evaluation the device-specific limit pursuant to the distributor's manual was used as limit for membrane conductance. Values greater than or equal to this limit were set to maximum respectively 100% for normalized data (Figure 50, grey shaded areas).

Figure 51 shows the concentration dependent effect of the AMPs LL-32, hBD-3-l, and PMB: Only for the α-helical peptide LL-32 a strong increase in membrane conductance was reached, whereas hBD-3-l and PMB showed only weak interference with cholesterol-containing membranes. In case of hBD-3-l, a slight increase in membrane activity was observed if the mixture was supplemented with 10mol% PS. Comparing tethered membranes composed of DOPC/SM/Chol and DOPC/SM/Chol with 10mol% of the negatively charged lipid species PS, showed no levels of significance for the peptides. Statistical analysis of the peptides among one another, shows significances at 3 µM and 10 µM. PMB (**, $p = 0.0011$ and **, $p = 0.0058$) and hBD-3-l (**, $p = 0.0014$ and **, $p = 0.0066$) exhibit significant lower permeabilization levels on tBLMs compared to LL-32, whereas hBD-3-l shows a higher impact (3 µM: *, $p = 0.0390$ and 10 µM: *, $p = 0.0203$) than the lipopeptide. An analog effect could be observed for the ternary lipid system supplemented with PS: Again, significances at 3 µM and 10 µM could be determined for PMB (**, $p = 0.0028$ and **, $p = 0.0021$) and hBD-3-l (**, $p = 0.0056$ and **, $p = 0.0016$). All compounds showed a marginal better reconstitution on the 2:2:1-mixture. Therefrom, replicates and statistics were only compiled for DOPC/SM/Chol tethered membranes with the 2:2:1 lipid ratio.

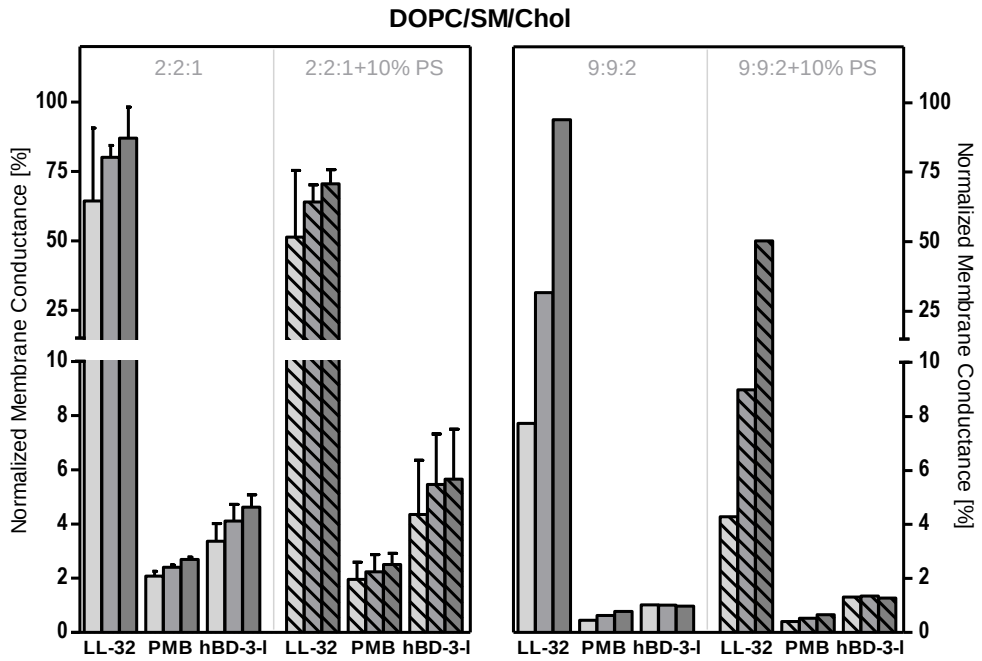

Figure 51 | Permeabilization effect of the antimicrobials LL-32, PMB and hBD-3-l on cholesterol-rich tethered membranes. Raw data were transformed into column diagrams by using a variant of equation 1. Antimicrobial peptides were tested on planar tethered membranes reconstituted from a mixture of DOPC/SM/Chol in lipid ratios of 2:2:1 (left) and 9:9:2 (right). Permeabilization was detected under 5 mM HEPES, 0.5 mM $CaCl_2$ x $2H_2O$; pH 7.4 (low-salt conditions). The increase in membrane conductance was detected over time at 37 °C. Peptide concentrations of 1, 3 and 10 µM were applied. Data was normalized to the maximum conductance (200 µS) in due consideration of the buffer conductance. Statistical analysis was performed for the 2:2:1-mixture in a two-tailed student's paired t-test (non-significant: ns ≥ 0.05; significant: * p ≤. 0.05; very significant: ** p ≤ 0.01). Data are plotted as mean +SD of three independent experiments (n = 3).

4.1.5 Free-Standing Lipid Bilayers

With the help of planar lipid bilayer, the closest system to physiological conditions was developed. Compared to all other methods presented so far in this thesis, the Montal-Mueller set-up is used for the reconstitution of free-standing lipid bilayers. Current measurements of these bilayers allow the detection of single pore forming events. Figure 52 shows the results of the current measurements for the whole spectra of substances presented within the framework of this thesis. All of the presented current measurements were run out at an applied membrane tension of +50 mV.

α-Hemolysin showed a characteristic step-like trend on charged POPE/POPG (4:1) membranes; well-defined under high-salt conditions and blurred in low-salt buffer due to a minimized step size. This trend is diminished on lipid bilayers reconstituted from the zwitterionic unsaturated phospholipid DOPC in presence of high concentrations of monovalent alkali metal ions (last row; Figure 52); the step-like increase in conductivity can't be observed in the same resolution as on charged lipid bilayers. In absence of potassium ions, no effect was observed in the current measurement for DOPC membranes. In contrast, the ionophore nonactin only functions under high-salt conditions: Both POPE/POPG- and DOPC-membranes show a sudden increase in current-flux; as expected no effect was detected under low-salt conditions (penultimate row; Figure 52). Compared to the larger pore formers, the representatives of the AMP-family behave differently: On uncharged lipid bilayers, LL-32 leads under high-salt conditions to large undefined lesions until complete membrane disintegration is reached (top row, +100 Mm KCl, Figure 52), whereas arenicin-1 forms distinct pores without achieving complete membrane rupture under the experimental conditions applied (third row, +100 mM KCl; Figure 52). Compared to LL-32 and arenicin-1, the defensin hBD-3-l showed no activity under high-salt conditions on membranes reconstituted from pure DOPC (second row, +100 mM KCl; Figure 52). Under low-salt conditions, small and well-defined pores are observed for LL-32 and arenicin-1 (top and third row, w/o KCl; Figure 52); hBD-3-l shows enhanced membrane active function when no potassium ions are present, resulting in the formation of defined pores with the hBD-3-l specific side-peak (second row, w/o KCl; Figure 52, blue arrow). On negatively charged lipid bilayers, arenicin-1 only exhibit very small pores with short lifetimes. In this distinct case, the membrane seems to be able to circumvent the pore formation induced by arenicin-1 if added from single-side (third row, Figure 52). It is known, that arenicin-1 induces more often the formation of defined pores when the peptide is applied on both sides of the experimental setup (data not shown). LL-32 shows the same trend on the charged lipid system as described for DOPC-membranes, leading either to complete membrane disintegration (top row, +100 mM KCl; Figure 52) or formation of small defined pores (top row, w/o KCl; Figure 52). However, the linear defensin, expressed activity under both conditions applied: In this

case, high-salt buffer conditions promoted the formation of small pores, closing and opening in short time lags (second row, +100 mM KCl; Figure 52). These intervals are prolonged under low-salt conditions (second row, w/o KCl; Figure 52).

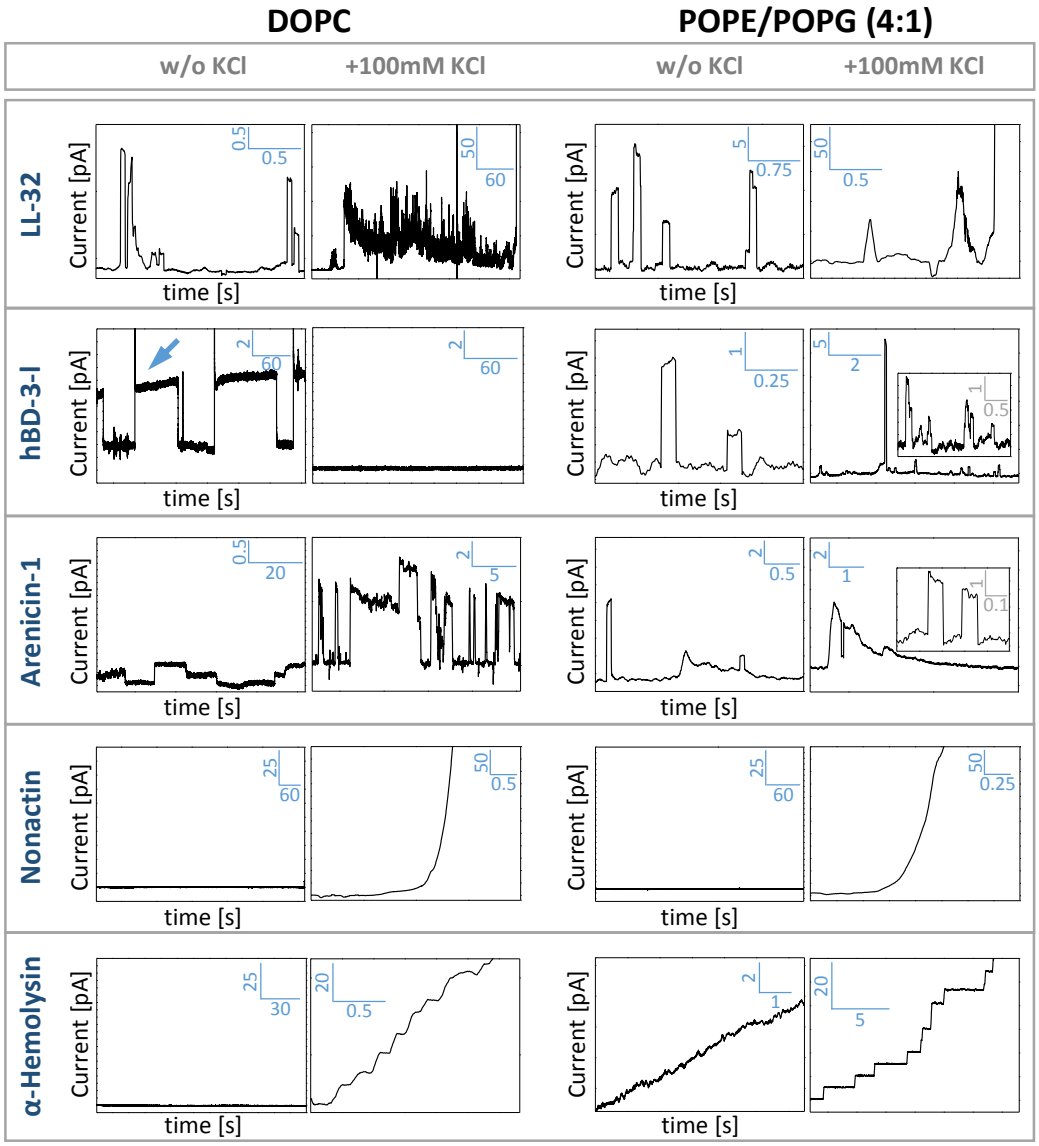

Figure 52 | Current measurements of planar lipid bilayers after incubation with membrane active compounds. The pore forming and membrane permeabilizing effect is detected and the conductivity is plotted over time with an applied membrane tension of +50 mV at 37 °C. Peptides were applied single-sided. Raw data were smoothed with a moving average of 20. Antimicrobial peptides (LL-32, hBD-3-l, and arenicin-1), nonactin and α-hemolysin were tested on planar lipid bilayers reconstituted from DOPC (upper panel) and POPE/POPG (4:1) (lower panel) pursuant to MONTAL & MUELLER. All experiments were run out under low- (w/o KCl) and high-salt (100 mM KCl) buffer conditions. The increase in conductivity was detected over time at 37 °C. One representative data curve is plotted for each condition and compound.

4.1.6 Peptide Intercalation Assay

Membrane activity can be recognized by either pore formation or membrane disintegration, resulting in complete failure of membrane tension and function or by membrane intercalation. Intercalation processes are determined by *FÖRSTER Resonance Energy Transfer* (FRET) in a liposome-based approach: Fluorescently labeled SUVs are prepared, with an incorporated FRET-pair in the membrane compound. As FRET-pair NBD-PE ($\lambda_{Ex(max)}$ = ~463 nm; $\lambda_{Em(max)}$ = 536 nm) and Rh-DHPE ($\lambda_{Ex(max)}$ = ~560 nm; $\lambda_{Em(max)}$ = 580 nm) are used by default (*q.v. section 3.5.2, page 105*). Peptide-induced intercalation is recognized fluorometrically by increasing FRET-signal resembling an increase in liposome diameter combined with a redistribution of the reconstituted FRET-pair. This phenomenon results in an extension of the local distribution of donor and acceptor dye and therefore in an increase of I_D/I_A-ratio. Peptide-specific membrane intercalation was investigated with respect to the whole spectrum of the standard buffer systems used (Table 13; *q.v. section 3.1.5, page 72*). For convenient data presentation, significance indices of one testing system were given representatively. For full statistical analysis and levels of significance of the data plotted in figure 53, please refer to table 19-21 in the supplemental data (*q.v. section 7*; *page 235 et seqq.*).

For the α-helical peptide LL-32 (Figure 53a) the degree of intercalation follows a concentration dependent trend in all cases without any significant influence of the membrane-label chosen as observed on liposomes reconstituted from DOPC/SM/Chol in a lipid ratio of 9:9:2. For the membrane mixture featuring higher levels of cholesterol (2:2:1), only under physiological salt supplementation with 100 mM NaCl, a significant ($p = 0.0163$, *****, 3 μM) to very significant ($p = 0.0039$, ******, 1 μM) enhancement of peptide intercalation was detected when the liquid-ordered domain is labeled. Beyond that, the intercalation ability in general is enhanced under high-salt conditions.

Contrasting 20mol% (2:2:1) with 10mol% cholesterol (9:9:2), gave high levels of significance when the FRET-pair is incorporated in the cholesterol-poor membrane regions: In absence of mono- and divalent cations, the intercalation ability for even small amounts of LL-32 resulted in

an extremely significant enhancement at cholesterol levels of 20mol% ($p = 0.0007$, ***, 1 μM); whereas in presence of Ca^{2+} and K^{+} ions a weakening of LL-32-intercalation with increasing levels of significance was detected ($p = 0.0355$, *, 1 μM; $p = 0.0011$, **, 3 μM; $p = 0.0006$, ***, 10 μM). Nevertheless, the highest change in acceptor-donor ratio, and there with the highest intercalation of LL-32, was detected on SUVs reconstituted from DOPC/SM/Chol in a lipid ratio of 9:9:2 under 100 mM NaCl as mimicry for human immune cells and physiological and biological buffer conditions. Supplementation of the particular buffer systems with 0.5 mM $CaCl_2$ x $2H_2O$ showed only in one specific case (5 mM HEPES w/ vs. w/o $CaCl_2$ x $2H_2O$) significant influence of the intercalation behavior of LL-32.

The small lipopeptide PMB showed only weak intercalation behavior (Figure 53b). The highest degree of intercalation was detected on SUVs reconstituted from DOPC/SM/Chol in a lipid ratio of 2:2:1 under 5 mM HEPES. For PMB, a strong influence of the membrane-label was observed, showing that the poor intercalation behavior of this peptide is better resolvable if the cholesterol-enriched domains (L_O-domains) are fluorescently highlighted ($p = 0.0008$, ***, 3 μM). Supplementation of the particular buffer systems with 0.5 mM $CaCl_2$ x $2H_2O$ showed to weaken the already poor intercalation behavior of this substance.

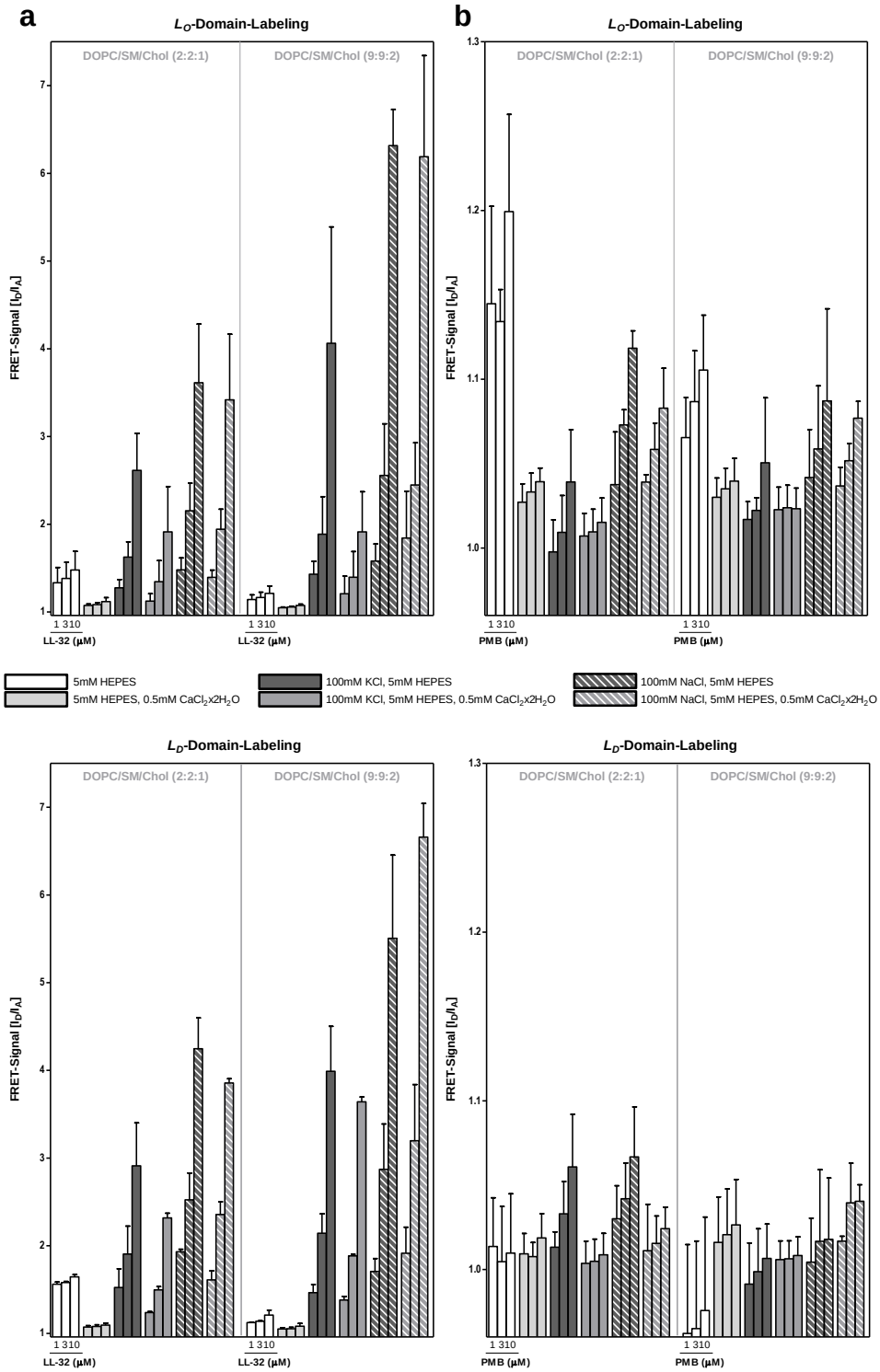

Figure 53 | Influence of the buffer system and domain-labeling on peptide-induced intercalation in cholesterol-rich SUVs. Intercalation ability for LL-32 (a) and PMB (b) was tested on DOPC/SM/Chol-SUVs in lipid ratios of 2:2:1 and 9:9:2 by detecting the change in FRET-signal. Intercalation behavior of the two peptides were investigated with respect to different domain-labels. The standard FRET-pair NBD-PE and Rh-DHPE was used for labeling of L_D-domains. Cholesterol-rich microdomains (L_O-Phase) were labeled by using NBD-12-cholesterol and Rh-DHPE as FRET-pair. Peptides were applied in final concentrations of 1, 3 and 10 µM. Raw data were transferred into column diagrams by determining the average of constant I_D/I_A-ratios after each injection. Data are plotted as mean +SD of three to five independent experiments (n = 3-5).

4.1.7 Fluorescent Dye Distribution Analysis (FDDA) of Labeled AMPs on Immobilized GUVs

Giant unilamellar vesicles (GUVs) are prepared as described in *section 3.3.3 (page 81)*. For fluorescent dye distribution analysis (FDDA) of labeled, membrane active compounds a self-written user procedure was used. With this tool, the intensities detected, can be plotted versus the azimuthal angle giving the fluorescence distribution of the labeled peptide and the membrane-bound fluorescent dye over the vesicle's whole membrane margin.

GUVs were reconstituted in all cases from DOPC/SM/Chol with a lipid ratio of 2:2:1 and immobilized via avidin-biotin chemistry (*q.v. section 3.5.1.2, page 102*)[148]. Giant vesicles of this composition undergo phase separation under the experimental conditions applied. The cholesterol-rich areas (L_O-domains) appear black before peptide injection, whereas the disordered cholesterol-poor areas (L_D-domains) are fluorescently highlighted by Atto633-DOPE. Immobilized GUVs exposed to the lipopeptide polymyxin B show no correlation between peptide- and membrane-bound fluorophore (Figure 54). PMB was applied in final concentrations of 22.5 µM to obtain optimal fluorescence intensities for further FDDA.

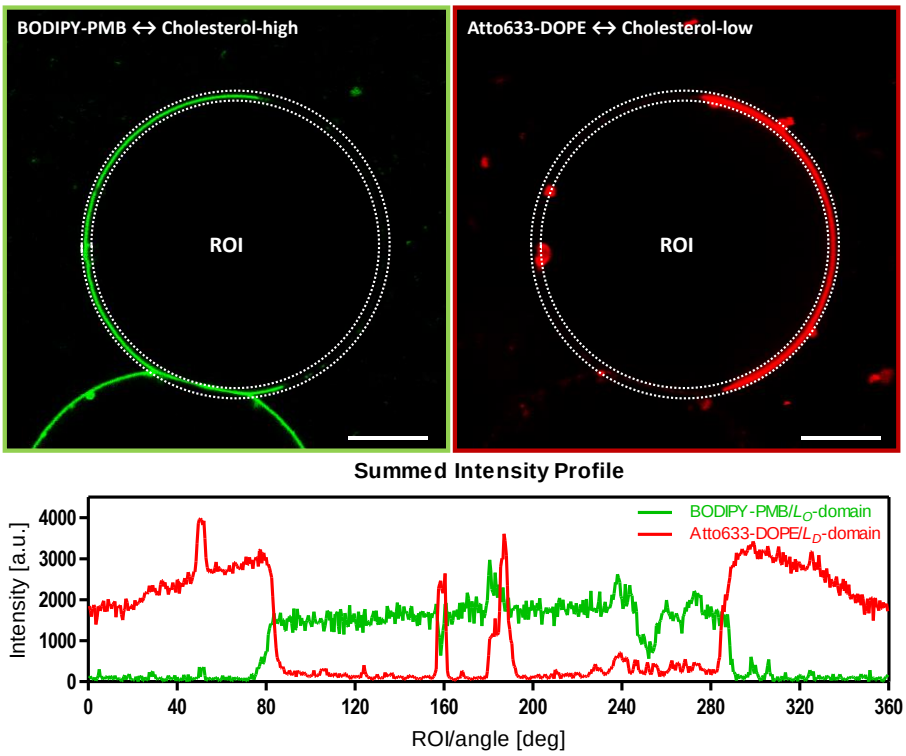

Figure 54 | Fluorescent dye distribution analysis (FDDA) of BODIPY-labeled PMB on immobilized giant vesicles reconstituted from the raft-mixture DOPC/SM/Chol in a lipid ratio of 2:2:1. L_D-domains are labeled by the lipid-bound fluorescent dye Atto633-DOPE (red). L_O-domains appear black prior to incubation with 22.5 µM BODIPY-PMB (green). FDDA show no correlation between the two dyes, reflecting a preference of PMB for cholesterol-enriched L_O-areas. Scale bars equal 10 µm. Images were obtained by confocal laser scanning microscopy with 60x object lens. Experiments were run out in 5 mM HEPES (pH 7.4) on a Leica SP5 motorized inverted confocal microscope stage at 23 °C.

The AMPs LL-32 and hBD-3-l were applied as rhodamine-labeled variants, therefore BODIPY-labeled PC was used as membrane-bound fluorophore, highlighting the cholesterol-poor areas of the vesicle. GUVs exposed to these antimicrobials show distinct correlation of the fluorophores used (Figure 55+56). LL-32 was applied in final concentrations of 4.5 µM and interacts exclusively with the liquid-disordered domains.

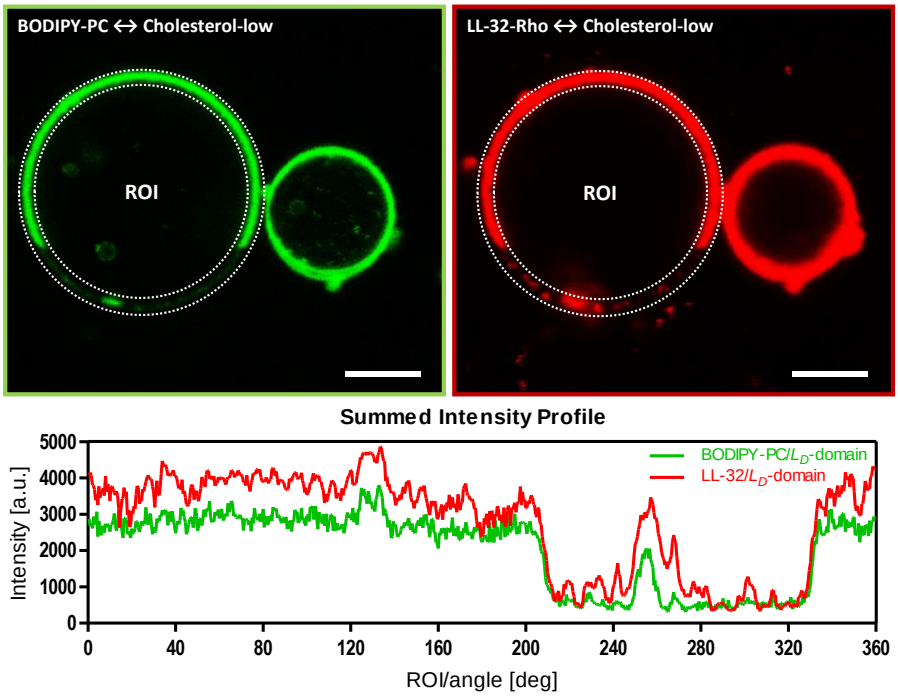

Figure 55 | Fluorescent dye distribution analysis (FDDA) of rhodamine-labeled LL-32 on immobilized giant vesicles reconstituted from the raft-mixture DOPC/SM/Chol in a lipid ratio of 2:2:1. L_D-domains are labeled by the lipid-bound fluorescent dye BODIPY-PC (green). L_O-domains appear black prior to incubation with 4.5 µM Rho-LL-32 (red). FDDA show distinct correlation between the two dyes, reflecting a preference of LL-32 for cholesterol-poor areas. Scale bars equal 10 µm. Images were obtained by confocal laser scanning microscopy with 60x object lens. Experiments were run out in 5 mM HEPES (pH 7.4) on a Leica SP5 motorized inverted confocal microscope stage at 23 °C.

For obtaining optimal staining of the GUV in presence of hBD-3-l, the applied concentration needed to be raised two-fold yielding 9 µM labeled peptide in the solution. Figure 56 shows unambiguously that the linear peptide preferentially interacts with the same membrane regions as detected for the α-helical peptide LL-32.

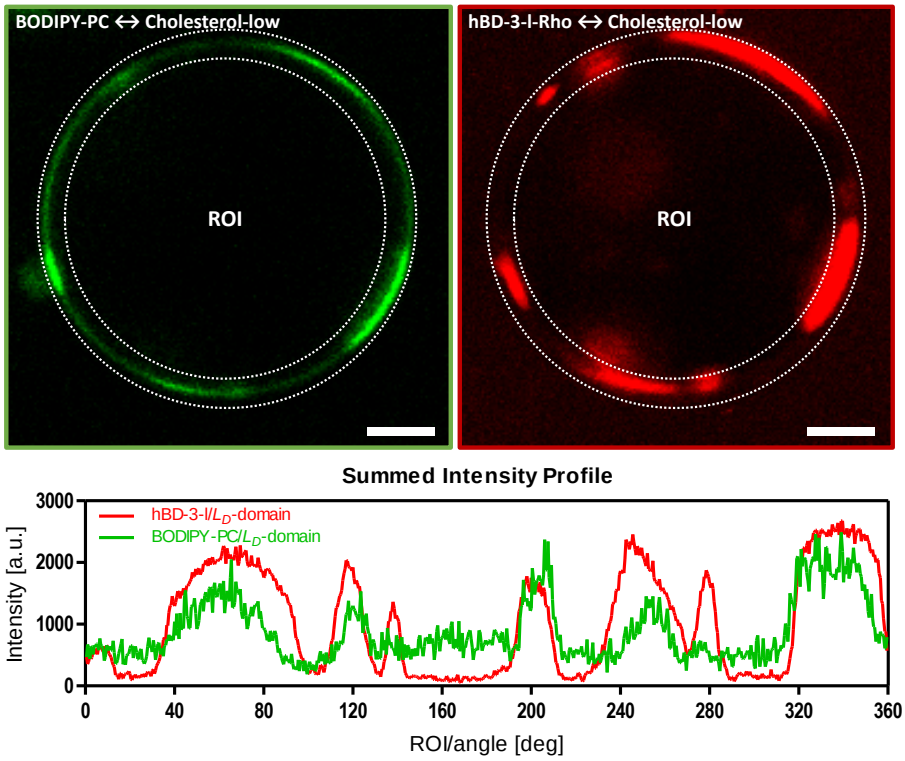

Figure 56 | Fluorescent dye distribution analysis (FDDA) of rhodamine-labeled hBD-3-l on immobilized giant vesicles reconstituted from the raft-mixture DOPC/SM/Chol in a lipid ratio of 2:2:1. L_D-domains are labeled by the lipid-bound fluorescent dye BODIPY-PC (green). L_O-domains appear black prior to incubation with 9 µM Rho-hBD-3-l (red). FDDA show distinct correlation between the two dyes, reflecting a preference of hBD-3-l for cholesterol-poor areas. Scale bars equal 5 µm. Images were obtained by confocal laser scanning microscopy with 60x object lens. Experiments were run out in 5 mM HEPES (pH 7.4) on a Leica SP5 motorized inverted confocal microscope stage at 23 °C.

All presented data in this section were obtained by using confocal laser scanning microscopy with 60x object lens and photo multiplier transmission (PMT) detectors set to maximum intensities (30%). Fluorescence images were taken in sequential mode between frames.

4.1.8 Polymyxin B-induced Fusion of Semi-Immobilized Phase Separated GUVs

M. Hammer already described the phenomenon of PMB-induced fusion of giant vesicles composed of PE/PG in a lipid ratio of 1:1. These vesicles showed no phase separation and were incubated with non-fluorescent PMB. The raft-mixture DOPC/SM/Chol enables the detection of the influence of L_O-domains in the fusion process caused by PMB. Furthermore, it is possible to track the distribution of the green-fluorescent lipopeptide. Figure 57 shows a time-resolved PMB-induced fusion process of semi-immobilized DOPC/SM/Chol-GUVs. Atto633-DOPE is used as membrane-bound fluorophore and appears red, whereas the green areas reflect the peptide distribution and simultaneously the cholesterol-enriched domains. In the image sequence, different events can be observed that are indicated by the arrows (Figure 57). The sequence represents one exemplary experiment. The fluorescence images show two giant vesicles attached to each other forming a tilted eight-shaped structure. The juncture of the vesicles is located within the liquid-ordered phase (L_O-domain). A closer look on the frames of t_1 to t_4 elucidates, that the two GUVs approximate each other without contact, in the first instance (t_1). From the frame t_3 on, a membrane interface appears, at which it looks like as if the two vesicles share one membrane leaflet. The liquid-disordered L_D-phase is completely excluded from this membrane juncture. In a second event, a cluster of vesicles, that is connected to this eight-shaped structure crumbles together in smaller sub-clusters (t_1–t_4). These small sub-clusters nurture the larger vesicles with lipids by increasing the vesicles diameter and equalizing the size of the two parts of the eight-shaped structure (t_4–t_7). The lower part of the eight-looking like structure shows overall peptide distribution (t_1–t_5), but after cluster-incorporation, phase separation is observed, leading to an increase in area of the L_D-domain (t_6+t_7). This part of the GUV starts fluctuating (t_8) until a collapse into smaller sub-clusters is induced (t_9). In these sub-clusters, fusion processes can be observed: Over time, this group of smaller vesicles start melting together. Co-existence of peptide and lipids in the liquid-disordered phase yield in a mixed color (yellow) of the two fluorophores. It seems that the peptide tries to escape from these unfavored membrane regions (t_9–t_{11}). The peptide is in an

overall outfaced oriented state (t_{10}) giving new hubs for further fusion processes. After 60 minutes (t_{16}) the sub-clusters are merged to maximum degree. At this stage, the lipopeptide is captured in this mix-up of lipids, exhibiting no clear arrangement, that is shown by the flamboyant yellow coloring. The remaining GUV is left with an enlarged liquid-disordered phase (t_{16}).

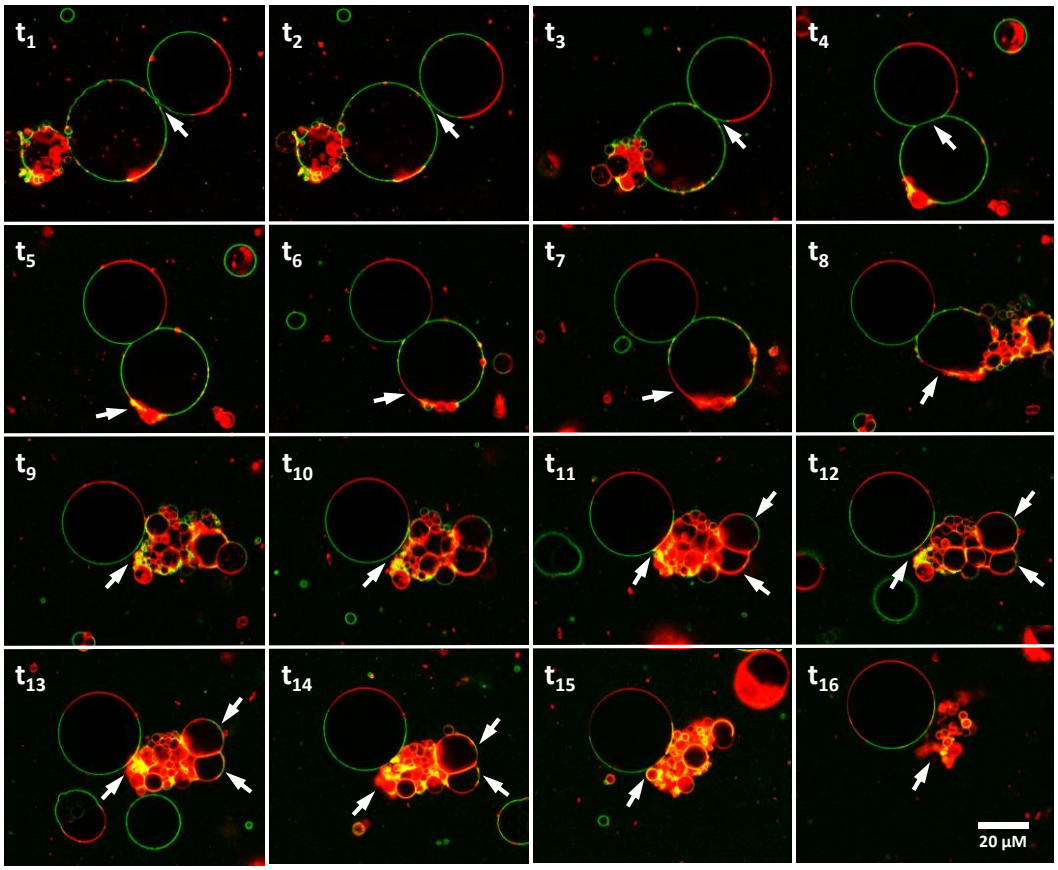

Figure 57 | Time-resolved fusion of semi-immobilized giant vesicles reconstituted from the raft-mixture DOPC/SM/Chol in a lipid ratio of 2:2:1 induced by PMB. L_D-domains are labeled by the membrane-bound fluorescent dye Atto633-DOPE. L_O-domains appear black prior to incubation with 22.5 µM BODIPY-PMB. Scale bar denotes 20 µm and is equal for each image of the series. Images were obtained by confocal laser scanning microscopy with 60x object lens. Experiments were run out in 5 mM HEPES (pH 7.4) on a Leica SP5 motorized inverted confocal microscope stage at 23 °C.

4.1.9 Fluorescence Recovery after Photobleaching

With the help of fluorescence recovery after photobleaching (FRAP), dynamic insights of the underlying membrane peptide interaction should

be collected. Therefore, small vesicles (SUVs) incorporated with 0.05mol% fluorescently lipid (Atto633-DOPE diluted in a volumetric ratio of 1:1000) were prepared and spread by overnight incubation under gentle shaking for obtaining a homogenous lipid bilayer. Experiments were performed in the lab of C. HÜBNER. Before each measurement, control wells were checked for homogenous distribution of the membrane-bound fluorophore before peptide addition. Membranes were bleached by 10 min full laser intensity and the fluorescence recovery was detected in linescan mode.

Membranes reconstituted from pure DOPC showed local clusters of PMB (Figure 58) and tend to be more prone for fluorescence bleaching after exposition to the lipopeptide. In these areas, the lipid-dye conjugate is displaced and lower fluorescence intensity values are detected, whereas the accumulation of the fluorescent peptide results in brighter fluorescence at exact these spots (depicted by the arrows; Figure 58).

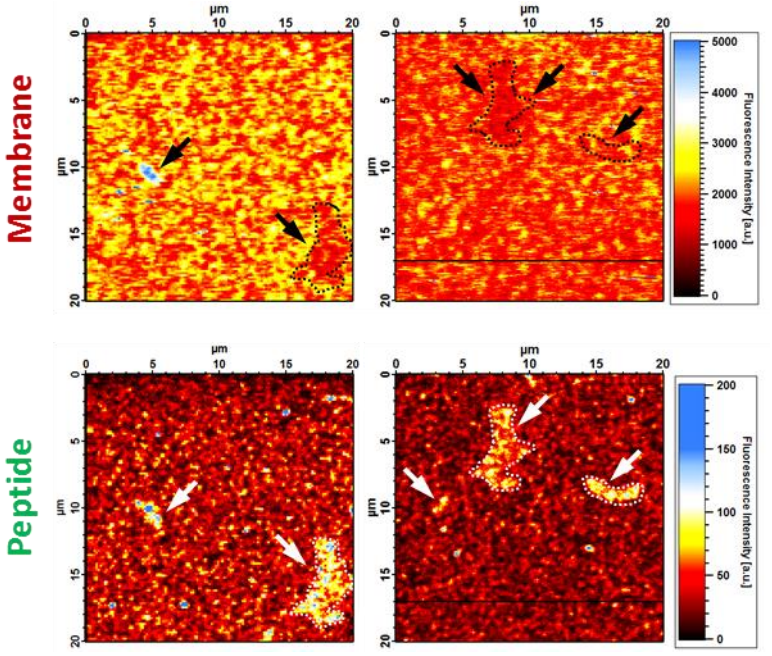

Figure 58 | Confocal images of a lipid bilayer reconstituted from pure DOPC after incubation with BODIPY-PMB at two different positions. Fluorophores were excited simultaneously: The membrane was fluorescently highlighted by incorporation of the lipid-dye conjugate Atto633-DOPE. Peptide distribution was studied by the detection of the peptide-dye conjugate BODIPY-PMB. The peptide was applied in a final concentration of 10 nM. Experiments were run out in duplicates in 5 mM HEPES (pH 7.4).

In contrast to the pure lipid bilayer, cholesterol-rich membranes showed the same local clusters of PMB (Figure 59) but with a different pattern: The PMB-clusters are smaller in size and distributed randomly over the whole membrane. Here again, local spots wherein the two fluorescent dyes anti-correlate are visible. This also illustrates, that peptide accumulation results in brighter fluorescence (depicted by the arrows; Figure 59) and a partial reorganization of the lipid matrix is deflected by the appearance of a circular type pattern exhibiting lower fluorescence in the peptide channel. This pattern emerges in close proximity to the local peptide clusters exhibiting high fluorescence. This effect is more pronounced when the buffer is supplemented with 0.5 mM $CaCl_2$ x $2H_2O$ (Figure 111; *q.v. Supplemental Data, section 7, page 235*).

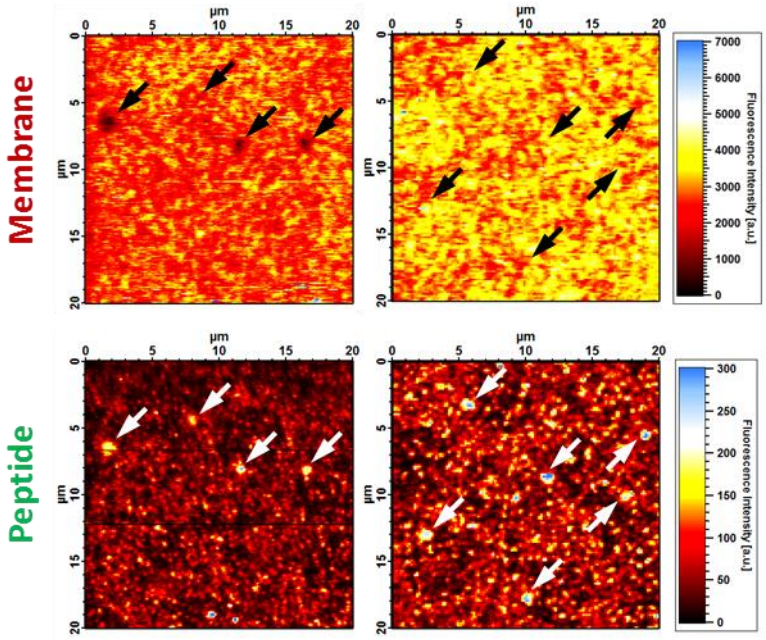

Figure 59 | Confocal images of a cholesterol-rich lipid bilayer reconstituted from DOPC/SM/Chol (2:2:1) after incubation with BODIPY-PMB at two different positions. Fluorophores were excited simultaneously: The membrane was fluorescently highlighted by incorporation of the lipid-dye conjugate Atto633-DOPE. Peptide distribution was studied by the detection of the peptide-dye conjugate BODIPY-PMB. The peptide was applied in a final concentration of 10 nM. Experiments were run out in duplicates in 5 mM HEPES (pH 7.4).

For PMB, mainly two distinctive events on the different membrane systems were observed: First, on DOPC lipid bilayers, a strong fluorescence signal was detected between 12 µm and 17 µm (Figure 60; indicated by the white arrows), leading to the assumption that, remaining SUVs out of the supernatant solution attach to this specific membrane region due to local accumulation of PMB and its membrane fusion induction potential. This could be the reason why in this distinct region for the lipid-dye conjugate an even stronger fluorescence signal was detected compared to the surrounding membrane area.

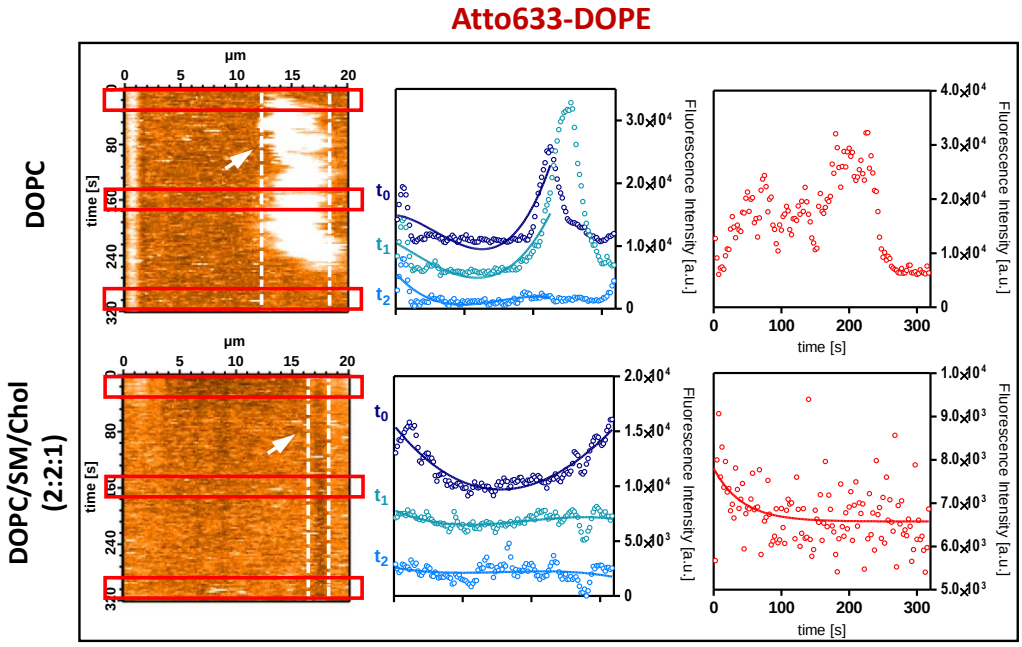

Figure 60 | Evaluated linescans of spread SUVs reconstituted from pure DOPC and DOPC/SM/Chol in a lipid ratio of 2:2:1. Membranes were incubated with 10 nM of BODIPY-PMB and the lipid-dye conjugate Atto633-DOPE was bleached under maximum laser intensity for 10 min. Fluorescence recovery was recorded and evaluated. Horizontal line profiles were taken at three different time points (t_0 = 0-32 s; t_1 = 142.5-175 s; t_2 = 285-317.5 s). Peculiarities are indicated by the arrow and vertical line profiles were plotted along the area highlighted by the dashed box. Experiments were run out in duplicates. One representative experiment is plotted for each peptide.

The second event observed, is more pronounced on the ternary lipid mixture, where the area between 16 µm and 18 µm exhibit low lipid fluorescence, giving rise to the suspicion that more cholesterol and therewith PMB was present in this specific region (Figure 61; indicated by

the white arrows). Further, the fluorescence intensities were extracted from horizontal line profiles at three different positions (t_0 = 0 to 32 s; t_1 = 142.5 to 175 s; t_2 = 285 to 317.5 s) and in vertical line profiles at one definite position.

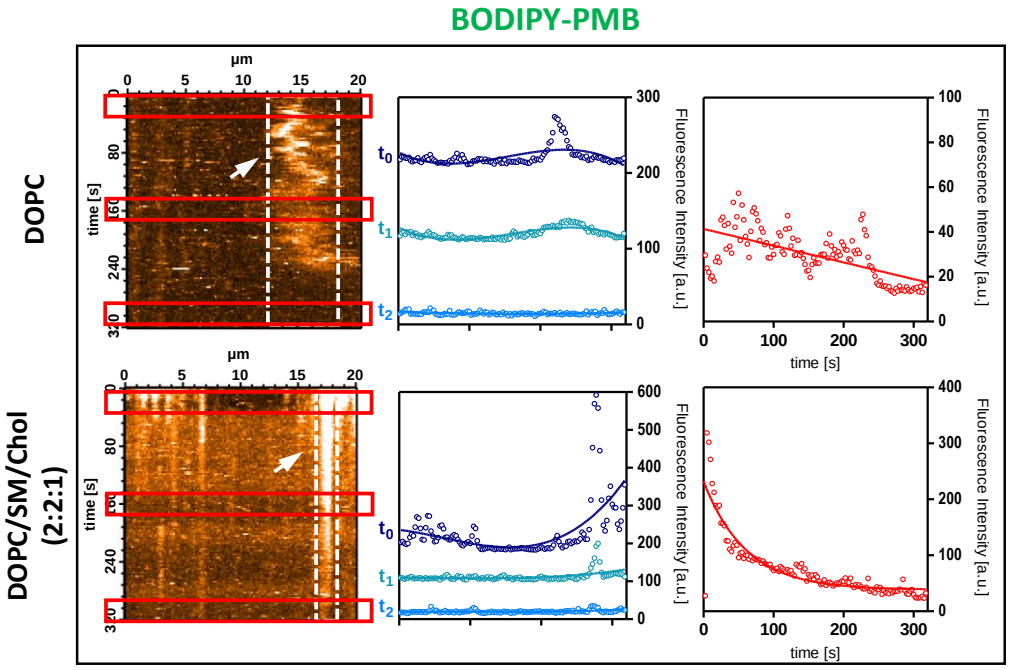

Figure 61 | Evaluated linescans of spread SUVs reconstituted from pure DOPC and DOPC/SM/Chol in a lipid ratio of 2:2:1. Membranes were incubated with 10 nM of BODIPY-PMB and the lipid-dye conjugate Atto633-DOPE was bleached under maximum laser intensity for 10 min. Fluorescence recovery was recorded and evaluated. Horizontal line profiles were taken at three different time points (t_0 = 0-32 s; t_1 = 142.5-175 s; t_2 = 285-317.5 s). Peculiarities are indicated by the arrows and vertical line profiles were plotted along the area highlighted (dashed box). Experiments were run out in duplicates. One representative experiment is plotted for each peptide.

For the α-helical peptide LL-32 an opposed behavior was observed (Figure 62): On DOPC membranes only weak fluorescence signals are detected for this AMP suggesting that the peptide is either arranged as random coil which is equipollent to membrane-inactive peptide monomers or the confocal plane does not show the very top of the membrane surface but slightly below and therewith only low peptide fluorescence is detectable due to sparsely population of peptide helices that are inserted into the membrane and the major fraction of peptide lying attached on the membrane surface.

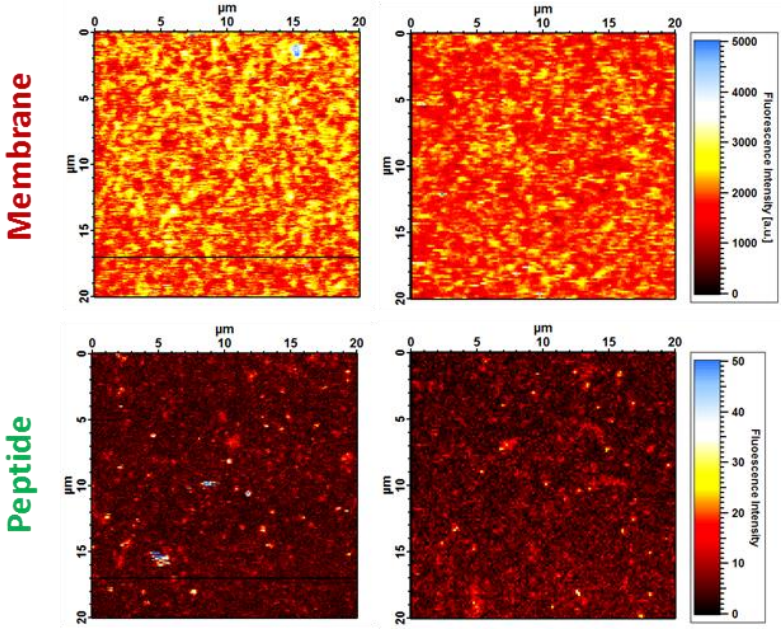

Figure 62 | Confocal images of a lipid bilayer reconstituted from pure DOPC after incubation with Atto488-LL-32 at two different positions. Fluorophores were excited simultaneously: The membrane was fluorescently highlighted by incorporation of the lipid-dye conjugate Atto633-DOPE. Peptide distribution was studied by the detection of the peptide-dye conjugate Atto488-LL-32. The peptide was applied in a final concentration of 10 nM. Experiments were run out in duplicates in 5 mM HEPES (pH 7.4).

An analog observation could be made on the ternary lipid system. Herein, LL-32 exhibits apparently an even weaker fluorescence in the peptide channel compared to the signal detected on pure DOPC bilayers. No obvious redistribution of the peptide on the membrane surface could be monitored. Chances are, that the fraction of cholesterol present within the membrane matrix perturb the peptide from membrane insertion or changes the kinetics for peptide intercalation (Figure 63).

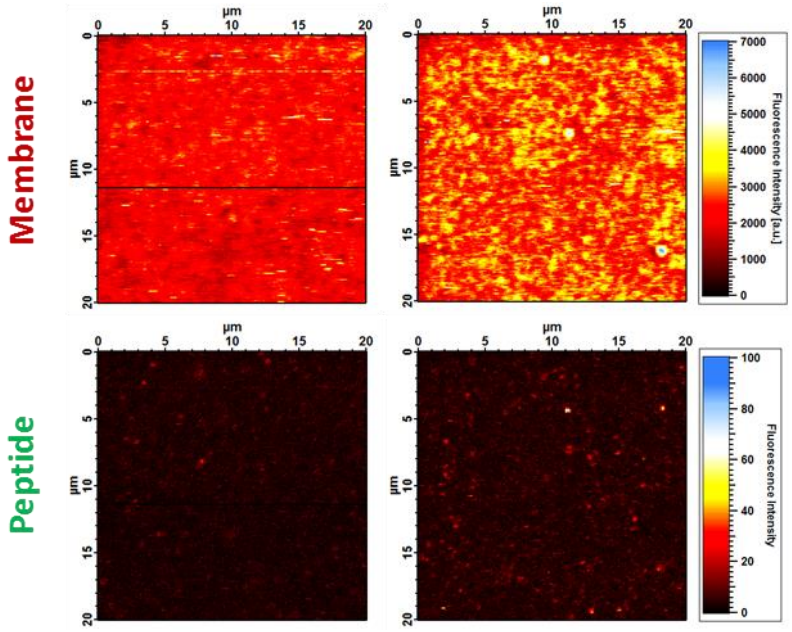

Figure 63 | Confocal images of a cholesterol-rich lipid bilayer reconstituted from DOPC/SM/Chol (2:2:1) after incubation with Atto488-LL-32 at two different positions. Fluorophores were excited simultaneously: The membrane was fluorescently highlighted by incorporation of the lipid-dye conjugate Atto633-DOPE. Peptide distribution was studied by the detection of the peptide-dye conjugate Atto488-LL-32. The peptide was applied in a final concentration of 10 nM. Experiments were run out in duplicates in 5 mM HEPES (pH 7.4).

The results extracted from the aforementioned confocal images, match the evaluated horizontal line profiles from FRAP-measurements (Figure 64): Cholesterol-rich membranes were found to be more prone for fluorescence bleaching than pure DOPC membranes. This result is substantiated by two major aspects; one, taken the distribution of the lipid-dye conjugate into account and a second, wherein the phase-separation and the preference for one phase, as primary interaction site, of the peptide is considered. The fluorophores allocated into the membrane, are homogenously distributed within the liquid-disordered domains, which are the same domains favored by LL-32 as herein before mentioned. The outcome of this is, that the peptide faces a larger interaction site on pure DOPC bilayers compared to cholesterol-rich membranes and therewith a higher fraction of the membrane surface can be covered with the α-helical peptide. Membrane association and in a progressed state

coverage with peptide might shield the lipid-dye conjugates and protects the membrane from fluorescence bleaching.

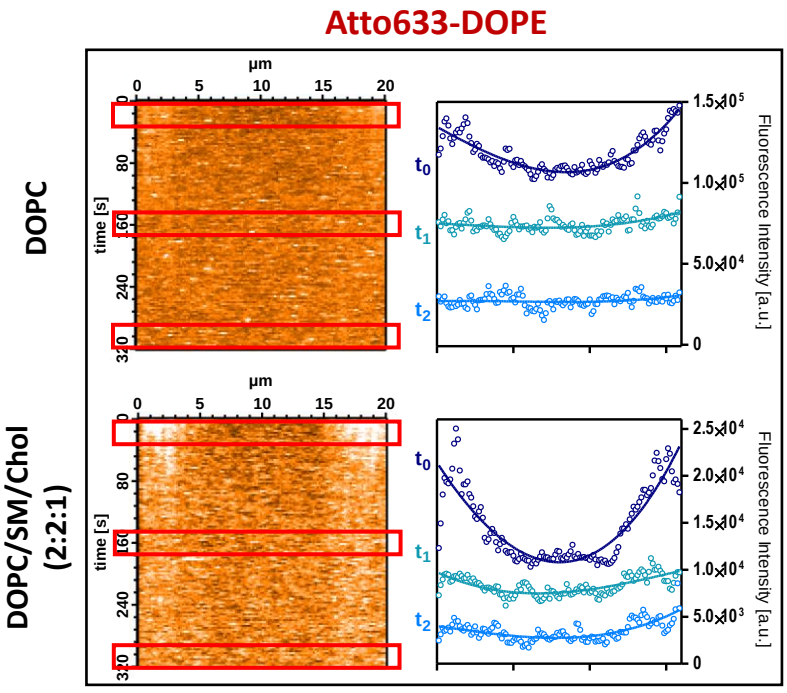

Figure 64 | Evaluated linescans of spread SUVs reconstituted from pure DOPC and DOPC/SM/Chol in a lipid ratio of 2:2:1. Membranes were incubated with 10 nM of Atto488-LL-32 and the lipid-dye conjugate Atto633-DOPE was bleached under maximum laser intensity for 10 min. Fluorescence recovery was recorded and evaluated. Horizontal line profiles were taken at three different time points (t_0 = 0-32 s; t_1 = 142.5-175 s; t_2 = 285-317.5 s). Experiments were run out in duplicates. One representative experiment is plotted for each peptide.

In the peptide channel, only single molecule effects could be detected (Figure 65; dashed box). Thus, it appears that peptide monomers were more affected by fluorescence bleaching on cholesterol-rich lipid bilayers, where the evaluation of the vertical line profile follows an exponential decay in fluorescence. On pure DOPC membranes, the fluorescence of the peptide-dye conjugate is more stable over the scanning interval.

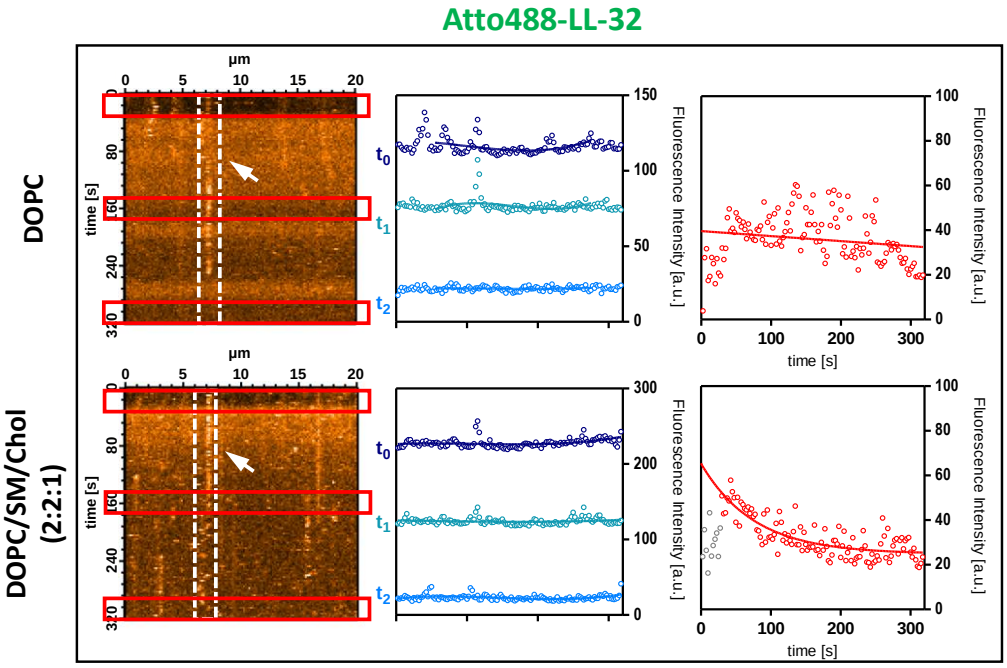

Figure 65 | Evaluated linescans of spread SUVs reconstituted from pure DOPC and DOPC/SM/Chol in a lipid ratio of 2:2:1. Membranes were incubated with 10 nM of Atto488-LL-32 and the lipid-dye conjugate Atto633-DOPE was bleached under maximum laser intensity for 10 min. Fluorescence recovery was recorded and evaluated. Horizontal line profiles were taken at three different time points (t_0 = 0-32 s; t_1 = 142.5-175 s; t_2 = 285-317.5 s). Peculiarities are indicated by the arrows and vertical line profiles were plotted along the area highlighted (dashed box). Experiments were run out in duplicates. One representative experiment is plotted for each peptide.

For hBD-3-l, a uniform distribution pattern was detected with spatial peptide enrichments. The isolated peptide accumulations were found on both membrane systems (Figure 66+67). On bilayers reconstituted from DOPC, no anti-correlation of the two dyes was observed. The white arrows depict the local peptide accumulations at λ = 488 nm whereas the black arrows depict the same spots at λ = 633 nm (Figure 66), showing no obvious lipid rearrangement.

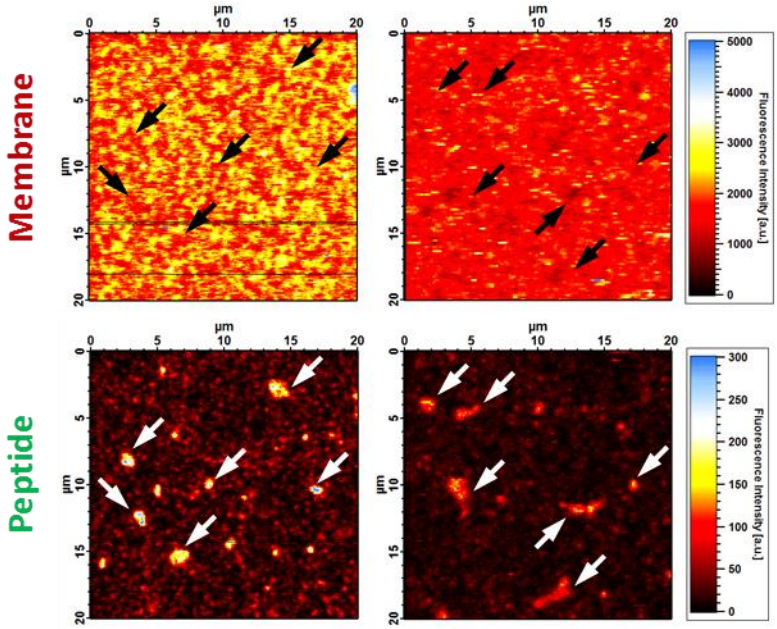

Figure 66 | Confocal images of a lipid bilayer reconstituted from pure DOPC after incubation with Atto488-hBD-3-l at two different positions. Fluorophores were excited simultaneously: The membrane was fluorescently highlighted by incorporation of the lipid-dye conjugate Atto633-DOPE. Peptide distribution was studied by the detection of the peptide-dye conjugate Atto488-hBD-3-l. The peptide was applied in a final concentration of 10 nM. Experiments were run out in duplicates in 5 mM HEPES (pH 7.4).

Contrariwise on cholesterol-rich lipid bilayers, herein a more homogenous peptide distribution was detected that is tantamount to a higher degree of peptide coverage of the membrane. The local peptide clusters feature a smaller size, but exhibiting a circular type pattern in close proximity with lower fluorescence intensity values (white arrows and dashed circles; Figure 67) as already seen for PMB. These distinct areas expose a higher fluorescence signal for the lipid-dye conjugate at λ = 633 nm. Consequently, the peptide hBD-3-l induces a redistribution of the membrane-incorporated fluorophores in the focus plane.

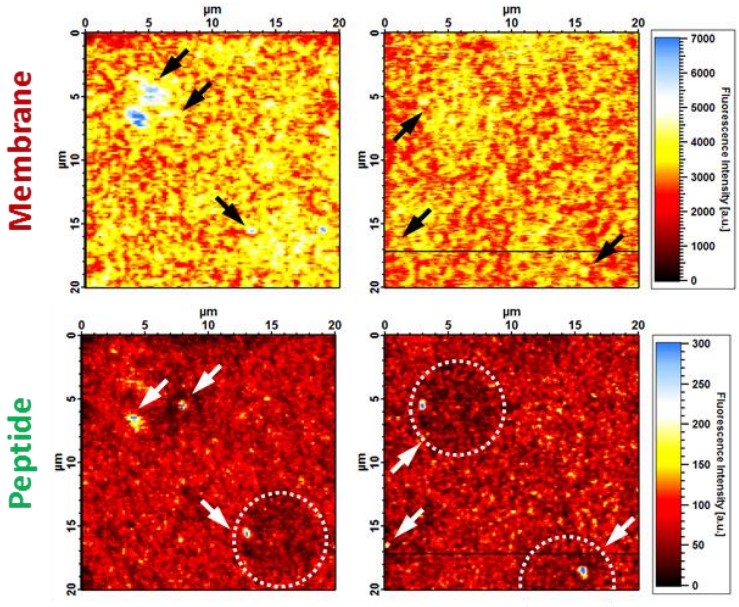

Figure 67 | Confocal images of a cholesterol-rich lipid bilayer reconstituted from DOPC/SM/Chol (2:2:1) after incubation with Atto488-hBD-3-l at two different positions. Fluorophores were excited simultaneously: The membrane was fluorescently highlighted by incorporation of the lipid-dye conjugate Atto633-DOPE. Peptide distribution was studied by the detection of the peptide-dye conjugate Atto488-hBD-3-l. The peptide was applied in a final concentration of 10 nM. Experiments were run out in duplicates in 5 mM HEPES (pH 7.4).

More in-depth information was given by the evaluation of the horizontal line profiles of the fluorescence intensity of the two fluorescent dyes at different positions. The lipid-dye conjugate Atto633-DOPE in lipid bilayers constituted of pure DOPC was only little affected by fluorescence bleaching as it is derived from the extracted line profiles (Figure 68): All data and the corresponding fits show no definite minimal turning points and follow more a trend of a horizontal line with a slope converging to zero. Lipid bilayers derived from the ternary lipid mixture behave differently and were more sustainable to fluorescence bleaching. At t_0, the fitted data extracted from the horizontal line profile exhibits a defined minimal turning point. With progressing linescan, the extracted data at t_1 and t_2 do not match a perfect parabolic fit and approximates a horizontal line fit that is put in direct context to maximum fluorescence recovery.

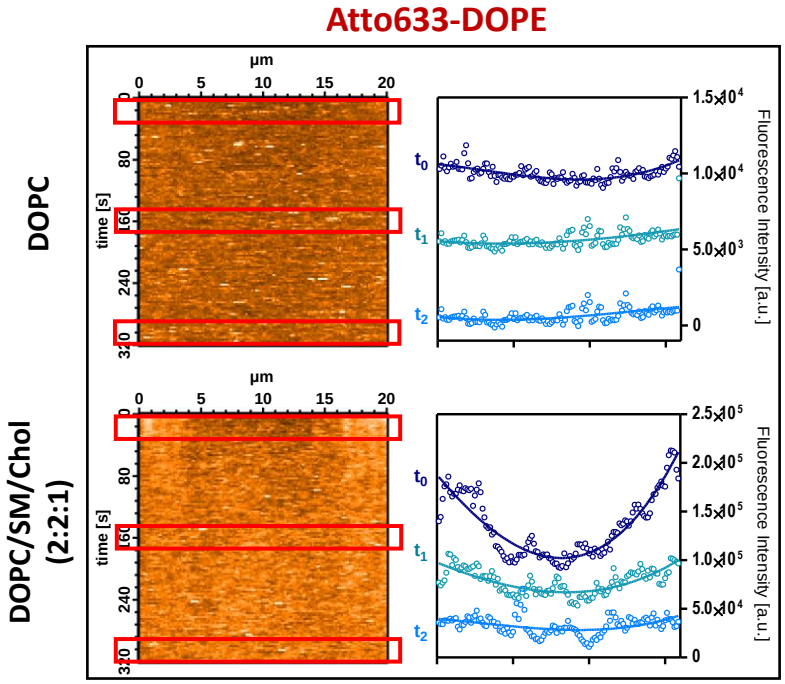

Figure 68 | Evaluated linescans of spread SUVs reconstituted from pure DOPC and DOPC/SM/Chol in a lipid ratio of 2:2:1. Membranes were incubated with 10 nM of Atto488-hBD-3-l and the lipid-dye conjugate Atto633-DOPE was bleached under maximum laser intensity for 10 min. Fluorescence recovery was recorded and evaluated. Horizontal line profiles were taken at three different time points (t_0 = 0-32 s; t_1 = 142.5-175 s; t_2 = 285-317.5 s). Experiments were run out in duplicates. One representative experiment is plotted for each peptide

For the fluorescent dye linked to the peptide, the fluorescence distribution in linescan mode is evidence for single molecule effects: On DOPC membranes no fluorescence recovery was detected in general, as it is seen from the horizontal line profiles (Figure 69). At this juncture, only two events traced back to single molecules were detected. One of these events were evaluated exemplarily by extraction of the vertical line profile. This data follows an exponential decay resembling progressing fluorescence bleaching over time of the peptide-dye conjugate.

On lipid bilayers containing 20mol% cholesterol, single molecule events were more pronounced. In any case, no fluorescence recovery of the peptide-bound fluorophore was detected, only continuous bleaching on the single molecule level could be observed.

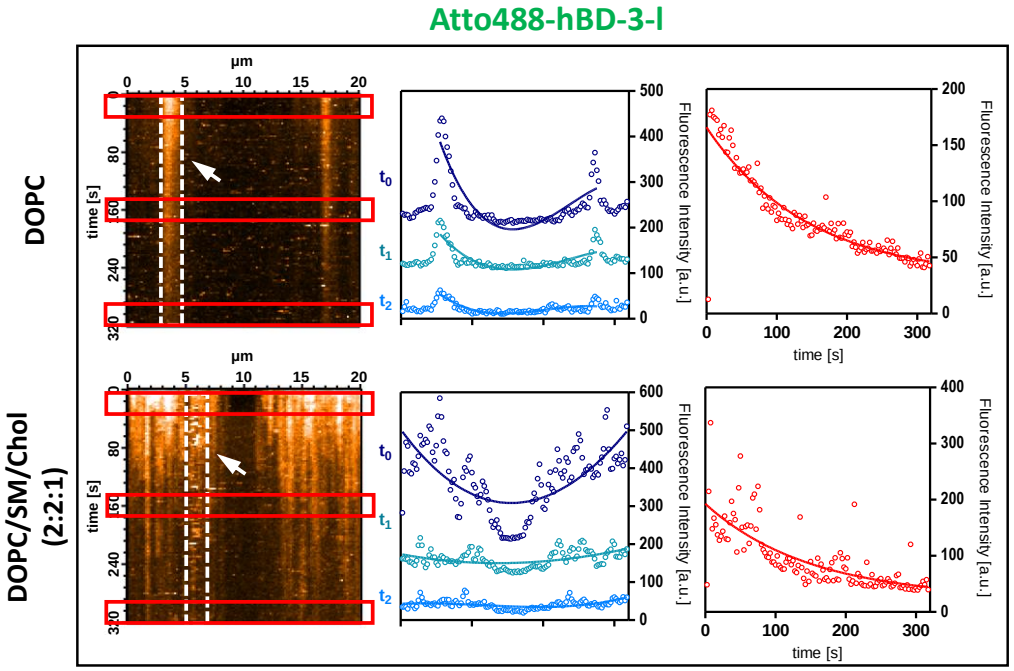

Figure 69 | Evaluated linescans of spread SUVs reconstituted from pure DOPC and DOPC/SM/Chol in a lipid ratio of 2:2:1. Membranes were incubated with 10 nM of Atto488-hBD-3-l and the lipid-dye conjugate Atto633-DOPE was bleached under maximum laser intensity for 10 min. Fluorescence recovery was recorded and evaluated. Horizontal line profiles were taken at three different time points (t_0 = 0-32 s; t_1 = 142.5-175 s; t_2 = 285-317.5 s). Peculiarities are indicated by the arrows and vertical line profiles were plotted along the area highlighted (dashed box). Experiments were run out in duplicates. One representative experiment is plotted for each peptide.

Using FRAP for studying membrane-peptide interactions and the corresponding dynamics of lipid molecules and peptides within a lipid bilayer, offers a promising tool for a deeper understanding on the single molecule level. Even we are only at the start in using this technical approach, the herein presented first experiments, demonstrate that only little adjustments and optimizations have to be accomplished in the future.

4.1.10 X-Ray Reflectivity & Electron Density Distribution

The investigation of solid supported phospholipid membranes by X-ray scattering have become a prominent tool for studying detailed structural parameters of lipid membranes. By this technique an experimental approach towards lipid-peptide interaction is given. Beyond the classical analysis of membrane structures, macromolecular self-assembly can be probed by X-ray reflectivity among fluctuation and interaction parameters. All data analyses were performed in cooperation with J. Wernecke. Approximations and corrections performed were processed as described in the doctoral research work of hers and are based on fitting the reflectivity curves over the full q_z-range. The electron density distribution was determined from the XRR data.

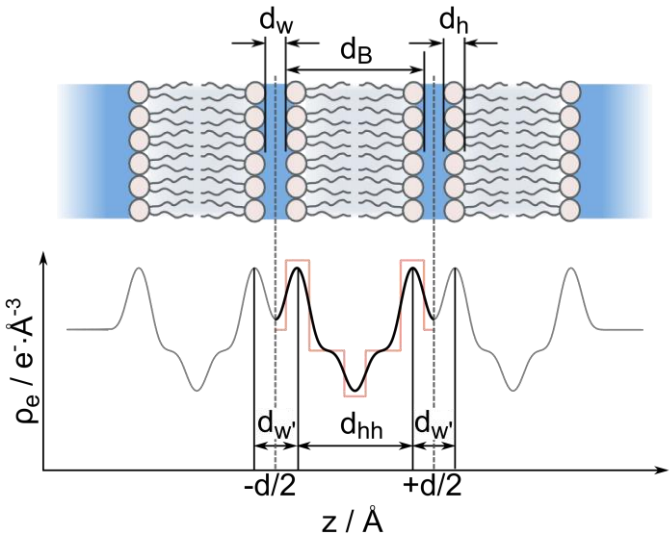

Figure 70 | Exemplary electron density distribution derived from XRR-profile of a lipid multilayer. Top: Illustration of a cross section of a membrane stack. Bottom: Corresponding electron density $\rho_e(z)$. The maxima of the electron density distribution refer to the lipid headgroups whereas the minima resemble the hydrophobic part where the fatty acid chains are located in. Cutline for the parameters: bilayer thickness (d_B), headgroup-headgroup distance (d_{hh}), lamellar spacing (d), thickness of water interface (d_w), thickness of headgroup region (d_h). Courtesy of J. Wernecke[12].

For the most ordinary membrane system, stacks composed of pure DOPC were prepared alone and in presence of the two compounds of

interest – LL-32 and PMB. For pure DOPC-membranes (Figure 71), the reflectivity profile is composed of single, well-defined Bragg peaks. Lack of phase-separation and membrane defects give the characteristic single peak pattern without any visible peak splitting or broadening. The headgroup-headgroup distance (d_{hh}) derived out of the relative electron density distribution ranges between 35.96 Å at 25 °C to 35.15 Å at 40 °C. The pure DOPC membrane system is only little affected in this temperature range.

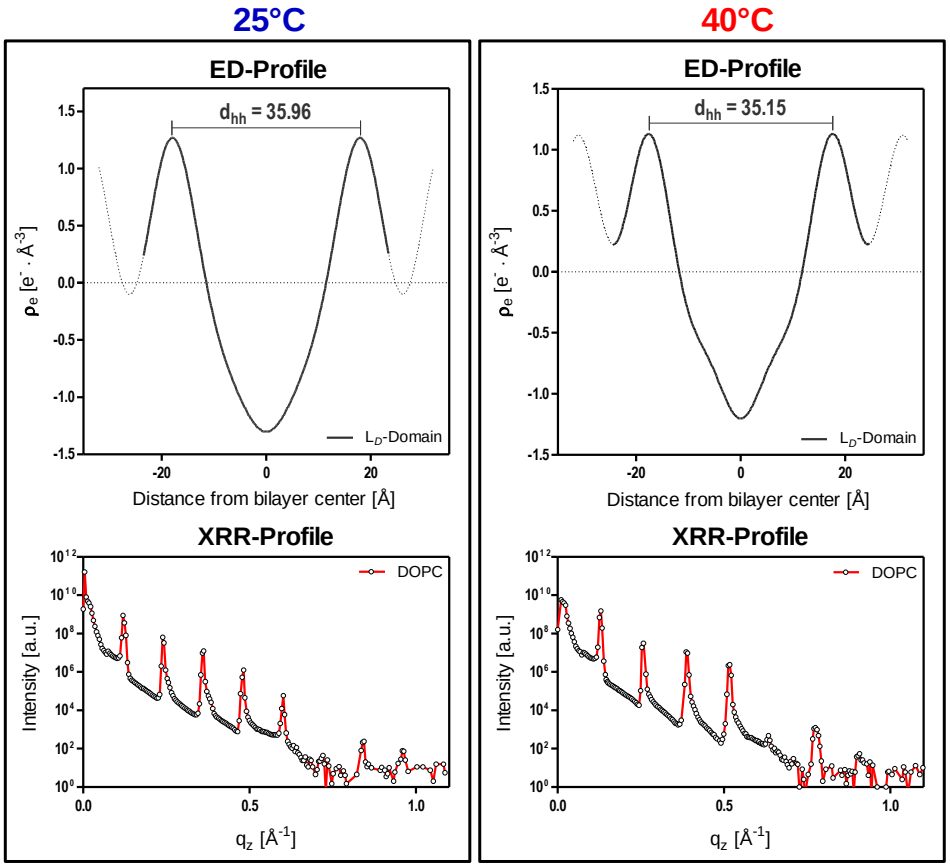

Figure 71 | Relative electron density distribution and XRR-profiles for pure DOPC. Left: Calculated electron density distribution at 25 °C with a determined headgroup-headgroup distance of 35.96 Å. The corresponding XRR-profile is stated below and features single, well-defined Bragg peaks. Right: Calculated electron density distribution at 40 °C with a determined d_{hh}-value of 35.15 Å. The corresponding XRR-profile below remains stable and shows no visible effects induced by heating. The headgroup interspace is reduced by 0.81 Å with respect to 25 °C-sample.

Exposure of this primary lipid system to LL-32 results in the first instance to no obvious changes: The single Bragg peak pattern remains stable under both temperature conditions (Figure 72).

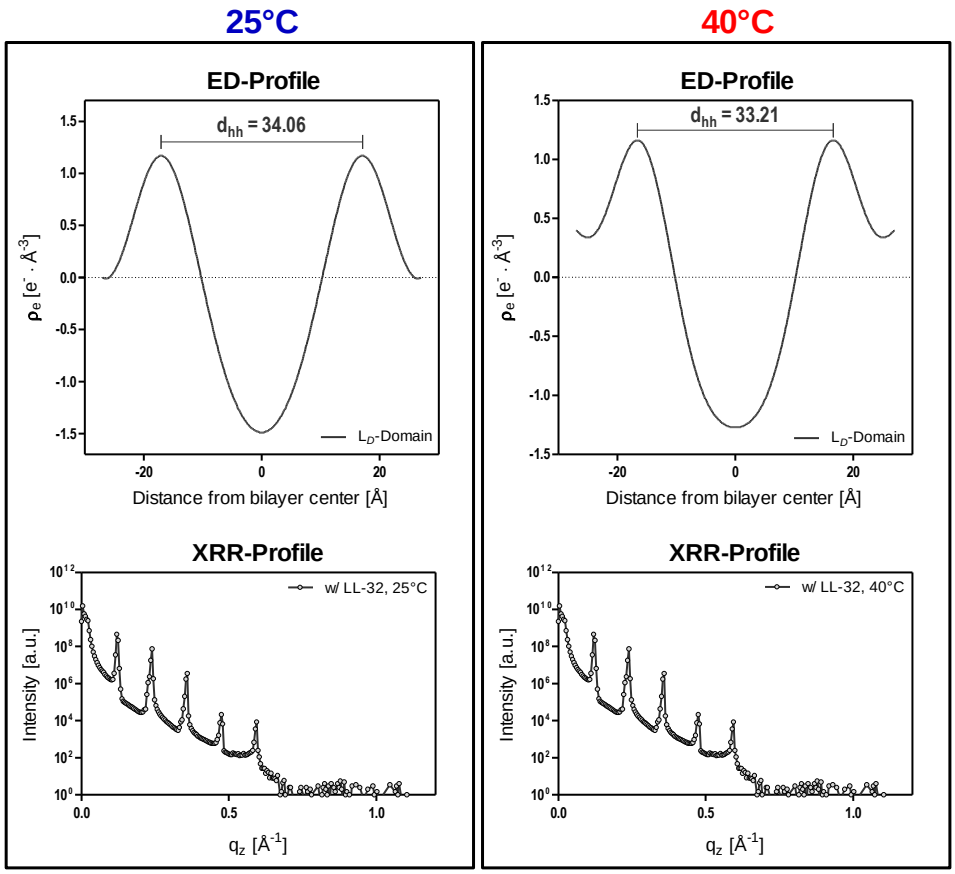

Figure 72 | Relative electron density distribution and XRR-profiles for DOPC-membrane stacks after exposure to LL-32. Left: Calculated electron density distribution at 25 °C with a determined headgroup-headgroup distance of 34.06 Å. The corresponding XRR-profile is stated below and features single, well-defined Bragg peaks. Right: Calculated electron density distribution at 40 °C with a determined d_{hh}-value of 33.21 Å. The corresponding XRR-profile below remains stable and shows no visible effects induced by heating. The headgroup interspace is reduced by 0.85 Å (compared with 25 °C-sample). With respect to the control, LL-32 induced membrane thinning and lead to a total decrease in d_{hh} of 2.75 Å. The peptide was applied in a volumetric ratio of 4:1.

The electron density distribution sheds more light on peptide-induced structural changes of the membrane. The headgroup-headgroup distance is reduced by 1.9 Å to a total interspace of 34.06 Å at 25 °C (left; Figure 72). This membrane thinning effect is more pronounced under heating: At 40 °C the headgroup-headgroup distance is

reduced by another 0.85 Å to an overall distance of 33.21 Å (right; Figure 72). These results indicate peptide-induced membrane thinning.

The lipopeptide PMB, in turn, affects the membrane in a different way: Due to its structure, PMB can easily mimic lipid molecules and integrate in the bilayer, therefore structural changes are not as pronounced as for DOPC-membranes exposed to LL-32 (Figure 73).

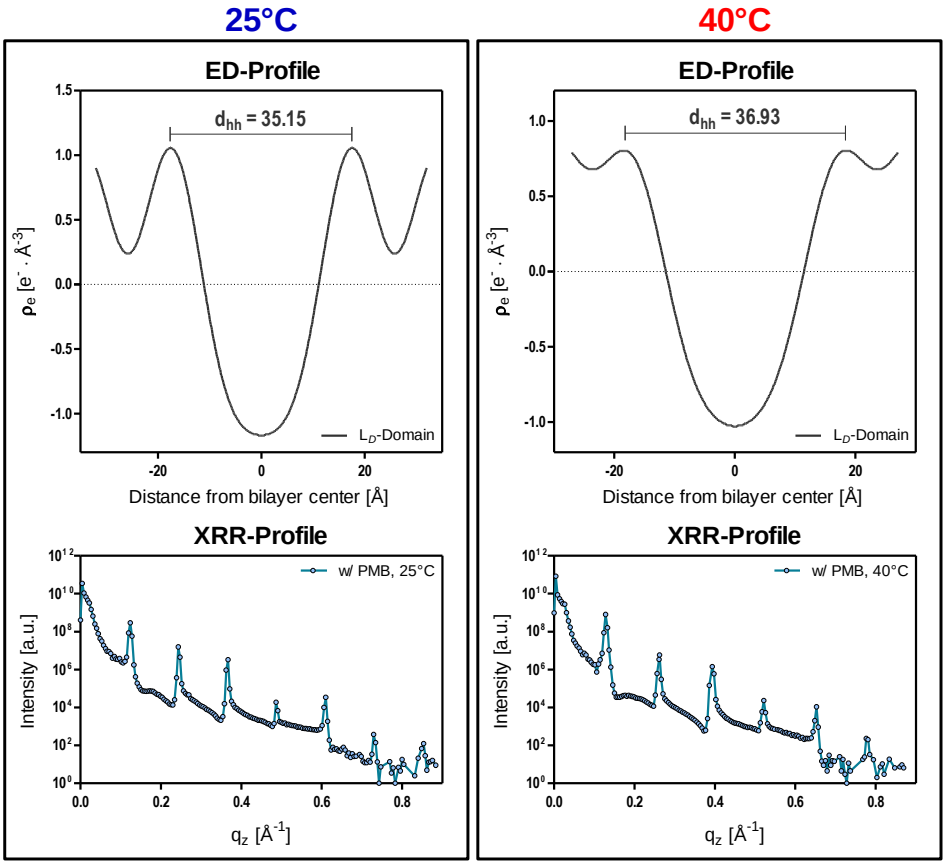

Figure 73 | Relative electron density distribution and XRR-profiles for pure DOPC exposed to the lipopeptide PMB. Left: Calculated electron density distribution at 25 °C with a determined headgroup-headgroup distance of 35.15 Å. The corresponding XRR-profile is stated below and features single, well-defined Bragg peaks. Right: Calculated electron density distribution at 40 °C with a determined d_{hh}-value of 36.93 Å. The corresponding XRR-profile below remains stable and shows no visible effects induced by heating. The headgroup interspace is raised by 1.78 Å with respect to both, control and w/PMB at 25 °C. Peptide was applied in a volumetric ratio of 4:1.

At 25 °C, PMB induces only a little decrease of 0.81 Å in d_{hh} (35.15 Å) compared with pure DOPC (35.96 Å) that can be regarded as smooth membrane thinning, whereas an increase in temperature (40 °C) resulted in

maximum membrane thickening when compared with both, DOPC multilayer without exposure to PMB (control) and with exposure to the lipopeptide at 25°C. For the first case, at 40 °C the headgroup-headgroup distance is raised by 1.78 Å from $d_{hh(DOPC)}$ = 35.15 Å to $d_{hh(w/PMB)}$ = 36.93 Å; for the latter an increase in the same order of magnitude (1.78 Å) was detected.

In the frame work of this experimental design, raft-forming lipid mixtures were reconstituted for synchrotron experiments additionally. Lipid membrane stacks exhibiting macroscopic cholesterol-rich domains undergo phase separation under the applied experimental conditions. The influence of these phase-separated multilayers on lipid-peptide interaction was studied on the 2:2:1-mixture, that turned out to be more suitable than the 9:9:2-mix. In the former, the resolved Bragg peak pattern of the membrane system containing 20mol% cholesterol can be unambiguously assigned over a wide temperature range. Figure 74 shows the calculated relative electron density distribution (upper panel) together with the corresponding reflectivity profiles (lower panel) for the pure ternary lipid mixture at 25 °C and 40 °C the phase transition temperature.

The XRR-profile at 25 °C significantly shows the presence of two different membrane domains that is derived from the characteristic Bragg peak pattern. The two domains were assigned by their equal interspace distances. The corresponding relative electron density distribution confirm these findings. The higher and therefore more ordered and cholesterol-enriched domain is given in blue with an headgroup-headgroup distance of 46.8 Å. The associated membrane domain constituted of lower amounts cholesterol are less ordered and constitute a thinner membrane region with a d_{hh} of 38.38 Å. Heating up the sample to 40 °C increases the membrane fluidity allowing the membrane domains to melt. This behavior is captured in the reflectivity profile by showing only single and defined Bragg peaks. The electron density of this interphase confirms the results by a headgroup interspace of 40.56 Å lying exactly in-between the two former separated domains.

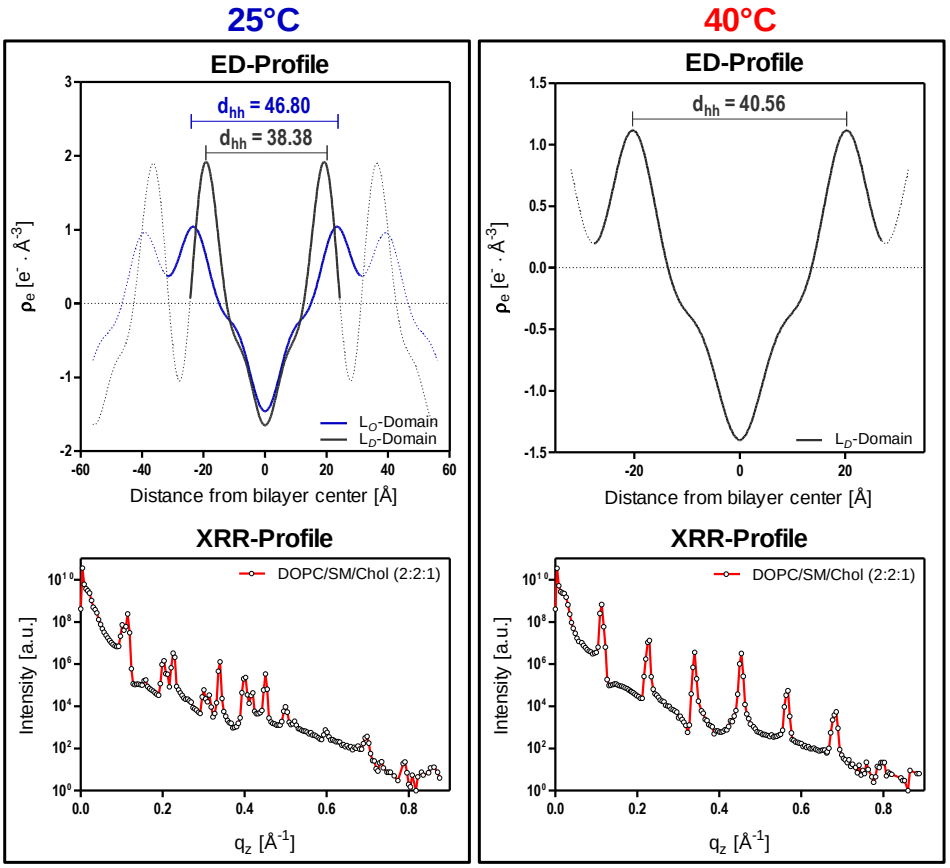

Figure 74 | Relative electron density distribution and XRR-profiles for the ternary lipid mixture DOPC/SM/Chol (2:2:1). Left: Calculated electron density distribution at 25 °C; the DOPC-enriched L_D-domain is depicted in dark grey and the cholesterol-rich L_O-domain is highlighted in blue. The headgroup-headgroup distance ranges from 38.38 Å in the cholesterol-poor areas to 46.8 Å in the cholesterol-enriched membrane regions. The corresponding XRR-profile confirms these findings by the detected Bragg peak pattern. Right: Calculated electron density distribution at 40 °C; only one mixed phase with an interspace of the lipid headgroups d_{hh} from 40.56 Å remains stable. The corresponding XRR-profile shows only one well-defined membrane domain due to the single Bragg peak pattern.

Is the ternary lipid mixture exposed to the peptide LL-32 in a volumetric ratio of 4:1, the previously described membrane characteristics are changed significantly: Figure 75 shows the XRR-profiles together with the corresponding electron densities under both temperature conditions applied. Furthermore, a representative AFM-image of the ternary lipid mixture containing 10mol% cholesterol (DOPC/SM/Chol, lipid ratio of 9:9:2 at 25 °C, courtesy of T. GUTSMANN) demonstrates the massive structural changes induced by the peptide and is represented for convenient prospect

of the following results (Figure 76). At the lower temperature, the Bragg peak pattern of the XRR-profile could be assigned to two different membrane domains with a dramatic change in total membrane thickness: At 25 °C, the thickness of the liquid-ordered domains is 2.5-fold ($d_{hh(2:2:1)}$ = 46.8 Å (control) to $d_{hh(w/\ LL\text{-}32)}$ = 116.2 ±6.1 Å) and of the liquid-disordered domains 1.4-fold higher compared to the control ($d_{hh(2:2:1)}$ = 38.38 Å (control) to $d_{hh(w/\ LL\text{-}32)}$ = 54.2 ±0.3 Å). Due to the close proximity with partial overlap of the Bragg peaks it was not possible to determine trustworthy d_{hh}-values for all cases, therefore only total d_B-values were calculated for the ternary mixture in presence of LL-32. The higher cholesterol-rich membrane domain depicted in blue, feature a total membrane thickness of 116.2 Å (±6.1 Å). The less ordered domain exhibits a small increase in membrane thickness within the resolution image with 54.2 Å (±0.3 Å). At 40 °C, the phase-separated characteristic Bragg peak pattern remains stable. The calculated electron density profiles show a slight decrease in overall membrane thickness that is traced back to the heating process. The d_B-values with 103.5 Å (±1.5 Å) for the L_O-domain and 47.1 Å (±0.7 Å) for the L_D-domain support the strong influence of LL-32 on raft-forming membranes.

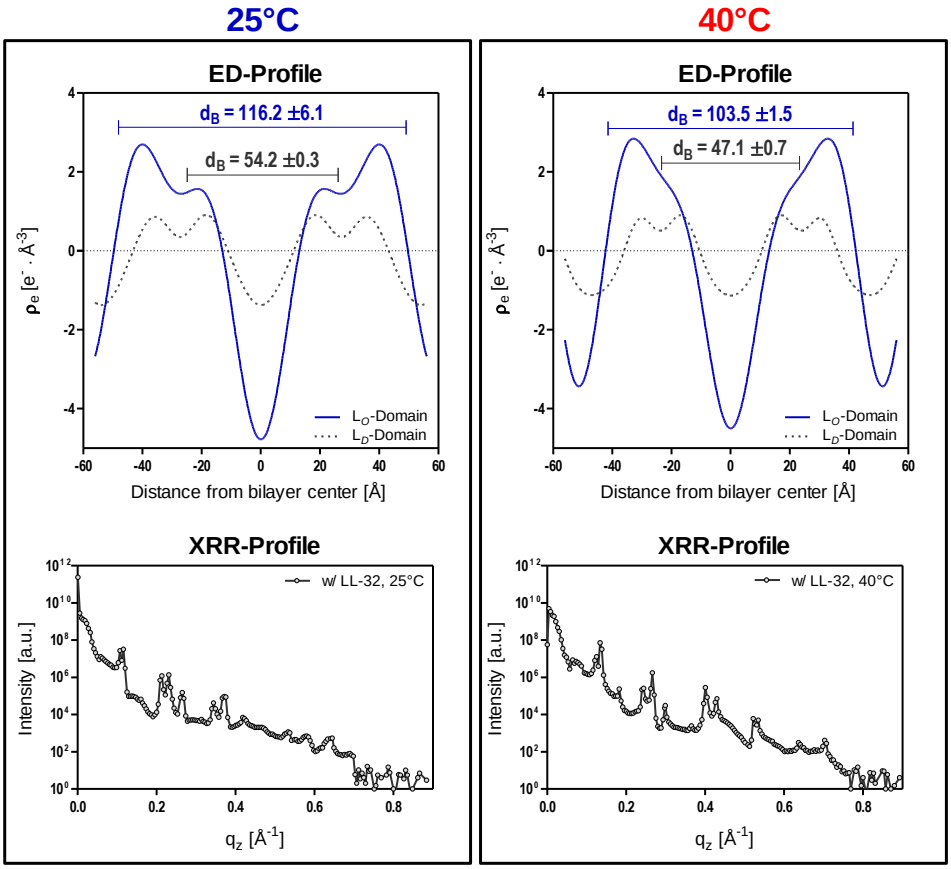

Figure 75 | Relative electron density distribution and XRR-profiles for the ternary lipid mixture DOPC/SM/Chol (2:2:1) in presence of LL-32. The calculated electron density distributions are depicted with the DOPC-enriched L_D-domain plotted in dark grey (dashed line) and the cholesterol-rich L_O-domain highlighted in blue. The overall membrane thickness ranges from 54.2 Å (±0.3 Å) at 25 °C (left panel) to 47.1 Å (±0.7 Å) at 40 °C (right panel) in the cholesterol-poor areas and from 116.2 Å (±6.1 Å) at 25 °C to 103.5 Å (±1.5 Å) at 40 °C in the cholesterol-enriched membrane regions. The corresponding XRR-profiles confirm the results by the characteristic multi Bragg peak pattern.

The peptide associates as seen from GUV-experiments with the liquid-disordered membrane areas resulting in a kind of "push-together" of the cholesterol-rich membrane regions and therewith a dramatic increase in membrane thickness (*q.v. AFM image provided in Figure 76*). These results from immobilized GUVs, AFM, and synchrotron experiments put together, significantly confirm the cholesterol-condensing (without increasing degree of membrane ordering at the same time) and domain-stabilizing ability of LL-32.

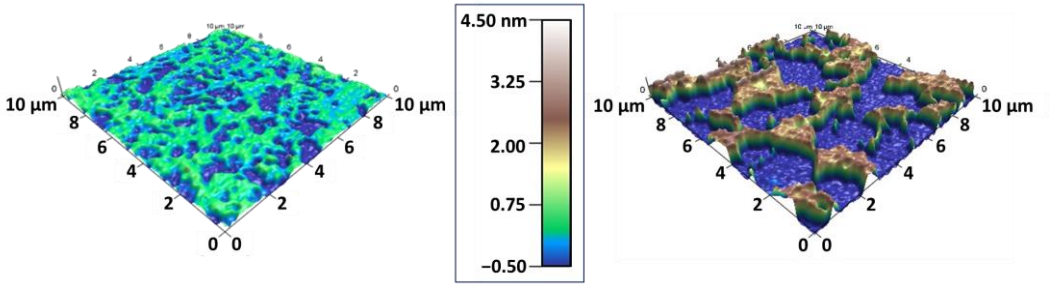

Figure 76 | AFM images of solid supported lipid bilayers reconstituted from DOPC/SM/Chol in a lipid ratio of 9:9:2. Left: Lipid bilayer before Injection of LL-32. Liquid-ordered domains are in a height range between 0.75 nm and 1.0 nm. Right: Lipid bilayer after exposure to LL-32. Liquid-ordered domains are significantly increased in height. Height range approximately between 2.0 nm and 3.0 nm. Courtesy of T. GUTSMANN.

The antibiotic peptide PMB introduces no massive changes on DOPC/SM/Chol (2:2:1) membranes: At 25 °C the XRR-profile detected features a similar pattern as the control. A closer look on the electron density distribution reveals a membrane thickening effect induced by PMB (Figure 77).

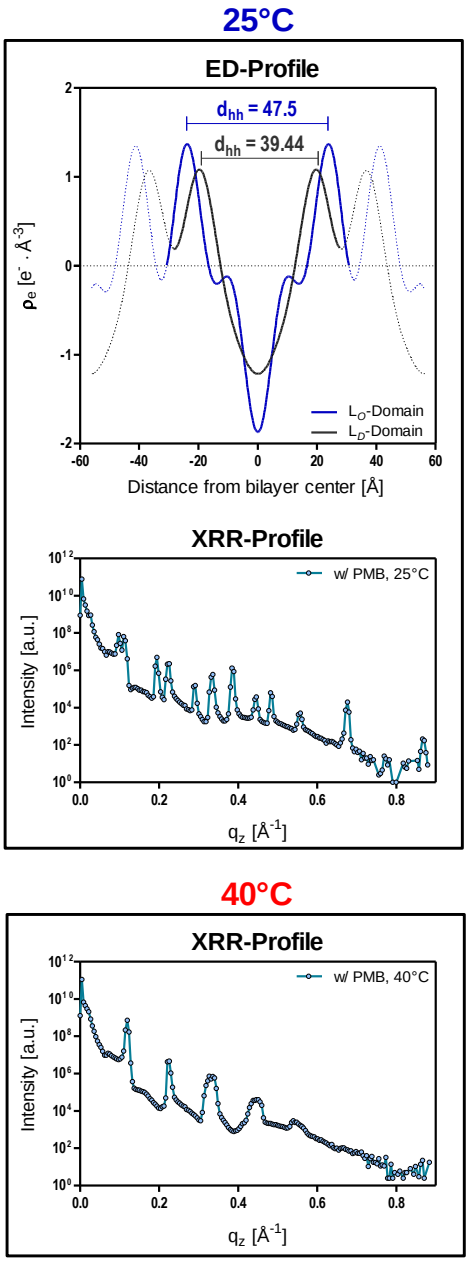

Figure 77 | Relative electron density distribution and XRR-profiles for the ternary lipid mixture DOPC/SM/Chol (2:2:1) in presence of the lipopeptide PMB. The calculated electron density distributions for the DOPC-enriched L_D-domain is depicted in dark grey; data points belonging to the next repeating unit are plotted in dashed lines. The cholesterol-rich L_O-domain is highlighted in blue. The headgroup-headgroup distance varies between 39.44 Å in the cholesterol-poor areas and 47.5 Å in the cholesterol-enriched membrane regions. The corresponding XRR-profiles are given for both temperature conditions. Due to insufficient Bragg peak isolation only the electron density profile at 25 °C was calculated. PMB was applied in a volumetric ratio of 4:1. The membrane domains feature increased thickness with respect to control of 1.06 Å (L_D-domain) and 0.7 Å (L_O-domain).

The distance between the lipid headgroups d_{hh} increases from 46.8 Å ($d_{hh(control)}$) to 47.5 Å ($d_{hh(w/ PMB)}$) for the cholesterol-enriched membrane region and from 38.38 Å ($d_{hh(control)}$) to 39.44 Å ($d_{hh(w/ PMB)}$) for the cholesterol-poor membrane fraction. The membrane regions with lower content in cholesterol undergo a stronger thickening (1.06 Å) than the membrane areas with higher degrees of cholesterol (0.7 Å).

At 40 °C, only the XRR-profile could be plotted due to Bragg peak broadening and overlap: The reflectivity profile indicates, especially in the Bragg peaks of third order and higher, that a second domain is still present but not stable. But due to incomplete melting, it is not possible to clearly differentiate to which domain the broadened Bragg peaks belong to. Therefore, it is not applicable and feasible to calculate the relative electron density for this condition. Solely, the conclusion can be made that PMB does neither exhibit the same lipid raft stabilizing function nor the cholesterol-condensing effect as identified for LL-32. The confirmed membrane thickening effect of PMB leads to the assumption that adhesion forces between membrane and the lipopeptide are present, facilitating a potential incorporation into the lipid matrix.

4.1.11 Grazing Incidence Small Angle X-Ray Scattering

For gaining insights on the average lateral structure of membrane stacks, the sample is aligned with an incident angle in the order of magnitude close to the critical angle. The reciprocal space map of the sample is captured with an area detector positioned behind the sample stage. Parameters like the maximum peak intensity (L_0) and the peak center (q_0) are determined by extracting the intensity profiles at a certain radial distribution (ϕ = 0° to 60°) along the chain correlation peak. The analysis of the chain correlation peak therein gives information about the correlation length ξ of the acyl chains and the average lateral chain distance a in turn.

GISAXS experiments were run out on mainly two different lipid systems whereof pure DOPC multimembrane stacks resemble the simplest approach. This lipid system was measured alone and in presence of the peptides PMB and LL-32. The latter was performed at a different beamtime where a different 2D plane detector was mounted. The extracted parameters are consistent but strongly contingent upon each other. The featured increase in correlation lengths and an enhancement in the average lateral chain distance are traced back to the use of a different plane detector during this beamtime yielding in a varied background and therewith to discrepancies of the two parameters ξ and a. Drawing a reliable comparison is not applicable because of the sensitive dependence of these two parameters on the fitting parameters. Consequently, the data of LL-32 on DOPC is neglected in figure 78. The data extracted from the reference spectra show the temperature-dependent shifts with an increased in chain-chain distance. The peak intensity and peak center is less pronounced at 40 °C and shows lower L_0 and q_z values compared to 25 °C.

In presence of PMB, the maximum intensity of the chain correlation peak is more pronounced with no significant change in q_z from the corresponding reference data. Furthermore, the correlation length is globally reduced around 0.7 Å (40 °C) to 1.5 Å (25 °C), whereas the chain-chain distance is below the reference at 25 °C and equal to above at 40 °C (Figure 78).

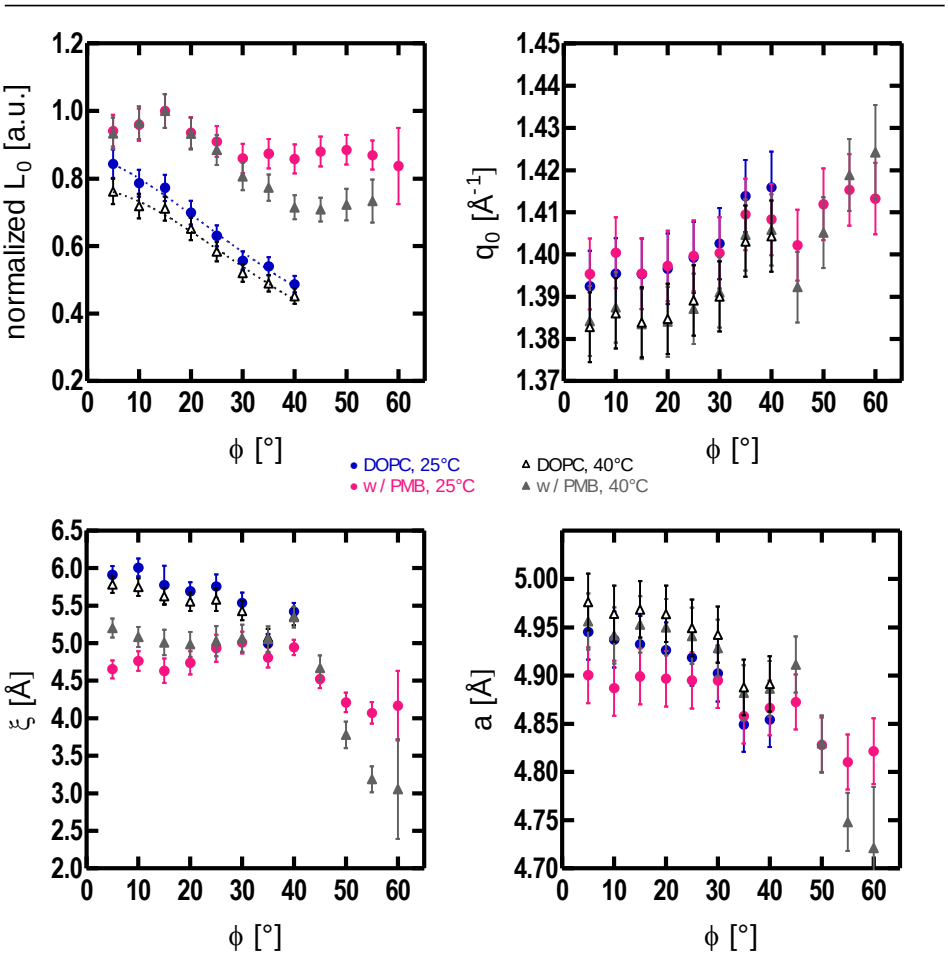

Figure 78 | Parameters extracted from reciprocal space maps of multimembrane stacks reconstituted from pure DOPC alone and in presence of PMB at 25 °C and 40 °C. Data are evaluated along an angular range from 0° to 60° in intervals of 5°. The chain correlation peak is analyzed by evaluating its azimuthal intensity distribution (L_0). Parameters such as the peak center (q_0), chain tilt (φ), correlation length of the acyl chains (ξ), and the averaged chain-chain distance (a) are determined. Color and symbol code state the following: Blue dots – DOPC reference at 25 °C; black framed triangle – DOPC reference at 40 °C; purple dots – DOPC in presence of PMB at 25 °C; grey triangle – DOPC in presence of PMB at 40 °C. PMB was applied in a volumetric ratio of 4:1.

Figure 79 shows the determined membrane stack parameters extracted from the chain correlation peak intensity along an angular range from 0° to 60°. For all sub-plots the reference membrane system (*here*: DOPC/SM/Chol in a lipid ratio of 2:2:1) is plotted together with the corresponding samples exposed to either LL-32 or PMB.

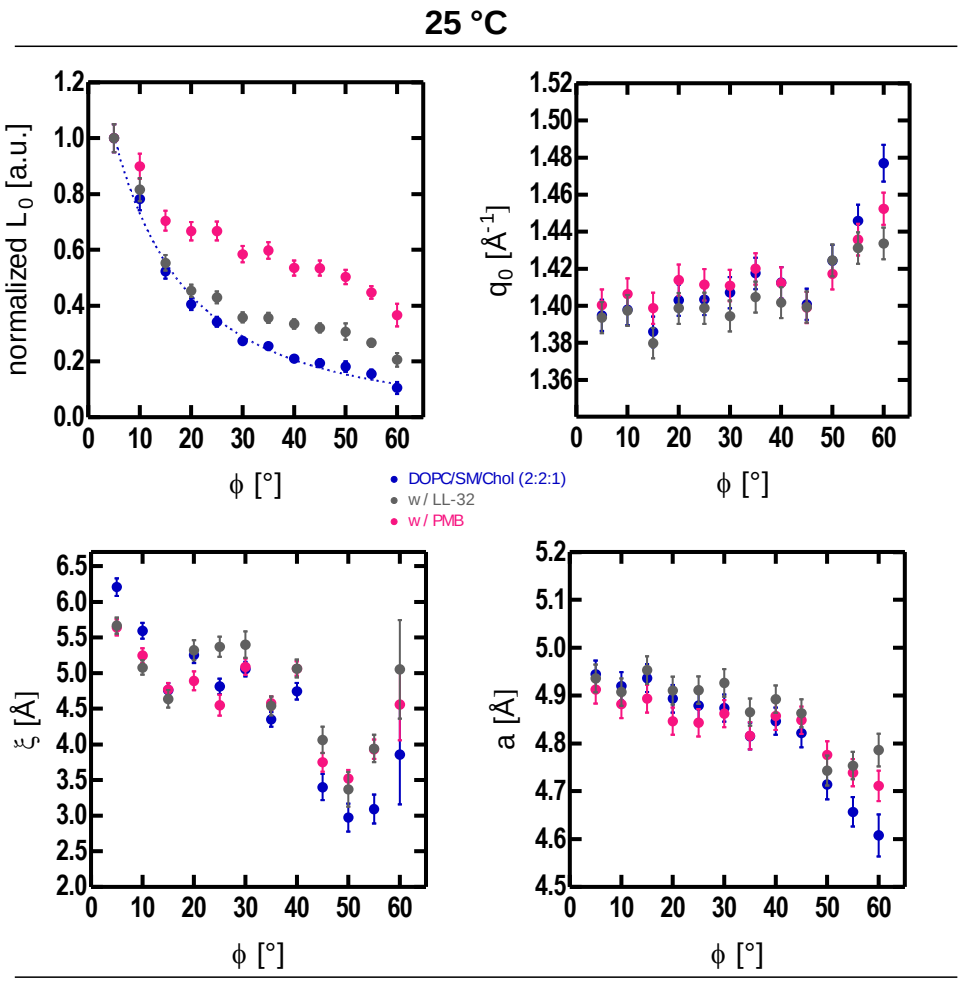

Figure 79 | Parameters extracted from reciprocal space maps of multimembrane stacks reconstituted from DOPC/SM/Chol (2:2:1) alone and in presence of LL-32 and PMB at 25 °C. Data are evaluated along an angular range from 0° to 60° in intervals of 5°. The chain correlation peak is analyzed by evaluating its azimuthal intensity distribution (L_0). Parameters such as the peak center (q_0), chain tilt (φ), correlation length of the acyl chains (ξ), and the averaged chain-chain distance (a) are determined.

At 25 °C, the normalized intensity L_0 of the chain correlation peak shows higher values along the angular range in presence of PMB. The reference lies slightly below the sample w/ LL-32 whereof both follow the

same trend and are below the sample w/ PMB. All other parameters show no significant difference and are therefore not further described.

GISAXS experiments of the same samples at 40 °C and the referring evaluated parameters do not change significantly (Figure 80).

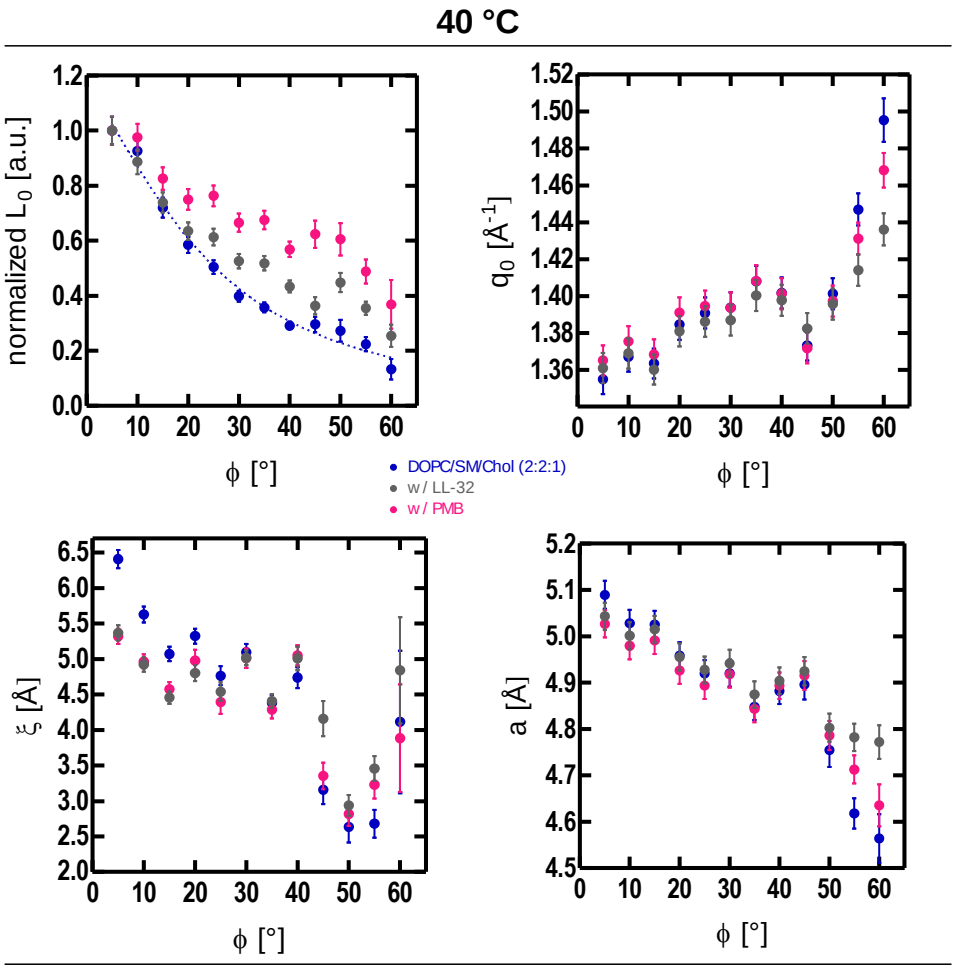

Figure 80 | Parameters extracted from reciprocal space maps of multimembrane stacks reconstituted from DOPC/SM/Chol (2:2:1) alone and in presence of LL-32 and PMB at 40 °C. Data are evaluated along an angular range from 0° to 60° in intervals of 5°. The chain correlation peak is analyzed by evaluating its azimuthal intensity distribution (L_0). Parameters such as the peak center (q_0), chain tilt (φ), correlation length of the acyl chains (ξ), and the averaged chain-chain distance (a) are determined.

The maximum peak intensity L_0 of the chain correlation peak is not as pronounced as at 25 °C and fades along the angular range. This effect is better resolved for PMB than for LL-32. As for higher temperatures expected, the averaged chain-chain distance increase as the lipid

environment gains fluidity and therewith flexibility. Figure 80 shows the collected parameters for lateral membrane information under inflammatory conditions (40 °C).

4.1.12 Small Angle X-Ray Scattering

Small angle X-ray scattering (SAXS) constitutes one of the most direct approaches for the identification of lipid mesophases and the corresponding structural parameters [158]. SAXS profiles were measured as a function of temperature in the range from 25 °C to 80 °C. For obtaining optimal output, data are given in the range of scattering vectors. This parameter gives information about the phase behavior of the pure lipid systems and after exposure to variable concentrations of LL-32 and PMB. For reasons of clarity, only the highest peptide concentration is depicted over a limited temperature range from 25 °C to 60 °C. The detected Bragg peak pattern can be further evaluated by calculating the average repeat distance (*q.v. section 3.6.3, page 114 et seqq.*; Equation 3) and the average number of spatially correlated bilayers within the stack (*q.v. section 3.6.3, page 114 et seqq.*; Equation 4) as mentioned elsewhere[153].

The pure lipid profile shows defined, moderate pronounced first and second order Bragg peaks that are flattened with increasing temperature, indicating moderate stacking of the vesicles in the direction along the bilayer normal (Figure 81). For DOPC vesicles an averaged repeat distance D_{av} (Equation 3) of 74.8 Å is calculated. Equation 4 gives the average number N_{av} (N_{av} = 12; 40 °C) of spatially correlated bilayers in the stack. In presence of LL-32, first and second order Bragg peaks are more pronounced, giving a higher degree of stacking and multilamellarity. At a temperature above 50 °C, the stacking is weakened. The averaged repeat distance stays the same whereas the average number of spatially correlated membranes within the stack is 1.7x lower (N_{av} = 7; 40 °C). For PMB, very similar scattering profiles were detected with eight correlated membranes per stack (N_{av} = 8.4; 40 °C), but with stable stacking of the vesicles over the whole temperature range. In both cases, the peakedness is reduced with increasing temperature.

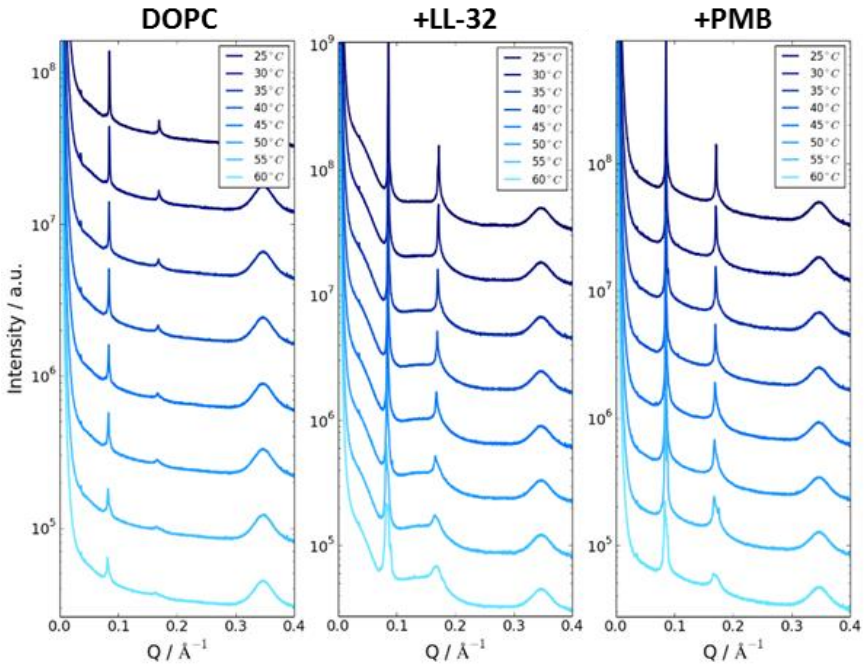

Figure 81 | SAXS profile of multilamellar vesicles reconstituted from pure DOPC (left), in presence of LL-32 (middle), and polymyxin B (right) at various temperatures (25 °C to 60 °C). Averaged repeat distance for pure DOPC was calculated with 74.8 Å. Peptides were applied in a P/L-ratio of 1:2 (v/v).

The ternary lipid mixture DOPC/SM/Chol (2:2:1) showed a compatible SAXS profile to multilamellar vesicles composed of pure DOPC (Figure 82). Differences appear in the height of first and second order Bragg peaks: first order Bragg peaks show no decrease in intensity with raising temperature, they appear stable and well-defined over the whole spectrum. The average repeat distance of the control profile (D_{av} = 81.6 Å) is above the primary lipid system. In average 19.3 membrane bilayers correlate in one three-dimensional stack at 40 °C. Second order Bragg peaks are best pronounced at 40 °C and 45 °C. The detected SAXS profile in presence of LL-32, showed an undefined third order Bragg peak between 0.2 $Å^{-1}$ and 0.3 $Å^{-1}$, allowing the hypothesis of a packing disorder at this stage. Furthermore, the second order peak is broadened showing less pronounced peak splitting. The average peak interspace is slightly lowered to 79.5 Å with three-dimensional correlation of 13.6 bilayers in average within the stack at 40 °C. In general, packing disorders can be characterized by a

broadening and lowering of the diffraction peak with increasing scattering angle. Vesicles exposed to PMB showed a scattering profile with higher characterized first and second order Bragg peaks as well as a narrowed and more defined third order Bragg peak. The interpeak distance remained the same as calculated in presence of LL-32, but the average number of spatial membranes correlating with each other went down to 9 at 40 °C. The profile for ternary lipid mixtures in presence of the antibiotic peptide, however, showed a higher degree of multilamellarity compared to LL-32. In this case, PMB induces a stronger bilayer stacking, which was also evident by the visible observation of some white precipitate in the capillaries.

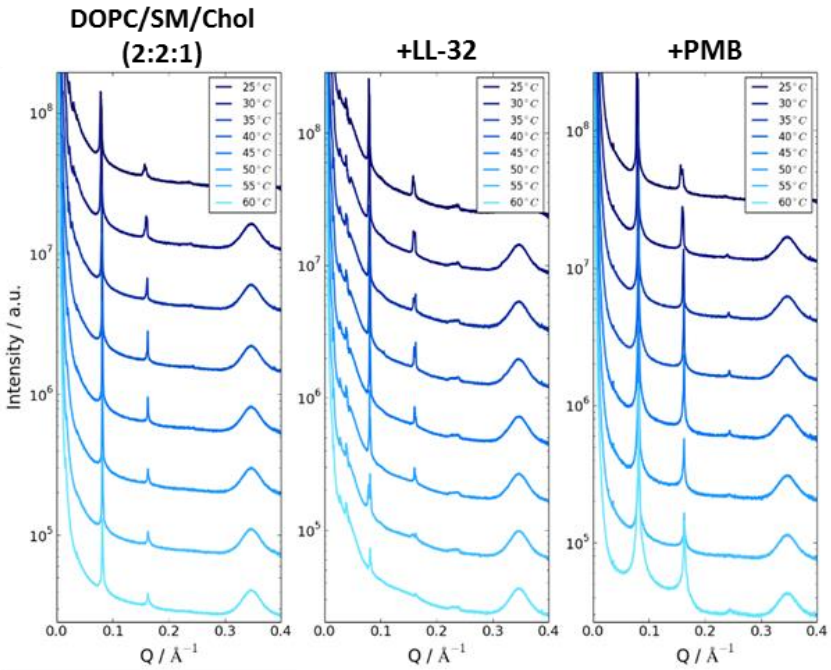

Figure 82 | SAXS profile of multilamellar vesicles reconstituted from pure DOPC/SM/Chol (2:2:1) (left), in presence of LL-32 (middle), and polymyxin B (right) at various temperatures (25 °C to 60 °C). Averaged repeat distance was determined to 81.6 Å (control) and 79.5 Å (with peptide). Peptides were applied in a P/L-ratio of 1:2 (v/v).

Is the ternary lipid mixture supplemented with 10mol% PS, a complete inhibition of multilamellarity was detected (Figure 83): Only hints of a first order Bragg peaks were found in the pure lipid mixture, the shape factor outweighs the structure factor. Under LL-32 exposure, these peaks are slightly more pronounced. No defined Bragg peaks of any order were

observed in presence of PMB. Due to the outweighing shape factor, no reliable average repeat distance and average spatial correlation number could be determined. For LL-32, both parameters were calculated because of an adequate Bragg peak formation. The average repeat distance of D_{av} = 79.7 Å and an average spatial correlation number of five lipid bilayers per stack were calculated (N_{av} = 5.4 at 40 °C). SAXS profiles of MLVs incubated with PMB feature no distinct differences from the control profile. Here again, it became apparent that no calculations of the parameter D_{av} and N_{av} were admissible. The negatively charged lipid amount distracts the multilamellar ordering massively.

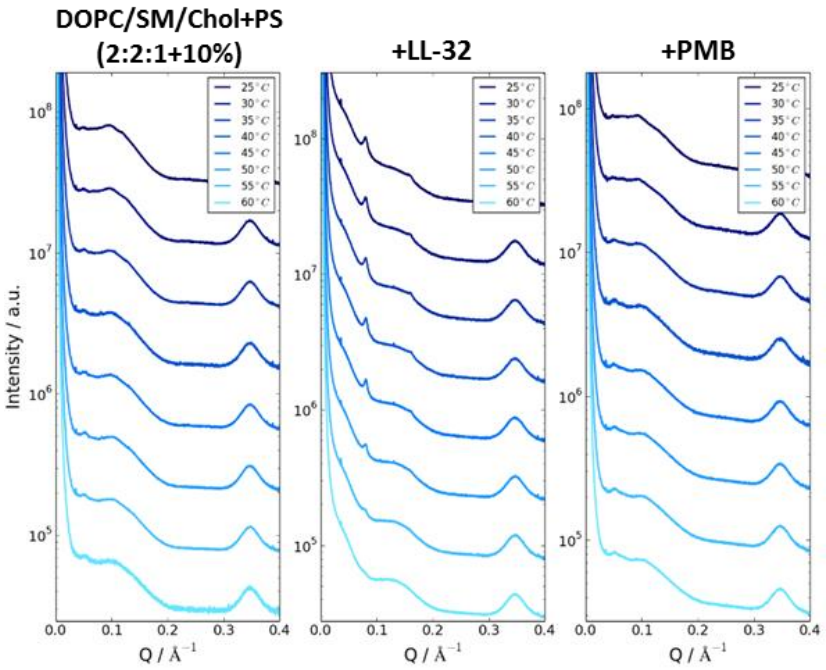

Figure 83 | SAXS profile of multilamellar vesicles reconstituted from pure DOPC/SM/Chol (2:2:1) supplemented with 10mol% PS (left), in presence of LL-32 (middle), and polymyxin B (right) at various temperatures (25 °C to 60 °C). Averaged repeat distance was calculated to 123.2 Å (control and in presence of PMB) and 79.7 Å (with LL-32). Peptides were applied in a P/L-ratio of 1:2 (v/v).

4.1.13 Oriented Circular Dichroism of LL-32

This technique allows the investigation of the membrane alignment of α-helical peptides and proteins in macroscopically oriented lipid bilayers

(SUVs) as mimicry for cellular membranes and provides qualitative to semi-quantitative information about the tilt angle of an α-helix with respect to the membrane normal. The OCD-setup comprises an extension to the conventional used benchtop CD spectrometers, that has been extensively applied to the structural characterization of peptides and proteins such as conformational studies and the secondary structural content[159]. These experiments were only run out with the peptide LL-32, having a defined α-helical structure. Figure 84 shows the OCD-spectra with respect to the different membrane reconstitution systems in presence of LL-32 with a peptide to lipid ratio (P/L) of 1:20. From the overall lowered signal intensity, a lower affinity of the peptide for this membrane system and therewith a smaller amount of peptide reconstituted in this oriented bilayer system can be deduced. Improved membrane alignment and degree of intercalation of LL-32 was obtained on DOPC/SM/Chol in a lipid ratio of 2:2:1. Supplementation of the different membrane systems with 10mol% PS showed only a marginal improved peptide reconstitution. Since there was no major difference detected for the membrane systems supplemented with 10mol%PS the focus was set on the 2:2:1-lipid mixture without PS.

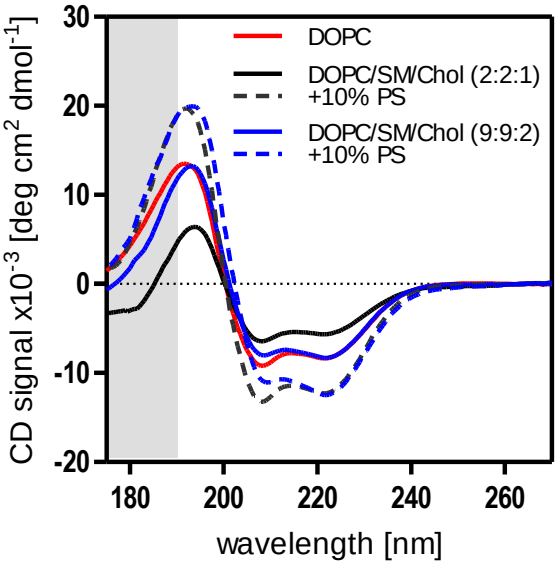

Figure 84 | OCD-data of the different reconstituted model membrane systems in presence of the α-helical peptide LL-32 (P/L = 1:20). Small membrane vesicles were reconstituted in 5 mM HEPES at pH 7.4 and homogeneously dried on pre-cleaned quartz glass windows. Wavelength-dependent gain determined by the voltage applied to the photomultiplier (high tension, HT). Area where the detector is saturated (high HT-voltage) is highlighted in grey.

In figure 85 the OCD-spectra of the concentration series of LL-32 from high to low P/L-ratios on DOPC/SM/Chol (2:2:1) membranes were plotted. As expected, LL-32 exposes a high degree in α-helicity at higher

concentrations (red and orange spectra, P/L = 1:10 and 1:20; Figure 85), that is deduced from the two pronounced minima at 220 nm and 208 nm. For the highest concentration of LL-32 (P/L = 1:10), one minima at 208 nm and a second at approximately 223 nm were detected (red spectrum; Figure 85). These two minima feature a similar intensity range representing rather similar contributions from I- (perpendicular orientation) and S-spectra (parallel orientation). From this balanced contribution, a tilt angle of the helix long with respect to the membrane normal between 30° to 60° can be derived. At P/L = 1:20 (orange spectrum; Figure 85), the spectrum shows an overall lowered signal intensity with two minima in the same wavelength range, both less pronounced compared to the red spectrum. Further lowering of the peptide concentration (P/L = 1/60, light blue spectrum), resulted in an imbalance of the contribution of I- and S-spectra. In this case, the contribution of the S-spectrum is among the I-spectrum. At high peptide concentrations, a slight membrane-inserted state towards T-state is observed. Whereas at low peptide concentrations (P/L = 1:100), the degree of α-helicity decreases which was detected by a dampening of peak intensity at 195 nm and a shift from 208 nm to 205 nm. Therefrom, the secondary structural content could be determined: The antimicrobial peptide LL-32 exerts no defined structural element at the lowest applied concentration. In this specific case, the peptide adopts to a certain fraction a random-coil; this means, that LL-32 is predominantly existent as monomer, that is oriented randomly but still bonded to adjacent units. Random-coil arrangements commonly absorb at wavelengths around 200 nm. Simulations revealed a random-coil to α-helix ratio of approximately 60%:40% (data not shown).

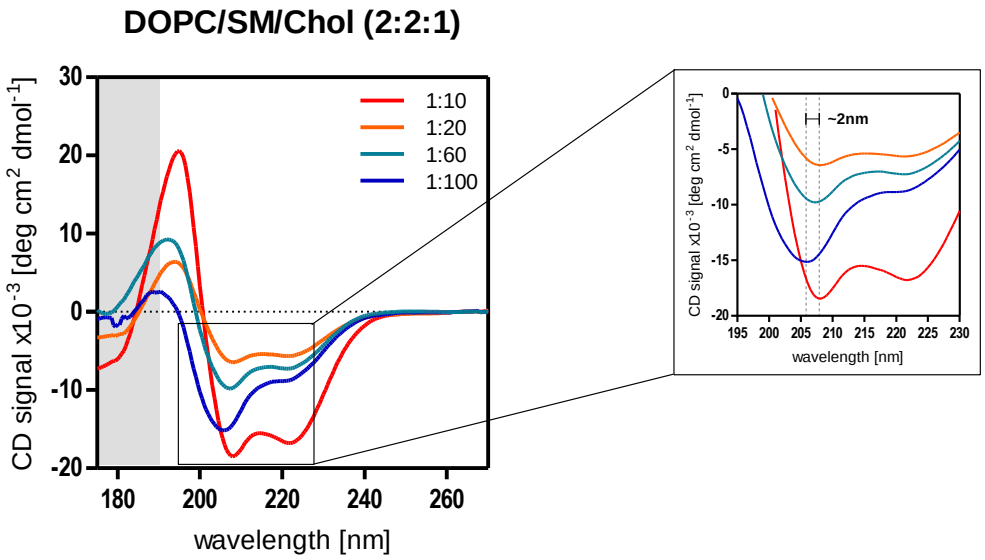

Figure 85 | OCD-data of P/L-series of the α-helical peptide LL-32 on DOPC/SM/Chol in a lipid ratio of 2:2:1. Small membrane vesicles were reconstituted in 5 mM HEPES at pH 7.4 and homogeneously dried on quartz glass crystals. Wavelength-dependent gain determined by the voltage applied to the photomultiplier (high tension, HT). Area where the detector is saturated (high HT-voltage) is highlighted in grey.

The LCD-data collected, support the results obtained in the OCD-setup. For proper LCD-data evaluation, one background spectrum was recorded by applying solely buffer into the cuvette. Figure 86 shows the evaluated CD profiles of pure LL-32 in solution (black spectrum) and with increasing number of lipids. It is evident that the pure peptide in buffer is arranged randomly, as it is reflected by the pronounced minimum at 200 nm. The same is true for small amounts of SUVs (P/L = 1:10). Continuous enriching of the solution with a higher number of lipids leads to a reorientation of the peptide: The fraction of random-coil arranged peptide monomers decreases whereas the fraction in α-helicity increases (light and dark blue spectra; Figure 86). In this setup, at P/L-ratios of 1:60 and 1:100, both the I- and S-spectra contribute in equal parts, indicating at higher lipid fractions a tilt angle of the peptide between 30° and 60°. Only in presence of a constant increase in lipids and therewith a higher level of membrane-peptide interaction, LL-32 rearranges to its characteristic α-helical form. These results match the ones collected on the OCD-setup and complement the structural information for LL-32.

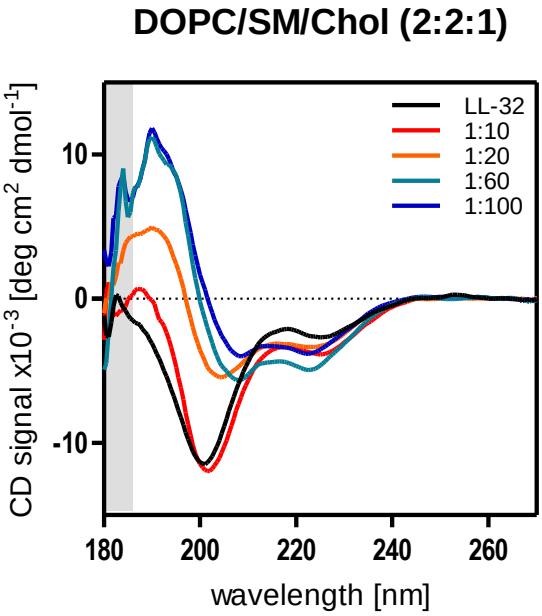

Figure 86 | Corresponding LCD-data of a P/L-series of the α-helical peptide LL-32 on model membranes reconstituted from DOPC/SM/Chol (2:2:1). SUVs were diluted in 5 mM HEPES (pH 7.4) and applied in a circular flow-through cuvette. Wavelength-dependent gain determined by the voltage applied to the photomultiplier (high tension, HT). Area where the detector is saturated (high HT-voltage) is highlighted in grey.

All OCD- and CD-spectra, were time averaged over all measurement angles. The background was corrected by removing any noise induced by the corresponding buffer system. The wavelength dependent gain is determined by the voltage applied to the photomultiplier. Data placed against a grey background exhibit high tension values above 160 V reflecting only poor absorbance of the sample and the saturation of the detector.

4.2 Immune Modulatory Function

4.2.1 HEK293-TLR4/MD2 Cell Culture Experiments

The immune regulatory and modulating function of HDPs was investigated in a wide range of stimulation experiments on a cell line derived from human embryonic kidney (HEK) cells expressing the TLR4/MD2- and IL-1-receptor complexes. This cell line is lacking the receptor complex associated protein CD14. Experiments where this protein is indispensable for proper receptor function, a transient transfection of CD14 is performed (*q.v. section 3.7.5.1, page 124*) prior to stimulation.

Figure 87 shows the effect of the human cathelicidin variant LL-32 and the lipopeptide-based antibiotic PMB on the response of these cells to LPS. This molecule triggers the detection of infections caused by Gram-negative bacteria and the related induction of sepsis and in the last resort septic shock. The LPS-control shows, that low doses (1 nM) leads to an activation of the inflammatory signaling cascade over TLR4; moderate doses (Figure 87, +10 nM LPS) already induces a strong inflammatory activation reflected by the release of the cytokine *Interleukin 8* (IL-8). Are the cells exposed to LL-32 prior to LPS-stimulation, a highly significant dose and concentration dependent decrease of cytokine release is detected. For PMB, total inhibition of LPS-response is observed in all cases.

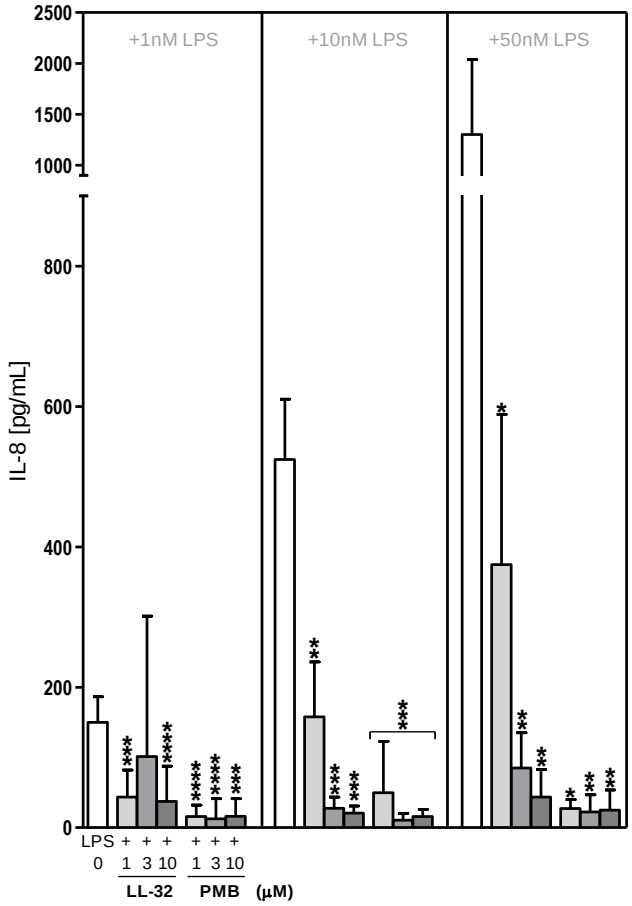

Figure 87 | Regulatory effect of LL-32 and PMB on the LPS-response of HEK293-TLR4/MD2 cells. Peptides were applied in final concentrations of 1, 3, and 10 µM. LPS-neutralizing function is detected by the decrease of IL-8 release. Statistical analysis was performed in a two-tailed student's paired t-test (non-significant: ns ≥ 0.05; significant: * p ≤. 0.05; very significant: ** p ≤ 0.01; highly significant: *** p ≤ 0.001; extremely significant: **** p ≤ 0.0001). Data are plotted as mean +SD of six (PMB) and seven (LL-32) independent experiments (n = 6-7).

To further elucidate the mode of action, how AMPs are involved in the process of dampening the immune response to LPS, other activation pathways as well as the membrane composition of immune cells were taken into account. The influence of cholesterol, as membrane component with unique features, together with its partitioning in the formation of so called lipid rafts was investigated regarding its effect on LPS-recognition and -neutralization. Figure 88 shows the LPS-response of cholesterol-depleted cells by the cyclic oligosaccharide cyclodextrin and with this, the effect of cholesterol on LPS-recognition and activation of the immune response via TLR4.

In the first set of experiments, a wide concentration range was tested to determine the maximum degree of cholesterol-depletion, showing that concentrations above 20 mM have a strong cytotoxic effect (data not shown). Cholesterol-depleted HEK293-TLR4/MD2 cells show a concentration dependent diminishment in LPS-response with increasing cyclodextrin concentration, meaning simultaneously a raising degree of depletion.

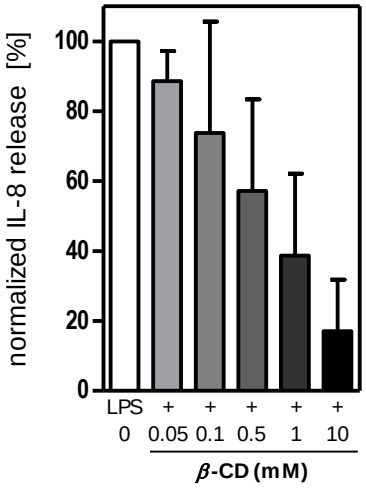

Figure 88 | Cholesterol-depletion of HEK293-TLR4/MD2 cells by the oligosaccharide methyl-β-cyclodextrin and its effect on LPS-response. Data were normalized to the highest LPS-response of untreated HEK293-TLR4/MD2 cells and plotted as mean +SD of two representative experiments (n = 5). Cells were treated with 50 nM LPS.

To monitor the LPS-neutralizing effect caused by the membrane-bound peptide, an extended stimulation protocol was established: The cells were treated as described before with the only difference that prior to LPS-addition, the cells undergo a treatment train consisting three centrifugation steps together with removal and replacing of culturing medium. This procedure is supposed to diminish the amount of unbound and excessive peptide. Figure 89 shows the effect on LPS-induced cytokine release under standard (w/o cell washing) and treatment train conditions (3x cell washing).

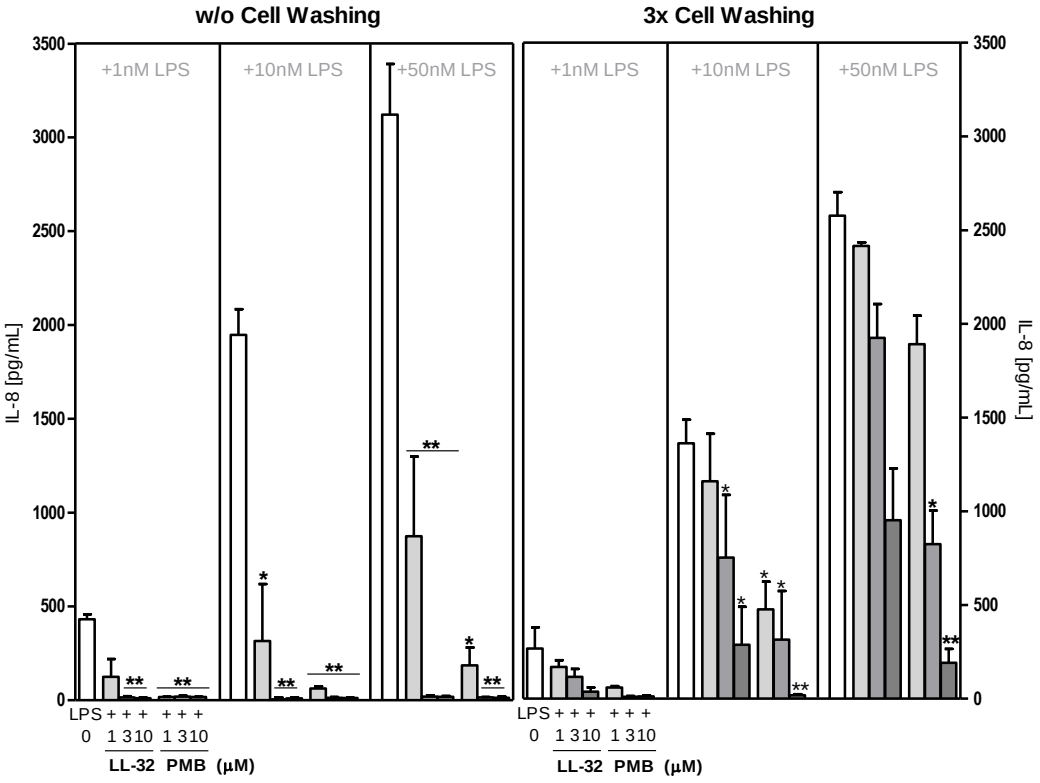

Figure 89 | Effect of membrane-associated LL-32 and PMB on the LPS-response of HEK293-TLR4/MD2 cells. Peptides were applied in final concentrations of 1, 3, and 10 µM. LPS-neutralizing function is detected by the decrease of IL-8 release under standard (w/o cell washing) and treatment train (3x cell washing) conditions. Statistical analysis was performed in a two-tailed student's paired t-test (non-significant: ns ≥ 0.05; significant: * p ≤. 0.05; very significant: ** p ≤ 0.01; highly significant: *** p ≤ 0.001; extremely significant: **** p ≤ 0.0001). Data are plotted as mean +SD of three independent experiments (n = 3).

To differentiate between direct and indirect LPS-neutralization, peptides were applied in two different preparation sets. For direct peptide-induced LPS-neutralization, the endotoxin was mixed with the peptide and incubated prior to addition onto the cells (peptide + LPS). Additionally, the neutralization of circulating endotoxin is further investigated on the membrane and receptor level by the standard protocol application for LPS-induced stimulation (cells + peptide + LPS), wherein the peptide is given prior to LPS exposure. Both experimental approaches were studied with respect to the amount of serum (FCS) in the cell culturing medium, where 1% FCS is the minimal supplementation for receiving LPS-response and 10% FCS resemble optimal experimental conditions. Figure 90 shows that the amount of serum, the medium is supplemented

with, has no dramatic effect on the results. Both experimental approaches reveal maximal dampening of LPS-induced cytokine release with extremely high significances under both concentrations applied (3 and 10 μM).

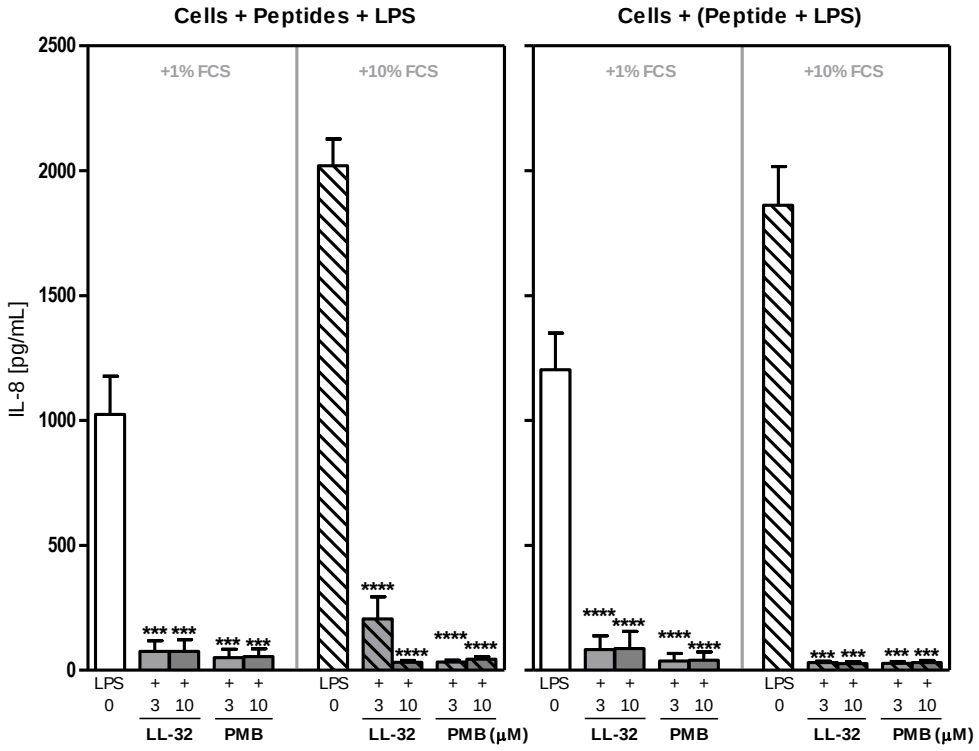

Figure 90 | LPS-neutralizing effect of LL-32 and PMB on HEK293-TLR4/MD2 cells. LPS-induced stimulation with respect to the amount of serum the culturing medium is supplemented with. Cells were treated pursuant to the standard protocol for LPS-stimulation experiments (cells + peptide + LPS) and in an extended protocol (cells + (peptide + LPS) where the AMPs are exposed to LPS and incubated with for 30 min prior to application onto the cells. Statistical analysis was performed in a two-tailed student's paired t-test (non-significant: ns ≥ 0.05; significant: * p ≤. 0.05; very significant: ** p ≤ 0.01; highly significant: *** p ≤ 0.001; extremely significant: **** p ≤ 0.0001). Data are plotted as mean +SD of five independent experiments (n = 5). LPS-dose given was 10 nM.

A wider set of substances was taken into account for investigating, if peptide-specific structural features have influence on the results given in figure 90. Among the α-helical peptide LL-32 and the small antibiotic lipopeptide PMB, the linear variant of the human β-defensin (hBD-3-l), a variant of the α-helical porcine NK-lysin (NK-2) and the newly-designed peptide LPep19-2.5 were tested in the same experimental setup (Figure 113; *q.v. section 7, page 235*).

Figure 91 shows that these structurally diverse compounds behave differently under the same experimental conditions compared to LL-32 and PMB as stated in figure 90: The human β-defensin variant hBD-3-l exhibits approximately 20% LPS-neutralizing activity under reduced serum supplementation in the culturing medium under standard experimental conditions, whereas the modified protocol for pre-incubation with LPS resulted in an enhanced LPS-neutralizing activity of 90%. All of the peptides tested in the extended substance spectrum, showed extremely high significances in the experimental approach for studying direct LPS-neutralization (cells + (peptide + LPS)). For analysis of indirect neutralization of LPS (cells + peptide + LPS) the same trend was observed in a less pronounced manner.

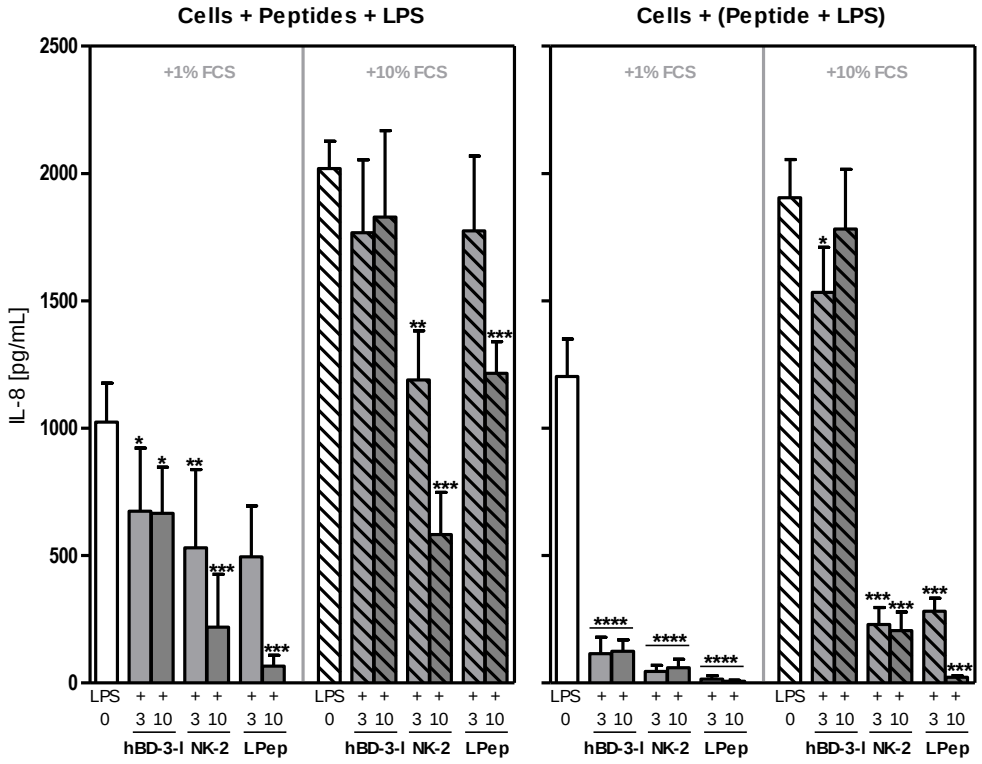

Figure 91 | LPS-neutralizing effect of hBD-3-l, NK-2 and LPep19-2.5 on HEK293-TLR4/MD2 cells. LPS-induced stimulation with respect to the amount of serum the culturing medium is supplemented with. Cells were treated pursuant to the standard protocol for LPS-stimulation experiments (peptide + cells) and in an extended protocol (peptide + LPS) where the HDPs are exposed to LPS and incubated with for 30 min prior to application onto the cells. Statistical analysis was performed in a two-tailed student's paired t-test (non-significant: ns ≥ 0.05; significant: * p ≤. 0.05; very significant: ** p ≤ 0.01; highly significant: *** p ≤ 0.001; extremely significant: **** p ≤ 0.0001). Data are plotted as mean +SD of five independent experiments (n = 5). LPS-dose given was 10 nM.

The HEK293 cell line used in this thesis does not express solely the TLR4-receptor complex. Despite this LPS-activated pathway, the IL-1-receptor complex is expressed additionally. To investigate, if the HDPs have a regulatory effect on this pathway as well, stimulation experiments with IL-1β were performed to gain insights of the mode of action of HDPs on the cellular level. Both receptor complexes feature a TIR (*Toll-IL-1 receptor*) domain in their cytoplasmic tail. Because AMPs are known to prevent a worsened inflammatory response by killing Gram-negative bacteria by membrane poration, allows the conclusion that these peptides might be able to exhibit their immune modulatory functions from the cytoplasmic site of the receptor after membrane permeation. Triggering the IL-1-receptor by IL-1b, induces an inflammatory signaling cascade over this specific pathway excluding TLR4. Is the immune response, that is detected by the cytokine release of IL-8, dampened in equal measure as it was observed for LPS-induced stimulation, the conclusion can be made that an intracellular interaction of the peptide with the TIR-domains contribute to the innate host defense strategy, even the extracellular regions differ remarkable in their compositions (immunoglobulin-like domains for IL-1-receptor complex *versus* LRR-repeats for TLR4-receptor complex (*q.v. section 1.5, page 46 et seqq.*).

Stimulation experiments within the concentration range from 3 ng/mL to 300 ng/mL showed a significant enhancement of the IL-8 release in all cases, whereas LL-32 resulted in a stronger enhancement by trend compared to PMB (Figure 92).

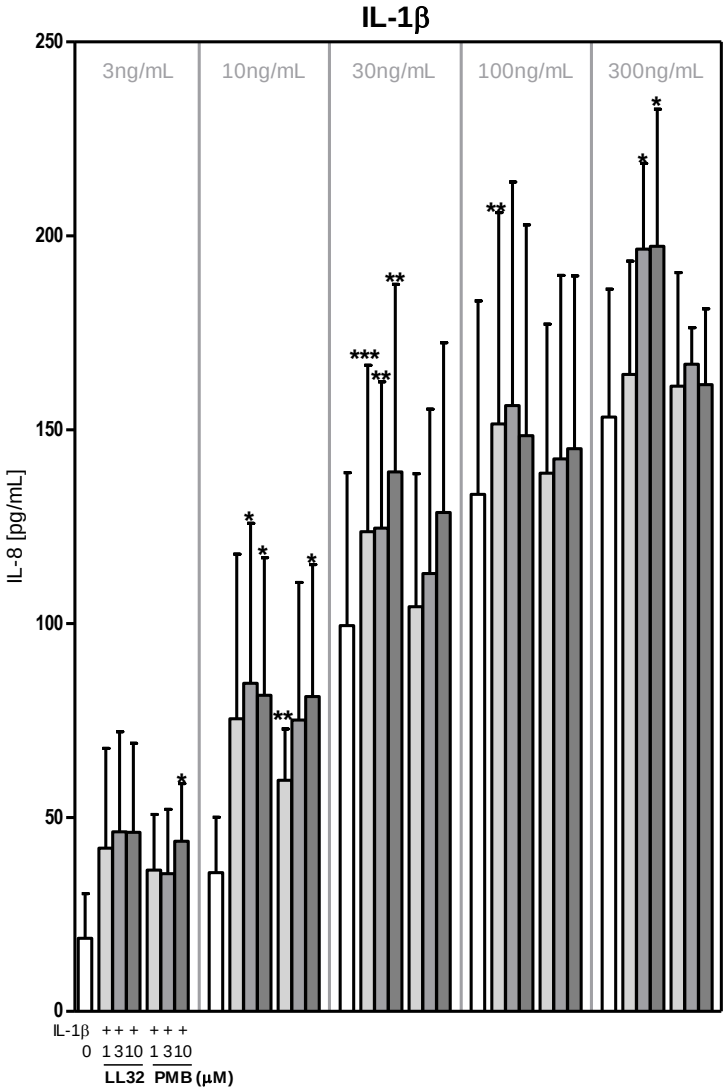

Figure 92 | Effect of LL-32 and PMB on the cytokine release induced by IL-1β stimulation of HEK293-TLR4/MD2 cells. Cells were treated pursuant to the standard protocol for LPS-stimulation experiments where LPS was replaced by IL-1β. The cytokine was applied in final doses of 3, 10, 30, 100 and 300 ng/mL. Statistical analysis was performed in a two-tailed student's paired t-test (non-significant: ns ≥ 0.05; significant: * p ≤. 0.05; very significant: ** p ≤ 0.01; highly significant: *** p ≤ 0.001). Data are plotted as mean +SD of three (300 ng/mL) to seven independent experiments (n = 3-7).

TNF-α is known to induce the same effector actions when it comes to the study of septic shock as LPS. To prove the LPS-specificity of the immunomodulatory route HDPs take, HEK293-TLR4/MD2 cells were exposed to different doses of TNF-α ranging from 3 ng/mL to 100 ng/mL (Figure 93). TNF-α induced stimulation showed no to only weak decrease

of the IL-8 release for LL-32. PMB induced under the same conditions a concentration dependent and significant to very significant enhancement (10 μM) of the cytokine release that is lost at high doses of TNF-α.

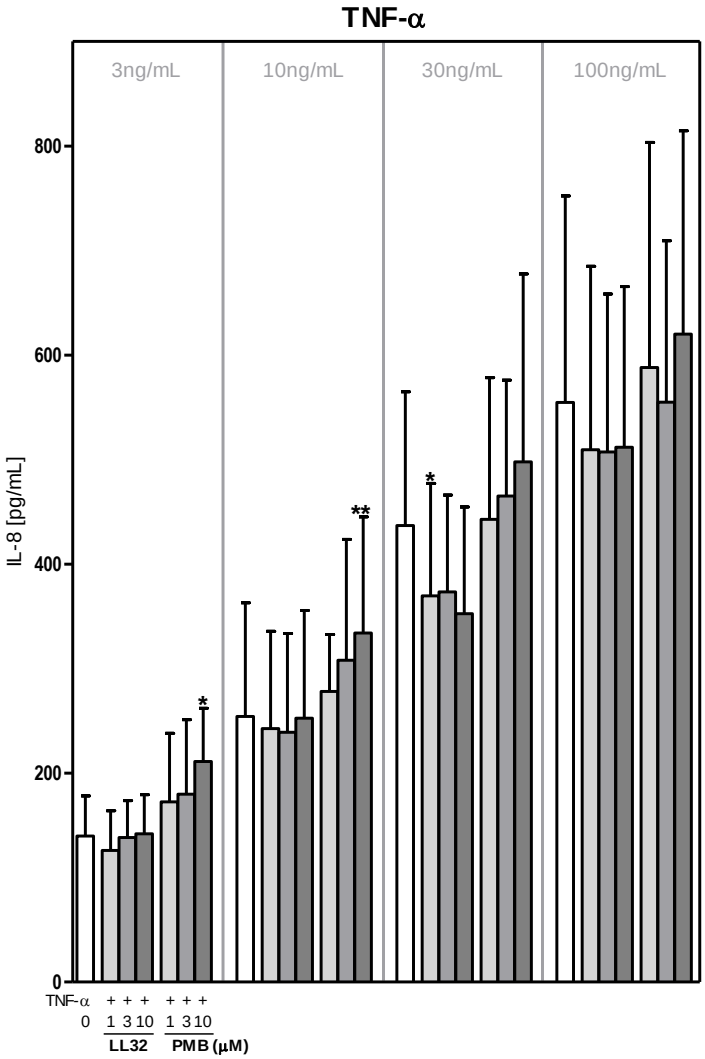

Figure 93 | Effect of LL-32 and PMB on the cytokine release induced by TNF-α stimulation of HEK293-TLR4/MD2 cells. Cells were treated pursuant to the standard protocol for LPS-stimulation experiments where LPS was replaced by TNF-α. The cytokine was applied in final doses of 3, 10, 30, and 100 ng/mL. Statistical analysis was performed in a two-tailed student's paired t-test (non-significant: ns ≥ 0.05; significant: * p ≤. 0.05; very significant: ** p ≤ 0.01). Data are plotted as mean +SD of four independent experiments (n = 4).

To gather more information about the specificity of the HDPs' mode of action, further experiments microbial and endogenous TLR4-ligands on CD14-transfected HEK293-TLR4/MD2 cells were performed (Figure 94). A

wide set of very diverse ligands were tested on transfected and non-transfected HEK293 cells. As ligands, despite the pathogen-associated molecular pattern (PAMP) LPS, the divalent transition metal cation Ni^{2+}, and the proteins MRP8, HMGB1 and Taxol were taken into account. The latter is a product of the evergreen tree *Taxus brevifolia* and is known to function as bacterial LPS mimetic on murine macrophages. BYRD-LEIFER *et al.* discovered by accident, that Taxol (also referred to as Paclitaxel) induces a down-regulation of type I TNF receptors on mouse macrophages in a manner indistinguishable from LPS[160]. Because nothing about the LPS mimetic potential of Taxol on human cells was known, this substance was considered as potential TLR4-ligand for this experimental series. The second candidate, is the DNA-binding protein HMGB1, a danger-associated molecular pattern (DAMP), that is already known to interact directly with the TLR4/MD2 complex in presence of CD14. K. TRACEY and his work group are able to express recombinant rat HMGB1 in *E. coli* and purify the protein without LPS contamination and maintain its biological activity[161]. Unfortunately, our request for an aliquot of HMGB1 was without success, thus the experiments were run out with a freely available testing aliquot where no guarantee of the biological activity was given.

Both substances, the anti-tumor agent Taxol and HMGB1 exhibited no cellular activity: Hence, the conclusion could be drawn, that Taxol expresses TLR4-ligand activity only on murine cells, whereas the testing aliquot HMGB1 exhibited no biological activity congenitally. Therefore, in figure 94 only the active TLR4-ligands LPS, Ni^{2+} and MRP8 are depicted.

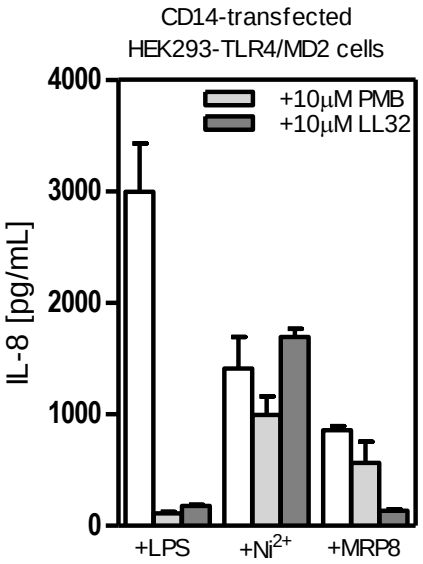

Figure 94 | HEK293-TLR4/MD2 cells with transient transfected CD14. As endogenous TLR4-ligands Ni^{2+} and MRP8 were tested together with LPS by default. Data are plotted as mean +SD of two independent experiments (n = 2).

The LPS-induced cytokine release on CD14 positive cells follows the same trend as described before. The IL-8 release induced by the endogenous TLR4-ligand Ni^{2+} is neither affected by PMB nor by LL-32, whereas MRP8-induced cytokine release is strongly diminished by LL-32 but not affected by PMB.

4.2.2 Staining of the TLR4/MD2 receptor complex

Staining of the TLR4/MD2 receptor complex on HEK293 cells was performed to complement the findings from fluorescent dye distribution analysis on model membranes (*q.v. section 4.1.7, page 153*): These experiments allowed to collect information about the distribution of peptides and TLR4 receptors on the membrane surface. For PMB a fast internalization was observed. Even under short incubation times (3 min) during the different staining and fixation steps and in presence of an endocytosis blocker (data not shown) it was not possible to protect the lipopeptide from uptake. PMB induced an increased formation of intracellular vesicles (detail image (A); Figure 95). Cells with high amounts of intracellular vesicles seem to remain low levels of TLR4-receptors,

whereas cells with no to little degree of vesiculation induced by PMB showed normal levels of stained TLR4 on their membrane surface.

Different from PMB, LL-32 is detected in defined spots on the membrane surface in proximity to TLR4 without any obvious changes on the membrane and intracellular level (detail image (B); Figure 95). Another member of the family of HDPs is a modified version of the human β-defensin-3 (hBD-3). This peptide, showed again another version of membrane surface interaction: hBD-3-l was found to be intracellularly distributed in a diffuse manner with local clusters at the nuclear membrane (detail image (C); Figure 95).

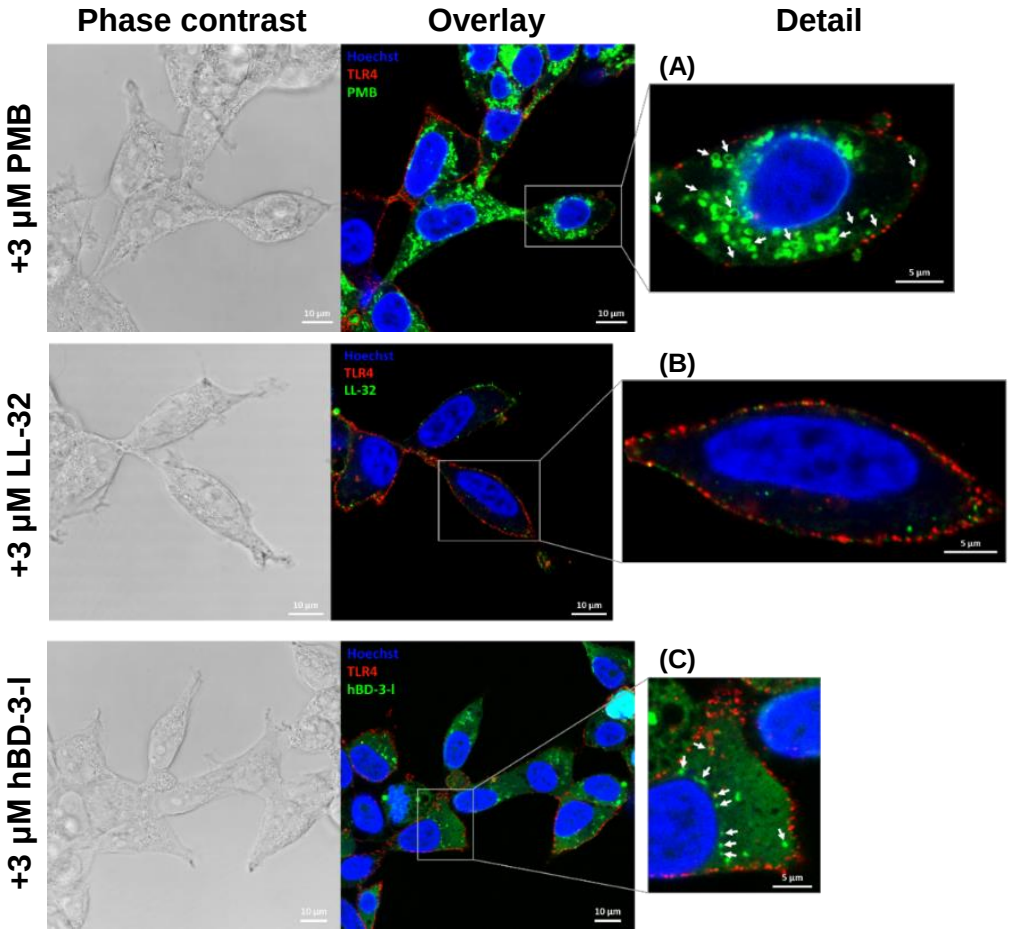

Figure 95 | Staining of the TLR4/MD2 receptor complex on HEK293 cells. The nucleus was stained with Hoechst (blue), TLR4/MD2 was stained with the antibody HTA125 conjugated to Alexa647 (red), PMB was labeled to size restriction with BODIPY, and LL-32 and hBD-3-l were labeled with Atto488 (green). The images show for each compound a representative image series containing phase contrast, overlay of the single fluorescence channels, and a detail image with highlighted conspicuous features (from left to right). All staining series were incubated with 3 µM peptide. White arrows depict abnormalities found for the respective compound.

For a more detailed analysis, the single channel images of TLR4- and peptide-fluorescence were evaluated along a region of interest (ROI) and the distribution of the two fluorophores was plotted for detecting potential areas of co-localization. Due to the rapid uptake of PMB, only low fluorescence intensity of the peptide remained on the membrane margin. In all staining experiments, HEK293 cells were not stimulated with LPS, therefore the TLR4 receptor is present in its monomeric form and is located within the liquid-disordered phases, whereas PMB was shown to be more prone for cholesterol enriched membrane regions as interaction site. The results obtained from model membranes match the results from stained native cells showing no significant levels of co-localization between the TLR4 receptor complex and the peptide antibiotic PMB (Figure 96).

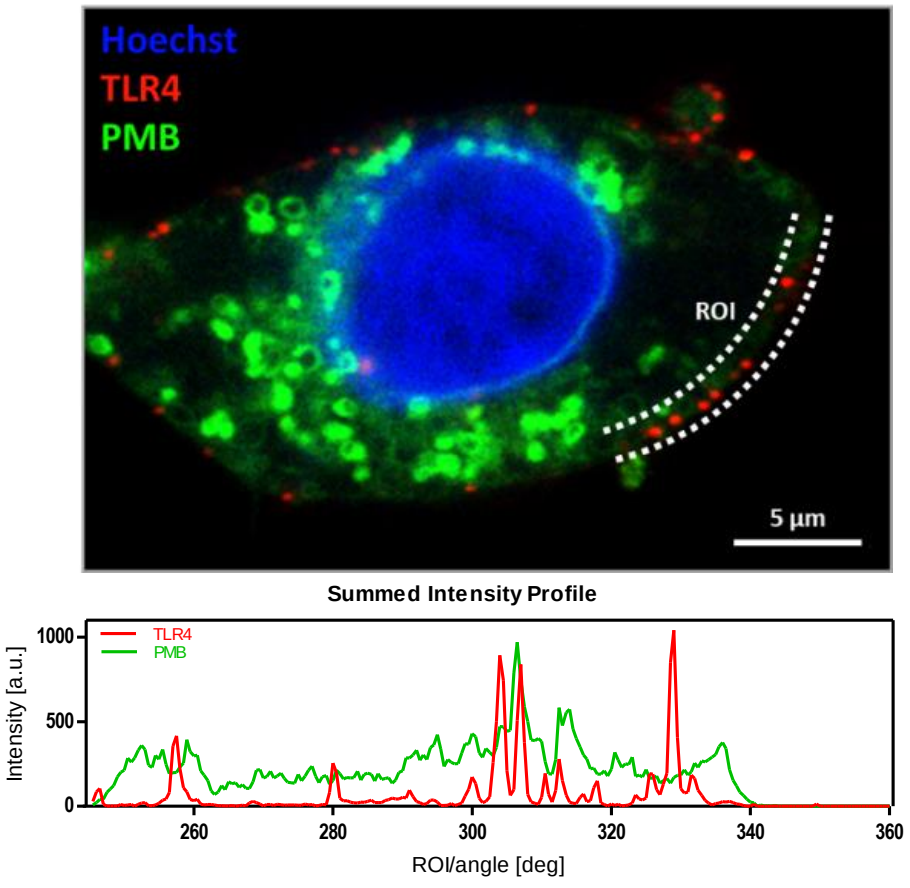

Figure 96 | Fluorescent dye distribution analysis (FDDA) of the detail image of TLR4/MD2 stained HEK293 cells incubated with 3 µM PMB. Dashed lines depict the angular sector of the evaluated ROI. Fluorescence intensity profile was given by counterclockwise data read-out. Scale bar measures 5 µm.

On immobilized GUVs, LL-32 was detected to interact prevalently with the cholesterol-poor areas of the membrane. Thereupon, it was expected to detect the peptide co-localized with TLR4. Both compounds are supposed to be located within the same lipid phase (liquid-disordered) when HEK293-TLR4/MD2 cells are unstimulated; interestingly, LL-32 was found to be in close spatial proximity to TLR4 when not co-localized with the receptor. Therefrom, for LL-32 sequential co-localization, as seen in the angular region between 140° and 200° (Figure 97; depicted by grey arrows), in stained HEK293 cells was detected.

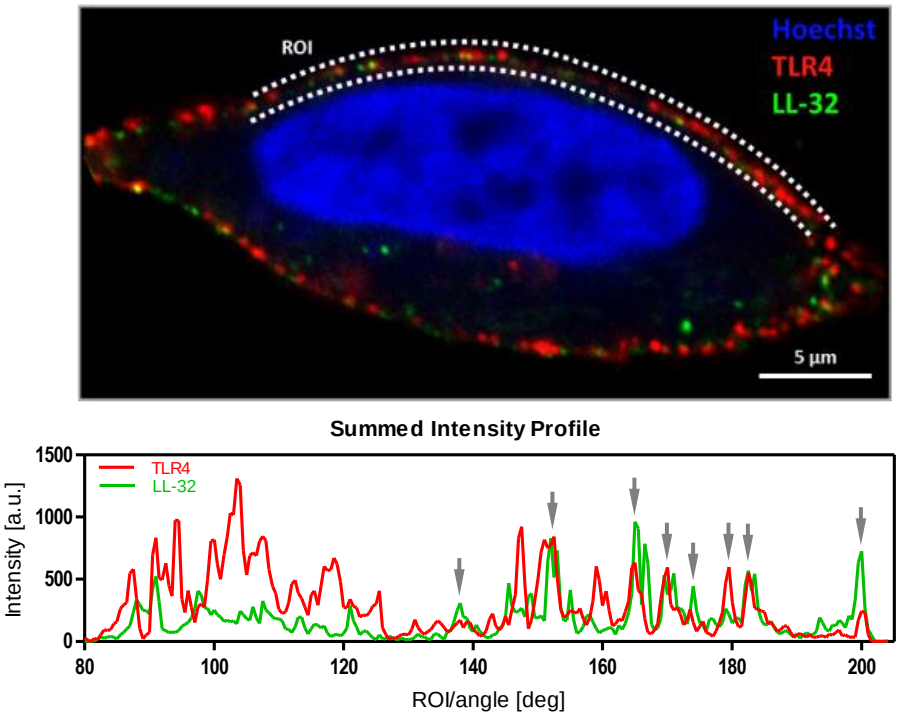

Figure 97 | Fluorescent dye distribution analysis (FDDA) of the detail image of TLR4/MD2 stained HEK293 cells incubated with 3 µM LL-32. Dashed lines depict the angular sector of the evaluated ROI. Fluorescence intensity profile was given by counterclockwise data read-out. For convenient visualization, the picture was rotated 90° counter clockwise. Scale bar measures 5 µm. Regions of co-localization are indicated by the grey arrows in the intensity profile.

In contrast to this knowledge, hBD-3-l is spread all over the cell: The confocal laser scanning microscopy images show a diffuse distribution of the fluorophore conjugated to the peptide (Figure 98). This peptide, is taken up into the intracellular space, where it was found to cluster and potentially

interact with the nuclear membrane or associate within the perinuclear space (Figure 95; *q.v. section 4.2.2, page 205*).

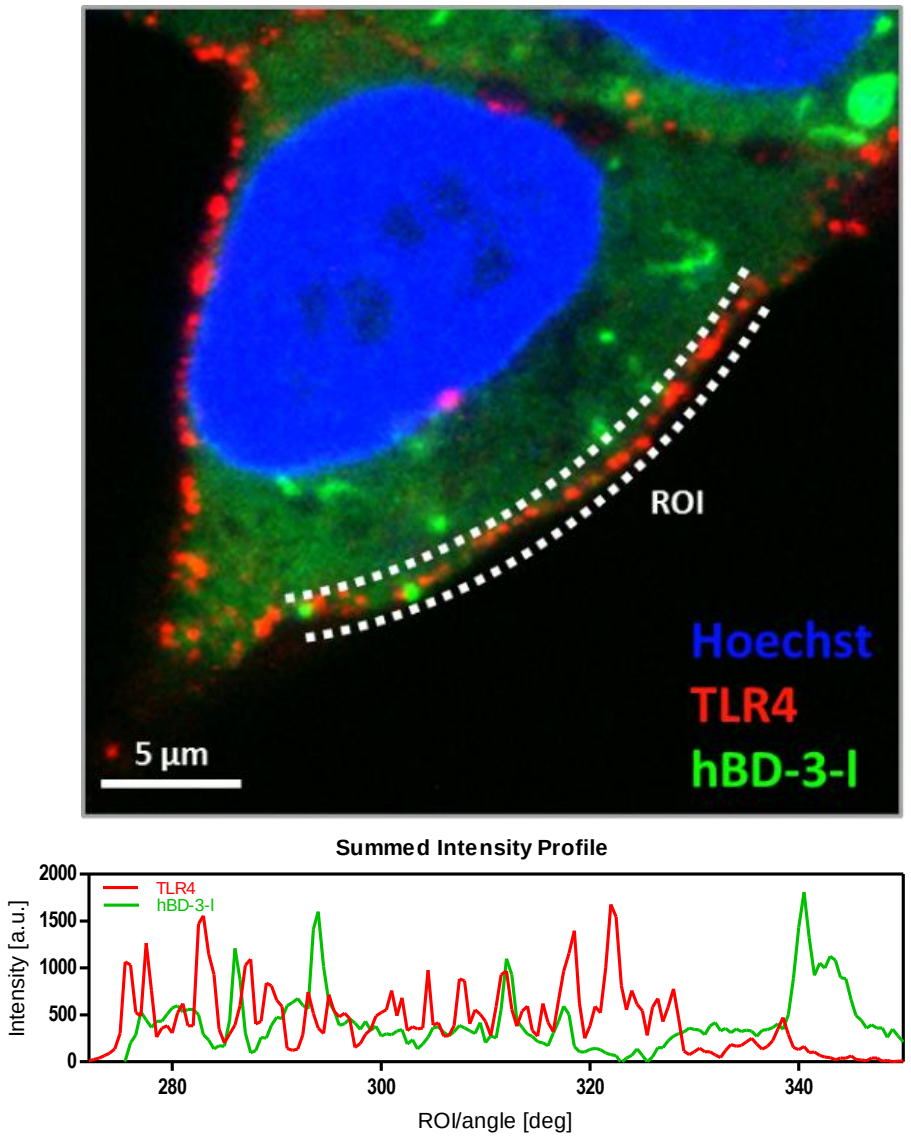

Figure 98 | Fluorescence dye distribution analysis (FDDA) of the detail image of TLR4/MD2 stained HEK293 cells incubated with 3 µM hBD-3-l. Dashed lines depict the angular sector of the evaluated ROI. Fluorescence intensity profile was given by counterclockwise data read-out. For significant analysis, a different detail of figure 63 was taken. Scale bar measures 5 µm.

5. DISCUSSION

The increasing number of resistant pathogens eagerly demand the development of alternative agents with an analogue functional spectrum as the common prescribed antibiotics. To implement host defense peptides as new therapeutic substances, it is necessary to understand their modes of action, points of interference, and their targets in detail. This family of multi-functional peptides exhibit a dual fundamental biological role in vivo: They protect the host from colonization of pathogenic microorganisms either by direct killing of the pathogen or by inhibition of the (bacterial) pathogenic factors. The basic concept is, to understand and combine both strategies, killing of the hostile microorganisms and neutralization of the pathogenic factors, in one molecule laying the foundation for the design of new therapeutic agents and overcome antibiotic resistance. Thus, to approach these two strategies, the research work, this thesis is based on, put membrane permeabilization and the neutralization of the bacterial endotoxin LPS in the forefront.

The antibiotic lipopeptide polymyxin B as last resort treatment and the antimicrobial α-helical peptide LL-32 were investigated in each step of inflammation and the corresponding signaling cascade. With the help of stimulation experiments, membrane permeabilization assays and microscopic analysis together with a wide field of scattering experiments, differences within the mode of action of these two compounds were identified. Further, it was possible to demonstrate that both substances exhibit the same immune regulatory effect, but functions over different target structures in the immune cells and therefore expose different points of interference on the membrane level. As a result of these studies, a detailed mechanism how LL-32 and PMB participate in the inhibition of the LPS-induced immune response was proposed and could be confirmed. Both, LL-32 and PMB protect the host by eliminating pathogenic microorganisms via a primary and a secondary mode of action. Most of the research dealing with LPS-induced inflammation and the regulation of the inflammatory response focus on the protein level. In the present thesis, light is casted on the

membrane level, revealing that it is not a single protein or receptor complex responsible for maintenance of host defense but rather the membrane and more specifically the components and compositions of the same. Therefore, a five-step working model was developed (*q.v. section 2, page 55*), wherein membrane- and receptor-mediated pathways were taken into account.

5.1 Host Defense Mechanisms of LL-32 and PMB

5.1.1 Membrane-mediated Interaction

The HDP LL-32 and the lipopeptide PMB only share the characteristic, that these two cationic compounds primary function over a membrane-mediated pathway. But their membrane associated mode of action takes contrary routes.

5.1.1.1 Peptide Interaction with the L_D-Domain of the Host Cell Membrane

To reveal how antimicrobial peptides are involved in the process of anti-inflammatory regulation, model systems mimicking the membrane of immune cells together with native immune cells were studied. For AMPs, it is known, that they exhibit high antimicrobial activity by interaction with the bacterial cell envelope. Several mechanisms for permeabilization of the lipid bilayer have been described during the last decades[11a, 15, 162]. The interaction routes described for (Gram-negative) bacterial membranes were supposed to cast light on the modes of action AMPs might follow on the host cell membrane level as well. In the first instance, intercalation and membrane permeabilization experiments were performed to verify the membrane activity of LL-32. From the intercalation experiments, it could be demonstrated that the peptide reduces the FRET-signal by increasing the diameter of the model membrane pushing the incorporated FRET-pair apart. Other model membrane systems, such as pore-spanning membranes,

tethered membranes, KI quenching assay revealed that LL-32 induces pores in the model immune cell system, leading to destabilization of the membrane and ultimately to its disintegration. These results showed the classical proposed functions of cationic host defense peptides. To differentiate, if the immune regulatory and modulatory function is traced back to the membrane activity of the peptide, different sets of stimulation series of a native immune cell system were developed. Stimulation of HEK293-TLR4/MD2 cells with IL-1β were performed to exclude any interactions of LL-32 from the cytoplasmic site of the host cell: The cytokine IL-1β herein activates the IL-1R receptor complex, both inflammatory signaling complexes, TLR4/MD2 and IL-1R, feature the same cytoplasmic TIR domain and induce the same downstreaming signaling cascade (Figure 99). In case LL-32 leads to a decrease in cytokine release (IL-8) through receptor inactivation by interaction with the cytoplasmic TIR domains of the two expressed receptor complexes, IL-1β induced stimulation is supposed to yield analogous results as LPS-induced stimulation via TLR4. The human cathelicidin fragment LL-32, however, exposed no immune regulatory effect by decreasing the IL-8 release via IL-1R in this experimental approach. From these results the conclusion can be drawn, that in this specific model the peptide LL-32 is put out of intracellular membrane associated targets.

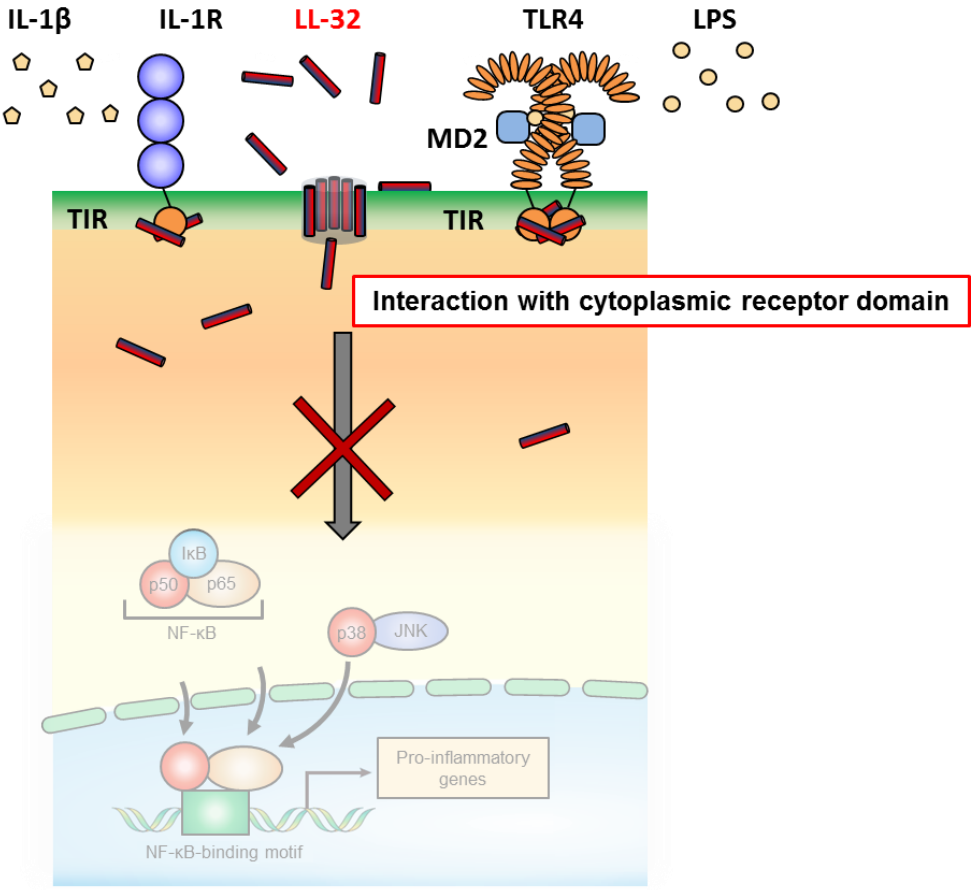

Figure 99 | Rejected mechanism for the host defense mechanism of LL-32 by interaction with the cytoplasmic TIR domains of the receptors IL-1R or TLR4. IL-1β-induced stimulation experiments on HEK293-TLR4/MD2 cells showed no decrease in cytokine release in presence of LL-32. The cytoplasmic TIR domains are not within the target spectrum of LL-32. This gave evidence for the rejection of the proposed mode of action.

On the model system, X-ray studies (*q.v. section 4.1.10, page 171*) and microscopy of immobilized GUVs (*q.v. section 4.1.7, page 153*) were used for elucidating the role of the α-helical peptide on the membrane. The analysis of membrane stacks composed of DOPC/SM/Chol in a lipid ratio of 9:9:2, showed that with increasing temperature the characteristic reflectivity pattern for cholesterol-containing membrane multilayers does not disappear and a two-phase state is still present (data not shown). These first findings allowed the assumption, that the antimicrobial peptide LL-32 exhibits a stabilizing function of the cholesterol-enriched membrane regions under inflammatory conditions (40 °C). This hypothesis could be confirmed after repeating the experimental approach on the same membrane system with the varied lipid ratio of 2:2:1 facilitating the detection of defined membrane domains over the set temperature range: Whereas the pure ternary mixture and in presence of PMB allowed a melting of the two domains at 40 °C, LL-32 stabilizes the domains and inhibits melting under the same conditions (Figure 100).

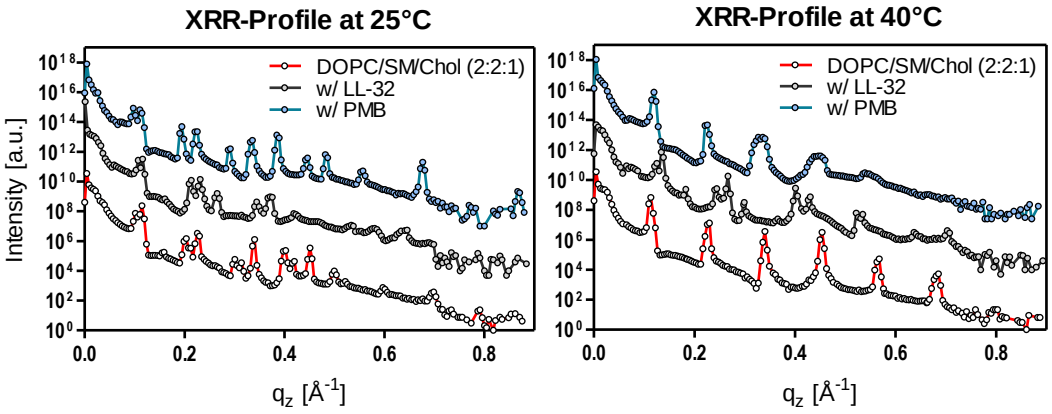

Figure 100 | The AMP LL-32 functions as stabilizer for cholesterol-rich microdomains. XRR-profile of the ternary lipid mixture DOPC/SM/Chol (2:2:1) alone and in presence of the AMP LL-32 and the lipopeptide PMB at 25 °C and 40 °C. At 25 °C all XRR-profiles indicate a two-phase state. At 40 °C, only for the sample w/ LL-32 the two coexisting domains remain stable. Color code indicates the following: Red – pure lipid mix; grey – w/ LL-32; light blue – w/ PMB. Peptides were applied in volumetric ratios of 4:1. For the sake of clear arrangement, data sets w/ LL-32 were shifted by a factor of 10^4 and w/ PMB by a factor of 10^7.

Together with the calculated corresponding electron density distribution, it was possible to confirm among the raft-stabilizing function a cholesterol-condensing activity. This feature is derived from the dramatic

membrane thickening effect from 116.2 Å ±6.1 Å at 25 °C to 103.5 Å ±1.5 Å at 40 °C and the massive structural changes seen in AFM images (*q.v. section 4.1.10, page 171*). These results put together allows the postulation of a new model for membrane-peptide interaction via a "table-cloth mechanism" factoring the cholesterol-condensing and raft-stabilizing function by interaction with the liquid-disordered domain into this proposed mode of action (Figure 101).

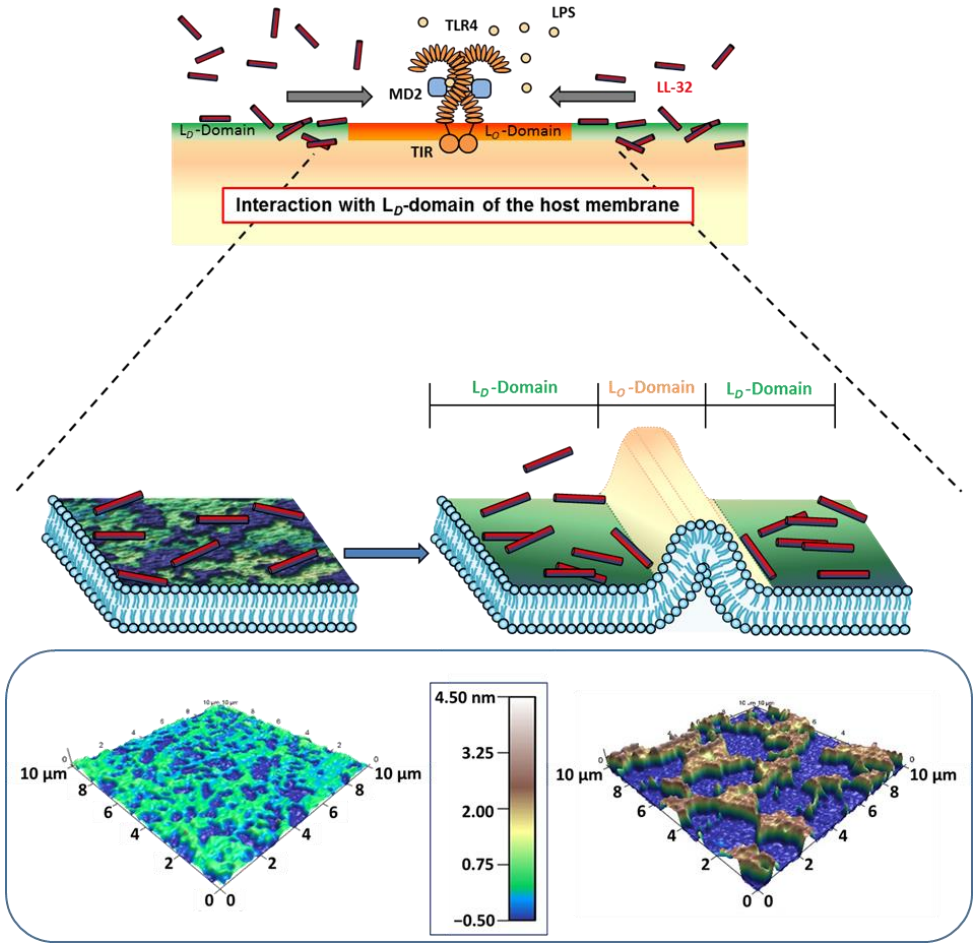

Figure 101 | Postulated *table-cloth mechanism* for the interaction of LL-32 with cholesterol-rich membranes in juxtaposition with the AFM images from *section 4.1.10*. This mode of action for membrane-peptide interaction factors cholesterol-condensing and stabilizing functions by interaction prevalently via the liquid-disordered membrane regions. No increase in membrane order could be observed and is disregarded by this proposed model.

To further analyze in which phase LL-32 is located in, confocal laser scanning microscopy (CLSM) of fluorescently labeled GUVs was

performed. For long-term microscopy (t ≥ 60 min) a protocol for the immobilization of GUVs was successfully established. With the help of immobilized GUVs, it was possible to characterize the distribution of the peptide within the membrane compound: The α-helical peptide is prevalently found in the liquid-disordered (L_D) or cholesterol-poor areas of the membrane. MATSUZAKI *et al.* showed that human erythrocytes were protected from attack by magainin-2[163] and that the binding affinity of AMPs and therewith their membrane permeabilizing activity is suppressed on membranes incorporating cholesterol[164]. The linked induction of increased mechanical stiffness of the membrane yield in AMP malfunction by preventing membrane bending required for permeabilization and pore formation processes.

Upon stimulating HEK293-TLR4/MD2 cells with LPS in the native membrane system, the TLR4-receptor complex is formed by recruiting of L_D-located TLR-monomers to the cholesterol-containing L_O-domain, building its functional dimeric unit. Fluorescence staining of the monomeric TLR4/MD2 receptor complex on unstimulated HEK293 cells together with a fluorescently-labeled variant of LL-32 and the information obtained from the model membrane studies, lead to the expectation, that LL-32 is co-localized with the receptor complex. Interestingly, the peptide LL-32 was found to be membrane associated and was detected in close proximity to the stained TLR4-receptor complex with areas of full co-localization (*q.v. Figure 97; section 4.2.2, page 207*) fulfilling the basic approach only partially.

This leads to the assumption, that LL-32 primary interacts with the cholesterol-poor regions of the host cell membrane, which in turn results in a stabilization and condensing of the cholesterol-enriched areas, claiming a further increase in membrane rigidity in these specific domains. TLR4-signaling is blocked due to receptor inactivation by progressive rigidization of the L_O-domain (Figure 102). The receptor is lacking sufficient flexibility to undergo conformational changes which resembles the final activation step of the inflammatory signaling cascade.

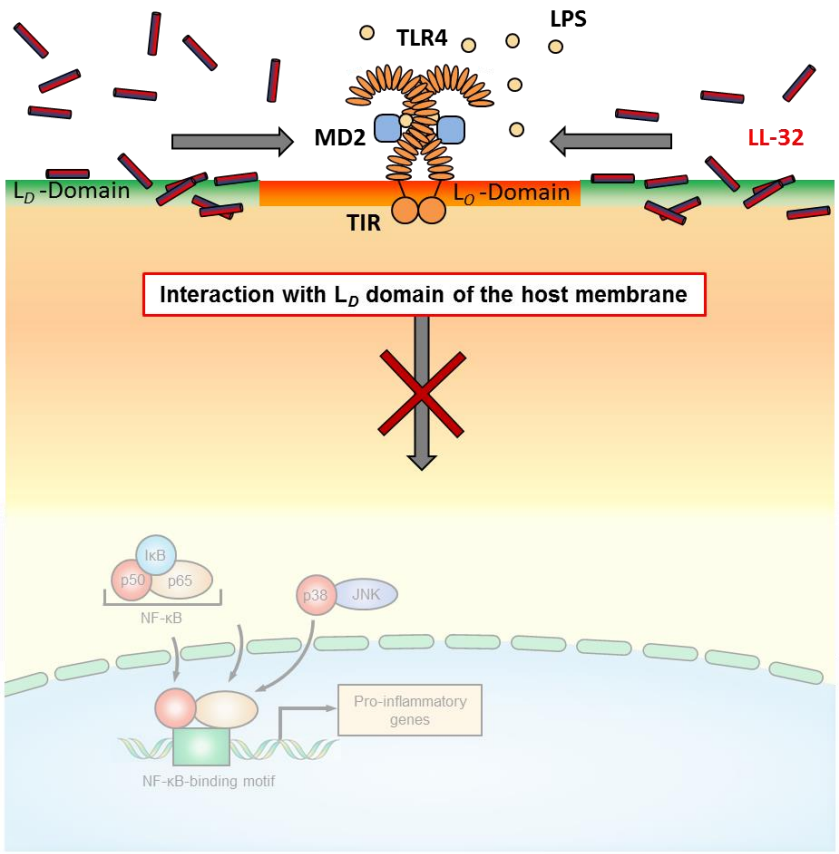

Figure 102 | Primary host defense mechanism of the antimicrobial peptide LL-32. The peptide interacts favorably with the liquid-disordered part of the host cell membrane. Intercalation into the membrane results in a condensing and stabilization of the cholesterol microdomains where the signaling receptor complex is located in. Together with an increase in rigidization, the receptor complex is not able to undergo conformational changes and transduce the inflammatory signal.

Combining the results collected on the cellular system and the data obtained from permeabilization experiments, that resemble the antibacterial killing strategy of the multi-functional peptide family (*which is discussed in more detail in the upcoming section 5.1.2 starting on page 223*), leads to the conclusion that only in case of severe inflammation, the local peptide concentration at the site of infection is increased to a degree where destructive pore formation, membrane disintegration, and as last resort apoptosis is induced by this AMP.

5.1.1.2 Peptide Interaction with Lo-Domain of the Host Cell Membrane

The lipopeptide PMB uses a different mechanism to protect the host from invading pathogens. In 1956, NEWTON performed a study on the mode of action of the polymyxins and their effect on cell permeability[165] on different bacterial strains. Since then, it was already known, that aqueous polymyxin solutions exhibit remarkable surface activity and that the polymyxin family share similarities with cationic detergents[165]. Thereby, NEWTON incubated *P. aeruginosa* cells with *N*-tolyl-α-naphthylamine-8-sulphonic acid (TNS), a dye that starts to fluoresce upon interaction with negatively charged protein groups at 436 nm, demonstrating an altered cell permeability induced by polymyxin[165]. Adding polymyxin to the cell suspension enabled the uptake of the dye to the protein-containing cell fractions[165]. This pioneer work indicated insistently the irreversible breakdown of the permeability barriers associated with the bactericidal action of polymyxins[166]. Further, NEWTON was able to show that the class of peptide antibiotics interact directly with bacterial cell surface components, including phospholipids[166]. Combining these early findings together with the structure and size of PMB, that allows this lipopeptide to easily mimic lipids and integrate in the membrane bilayer, led to the model developed by HANCOCK and CHAPPLE in 1999 (Figure 103)[14]. Under physiological conditions, PMB exhibits an overall cationic surface charge, which promotes membrane insertion and the disruption of the bacterial cell envelope.

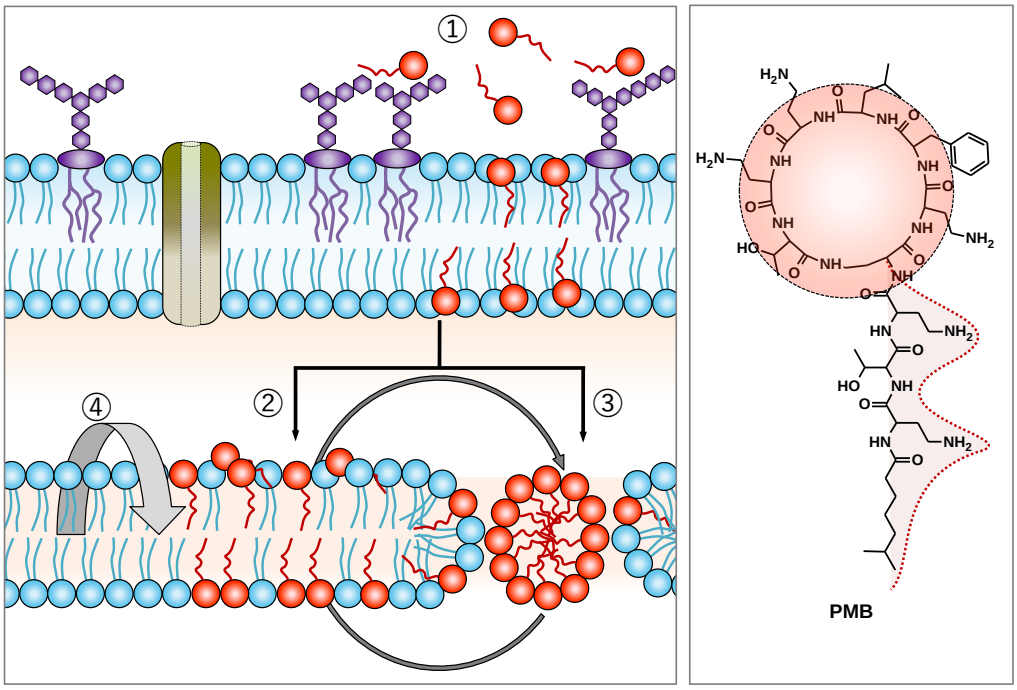

Figure 103 | Model for the uptake of cationic peptide antibiotics (e.g. Polymyxin B) in Gram-negative bacteria (adapted)[14]. (a) ① Peptide monomers in solution (red); in the initial step, the peptide can either interact directly with the negative surface charges on the membrane or bind to the cationic binding sites on LPS. ② After crossing the outer membrane, peptide monomers are located within the peptidoglycan layer where they bind to the negative charges on the inner membrane surface or ③ oligomerize and facilitate micellization and transient pore formation. ④ The peptide scaffold and size allows flip-flopping across the membrane, where the peptide then can dissociate from the membrane and is released into the cytoplasm. (b) Chemical structure of PMB with highlighted head and tail region.

For this lipid-like compound, experimental studies of black lipid membranes of varying phospholipid compositions exhibiting different surface charges by MILLER, BACH and TEUBER revealed that PMB destabilizes the membrane but remained penetration-resistant[167]. WIESE *et al.* have proposed a detergent-like mechanism for the interaction with bacterial outer membranes[168]. They performed planar lipid bilayer experiments in accordance with the MONTAL-MUELLER technique on asymmetric LPS-containing membranes and detected lesions within a size range (Ø = 2.4 nm ±8%) capable for self-promoted uptake[168]. Other bacteria genera, such as *mycobacteria*, *Helicobacter pylori*, and *chlamydiae* are known to target cholesterol-rich domains by either featuring a cholesterol-binding site[169], associating directly with lipid rafts[170], or inducing local

cholesterol-accumulations[31a]. Bearing in mind, that PMB belongs to a substance class of peptide antibiotics extracted from the Gram-positive bacterial strain *Paenibacillus polymyxa*, it is not that remarkable that the peptide is found to co-localize with the liquid-ordered membrane regions.

In the host cell, as recently mentioned, the peptide antibiotic prefers the liquid-ordered (L_o) domains or cholesterol-rich microdomains as target. The peptide intercalates into these distinct areas and induces more flexibility in the rigid domains. X-ray reflectivity studies revealed, that PMB exhibits no stabilizing effect on cholesterol-rich membrane regions under inflammatory conditions (40 °C) compared to LL-32, where the characteristic peak pattern is still present (*q.v. section 4.1.10, page 171 et seqq.*). These findings, substantiate the suspicion, that PMB functions over a different mediated host defense pathway: The lipopeptide can insert into the host membrane where the compound is preferentially located at the higher ordered and cholesterol-rich site of the membrane, as it is detected on immobilized GUVs (*q.v. section 4.1.7, page 153 et seqq.*) following an analogue mechanism confirmed for the insertion into Gram-negative bacteria. Piecing all of these aspects together, lead to the proposed model as depicted in figure 104.

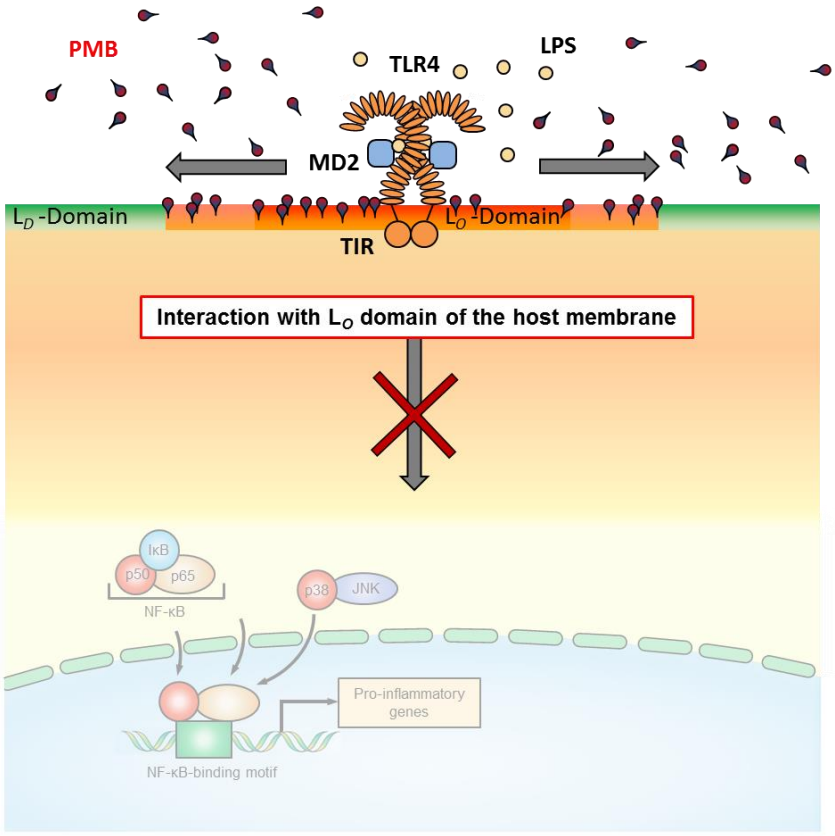

Figure 104 | Membrane-mediated host defense mechanism by interaction of PMB with liquid-ordered membrane domains. PMB interacts prevalently with the cholesterol-enriched regions introducing higher flexibility in these stiff areas. This results in an enlargement of the cholesterol-rich domains and further PMB-insertion (depicted by the outward pointing arrows).

These results appear reasonable, when the scaffold of the bacterial cell envelope is taken into account – herein no cholesterol is present; in the bacterial cell membrane the sterol is replaced by hopanoids[171] leading to an increased membrane stiffness and therefore a higher degree in lipid-ordering together with a high amount of LPS molecules. Hopanoids comprise a substance class of natural occurring pentacyclic compounds that are structurally related to hopane, one of the basic skeletons of pentacyclic triterpenes (Figure 105). This leads to the assumption, that PMB requires a certain degree of rigidity in the membrane for intercalation. This sterol analogue is said to have modulatory properties on the plasma membrane, such as fluidity and formation of liquid-ordered domains[172]. Apart from that, hopanoids influence the membrane permeability, rigidity as well as

significant features in bacteria, compatible to the function of cholesterol in eukaryotes[172].

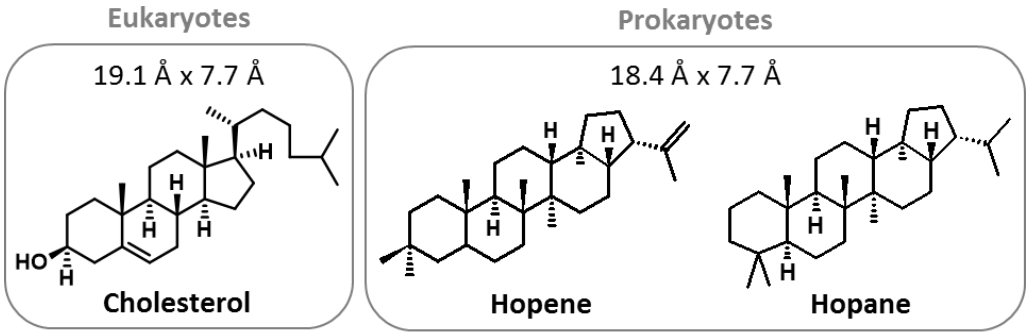

Figure 105 | Structural chemical formula and dimensions of the eukaryotic sterol cholesterol and the bacterial analogue hopanoid and its structural relative hopane. Hopanoids comprise the sterol membrane building block in certain bacterial membranes comparable to cholesterol in eukaryotic plasma membranes. The strong structural and dimensional similarity gives hopanoids compatible properties as cholesterol.

By addition reaction of water to the alkene hopene, that is also known as diploptene, the hydroxyl-substituted cholesterol-like compound diplopterol can be obtained. K. SIMONS *et al.* showed that diplopterol and cholesterol both interact with sphingomyelin and promote phase separation, forming a liquid-ordered and liquid-disordered phase in giant vesicles at 22 °C[172]. Considering the scaffold of the bacterial cell envelope, *lipid A* is the major component of the extracellular leaflet of the bilayer and features structural conformities with sphingomyelin in eukaryotes, thereunder amide-linked saturated acyl chains and hydroxylations[172-173]. Taking these parallels into account, diplopterol is suspected to interact with *lipid A*-containing membranes in an analogue manner as cholesterol and sphingomyelin do in the host cell membrane. Recent publications showed, that *lipid A* undergoes a pH-dependent change in order[174]: Increasing acidification decreases the fluidity of the outer leaflet, approaching a gel state. Hence, it can be concluded that the integrity and biochemical functionality of the bacterial outer membrane is massively affected by extreme pH-values and therewith modulations in the ordering of *lipid A*. K. BRANDENBURG and U. SEYDEL showed by FT-IR phase-transition studies, that both cholesterol and diplopterol exhibit a condensing effect not only on

sphingomyelin but also on KDO-lipid A[174]. Piecing these findings together, demonstrate that diplopterol and cholesterol exhibit a *lipid A* condensing effect by simultaneous inhibition of gel phase formation, thus attenuating the effects of low pH on *lipid A*[172].

Furthermore, long-term microscopy studies of semi-immobilized GUVs (*q.v. section 4.1.8, page 157*) showed, that PMB induces membrane fusion wherein the cholesterol-rich domains play a major role. In the initial step, PMB binds to the cholesterol-rich membrane areas, sensing other membrane-bound monomers increasing the local peptide concentration. The destabilized membrane starts to collapse at the peptide- and cholesterol-low areas, dividing into smaller vesicular structures. This phenomenon can be adapted to the host cell system. TLR4-staining of fixed HEK293-TLR4/MD2 cells showed high amount of intracellular peptide bound to vesicular structures, whereas control cells showed no dramatic vesiculation to the cytoplasm of the cell. This knowledge allows the proposal of the membrane-mediated host defense mechanism as follows (Figure 106):

PMB binds to the host cell membrane at the cholesterol-rich regions. It intercalates into the membrane with introducing higher flexibility to the L_o-domains. This is the prerequisite for peptide-aggregation in the membrane-bound state, resulting in an increase in membrane surface and tension. To overcome this cell stress, distinct membrane regions are constricted in a *caveolae*-like manner and taken up into the cytoplasm by *caveolae*/raft-dependent endocytosis (Figure 106). PELKMANS and HELENIUS showed that this specialized form of lipid rafts found in the plasma membrane of highly differentiated mammalian cells, are used by certain viruses for entering the intracellular space[175]. VAN DUYL *et al.* investigated the role of tryptophan-cholesterol interactions in modulating the membrane curvature[176] and in a study by GRAU-CAMPISTANY *et al.* polymyxin B comprises the chemical scaffold for the synthesis of tryptophan-containing lipopeptide antibiotics[177]. As PMB comprises the amino acid phenylalanine in its chemical structure, technically speaking of a structural and modifiable precursor for tryptophan residues, it is not completely dismissed that this small lipopeptide itself is able to induce membrane curvature budding in *caveolae*-like structures at membrane regions where the local concentration

of PMB is enriched. On the cytoplasmic site, however, the peptide antibiotic can protect the host by e.g. inhibiting the synthesis of pro-inflammatory cytokines through the induction of an enhanced membrane curvature (Figure 106).

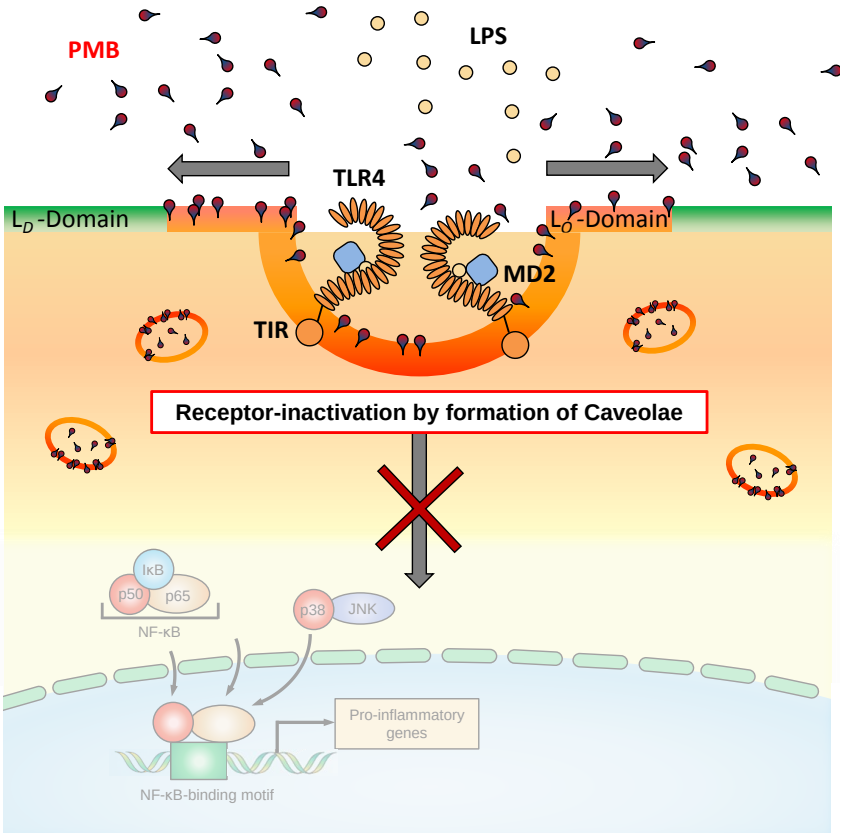

Figure 106 | Proposed model for *Caveolae* formation – a potential mode of action for inactivating the inflammatory signaling cascade via TLR4. PMB seems to induce higher flexibility in the cholesterol-enriched membrane regions, resulting in an enlargement of the liquid-ordered domains. At a certain threshold concentration, the cell stress is overcome by contracting vesicles or formation of *Caveolae*: PMB is either taken up to the cytoplasm and able to inhibit the expression of pro-inflammatory genes, or increasing membrane curvature unfavors the receptor homodimerization or the required conformational changes for signaling.

5.1.2 Membrane Permeabilization

The membrane-mediated interaction model for LL-32 and PMB as aforementioned is only one piece of a very complex mode of action these molecules have been taught by evolution. To gain a deeper insight of the

interaction on the membrane level, an extensive set of substances going beyond membrane-permeabilizing AMPs was chosen, covering among LL-32 the antimicrobials arenicin-1 and hBD-3-l together with the small ammonium ionophore nonactin and the large pore-former α-hemolysin. Only by understanding the mechanism behind membrane permeation, permeabilization and pore formation these molecules can be introduced as novel antimicrobial agents. A multitude of models have been described to date, some of phenomenological nature, others on a quantitative basis and again others of a semi-molecular approach[135]. All of the models for the interaction of AMPs on the membrane level known to date, have mainly one thing in common: Many aspects have been considered, but none of them capture the whole range of membrane-peptide interaction and therewith questions regarding membrane permeabilization and pore formation remain still unanswered[135]. By using a wide array of methods, it has been able to shed light on the dark how membrane permeabilization is affected by parameters such as membrane composition, membrane curvature, salt concentration and molecular weight. Combining liposome based assays and planar systems enables a precise decoding of peptide-induced membrane permeabilization: Liposomes with an entrapped fluorescent dye (calcein release assay; *q.v. section 4.1.1, page 131*) and liposomes with an incorporated lipid-dye conjugate (KI quenching assay, *q.v. section 4.1.2, page 134*) monitor pore formation with different orders of magnitude. Together with the planar systems, wherein analysis of single pores (free-standing membranes according to MONTAL & MUELLER; *q.v. section 4.1.5, page 147*), recording of membrane conductance (tethered membranes; *q.v. section 4.1.4, page 143*) and permeabilization kinetics by time-resolved dye release (pore-spanning membranes; *q.v. section 4.1.3, page 139*) could be investigated, allow a full overview and therewith the differentiation between transmembrane pore models and non-pore models as it was already announced in the early 90s with the development of the barrel stave and toroidal pore model and the carpet model as the most prominent non-pore model[178]. Among these classical modes of action, the discussion of molecular shape and lipid clustering and therewith new models came up almost 20 years later[179]. In these models, peptide-lipid interaction is taken into consideration as well as the ability of peptides to induce phase separation of lipids. In these models, boundary defects at the

interfaces form the seed for leakage. These new models fit the results obtained from permeabilization experiments and match the phenomena observed in XRR-experiments and immobilized GUVs. Piecing all aspects together, the conjecture can be made, that LL-32 interacts on pure DOPC lipid bilayers by the prominent carpet model, but on cholesterol-rich ternary membrane systems this AMP follows more the lipid clustering model. The latter is confirmed by the dramatic increase in membrane thickness and the cholesterol-condensing effect as it was detected by XRR measurements (*q.v. section 4.1.10, page 171*), whereas the former is substantiated by instant calcein release (Figure 43; *q.v. section 4.1.1, page 133*) and membrane permeabilization on tethered membranes (Figure 50; *q.v. section 4.1.4, page 145*). These findings were reinforced by the fast permeabilization kinetics detected by dye release on pore-spanning membranes (Figure 46; *q.v. section 4.1.3, page 140*) at concentrations already below 1 μM. The membrane activity of LL-32 is diminished when the experimental conditions are changed to higher concentrations of alkali ions. As counted to the same substance family, the AMPs arenicin-1 and hBD-3-l show related action: Both compounds exhibit lower affinity on pure DOPC membranes compared with the activity of LL-32. While arenicin-1 is only little affected by changes in salt concentration, hBD-3-l appears to be inactivated. The kinetics for membrane permeabilization follows the same trend on DOPC membranes, whereas on the bacterial membrane mimicry the ability of arenicin-1 for membrane permeabilization is changed significantly. In summary, it can be concluded that AMPs do not only exhibit a synergistic effect on lipid bilayers but they also work in concert: Bacterial infections and the triggered inflammatory response induce the expression of an orchestra of AMPs, that use the full spectrum of the current known modes of action that are controlled by the target membrane composition and the ambient conditions. This universalization of the mode of action meets most AMPs, but possible exceptions may exist – which is often the case.

5.1.3 RECEPTOR-MEDIATED INTERACTION

Host defense peptides, in specific LL-32, do not take a single route for helping the organism to fight bacterial infections. A decrease of pro-inflammatory cytokine release was found to be realized by two different pathways: a primary interfering on the membrane level and a secondary mechanism executed on the receptor level. The latter was identified by examining the ligand-functioning potential of LL-32 and therefrom a receptor-mediated interaction pathway is supposed to be the secondary mechanism of host defense in presence of CD14 (Figure 108). Both, LL-32 and PMB were tested for ligand functioning. The two substances were applied on CD14 transient transfected HEK293 cells together with known endogenous TLR4-ligands (e.g. Ni^{2+} and MRP8) and LPS. LL-32 and PMB are able to neutralize LPS-induced cytokine release, whereas for Ni^{2+} only PMB showed a decrease; for LL-32 an enhancement in cytokine release was observed. The third substance, MRP8 (also known as S100A8), belongs to the calcium-binding S100 protein family. Cytokine release induced by MRP8 cannot be inhibited by PMB but by LL-32. SCHMIDT *et al.* identified TLR4 as the nickel receptor and elucidated the nickel binding site[11b, 120]. This transition metal is capable of the activation of TLR4 homodimer formation, which is the prerequisite for signal transduction and the expression of pro-inflammatory genes (Figure 107). LPS and Ni^{2+} are known to induce hyperphosphorylation in the receptor domains[17]. This leads to the assumption that these two compounds feature similar binding sites at the TLR4/MD2-receptor complex, whereas MRP8 acts over a contrary interaction site, standing in competition with the antimicrobial compound LL-32.

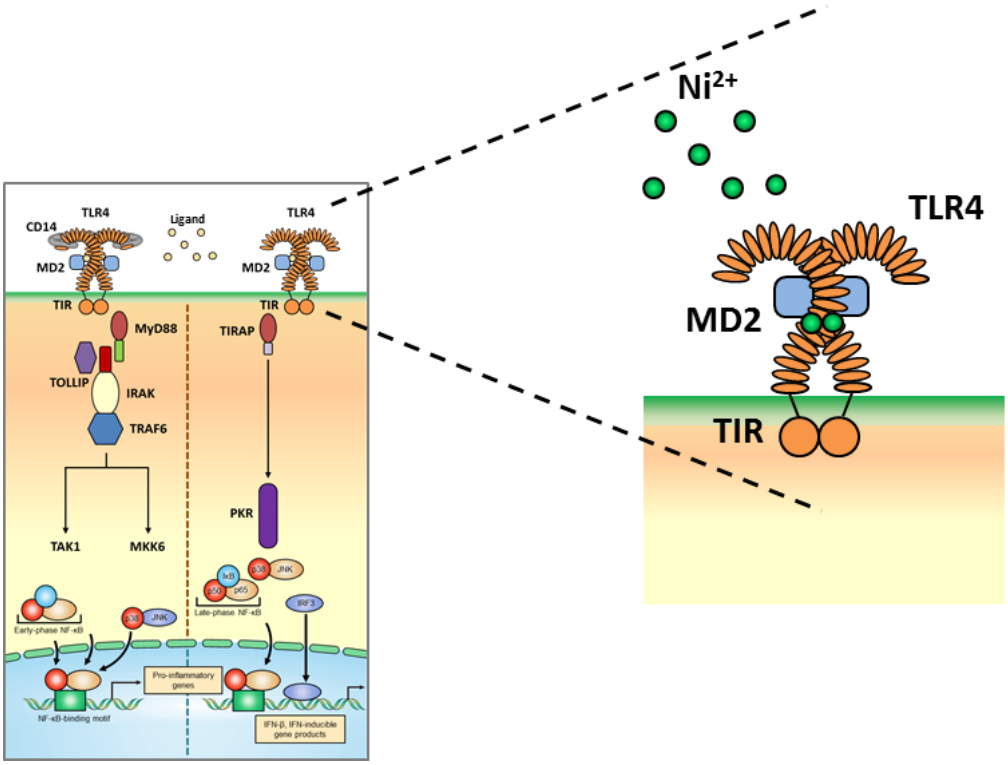

Figure 107 | Binding of Ni^{2+} ions to the TLR4 receptor complex. Nickel ions tend to function as TLR4-specific endogenous ligands compared to LPS. The transition metal ions bind directly to the TLR4 receptor complex, primarily at the histidine residues located at the dimerization face of the receptor. Binding of Ni^{2+} is sufficient for TLR4 activation in absence of LPS and induction of the inflammatory signaling cascade[17].

With the help of transient transfected HEK293/TLR4-MD2 cells and stimulation with physiological TLR4-ligands, it was possible to identify LL-32 as TLR4-specific ligand and to propose a secondary host defense mechanism (Figure 108): The data indicate that LL-32 functions as ligand for TLR4 and regulates immune cells by inhibiting the pro-inflammatory signaling cascade by direct binding to the ectodomains of the receptor.

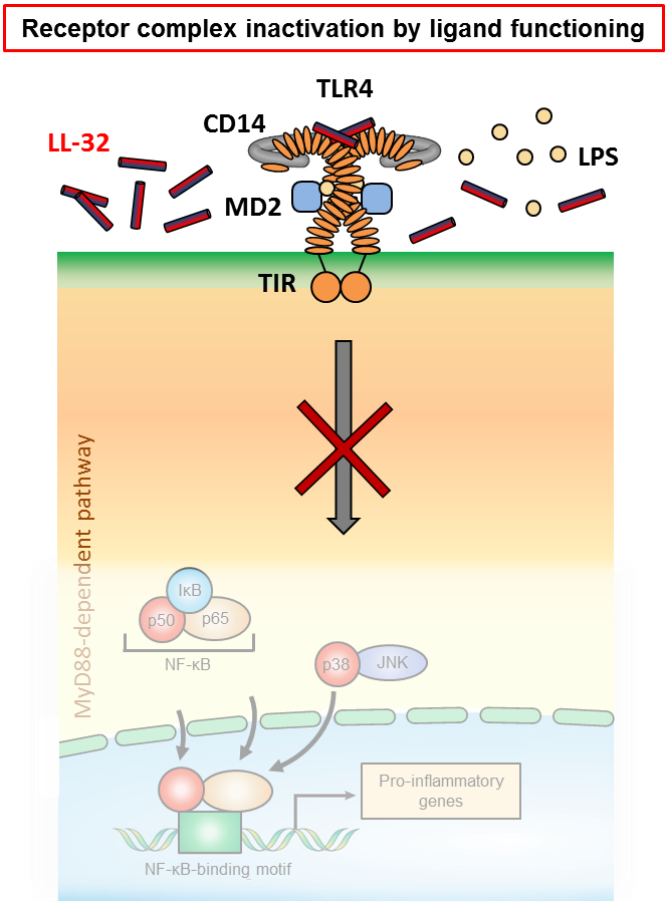

Figure 108 | Receptor-mediated pathway and secondary host defense mechanism of LL-32. HEK293-TLR4/MD2 cells were transient transfected with the TLR4 accessory protein MD2. Upon stimulation, the MyD88-dependent pathway is activated and leads to release of the inflammatory mediator IL-8. LL-32 inactivates the pro-inflammatory signaling complex by direct binding to the ectodomains of the receptor unit and thereby functions as specific TLR4-ligand. The signaling cascade is inhibited and the host is prevented from immune overresponse.

5.1.3 Direct Neutralization of LPS

To figure out to what extent LL-32 and PMB take direct interaction routes with LPS, HEK293-TLR4/MD2 were stimulated with TNF-α and with LPS in *cell washing* series together with two different incubation sequences. In the standard sequence, cells are first exposed to the HDP of interest before LPS is applied (Figure 87; *q.v. section 4.2.1, page 195 et seqq.*). In the second experimental sequence, HDPs are pre-incubated with LPS

before applied onto the cells (Figure 90; *q.v. section 4.2.1, page 198*). Putting all these results together, enables the determination of the specific interaction with LPS. MORRISON and JACOBS performed binding experiments between PMB and Re595-LPS, a polysaccharide-free mutant, demonstrating, that PMB and LPS form a stable complex wherein the lipopeptide directly interacts with the lipid A moiety of LPS[180]. The complex formation appears to be of stoichiometric nature, this means that one molecule PMB binds one molecule of lipid A[180]. To observe, if this applies only to the endotoxin or even to other chemokines and cytokines released during inflammatory stress, stimulation experiments with TNF-α were performed. This cytokine induces a severe inflammatory immune response in a similar vein to LPS by activating TLR4-signaling. In these experimental series, LL-32 showed no decrease of IL-8 release, whereas PMB leads to a concentration dependent enhancement of TNF-α induced cytokine release (Figure 93; *q.v. section 4.2.1, page 202 et seqq.*). The herein presented results from cell culture experiments demonstrate not only the dual role of the AMP LL-32 but also of the peptide antibiotic PMB: Cells pre-incubated with one of the two compounds undergoing cell washing exhibit still a concentration dependent decrease in cytokine release (Figure 89; *q.v. section 4.2.1, page 197 et seqq.*). However, the incubation orders of peptides pursuant to sequential incubation or pre-incubation with LPS did not make a significant difference (Figure 90; *q.v. section 4.2.1, page 198 et seqq.*): Sequential incubation and pre-incubation experiments showed that LL-32 and PMB are able to directly neutralize LPS whereas in the sequential approach the activity is equal distributed to membrane- and LPS-interaction, giving a diminished regulatory effect. Combining the information obtained from these experimental sets demonstrate, that PMB does not exclusively act by direct LPS-neutralization but also by interaction on the membrane level. Together with the outcome from TNF-α induced stimulation, the direct neutralization of other cytokines by LL-32 and PMB can be ruled out.

6. CONCLUDING REMARKS & OUTLOOK

In the framework of this doctoral research work, it was possible to introduce a model for the membrane-peptide interaction of the cathelicidin derivative LL-32 and the lipopeptide PMB. For LL-32, the two major strategic routes of interaction were combined: First, antimicrobial killing wherein the peptide functions as AMP and interacts with the bacterial membrane; and second, the immunomodulatory activity, wherein LL-32 functions as HDP by neutralizing directly pathogenicity factors or dampening the release of cytokines (TNF-α).

OCD experiments gave information about the structural orientation of LL-32 on the membrane surface: At low concentrations, the peptide is prevalently arranged as unfolded random coil in solution (Figure 86; *q.v. section 4.1.13, page 193*). With raising concentrations, the peptide monomers get in proximity to each other, resulting in enhanced peptide-peptide interactions that facilitate a structural redesigning of the peptide backbone to the membrane active α-helical form (Figure 86; *q.v. section 4.1.13, page 193*). For LL-32 a dual role on the host cell level is suggested by acting via a primary membrane-mediated mechanism and a secondary receptor-mediated mechanism. Both, primary and secondary, mechanisms are accompanied by direct neutralization of pathogenicity factors (Figure 90; *q.v. section 4.2.1, page 198*). Only in severe cases of inflammation and an over expression of HDPs, LL-32 induces total membrane lysis and therewith apoptosis.

For the primary membrane-mediated mode of action, the AMP-characteristic models described for the interaction with bacterial membranes were confirmed and resolved for LL-32 on both, the bacterial and host cell membrane mimicry, from membrane insertion (Figure 53a; *q.v. section 4.1.6, page 152*) over pore formation (Figure 52; *q.v. section 4.1.5, page 149*) to total membrane disintegration (Figure 50; *q.v. section 4.1.4, page 145*) by use of a wide set of biophysical methods (*q.v. section 4.1,*

page 130 et seqq.). The combination of leakage (Figure 43; *q.v. section 4.1.1, page 133*) and quenching assay (Figure 44; *q.v. section 4.1.2, page 136*) and permeabilization kinetics obtained from pore-spanning membranes (Figure 46-49; *q.v. section 4.1.3, page 140 et seqq.*) revealed, that LL-32 takes different routes depending on the reconstituted model membrane system. It was possible to demonstrate for the fragment of the human cathelicidin, that the permeabilization process on pure DOPC membranes follow a non-pore model, in specific the carpet model. Whereas on more complex membrane systems, such as cholesterol-rich membranes, the mode of action adapts to the predominant membrane properties and moves from the non-pore model to the lipid clustering model. The fast process of membrane permeabilization as observed for DOPC membranes matches the findings from FRAP experiments, wherein the full fluorescence intensity could be regained (mobile lipid fraction of 100%) and information of the lipid mobility were captured. By contrast, on cholesterol-rich membranes, this mobile lipid fraction in presence of LL-32 was found to be 69.4% (Figure 110 and table 22; *q.v. Supplemental Data, section 7, page 239*). This supports the hypothesis of LL-32 adapting its primary mode of action to the membrane composition. Furthermore, it was possible to reveal the primary interaction site on the membrane for LL-32 by use of immobilized GUVs (Figure 55; *q.v. section 4.1.7, page 155*). This AMP favors the cholesterol-poor areas. Same applies to the stained HEK293-TLR4/MD2 cells, whereon the peptide was either detected in proximity to the TLR4-receptor or the two fluorophores were clearly established to be co-localized (Figure 97; *q.v. section 4.2.2, page 207*).

To gather information of a potential TLR4-mediated mode of action for LL-32 by functioning as ligand for this receptor, HEK293-TLR4/MD2 cells were transient transfected with the accessory protein CD14 (Figure 94; *q.v. section 4.2.1, page 204*). Therefore, the secondary route is supposed to resemble a CD14-dependent host defense mechanism. In presence of CD14, the MyD88-dependent pathway is activated. Up to now, it is largely unknown if CD14 features a binding site for LL-32, or in more general a HDP-specific binding site, and promotes the anti-inflammatory regulation of this peptide family[181].

The peptide antibiotic PMB interacts mainly by direct LPS-neutralization and via a membrane-mediated mode of action. PMB can bind to LPS over the DAB-residues located at the peptide's hydrophilic tail. For determining membrane distribution, PMB was successfully furnished with a small fluorophore. The fluorescently labeled compound allowed microscopy studies on cellular and model membrane level. This enabled the detection of PMB and its favored interaction site on the membrane level: PMB interacts predominantly with the cholesterol-rich membrane regions (Figure 54; *q.v. section 4.1.7, page 154 et seqq.*). These results lead to the introduction of a FRET-pair that included a labeled cholesterol species, which facilitated the investigation of membrane insertion. The window of experimental conditions under which PMB undergoes membrane insertion was found to be very narrow and was effectively defined (Figure 53b; *q.v. section 4.1.6, page 152*): For the lipopeptide, intercalation-induced FRET-effects could only be detected when the liquid-ordered membrane regions were labelled with one component of the FRET-pair and mono and divalent cations were absent. In this case, LL-32 exhibited on cholesterol-rich membranes with a cholesterol fraction of 10mol% an I_D/I_A-ratio, that lies in the same order of magnitude as the one for PMB. The same applies to the higher fraction of cholesterol with 20mol%. When divalent cations (Ca^{2+}) were present, changes in the I_D/I_A-ratio remain small after exposure to PMB and were unaffected by the fraction of cholesterol. A similar situation also applies to the conditional change shifting to physiological salt concentration, but only in presence of sodium chloride. Under the selected physiological salt concentration of 100 mM NaCl, PMB showed at 10mol% cholesterol in average a 5.7-fold lower I_D/I_A-ratio in comparison to the AMP. At higher fractions of cholesterol (20mol%), the I_D/I_A-ratio of PMB is only 2.9-fold lower compared to LL-32. This demonstrates that the content of cholesterol within the membrane modulates the membrane-peptide interaction, herein especially the intercalation ability of the AMP LL-32. In retrospect, these aspects taken together appear coherent, because PMB is applied exogenously and is not expressed by the target organism itself. Thus, as exogenous LPS-neutralizer, the cation concentration of the extracellular fluid (ECF) belongs to one of the main factors having a direct effect on the activity of PMB. The ECF in humans contains approximately 136-145 mM Na^+-ions[182]. These

monovalent cations may facilitate the intercalation process of PMB, whereas in case of LL-32, membrane insertion is influenced by the molar fractions of cholesterol present in the lipid bilayer.

On the cellular membrane level, a rapid uptake of PMB together with a high number of intracellular vesicles were monitored. Cells exhibiting a high degree of intracellular vesicles were found to have a reduced TLR4-recpetor staining on the membrane margin, whereas cells with evidently low intracellular vesicles expose a higher degree in TLR4 staining on the membrane surface (Figure 95; *q.v. section 4.2.2, page 205*). This leads to the hypothesis that PMB induces a specific form of rafts – so called *Caveolae* – and to the conclusion of the proposed host defense mechanism: As initial step, the lipopeptide integrates within the membrane network, where it is responsible for increasing membrane surface. Progressively, induction of fluidization within these regions allow the membrane to form vesicles that are taken up. Assuming, that the formed intracellular vesicles exhibit a higher degree of PMB, would facilitate vesicle fusion in the cytoplasm, that might lead to an increase in membrane tension and pressure. By implication, this membrane stress could possibly be overcome at a certain point by the induction of cell rupture and, as last resort reaction, cell death by apoptosis.

In the future, reconstituted membranes with various cholesterol levels are supposed to be investigated regarding domain formation and at what level the activity of AMPs is decreased to a minimum, where these molecules are beyond the target range of the host cell. Further, a HEK293-TLR4/MD2 cell line with stable transfected CD14 is in preparation, allowing to investigate differences between the two signaling cascades transduced in case of inflammation. Despite, further staining experiments are considered with LPS-stimulated HEK293-TLR4/MD2 cells, monitoring the recruiting of the TLR4-receptors to the cholesterol-rich domains and a predicted redistribution of the respective fluorescently labeled molecules. All aspects from these experimental approaches taken together, give the basis for future experiments on the single molecule level, thereunder FCS experiments, whereby lipid and peptide dynamics are studied and how these two major components influence each other enables the investigation of membrane-peptide interaction from all perspectives.

In conclusion, it was possible to point out the importance of cholesterol levels and the cholesterol fraction (10mol% vs. 20mol%) of the corresponding cholesterol-rich microdomains as resolution condition for monitoring membrane-associated effects induced by LL-32 and PMB. In this work, the focus was set on the membrane level and the lipid composition as main modulator for both, host defense efficiency and antimicrobial killing. Most of the ongoing research to date opt for a different focus, such as single protein targets. Same applies to the development of clinically useable antibiotics. Conventional antibiotics are often synthesized with the state of knowledge that each antibiotic features a specific primary target by interacting via a single mode of action, although this may not entirely apply to all of the current available antibiotics. But nature has showed us a different concept for the evolution of the innate host defense peptides, favoring the design of small molecules exhibiting antibiotic function, that interact with multiple targets rather than blocking a specific high-affinity target. To overcome the urgent need for new antibiotics and to prevent the outburst of an "pre-antibiotic era", where life-saving surgeries turn life-threatening, as recently stated by the WHO[183]. Continuous research in this field and the decoding of the modes of action of AMPs and hence the HDPs is more important in today's modern world than ever before and may open up new opportunities for novel therapeutic approaches where this peptide family may serve as template.

7. SUPPLEMENTAL DATA

TABLE 19. STATISTICAL EVALUATION OF FRET-DATA (q.v. SECTION 4.1.6, PAGE 150). DATA WERE ANALYZED IN A TWO-TAILED STUDENT'S PAIRED T-TEST. CONDITION TESTED: Labeled L_O- vs. labeled L_D-domain

NBD-12-Chol vs. NBD-PE		LL-32		PMB	
DOPC:SM:Chol (2:2:1)	**[µM]**	**p-Value**	**Significance**	**p-Value**	**Significance**
5mM HEPES, 0.5mM $CaCl_2x2H_2O$	1	0.8963	**ns**	0.3360	**ns**
	3	0.7388	**ns**	0.1417	**ns**
	10	0.3339	**ns**	0.2613	**ns**
100mM KCl, 5mM HEPES, 0.5mM $CaCl_2x2H_2O$	1	0.2383	**ns**	0.9996	**ns**
	3	0.5963	**ns**	0.9376	**ns**
	10	0.4947	**ns**	0.8334	**ns**
100mM NaCl, 5mM HEPES, 0.5mM $CaCl_2x2H_2O$	1	0.0039	**	0.2460	**ns**
	3	0.0163	*	0.0407	*
	10	0.4155	**ns**	0.0616	**ns**
5mM HEPES	1	0.0448	*	0.0265	*
	3	0.2541	**ns**	0.0008	***
	10	0.4436	**ns**	0.0255	*
100mM KCl, 5mM HEPES	1	0.0348	*	0.4467	**ns**
	3	0.0721	**ns**	0.1047	**ns**
	10	0.2008	**ns**	0.1484	**ns**
100mM NaCl, 5mM HEPES	1	0.0517	**ns**	0.8168	**ns**
	3	0.0225	*	0.1492	**ns**
	10	0.0816	**ns**	0.0441	*
DOPC:SM:Chol (9:9:2)	**[µM]**	**p-Value**	**Significance**	**p-Value**	**Significance**
5mM HEPES, 0.5mM $CaCl_2x2H_2O$	1	0.9059	**ns**	0.4368	**ns**
	3	0.7816	**ns**	0.4447	**ns**
	10	0.8365	**ns**	0.4410	**ns**
100mM KCl, 5mM HEPES, 0.5mM $CaCl_2x2H_2O$	1	0.4343	**ns**	0.0426	*
	3	0.1632	**ns**	0.0386	*
	10	0.0341	*	0.0279	*
100mM NaCl, 5mM HEPES, 0.5mM $CaCl_2x2H_2O$	1	0.8782	**ns**	0.1217	**ns**
	3	0.8232	**ns**	0.4965	**ns**
	10	0.6476	**ns**	0.0755	**ns**
5mM HEPES	1	0.8226	**ns**	0.0341	*
	3	0.4114	**ns**	0.0235	*
	10	0.8163	**ns**	0.0374	*
100mM KCl, 5mM HEPES	1	0.6671	**ns**	0.2290	**ns**
	3	0.1590	**ns**	0.2240	**ns**
	10	0.8877	**ns**	0.2311	**ns**
100mM NaCl, 5mM HEPES	1	0.1027	**ns**	0.3474	**ns**
	3	0.0887	**ns**	0.4581	**ns**
	10	0.7991	**ns**	0.3167	**ns**

TABLE 20. STATISTICAL EVALUATION OF FRET-DATA (q.v. SECTION 4.1.6, PAGE 150). DATA WERE ANALYZED IN A TWO-TAILED STUDENT'S PAIRED T-TEST. CONDITION TESTED: INFLUENCE OF THE CHOLESTEROL LEVEL OF THE TWO TERNARY LIPOSOME MIXTURES – DOPC/SM/Chol (2:2:1) vs. DOPC/SM/Chol (9:9:2)

Cholesterol content		LL-32		PMB	
NBD-12-Chol	**[µM]**	**p-Value**	**Significance**	**p-Value**	**Significance**
5mM HEPES, 0.5mM $CaCl_2x2H_2O$	1	0.0239	*	0.0346	*
	3	0.0466	*	0.0020	**
	10	0.0954	ns	0.0143	*
100mM KCl, 5mM HEPES, 0.5mM $CaCl_2x2H_2O$	1	0.2498	ns	0.3392	ns
	3	0.1705	ns	0.9885	ns
	10	0.9842	ns	0.3276	ns
100mM NaCl, 5mM HEPES, 0.5mM $CaCl_2x2H_2O$	1	0.2608	ns	0.9497	ns
	3	0.1759	ns	0.3170	ns
	10	0.0294	*	0.6237	ns
5mM HEPES	1	0.1024	ns	0.1250	ns
	3	0.0600	ns	0.0857	ns
	10	0.0315	*	0.0451	*
100mM KCl, 5mM HEPES	1	0.0713	ns	0.4704	ns
	3	0.1518	ns	0.7623	ns
	10	0.0544	ns	0.2318	ns
100mM NaCl, 5mM HEPES	1	0.1116	ns	0.7927	ns
	3	0.1255	ns	0.7459	ns
	10	0.0881	ns	0.7767	ns
NBD-PE	**[µM]**	**p-Value**	**Significance**	**p-Value**	**Significance**
5mM HEPES, 0.5mM $CaCl_2x2H_2O$	1	0.3734	ns	0.7749	ns
	3	0.3322	ns	0.5451	ns
	10	0.7293	ns	0.7599	ns
100mM KCl, 5mM HEPES, 0.5mM $CaCl_2x2H_2O$	1	0.0355	*	0.8148	ns
	3	0.0011	**	0.8745	ns
	10	0.0006	***	0.9650	ns
100mM NaCl, 5mM HEPES, 0.5mM $CaCl_2x2H_2O$	1	0.3187	ns	0.7794	ns
	3	0.2044	ns	0.2276	ns
	10	0.0050	**	0.0108	*
5mM HEPES	1	0.0007	***	0.1397	ns
	3	0.0005	***	0.1378	ns
	10	0.0059	**	0.2529	ns
100mM KCl, 5mM HEPES	1	0.4533	ns	0.1208	ns
	3	0.0271	*	0.0993	ns
	10	0.0046	**	0.0537	ns
100mM NaCl, 5mM HEPES	1	0.2605	ns	0.3164	ns
	3	0.1049	ns	0.4547	ns
	10	0.0690	ns	0.2273	ns

TABLE 21. STATISTICAL EVALUATION OF FRET-DATA (q.v. SECTION 4.1.6, PAGE 150). DATA WERE ANALYZED IN A TWO-TAILED STUDENT'S PAIRED T-TEST. CONDITION TESTED: INFLUENCE OF BUFFERS CONTAINING DIVALENT CATIONS – w/ 0.5 mM vs. w/o 0.5 mM $CaCl_2 \times 2H_2O$

w/ vs. w/o $CaCl_2x2H_2O$			LL-32		PMB	
	DOPC/SM/Chol (2:2:1)	[µM]	p-Value	Significance	p-Value	Significance
NBD-12-Chol	**5mM HEPES,** *0.5mM* $CaCl_2x2H_2O$	1	0.0666	**ns**	0.7799	**ns**
		3	0.0545	**ns**	0.8704	**ns**
		10	0.0418	*	0.9728	**ns**
	100mM KCl, 5mM HEPES, *0.5mM* $CaCl_2x2H_2O$	1	0.1346	**ns**	0.2150	**ns**
		3	0.1694	**ns**	0.2381	**ns**
		10	0.1471	**ns**	0.4308	**ns**
	100mM NaCl, 5mM HEPES, *0.5mM* $CaCl_2x2H_2O$	1	0.1548	**ns**	0.8226	**ns**
		3	0.0840	**ns**	0.6782	**ns**
		10	0.0414	*	0.7744	**ns**
NBD-PE	**5mM HEPES,** *0.5mM* $CaCl_2x2H_2O$	1	0.0003	***	0.9661	**ns**
		3	<0.0001	****	0.5385	**ns**
		10	0.0002	***	0.4132	**ns**
	100mM KCl, 5mM HEPES, *0.5mM* $CaCl_2x2H_2O$	1	0.1709	**ns**	0.0678	**ns**
		3	0.1790	**ns**	0.0384	*
		10	0.1741	**ns**	0.0673	**ns**
	100mM NaCl, 5mM HEPES, *0.5mM* $CaCl_2x2H_2O$	1	0.1478	**ns**	0.4775	**ns**
		3	0.2277	**ns**	0.1192	**ns**
		10	0.1907	**ns**	0.1035	**ns**
	DOPC/SM/Chol (9:9:2)	[µM]	p-Value	Significance	p-Value	Significance
NBD-12-Chol	**5mM HEPES,** *0.5mM* $CaCl_2x2H_2O$	1	0.0346	*	0.0265	*
		3	0.0272	*	0.1329	**ns**
		10	0.0335	*	0.0103	*
	100mM KCl, 5mM HEPES, *0.5mM* $CaCl_2x2H_2O$	1	0.1042	**ns**	0.2076	**ns**
		3	0.2089	**ns**	0.3706	**ns**
		10	0.0550	**ns**	0.6319	**ns**
	100mM NaCl, 5mM HEPES, *0.5mM* $CaCl_2x2H_2O$	1	0.5082	**ns**	0.8864	**ns**
		3	0.5111	**ns**	0.6480	**ns**
		10	0.3729	**ns**	0.4182	**ns**
NBD-PE	**5mM HEPES,** *0.5mM* $CaCl_2x2H_2O$	1	0.0242	*	0.1490	**ns**
		3	0.0094	**	0.1214	**ns**
		10	0.0358	*	0.1670	**ns**
	100mM KCl, 5mM HEPES, *0.5mM* $CaCl_2x2H_2O$	1	0.3032	**ns**	0.6522	**ns**
		3	0.2323	**ns**	0.4157	**ns**
		10	0.3869	**ns**	0.4934	**ns**
	100mM NaCl, 5mM HEPES, *0.5mM* $CaCl_2x2H_2O$	1	0.5032	**ns**	0.5325	**ns**
		3	0.6708	**ns**	0.2828	**ns**
		10	0.2382	**ns**	0.3071	**ns**

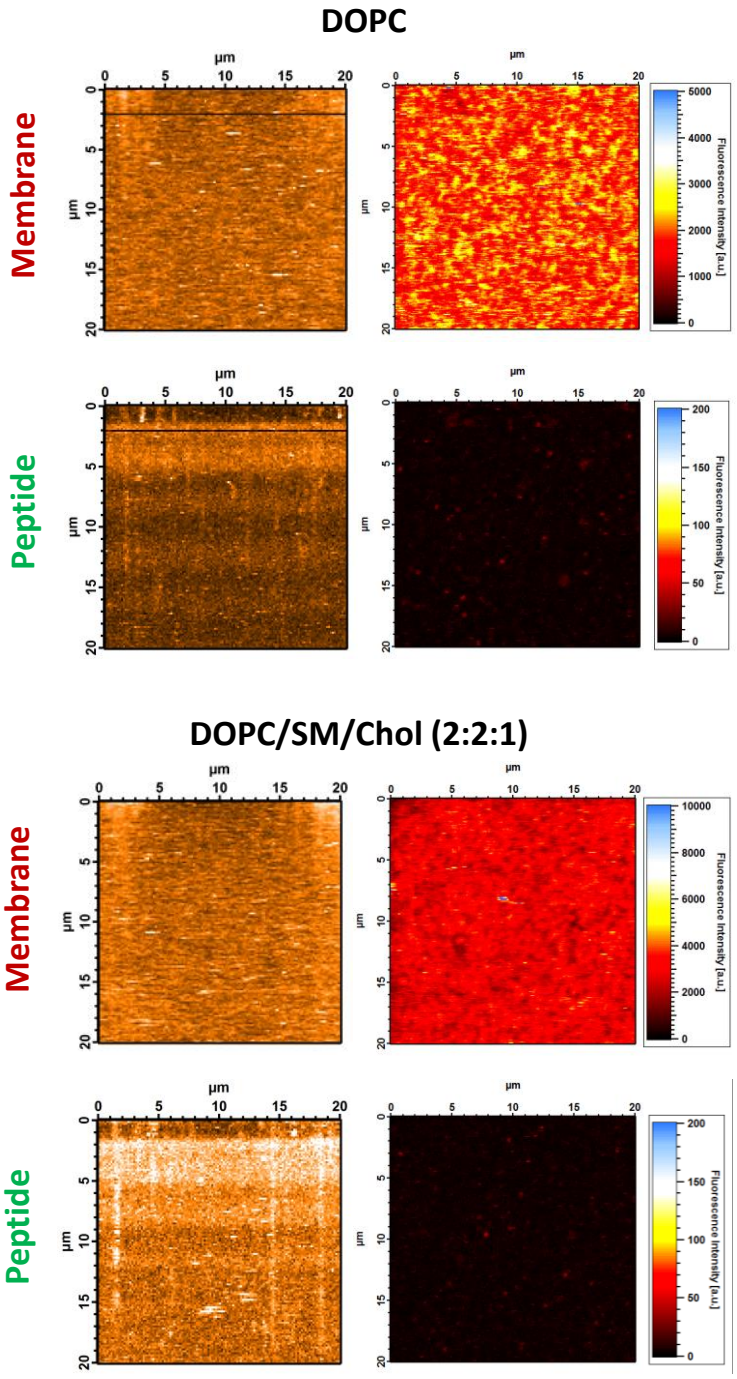

Supplemental Figure 109 | Fluorescence recovery after photobleaching (FRAP) profiles of lipid membranes reconstituted from pure DOPC and from DOPC/SM/Chol in a lipid ratio of 2:2:1. For the membrane-bound fluorophore Atto633 a homogenous distribution of fluorescent molecules was detected. All linescan profiles were adapted to the same color code.

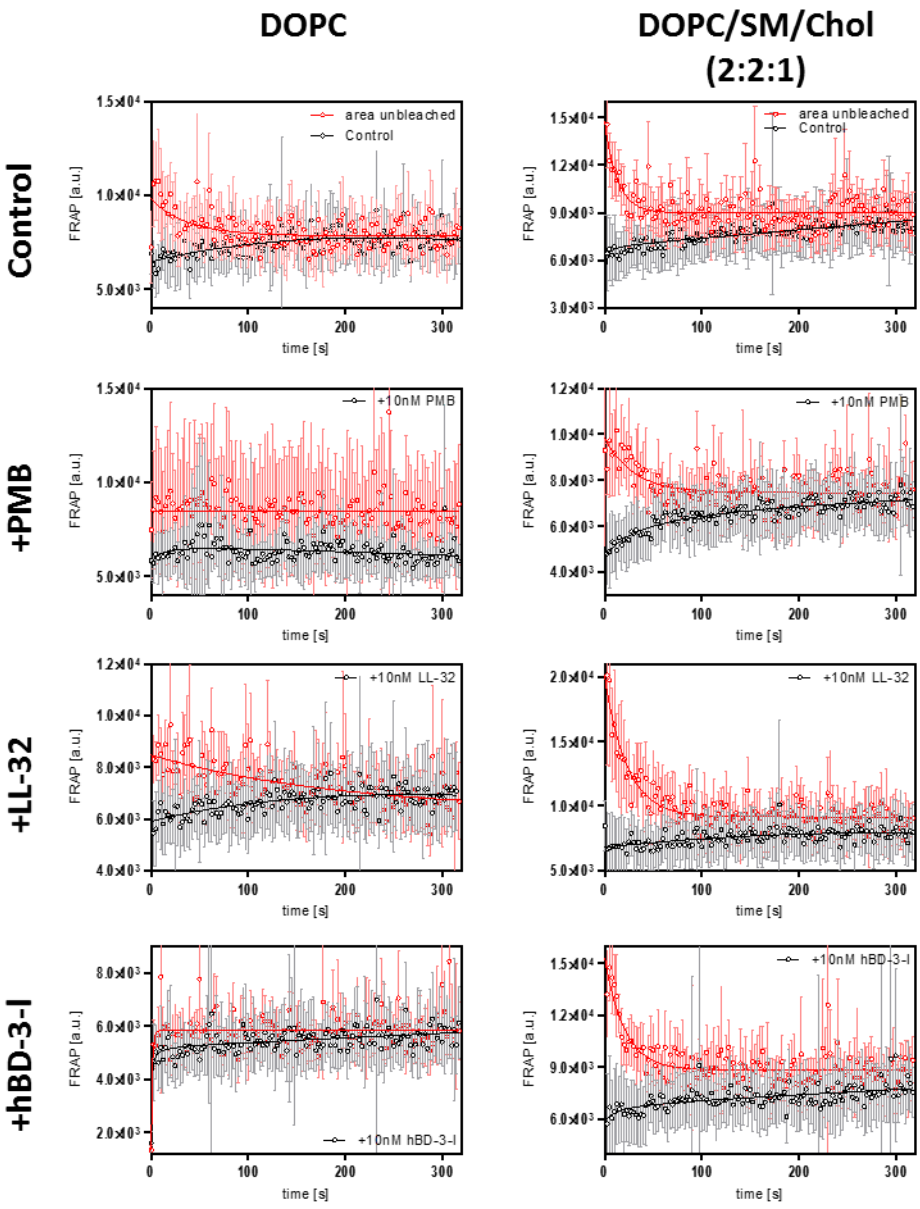

Supplemental Figure 110 | Fluorescence recovery after photobleaching (FRAP) profiles of pure lipid membranes and in presence of antimicrobial compounds. Data extracted from linescan profiles. Data points colored black stand for the fluorescence recovery after 10 min exposure to maximum laser intensity, whereas data points colored red resemble the surrounding and unbleached area. Peptides were applied in final concentrations of 10 nM.

TABLE 22. MOBILE AND IMMOBILE FRACTION DETERMINED FROM FRAP-DATA PLOTTED IN FIGURE 110.

	Fraction [%]	Control	+PMB	+LL-32	+hBD-3-l
DOPC	Mobile	95.9	47.3	100	97.6
	Immobile	4.1	53.6	0	3.05
2:2:1	Mobile	90.55	91.9	69.4	78.2
	Immobile	9.45	7.35	29.2	22.7

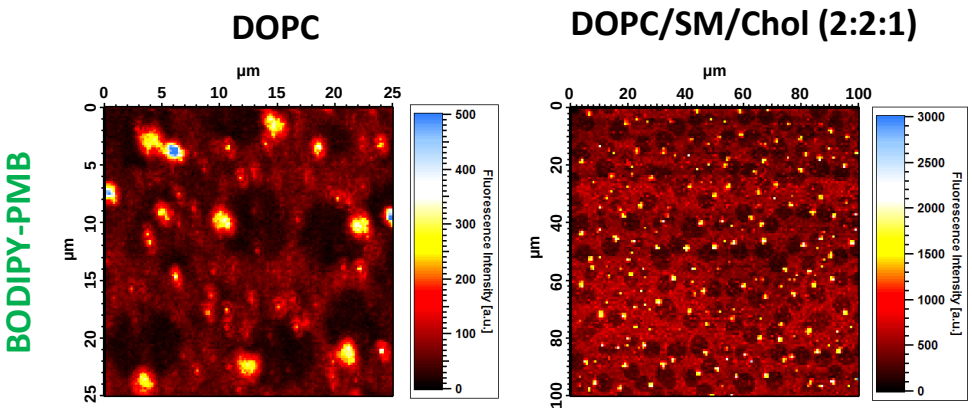

Supplemental Figure 111 | Confocal images of lipid membranes reconstituted from pure DOPC and from DOPC/SM/Chol in a lipid ratio of 2:2:1 after exposure to BODIPY-PMB. The peptide was applied in a final concentration of 1 nM. Liposomes were prepared in Ca^{2+}-ions containing buffer (5 mM HEPES, 0.5 mM $CaCl_2$ x $2H_2O$) at pH 7.4.

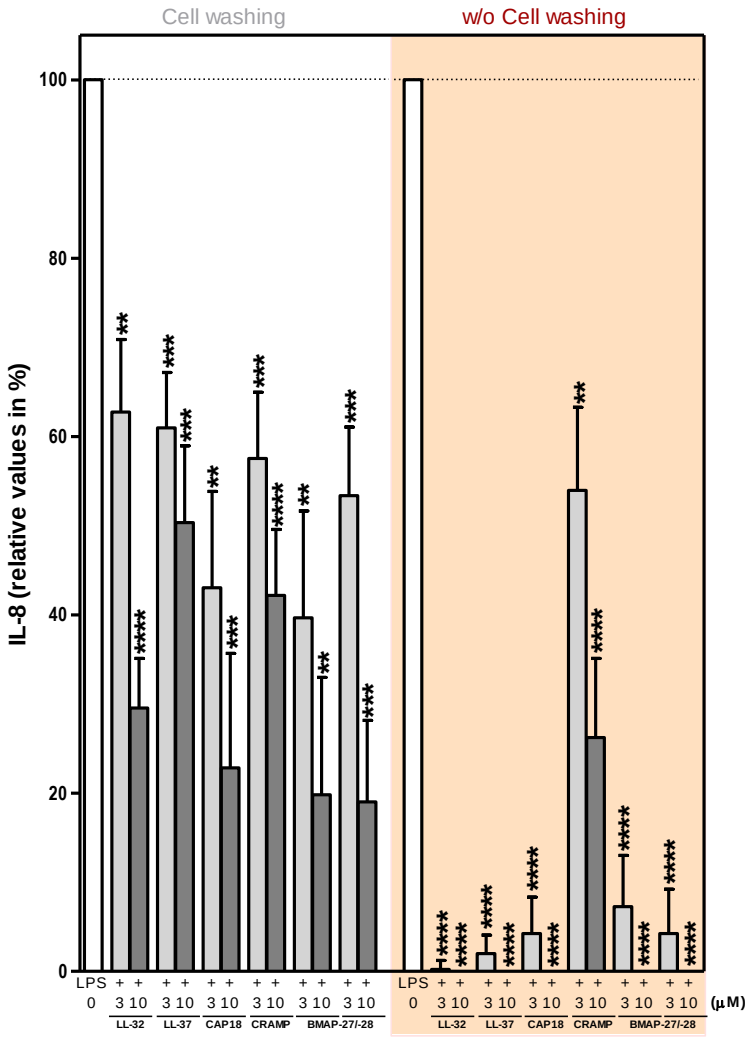

Supplemental Figure 112 | Cell washing series of cathelicidin-related antimicrobial peptides performed on HEK293-TLR4/MD2 cells. Cells were incubated with final peptide concentrations of 3 µM and 10 µM and treated with 10 nM LPS. Cells were either washed three times with fresh culturing medium (10% FCS) or treated pursuant to the standard protocol. Data are plotted as mean of five (LL-32, LL-37, CRAMP) or four (CAP18, BMAP-27, BMAP-28) representative experiments +SD (n = 10). Statistical analysis was performed in a two-tailed student's paired t-test (non-significant: ns ≥ 0.05; significant: * p ≤. 0.05; very significant: ** p ≤ 0.01; highly significant: *** p ≤ 0.001; extremely significant: **** p ≤ 0.0001).

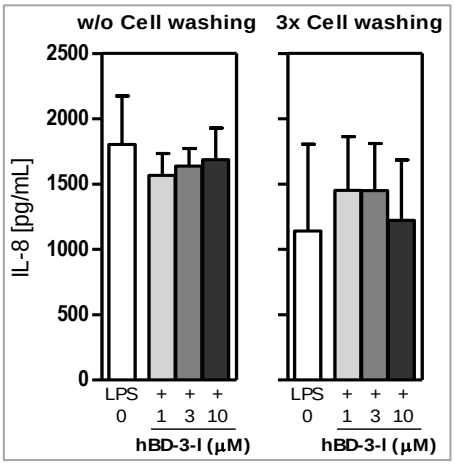

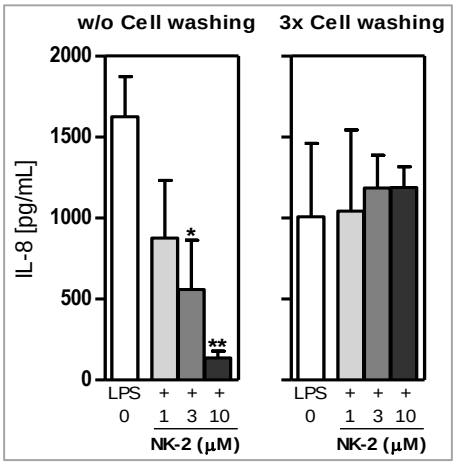

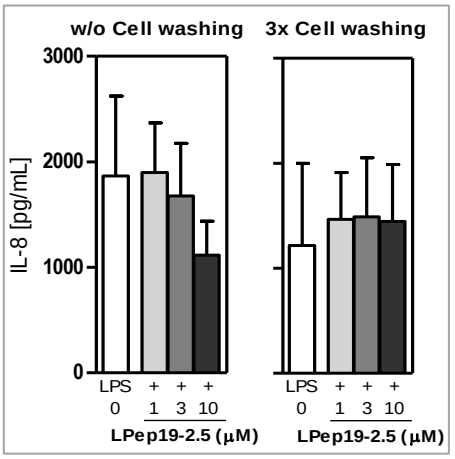

Supplemental Figure 113 | Cell washing series of HEK293-TLR4/MD2 cells incubated with hBD-3-l, NK-2 and LPep19-2.5. All substances were applied in final concentrations of 1 µM, 3 µM, and 10 µM and treated with 10 nM LPS. The IL-8 release was detected by ELISA. Data are plotted as mean +SD (n = 3). Statistical analysis was performed in a two-tailed student's paired t-test (non-significant: ns ≥ 0.05; significant: * p ≤. 0.05; very significant: ** p ≤ 0.01).

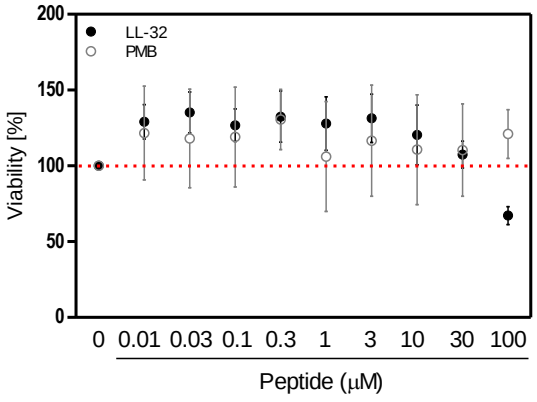

Supplemental Figure 114 | Cell viability assay of HEK293-TLR4/MD2 cells incubated over 24 h with LL-32 or PMB. Mitochondrial activity was measured by the colorimetric reduction of the yellow MTT reagent to the purple formazan. Cells were incubated in a peptide concentration range from 0.01 µM to 100 µM. LL-32 exhibits cytotoxicity on HEK293 cells at concentrations over 30 µM. PMB can be applied in even higher concentrations. Data are plotted as mean of three independent experiments (n = 3).

EXCERPT FROM THE TABLE OF CONTENTS

APPENDIX I

LIST OF REFERENCES

1. Medzhitov, R.; Shevach, E. M.; Trinchieri, G.; Mellor, A. L.; Munn, D. H.; Gordon, S.; Libby, P.; Hansson, G. K.; Shortman, K.; Dong, C.; Gabrilovich, D.; Gabrysova, L.; Howes, A.; O'Garra, A., Highlights of 10 years of immunology in Nature Reviews Immunology. *Nat Rev Immunol* **2011,** *11* (10), 693-702.

2. Akira, S.; Takeda, K., Toll-like receptor signalling. *Nat Rev Immunol* **2004,** *4* (7), 499-511.

3. (a) Lai, Y.; Gallo, R. L., AMPed up immunity: how antimicrobial peptides have multiple roles in immune defense. *Trends Immunol* **2009,** *30* (3), 131-41; (b) Phoenix, D. A.; Dennison, S. R.; Harris, F., Antimicrobial peptides: their history, evolution, and functional promiscuity. *Antimicrobial peptides* **2013**, 1-37.

4. (a) Lee, C. C.; Avalos, A. M.; Ploegh, H. L., Accessory molecules for Toll-like receptors and their function. *Nat Rev Immunol* **2012,** *12* (3), 168-79; (b) Medzhitov, R., Toll-like receptors and innate immunity. *Nat Rev Immunol* **2001,** *1* (2), 135-45.

5. Ross, M. H.; Pawlina, W., *Histology*. Lippincott Williams & Wilkins: 2006.

6. Voncina, B.; Vivod, V., *Cyclodextrins in textile finishing*. INTECH Open Access Publisher: 2013.

7. Alberts, B.; Johnson, A.; Lewis, J.; Raff, M.; Roberts, K.; Walter, P., Membrane structure. **2002**.

8. Sommer, L. Structural characterization of the membrane mimetic interactions of the FATC domains of the protein kinase 'target of rapamycin' and related kinases. Dissertation, Technical University of Munich, 2013.

9. Saathoff, A. Biophysical Investigations into the Interactions between Antimicrobial Peptides of the Epithelial Defense and Microbial Cell

Envelopes. Dissertation, University of Lübeck, Research Center Borstel, 2013.

10. (a) Park, B. S.; Song, D. H.; Kim, H. M.; Choi, B. S.; Lee, H.; Lee, J. O., The structural basis of lipopolysaccharide recognition by the TLR4-MD-2 complex. *Nature* **2009,** *458* (7242), 1191-5; (b) Kang, J. Y.; Lee, J. O., Structural biology of the Toll-like receptor family. *Annu Rev Biochem* **2011,** *80*, 917-41.

11. (a) Zasloff, M., Antimicrobial peptides of multicellular organisms. *Nature* **2002,** *415* (6870), 389-95; (b) Rothenberg, M. E., Innate sensing of nickel. *Nat Immunol* **2010,** *11* (9), 781-2.

12. Wernecke, J. Biophysical Characterisation of the Fungal Peptide Toxin Ece1-III and its Interaction with Lipid Membranes. Dissertation, University of Lübeck, Deutsches Elektronen-Synchrotron DESY and Research Center Borstel, 2016.

13. Walsh, C., *Antibiotics*. American Society of Microbiology: 2003.

14. Hancock, R. E.; Chapple, D. S., Peptide antibiotics. *Antimicrob Agents Chemother* **1999,** *43* (6), 1317-23.

15. Bahar, A. A.; Ren, D., Antimicrobial peptides. *Pharmaceuticals (Basel)* **2013,** *6* (12), 1543-75.

16. Cranfield, C. G.; Cornell, B. A.; Grage, S. L.; Duckworth, P.; Carne, S.; Ulrich, A. S.; Martinac, B., Transient potential gradients and impedance measures of tethered bilayer lipid membranes: pore-forming peptide insertion and the effect of electroporation. *Biophysical journal* **2014,** *106* (1), 182-189.

17. Oblak, A.; Pohar, J.; Jerala, R., MD-2 determinants of nickel and cobalt-mediated activation of human TLR4. *PLoS One* **2015,** *10* (3), e0120583.

18. Diamond, G.; Beckloff, N.; Weinberg, A.; Kisich, K. O., The roles of antimicrobial peptides in innate host defense. *Curr Pharm Des* **2009,** *15* (21), 2377-92.

19. Simons, K.; Sampaio, J. L., Membrane organization and lipid rafts. *Cold Spring Harb Perspect Biol* **2011,** *3* (10), a004697.

20. Singer, S.; Nicolson, G. L., The fluid mosaic model of the structure of cell membranes. *Membranes and Viruses in Immunopathology; Day, SB, Good, RA, Eds* **1972**, 7-47.

21. Alberts, B. J., A.; Lewis, J.; Raff, M.; Roberts, K.; Walter, P., *Molecular Biology of the Cell*. 5th ed.; Garland Science: New York, USA, 2007; p 1392.

22. Simons, K.; Toomre, D., Lipid rafts and signal transduction. *Nat Rev Mol Cell Biol* **2000,** *1* (1), 31-9.

23. Varshney, P.; Yadav, V.; Saini, N., Lipid rafts in immune signaling: Current progress and future perspective. *Immunology* **2016**.

24. Vance, D. E.; Van den Bosch, H., Cholesterol in the year 2000. *Biochim Biophys Acta* **2000,** *1529* (1-3), 1-8.

25. Ohvo-Rekila, H.; Ramstedt, B.; Leppimaki, P.; Slotte, J. P., Cholesterol interactions with phospholipids in membranes. *Prog Lipid Res* **2002,** *41* (1), 66-97.

26. Villalain, J., Location of cholesterol in model membranes by magic-angle-sample-spinning NMR. *Eur J Biochem* **1996,** *241* (2), 586-93.

27. Bittman, R., Has nature designed the cholesterol side chain for optimal interaction with phospholipids? *Subcell Biochem* **1997,** *28*, 145-71.

28. Chaudhuri, A.; Chattopadhyay, A., Transbilayer organization of membrane cholesterol at low concentrations: Implications in health and disease. *Biochim Biophys Acta* **2011,** *1808* (1), 19-25.

29. Pandit, S. A.; Jakobsson, E.; Scott, H. L., Simulation of the early stages of nano-domain formation in mixed bilayers of sphingomyelin, cholesterol, and dioleylphosphatidylcholine. *Biophys J* **2004,** *87* (5), 3312-22.

30. Lippold, B. Cholesterin. http://www.chemie.de/lexikon/Cholesterin.html (accessed 15 June 2016).

31. (a) Goluszko, P.; Nowicki, B., Membrane cholesterol: a crucial molecule affecting interactions of microbial pathogens with mammalian cells. *Infect Immun* **2005,** *73* (12), 7791-6; (b) Yeagle, P. L., Cholesterol and the cell membrane. *Biochim Biophys Acta* **1985,** *822* (3-4), 267-87.

32. Silvius, J. R., Role of cholesterol in lipid raft formation: lessons from lipid model systems. *Biochim Biophys Acta* **2003,** *1610* (2), 174-83.

33. (a) Ipsen, J. H.; Karlstrom, G.; Mouritsen, O. G.; Wennerstrom, H.; Zuckermann, M. J., Phase equilibria in the phosphatidylcholine-cholesterol system. *Biochim Biophys Acta* **1987,** *905* (1), 162-72; (b) Ipsen, J. H.; Mouritsen,

O. G.; Zuckermann, M. J., Theory of thermal anomalies in the specific heat of lipid bilayers containing cholesterol. *Biophys J* **1989,** *56* (4), 661-7.

34. Yeagle, P. L., Modulation of membrane function by cholesterol. *Biochimie* **1991,** *73* (10), 1303-10.

35. Jenssen, H.; Hamill, P.; Hancock, R. E., Peptide antimicrobial agents. *Clin Microbiol Rev* **2006,** *19* (3), 491-511.

36. (a) Erridge, C.; Bennett-Guerrero, E.; Poxton, I. R., Structure and function of lipopolysaccharides. *Microbes Infect* **2002,** *4* (8), 837-51; (b) Rosenfeld, Y.; Shai, Y., Lipopolysaccharide (Endotoxin)-host defense antibacterial peptides interactions: role in bacterial resistance and prevention of sepsis. *Biochim Biophys Acta* **2006,** *1758* (9), 1513-22.

37. Holst, O., Structure of the lipopolysaccharide core region. In *Bacterial Lipopolysaccharides*, Springer: 2011; pp 21-39.

38. Netea, M. G.; van Deuren, M.; Kullberg, B. J.; Cavaillon, J. M.; Van der Meer, J. W., Does the shape of lipid A determine the interaction of LPS with Toll-like receptors? *Trends Immunol* **2002,** *23* (3), 135-9.

39. Rietschel, E. T.; Brade, H.; Brade, L.; Brandenburg, K.; Schade, U.; Seydel, U.; Zahringer, U.; Galanos, C.; Luderitz, O.; Westphal, O.; et al., Lipid A, the endotoxic center of bacterial lipopolysaccharides: relation of chemical structure to biological activity. *Prog Clin Biol Res* **1987,** *231*, 25-53.

40. Tanamoto, K.; Zahringer, U.; McKenzie, G. R.; Galanos, C.; Rietschel, E. T.; Luderitz, O.; Kusumoto, S.; Shiba, T., Biological activities of synthetic lipid A analogs: pyrogenicity, lethal toxicity, anticomplement activity, and induction of gelation of Limulus amoebocyte lysate. *Infect Immun* **1984,** *44* (2), 421-6.

41. (a) Dubos, R. J., Studies on a Bactericidal Agent Extracted from a Soil Bacillus : I. Preparation of the Agent. Its Activity in Vitro. *J Exp Med* **1939,** *70* (1), 1-10; (b) Dubos, R. J., Studies on a Bactericidal Agent Extracted from a Soil Bacillus : Ii. Protective Effect of the Bactericidal Agent against Experimental Pneumococcus Infections in Mice. *J Exp Med* **1939,** *70* (1), 11-7.

42. Hotchkiss, R. D.; Dubos, R. J., Chemical properties of bactericidal substances isolated from cultures of a soil Bacillus. *Journal of Biological Chemistry* **1940,** *132* (2), 793-794.

43. Gause, G.; Brazhnikova, M., Gramicidin S and its use in the treatment of infected wounds. *Nature* **1944,** *154*, 703.

44. Van Epps, H. L., René Dubos: unearthing antibiotics. *Journal of Experimental Medicine* **2006,** *203* (2), 259.

45. Fleming, A., On the antibacterial action of cultures of a penicillium, with special reference to their use in the isolation of B. influenzae. 1929. *Bull World Health Organ* **2001,** *79* (8), 780-90.

46. Schatz, A.; Bugie, E.; Waksman, S. A., Streptomycin, a substance exhibiting antibiotic activity against gram-positive and gram-negative bacteria. 1944. *Clin Orthop Relat Res* **2005,** (437), 3-6.

47. Nakatsuji, T.; Gallo, R. L., Antimicrobial peptides: old molecules with new ideas. *J Invest Dermatol* **2012,** *132* (3 Pt 2), 887-95.

48. Croce, G.; Giglioli, N.; Bolognani, L., Antimicrobial activity in the skin secretions of Bombina variegata pachypus. *Toxicon* **1973,** *11* (1), 99-100.

49. Groves, M. L.; Peterson, R. F.; Kiddy, C. A., Poliomorphism in the red protein isolated from milk of individual cows. *Nature* **1965,** *207* (5000), 1007-8.

50. Levy, O., Antimicrobial proteins and peptides: anti-infective molecules of mammalian leukocytes. *J Leukoc Biol* **2004,** *76* (5), 909-25.

51. Ganz, T.; Selsted, M. E.; Szklarek, D.; Harwig, S. S.; Daher, K.; Bainton, D. F.; Lehrer, R. I., Defensins. Natural peptide antibiotics of human neutrophils. *J Clin Invest* **1985,** *76* (4), 1427-35.

52. Steiner, H.; Hultmark, D.; Engstrom, A.; Bennich, H.; Boman, H. G., Sequence and specificity of two antibacterial proteins involved in insect immunity. *Nature* **1981,** *292* (5820), 246-8.

53. Zasloff, M., Magainins, a class of antimicrobial peptides from Xenopus skin: isolation, characterization of two active forms, and partial cDNA sequence of a precursor. *Proc Natl Acad Sci U S A* **1987,** *84* (15), 5449-53.

54. Selsted, M. E.; Tang, Y. Q.; Morris, W. L.; McGuire, P. A.; Novotny, M. J.; Smith, W.; Henschen, A. H.; Cullor, J. S., Purification, primary structures, and antibacterial activities of beta-defensins, a new family of

antimicrobial peptides from bovine neutrophils. *J Biol Chem* **1993,** *268* (9), 6641-8.

55. Tang, Y. Q.; Yuan, J.; Osapay, G.; Osapay, K.; Tran, D.; Miller, C. J.; Ouellette, A. J.; Selsted, M. E., A cyclic antimicrobial peptide produced in primate leukocytes by the ligation of two truncated alpha-defensins. *Science* **1999,** *286* (5439), 498-502.

56. Zhao, X.; Wu, H.; Lu, H.; Li, G.; Huang, Q., LAMP: A Database Linking Antimicrobial Peptides. *PLoS One* **2013,** *8* (6), e66557.

57. Hoffmann, J. A.; Kafatos, F. C.; Janeway, C. A.; Ezekowitz, R. A., Phylogenetic perspectives in innate immunity. *Science* **1999,** *284* (5418), 1313-8.

58. Brown, K. L.; Hancock, R. E., Cationic host defense (antimicrobial) peptides. *Curr Opin Immunol* **2006,** *18* (1), 24-30.

59. Bowdish, D. M.; Davidson, D. J.; Scott, M. G.; Hancock, R. E., Immunomodulatory activities of small host defense peptides. *Antimicrob Agents Chemother* **2005,** *49* (5), 1727-32.

60. Auvynet, C.; Rosenstein, Y., Multifunctional host defense peptides: antimicrobial peptides, the small yet big players in innate and adaptive immunity. *FEBS J* **2009,** *276* (22), 6497-508.

61. (a) Horne, W. S.; Wiethoff, C. M.; Cui, C.; Wilcoxen, K. M.; Amorin, M.; Ghadiri, M. R.; Nemerow, G. R., Antiviral cyclic D,L-alpha-peptides: targeting a general biochemical pathway in virus infections. *Bioorg Med Chem* **2005,** *13* (17), 5145-53; (b) Bastian, A.; Schafer, H., Human alpha-defensin 1 (HNP-1) inhibits adenoviral infection in vitro. *Regul Pept* **2001,** *101* (1-3), 157-61.

62. Belaid, A.; Aouni, M.; Khelifa, R.; Trabelsi, A.; Jemmali, M.; Hani, K., In vitro antiviral activity of dermaseptins against herpes simplex virus type 1. *J Med Virol* **2002,** *66* (2), 229-34.

63. (a) Robinson, W. E., Jr.; McDougall, B.; Tran, D.; Selsted, M. E., Anti-HIV-1 activity of indolicidin, an antimicrobial peptide from neutrophils. *J Leukoc Biol* **1998,** *63* (1), 94-100; (b) Sitaram, N.; Nagaraj, R., Interaction of antimicrobial peptides with biological and model membranes: structural and charge requirements for activity. *Biochim Biophys Acta* **1999,** *1462* (1-2), 29-54.

64. (a) Tamamura, H.; Ishihara, T.; Otaka, A.; Murakami, T.; Ibuka, T.; Waki, M.; Matsumoto, A.; Yamamoto, N.; Fujii, N., Analysis of the interaction of an anti-HIV peptide, T22 ([Tyr5, 12, Lys7]-polyphemusin II), with gp120 and CD4 by surface plasmon resonance. *Biochim Biophys Acta* **1996,** *1298* (1), 37-44; (b) Song, B. H.; Lee, G. C.; Moon, M. S.; Cho, Y. H.; Lee, C. H., Human cytomegalovirus binding to heparan sulfate proteoglycans on the cell surface and/or entry stimulates the expression of human leukocyte antigen class I. *J Gen Virol* **2001,** *82* (Pt 10), 2405-13.

65. Klotman, M. E.; Chang, T. L., Defensins in innate antiviral immunity. *Nat Rev Immunol* **2006,** *6* (6), 447-56.

66. Howell, M. D.; Jones, J. F.; Kisich, K. O.; Streib, J. E.; Gallo, R. L.; Leung, D. Y., Selective killing of vaccinia virus by LL-37: implications for eczema vaccinatum. *J Immunol* **2004,** *172* (3), 1763-7.

67. (a) VanCompernolle, S. E.; Taylor, R. J.; Oswald-Richter, K.; Jiang, J.; Youree, B. E.; Bowie, J. H.; Tyler, M. J.; Conlon, J. M.; Wade, D.; Aiken, C.; Dermody, T. S.; KewalRamani, V. N.; Rollins-Smith, L. A.; Unutmaz, D., Antimicrobial peptides from amphibian skin potently inhibit human immunodeficiency virus infection and transfer of virus from dendritic cells to T cells. *J Virol* **2005,** *79* (18), 11598-606; (b) Lorin, C.; Saidi, H.; Belaid, A.; Zairi, A.; Baleux, F.; Hocini, H.; Belec, L.; Hani, K.; Tangy, F., The antimicrobial peptide dermaseptin S4 inhibits HIV-1 infectivity in vitro. *Virology* **2005,** *334* (2), 264-75.

68. Brogden, K. A., Antimicrobial peptides: pore formers or metabolic inhibitors in bacteria? *Nat Rev Microbiol* **2005,** *3* (3), 238-50.

69. (a) De Lucca, A. J.; Bland, J. M.; Jacks, T. J.; Grimm, C.; Walsh, T. J., Fungicidal and binding properties of the natural peptides cecropin B and dermaseptin. *Med Mycol* **1998,** *36* (5), 291-8; (b) De Lucca, A. J.; Walsh, T. J., Antifungal peptides: novel therapeutic compounds against emerging pathogens. *Antimicrob Agents Chemother* **1999,** *43* (1), 1-11; (c) Muller, F. M.; Lyman, C. A.; Walsh, T. J., Antimicrobial peptides as potential new antifungals. *Mycoses* **1999,** *42 Suppl 2*, 77-82.

70. (a) Yokoyama, S.; Iida, Y.; Kawasaki, Y.; Minami, Y.; Watanabe, K.; Yagi, F., The chitin-binding capability of Cy-AMP1 from cycad is essential to antifungal activity. *J Pept Sci* **2009,** *15* (7), 492-7; (b) Pushpanathan, M.; Rajendhran, J.; Jayashree, S.; Sundarakrishnan, B.; Jayachandran, S.; Gunasekaran, P., Identification of a novel antifungal peptide with chitin-

binding property from marine metagenome. *Protein Pept Lett* **2012,** *19* (12), 1289-96.

71. Park, Y.; Jang, S. H.; Lee, D. G.; Hahm, K. S., Antinematodal effect of antimicrobial peptide, PMAP-23, isolated from porcine myeloid against Caenorhabditis elegans. *J Pept Sci* **2004,** *10* (5), 304-11.

72. Hallock, K. J.; Lee, D. K.; Ramamoorthy, A., MSI-78, an analogue of the magainin antimicrobial peptides, disrupts lipid bilayer structure via positive curvature strain. *Biophys J* **2003,** *84* (5), 3052-60.

73. (a) Scott, M. G.; Yan, H.; Hancock, R. E., Biological properties of structurally related alpha-helical cationic antimicrobial peptides. *Infect Immun* **1999,** *67* (4), 2005-9; (b) Sato, H.; Feix, J. B., Peptide-membrane interactions and mechanisms of membrane destruction by amphipathic alpha-helical antimicrobial peptides. *Biochim Biophys Acta* **2006,** *1758* (9), 1245-56.

74. (a) Chen, F. Y.; Lee, M. T.; Huang, H. W., Evidence for membrane thinning effect as the mechanism for peptide-induced pore formation. *Biophys J* **2003,** *84* (6), 3751-8; (b) Lee, M. T.; Chen, F. Y.; Huang, H. W., Energetics of pore formation induced by membrane active peptides. *Biochemistry* **2004,** *43* (12), 3590-9.

75. Silvestro, L.; Axelsen, P. H., Membrane-induced folding of cecropin A. *Biophys J* **2000,** *79* (3), 1465-77.

76. Steiner, H.; Andreu, D.; Merrifield, R. B., Binding and action of cecropin and cecropin analogues: antibacterial peptides from insects. *Biochim Biophys Acta* **1988,** *939* (2), 260-6.

77. Benachir, T.; Lafleur, M., Osmotic and pH transmembrane gradients control the lytic power of melittin. *Biophysical journal* **1996,** *70* (2), 831.

78. Gennis, R. B., *Biomembranes: molecular structure and function*. Springer Science & Business Media: 2013.

79. Ludtke, S. J.; He, K.; Heller, W. T.; Harroun, T. A.; Yang, L.; Huang, H. W., Membrane pores induced by magainin. *Biochemistry* **1996,** *35* (43), 13723-8.

80. (a) Henzler-Wildman, K. A.; Martinez, G. V.; Brown, M. F.; Ramamoorthy, A., Perturbation of the hydrophobic core of lipid bilayers by

the human antimicrobial peptide LL-37. *Biochemistry* **2004,** *43* (26), 8459-8469; (b) Henzler Wildman, K. A.; Lee, D.-K.; Ramamoorthy, A., Mechanism of lipid bilayer disruption by the human antimicrobial peptide, LL-37. *Biochemistry* **2003,** *42* (21), 6545-6558; (c) Porcelli, F.; Verardi, R.; Shi, L.; Henzler-Wildman, K. A.; Ramamoorthy, A.; Veglia, G., NMR structure of the cathelicidin-derived human antimicrobial peptide LL-37 in dodecylphosphocholine micelles†. *Biochemistry* **2008,** *47* (20), 5565-5572.

81. Baumann, G.; Mueller, P., A molecular model of membrane excitability. *J Supramol Struct* **1974,** *2* (5-6), 538-57.

82. (a) Yang, L.; Weiss, T. M.; Lehrer, R. I.; Huang, H. W., Crystallization of antimicrobial pores in membranes: magainin and protegrin. *Biophys J* **2000,** *79* (4), 2002-9; (b) Matsuzaki, K., Why and how are peptide-lipid interactions utilized for self-defense? Magainins and tachyplesins as archetypes. *Biochim Biophys Acta* **1999,** *1462* (1-2), 1-10; (c) Shai, Y., Mechanism of the binding, insertion and destabilization of phospholipid bilayer membranes by alpha-helical antimicrobial and cell non-selective membrane-lytic peptides. *Biochim Biophys Acta* **1999,** *1462* (1-2), 55-70.

83. Brender, J. R.; McHenry, A. J.; Ramamoorthy, A., Does cholesterol play a role in the bacterial selectivity of antimicrobial peptides? *Front Immunol* **2012,** *3*, 195.

84. Peschel, A.; Sahl, H. G., The co-evolution of host cationic antimicrobial peptides and microbial resistance. *Nat Rev Microbiol* **2006,** *4* (7), 529-36.

85. Peschel, A., How do bacteria resist human antimicrobial peptides? *Trends in microbiology* **2002,** *10* (4), 179-186.

86. Domingues, M. M.; Inacio, R. G.; Raimundo, J. M.; Martins, M.; Castanho, M. A.; Santos, N. C., Biophysical characterization of polymyxin B interaction with LPS aggregates and membrane model systems. *Biopolymers* **2012,** *98* (4), 338-44.

87. Zavascki, A. P.; Goldani, L. Z.; Li, J.; Nation, R. L., Polymyxin B for the treatment of multidrug-resistant pathogens: a critical review. *J Antimicrob Chemother* **2007,** *60* (6), 1206-15.

88. (a) Zhang, L.; Dhillon, P.; Yan, H.; Farmer, S.; Hancock, R. E., Interactions of bacterial cationic peptide antibiotics with outer and cytoplasmic membranes of Pseudomonas aeruginosa. *Antimicrob Agents*

Chemother **2000,** *44* (12), 3317-21; (b) Wu, M.; Maier, E.; Benz, R.; Hancock, R. E., Mechanism of interaction of different classes of cationic antimicrobial peptides with planar bilayers and with the cytoplasmic membrane of Escherichia coli. *Biochemistry* **1999,** *38* (22), 7235-42.

89. Baltz, R. H.; Miao, V.; Wrigley, S. K., Natural products to drugs: daptomycin and related lipopeptide antibiotics. *Natural product reports* **2005,** *22* (6), 717-741.

90. (a) Newton, B. A., A fluorescent derivative of polymyxin: its preparation and use in studying the site of action of the antibiotic. *J Gen Microbiol* **1955,** *12* (2), 226-36; (b) Rocco, R. M., Method and compound for detecting low levels of microorganisms. Google Patents: 2000.

91. Azad, M. A.; Yun, B.; Roberts, K. D.; Nation, R. L.; Thompson, P. E.; Velkov, T.; Li, J., Measuring polymyxin uptake by renal tubular cells: is BODIPY-polymyxin B an appropriate probe? *Antimicrobial agents and chemotherapy* **2014,** *58* (10), 6337-6338.

92. Janeway, C. A., Jr.; Medzhitov, R., Introduction: the role of innate immunity in the adaptive immune response. *Semin Immunol* **1998,** *10* (5), 349-50.

93. Bianchi, M. E., DAMPs, PAMPs and alarmins: all we need to know about danger. *J Leukoc Biol* **2007,** *81* (1), 1-5.

94. Lemaitre, B.; Nicolas, E.; Michaut, L.; Reichhart, J. M.; Hoffmann, J. A., The dorsoventral regulatory gene cassette spatzle/Toll/cactus controls the potent antifungal response in Drosophila adults. *Cell* **1996,** *86* (6), 973-83.

95. Leon, C. G.; Tory, R.; Jia, J.; Sivak, O.; Wasan, K. M., Discovery and development of toll-like receptor 4 (TLR4) antagonists: a new paradigm for treating sepsis and other diseases. *Pharm Res* **2008,** *25* (8), 1751-61.

96. Janeway, C. A. In *Approaching the asymptote? Evolution and revolution in immunology*, Cold Spring Harbor symposia on quantitative biology, Cold Spring Harbor Laboratory Press: 1989; pp 1-13.

97. Dobrovolskaia, M. A.; Vogel, S. N., Toll receptors, CD14, and macrophage activation and deactivation by LPS. *Microbes and Infection* **2002,** *4* (9), 903-914.

98. Needham, B. D.; Trent, M. S., Fortifying the barrier: the impact of lipid A remodelling on bacterial pathogenesis. *Nat Rev Microbiol* **2013,** *11* (7), 467-81.

99. Wright, S. D.; Ramos, R. A.; Tobias, P. S.; Ulevitch, R. J.; Mathison, J. C., CD14, a receptor for complexes of lipopolysaccharide (LPS) and LPS binding protein. *Science* **1990,** *249* (4975), 1431-3.

100. (a) Shimazu, R.; Akashi, S.; Ogata, H.; Nagai, Y.; Fukudome, K.; Miyake, K.; Kimoto, M., MD-2, a molecule that confers lipopolysaccharide responsiveness on Toll-like receptor 4. *J Exp Med* **1999,** *189* (11), 1777-82; (b) Nagai, Y.; Akashi, S.; Nagafuku, M.; Ogata, M.; Iwakura, Y.; Akira, S.; Kitamura, T.; Kosugi, A.; Kimoto, M.; Miyake, K., Essential role of MD-2 in LPS responsiveness and TLR4 distribution. *Nat Immunol* **2002,** *3* (7), 667-72.

101. Medzhitov, R.; Preston-Hurlburt, P.; Janeway, C. A., Jr., A human homologue of the Drosophila Toll protein signals activation of adaptive immunity. *Nature* **1997,** *388* (6640), 394-7.

102. Jiang, Z.; Georgel, P.; Du, X.; Shamel, L.; Sovath, S.; Mudd, S.; Huber, M.; Kalis, C.; Keck, S.; Galanos, C.; Freudenberg, M.; Beutler, B., CD14 is required for MyD88-independent LPS signaling. *Nat Immunol* **2005,** *6* (6), 565-70.

103. (a) Ganz, T.; Lehrer, R. I., Antibiotic peptides from higher eukaryotes: biology and applications. *Mol Med Today* **1999,** *5* (7), 292-7; (b) Steinstraesser, L.; Kraneburg, U.; Jacobsen, F.; Al-Benna, S., Host defense peptides and their antimicrobial-immunomodulatory duality. *Immunobiology* **2011,** *216* (3), 322-33.

104. Zanetti, M., Cathelicidins, multifunctional peptides of the innate immunity. *J Leukoc Biol* **2004,** *75* (1), 39-48.

105. Gautier, R.; Douguet, D.; Antonny, B.; Drin, G., HELIQUEST: a web server to screen sequences with specific alpha-helical properties. *Bioinformatics* **2008,** *24* (18), 2101-2.

106. Dannehl, C.; Gutsmann, T.; Brezesinski, G., Surface activity and structures of two fragments of the human antimicrobial LL-37. *Colloids and Surfaces B: Biointerfaces* **2013,** *109*, 129-135.

107. Larrick, J. W.; Hirata, M.; Shimomoura, Y.; Yoshida, M.; Zheng, H.; Zhong, J.; Wright, S. C., Antimicrobial activity of rabbit CAP18-derived peptides. *Antimicrob Agents Chemother* **1993,** *37* (12), 2534-9.

108. Gallo, R. L.; Kim, K. J.; Bernfield, M.; Kozak, C. A.; Zanetti, M.; Merluzzi, L.; Gennaro, R., Identification of CRAMP, a cathelin-related antimicrobial peptide expressed in the embryonic and adult mouse. *J Biol Chem* **1997,** *272* (20), 13088-93.

109. Risso, A.; Zanetti, M.; Gennaro, R., Cytotoxicity and apoptosis mediated by two peptides of innate immunity. *Cell Immunol* **1998,** *189* (2), 107-15.

110. Gutsmann, T.; Hagge, S. O.; David, A.; Roes, S.; Bohling, A.; Hammer, M. U.; Seydel, U., Lipid-mediated resistance of Gram-negative bacteria against various pore-forming antimicrobial peptides. *J Endotoxin Res* **2005,** *11* (3), 167-73.

111. Ovchinnikova, T. V.; Aleshina, G. M.; Balandin, S. V.; Krasnosdembskaya, A. D.; Markelov, M. L.; Frolova, E. I.; Leonova, Y. F.; Tagaev, A. A.; Krasnodembsky, E. G.; Kokryakov, V. N., Purification and primary structure of two isoforms of arenicin, a novel antimicrobial peptide from marine polychaeta Arenicola marina. *FEBS Lett* **2004,** *577* (1-2), 209-14.

112. Cho, J.; Lee, D. G., The antimicrobial peptide arenicin-1 promotes generation of reactive oxygen species and induction of apoptosis. *Biochim Biophys Acta* **2011,** *1810* (12), 1246-51.

113. (a) Andra, J.; Leippe, M., Candidacidal activity of shortened synthetic analogs of amoebapores and NK-lysin. *Med Microbiol Immunol* **1999,** *188* (3), 117-24; (b) Schroder-Borm, H.; Willumeit, R.; Brandenburg, K.; Andra, J., Molecular basis for membrane selectivity of NK-2, a potent peptide antibiotic derived from NK-lysin. *Biochim Biophys Acta* **2003,** *1612* (2), 164-71.

114. Gouaux, J. E.; Braha, O.; Hobaugh, M. R.; Song, L.; Cheley, S.; Shustak, C.; Bayley, H., Subunit stoichiometry of staphylococcal alpha-hemolysin in crystals and on membranes: a heptameric transmembrane pore. *Proc Natl Acad Sci U S A* **1994,** *91* (26), 12828-31.

115. Bantel, H.; Sinha, B.; Domschke, W.; Peters, G.; Schulze-Osthoff, K.; Jänicke, R. U., α-Toxin is a mediator of Staphylococcus aureus–induced cell

death and activates caspases via the intrinsic death pathway independently of death receptor signaling. *The Journal of cell biology* **2001,** *155* (4), 637-648.

116. Galanos, C.; Lüderitz, O.; Westphal, O., A new method for the extraction of R lipopolysaccharides. *European Journal of Biochemistry* **1969,** *9* (2), 245-249.

117. (a) Brabetz, W.; Muller-Loennies, S.; Brade, H., 3-Deoxy-D-manno-oct-2-ulosonic acid (Kdo) transferase (WaaA) and kdo kinase (KdkA) of Haemophilus influenzae are both required to complement a waaA knockout mutation of Escherichia coli. *J Biol Chem* **2000,** *275* (45), 34954-62; (b) Brabetz, W.; Schirmer, C. E.; Brade, H., 3-Deoxy-D-manno-oct-2-ulosonic acid (Kdo) transferase of Legionella pneumophila transfers two kdo residues to a structurally different lipid A precursor of Escherichia coli. *J Bacteriol* **2000,** *182* (16), 4654-7.

118. (a) Alexander, C.; Rietschel, E. T., Bacterial lipopolysaccharides and innate immunity. *J Endotoxin Res* **2001,** *7* (3), 167-202; (b) Garcia-Verdugo, I.; Sanchez-Barbero, F.; Soldau, K.; Tobias, P. S.; Casals, C., Interaction of SP-A (surfactant protein A) with bacterial rough lipopolysaccharide (Re-LPS), and effects of SP-A on the binding of Re-LPS to CD14 and LPS-binding protein. *Biochem J* **2005,** *391* (Pt 1), 115-24.

119. Parameswaran, N.; Patial, S., Tumor necrosis factor-alpha signaling in macrophages. *Crit Rev Eukaryot Gene Expr* **2010,** *20* (2), 87-103.

120. Schmidt, M.; Raghavan, B.; Müller, V.; Vogl, T.; Fejer, G.; Tchaptchet, S.; Keck, S.; Kalis, C.; Nielsen, P. J.; Galanos, C., Crucial role for human Toll-like receptor 4 in the development of contact allergy to nickel. *Nature immunology* **2010,** *11* (9), 814-819.

121. Vogl, T.; Tenbrock, K.; Ludwig, S.; Leukert, N.; Ehrhardt, C.; van Zoelen, M. A.; Nacken, W.; Foell, D.; van der Poll, T.; Sorg, C.; Roth, J., Mrp8 and Mrp14 are endogenous activators of Toll-like receptor 4, promoting lethal, endotoxin-induced shock. *Nat Med* **2007,** *13* (9), 1042-9.

122. Dulbecco, R.; Vogt, M., Plaque formation and isolation of pure lines with poliomyelitis viruses. *J Exp Med* **1954,** *99* (2), 167-82.

123. Moore, G. E.; Gerner, R. E.; Franklin, H. A., Culture of normal human leukocytes. *JAMA* **1967,** *199* (8), 519-24.

124. Dulbecco, R.; Freeman, G., Plaque production by the polyoma virus. *Virology* **1959,** *8* (3), 396-7.

125. Ladokhin, A. S.; Wimley, W. C.; White, S. H., Leakage of membrane vesicle contents: determination of mechanism using fluorescence requenching. *Biophys J* **1995,** *69* (5), 1964-71.

126. Matsuzaki, K.; Yoneyama, S.; Miyajima, K., Pore formation and translocation of melittin. *Biophys J* **1997,** *73* (2), 831-8.

127. Montal, M.; Mueller, P., Formation of bimolecular membranes from lipid monolayers and a study of their electrical properties. *Proc Natl Acad Sci U S A* **1972,** *69* (12), 3561-6.

128. (a) Szoka Jr, F.; Papahadjopoulos, D., Comparative properties and methods of preparation of lipid vesicles (liposomes). *Annual review of biophysics and bioengineering* **1980,** *9* (1), 467-508; (b) Huang, C.-H., Phosphatidylcholine vesicles. Formation and physical characteristics. *Biochemistry* **1969,** *8* (1), 344-352.

129. Wesolowska, O.; Michalak, K.; Maniewska, J.; Hendrich, A. B., Giant unilamellar vesicles - a perfect tool to visualize phase separation and lipid rafts in model systems. *Acta Biochim Pol* **2009,** *56* (1), 33-9.

130. Angelova, M. I.; Dimitrov, D. S., Liposome electroformation. *Faraday discussions of the Chemical Society* **1986,** *81*, 303-311.

131. Veatch, S. L., Electro-formation and fluorescence microscopy of giant vesicles with coexisting liquid phases. *Methods Mol Biol* **2007,** *398*, 59-72.

132. (a) Latal, A.; Degovics, G.; Epand, R. F.; Epand, R. M.; Lohner, K., Structural aspects of the interaction of peptidyl-glycylleucine-carboxyamide, a highly potent antimicrobial peptide from frog skin, with lipids. *Eur J Biochem* **1997,** *248* (3), 938-46; (b) Lohner, K., *Development of novel antimicrobial agents: emerging strategies*. Horizon Scientific Press: 2001.

133. Pabst, G.; Kučerka, N.; Nieh, M.-P.; Katsaras, J., *Liposomes, lipid bilayers and model membranes: from basic research to application*. CRC Press: 2014.

134. Huang, H. W., Molecular mechanism of antimicrobial peptides: the origin of cooperativity. *Biochim Biophys Acta* **2006,** *1758* (9), 1292-302.

135. Wimley, W. C.; Hristova, K., Antimicrobial peptides: successes, challenges and unanswered questions. *J Membr Biol* **2011,** *239* (1-2), 27-34.

136. (a) Weinstein, J. N.; Yoshikami, S.; Henkart, P.; Blumenthal, R.; Hagins, W. A., Liposome-cell interaction: transfer and intracellular release of a trapped fluorescent marker. *Science* **1977,** *195* (4277), 489-92; (b) Blumenthal, R.; Weinstein, J. N.; Sharrow, S. O.; Henkart, P., Liposome--lymphocyte interaction: saturable sites for transfer and intracellular release of liposome contents. *Proc Natl Acad Sci U S A* **1977,** *74* (12), 5603-7.

137. (a) Patel, H.; Tscheka, C.; Heerklotz, H., Characterizing vesicle leakage by fluorescence lifetime measurements. *Soft Matter* **2009,** *5* (15), 2849-2851; (b) Andersson, A.; Danielsson, J.; Gräslund, A.; Mäler, L., Kinetic models for peptide-induced leakage from vesicles and cells. *European Biophysics Journal* **2007,** *36* (6), 621-635.

138. Torchilin, V.; Weissig, V., *Liposomes: a practical approach*. Oxford University Press: 2003.

139. (a) Bu, J. H.; Zheng, Q. Y.; Chen, C. F.; Huang, Z. T., New fluorescence-quenching process through resumption of PET process induced by complexation of alkali metal ion. *Org Lett* **2004,** *6* (19), 3301-3; (b) Lakowicz, J. R., *Principles of fluorescence spectroscopy*. Springer Science & Business Media: 2013.

140. (a) Lehrer, S., Solute perturbation of protein fluorescence. Quenching of the tryptophyl fluorescence of model compounds and of lysozyme by iodide ion. *Biochemistry* **1971,** *10* (17), 3254-3263; (b) Pownall, H. J.; Smith, L. C., Fluorescence quenching of anthracene in charged micelles by pyridinium and iodide ions. *Biochemistry* **1974,** *13* (12), 2594-2597; (c) Christiaens, B.; Symoens, S.; Vanderheyden, S.; Engelborghs, Y.; Joliot, A.; Prochiantz, A.; Vandekerckhove, J.; Rosseneu, M.; Vanloo, B., Tryptophan fluorescence study of the interaction of penetratin peptides with model membranes. *European Journal of Biochemistry* **2002,** *269* (12), 2918-2926.

141. Kusters, I.; van Oijen, A. M.; Driessen, A. J., Membrane-on-a-chip: microstructured silicon/silicon-dioxide chips for high-throughput screening of membrane transport and viral membrane fusion. *ACS Nano* **2014,** *8* (4), 3380-92.

142. Gebauer, N. Charakterisierung der membranpermeabilisierenden Aktivität von antimikrobiellen Peptiden an Bakterien und rekonstituierten

Lipidmembranen. Master Thesis, Hamburg University of Applied Sciences, Research Center Borstel, 2015.

143. Krishna, G.; Schulte, J.; Cornell, B. A.; Pace, R. J.; Osman, P. D., Tethered bilayer membranes containing ionic reservoirs: selectivity and conductance. *Langmuir* **2003,** *19* (6), 2294-2305.

144. Cranfield, C.; Carne, S.; Martinac, B.; Cornell, B., The assembly and use of tethered bilayer lipid membranes (tBLMs). *Methods Mol Biol* **2015,** *1232*, 45-53.

145. Adam, G.; Läuger, P.; Stark, G., *Physikalische chemie und biophysik*. Springer-Verlag: 2009.

146. Boheim, G., Statistical analysis of alamethicin channels in black lipid membranes. *The Journal of membrane biology* **1974,** *19* (1), 277-303.

147. Gutsmann, T.; Heimburg, T.; Keyser, U.; Mahendran, K. R.; Winterhalter, M., Protein reconstitution into freestanding planar lipid membranes for electrophysiological characterization. *Nat Protoc* **2015,** *10* (1), 188-98.

148. Boukobza, E.; Sonnenfeld, A.; Haran, G., Immobilization in surface-tethered lipid vesicles as a new tool for single biomolecule spectroscopy. *The Journal of Physical Chemistry B* **2001,** *105* (48), 12165-12170.

149. (a) Groves, J. T.; Wulfing, C.; Boxer, S. G., Electrical manipulation of glycan-phosphatidyl inositol-tethered proteins in planar supported bilayers. *Biophys J* **1996,** *71* (5), 2716-23; (b) Bayerl, T. M.; Bloom, M., Physical properties of single phospholipid bilayers adsorbed to micro glass beads. A new vesicular model system studied by 2H-nuclear magnetic resonance. *Biophys J* **1990,** *58* (2), 357-62; (c) Johnson, S. J.; Bayerl, T. M.; McDermott, D. C.; Adam, G. W.; Rennie, A. R.; Thomas, R. K.; Sackmann, E., Structure of an adsorbed dimyristoylphosphatidylcholine bilayer measured with specular reflection of neutrons. *Biophys J* **1991,** *59* (2), 289-94.

150. Carisey, A.; Stroud, M.; Tsang, R.; Ballestrem, C., Fluorescence recovery after photobleaching. *Cell Migration: Developmental Methods and Protocols* **2011**, 387-402.

151. Borner, R.; Ehrlich, N.; Hohlbein, J.; Hubner, C. G., Single Molecule 3D Orientation in Time and Space: A 6D Dynamic Study on Fluorescently Labeled Lipid Membranes. *J Fluoresc* **2016,** *26* (3), 963-75.

152. Bartlett, P. N., *Bioelectrochemistry: fundamentals, experimental techniques and applications*. John Wiley & Sons: 2008.

153. Bolze, J.; Fujisawa, T.; Nagao, T.; Norisada, K.; Saitô, H.; Naito, A., Small angle X-ray scattering and 31 P NMR studies on the phase behavior of phospholipid bilayered mixed micelles. *Chemical Physics Letters* **2000,** *329* (3), 215-220.

154. Wallace, B. A., Protein characterisation by synchrotron radiation circular dichroism spectroscopy. *Quarterly reviews of biophysics* **2009,** *42* (04), 317-370.

155. Burck, J.; Roth, S.; Windisch, D.; Wadhwani, P.; Moss, D.; Ulrich, A. S., UV-CD12: synchrotron radiation circular dichroism beamline at ANKA. *J Synchrotron Radiat* **2015,** *22* (Pt 3), 844-52.

156. Lees, J. G.; Smith, B. R.; Wien, F.; Miles, A. J.; Wallace, B. A., CDtool-an integrated software package for circular dichroism spectroscopic data processing, analysis, and archiving. *Anal Biochem* **2004,** *332* (2), 285-9.

157. Burck, J.; Wadhwani, P.; Fanghanel, S.; Ulrich, A. S., Oriented Circular Dichroism: A Method to Characterize Membrane-Active Peptides in Oriented Lipid Bilayers. *Acc Chem Res* **2016,** *49* (2), 184-92.

158. Joseph, J. S.; Liu, W.; Kunken, J.; Weiss, T. M.; Tsuruta, H.; Cherezov, V., Characterization of lipid matrices for membrane protein crystallization by high-throughput small angle X-ray scattering. *Methods* **2011,** *55* (4), 342-9.

159. Wallace, B. A.; Lees, J. G.; Orry, A. J.; Lobley, A.; Janes, R. W., Analyses of circular dichroism spectra of membrane proteins. *Protein Sci* **2003,** *12* (4), 875-84.

160. Byrd-Leifer, C. A.; Block, E. F.; Takeda, K.; Akira, S.; Ding, A., The role of MyD88 and TLR4 in the LPS-mimetic activity of Taxol. *European journal of immunology* **2001,** *31* (8), 2448-2457.

161. Kim, S.; Kim, S. Y.; Pribis, J. P.; Lotze, M.; Mollen, K. P.; Shapiro, R.; Loughran, P.; Scott, M. J.; Billiar, T. R., Signaling of high mobility group box 1 (HMGB1) through toll-like receptor 4 in macrophages requires CD14. *Mol Med* **2013,** *19* (5), 88-98.

162. Nguyen, L. T.; Haney, E. F.; Vogel, H. J., The expanding scope of antimicrobial peptide structures and their modes of action. *Trends Biotechnol* **2011,** *29* (9), 464-72.

163. Matsuzaki, K.; Sugishita, K.; Fujii, N.; Miyajima, K., Molecular basis for membrane selectivity of an antimicrobial peptide, magainin 2. *Biochemistry* **1995,** *34* (10), 3423-9.

164. Matsuzaki, K.; Murase, O.; Fujii, N.; Miyajima, K., Translocation of a channel-forming antimicrobial peptide, magainin 2, across lipid bilayers by forming a pore. *Biochemistry* **1995,** *34* (19), 6521-6.

165. Newton, B. A., The properties and mode of action of the polymyxins. *Bacteriol Rev* **1956,** *20* (1), 14-27.

166. HsuChen, C. C.; Feingold, D. S., The mechanism of polymyxin B action and selectivity toward biologic membranes. *Biochemistry* **1973,** *12* (11), 2105-11.

167. Miller, I.; Bach, D.; Teuber, M., Effect of polymyxin B on the structure and the stability of lipid layers. *The Journal of membrane biology* **1978,** *39* (1), 49-56.

168. Wiese, A.; Münstermann, M.; Gutsmann, T.; Lindner, B.; Kawahara, K.; Zähringer, U.; Seydel, U., Molecular mechanisms of polymyxin B-membrane interactions: direct correlation between surface charge density and self-promoted transport. *The Journal of membrane biology* **1998,** *162* (2), 127-138.

169. Pieters, J., Entry and survival of pathogenic mycobacteria in macrophages. *Microbes Infect* **2001,** *3* (3), 249-55.

170. Jutras, I.; Abrami, L.; Dautry-Varsat, A., Entry of the lymphogranuloma venereum strain of Chlamydia trachomatis into host cells involves cholesterol-rich membrane domains. *Infect Immun* **2003,** *71* (1), 260-6.

171. Ourisson, G.; Rohmer, M.; Poralla, K., Prokaryotic hopanoids and other polyterpenoid sterol surrogates. *Annu Rev Microbiol* **1987,** *41*, 301-33.

172. Saenz, J. P.; Sezgin, E.; Schwille, P.; Simons, K., Functional convergence of hopanoids and sterols in membrane ordering. *Proc Natl Acad Sci U S A* **2012,** *109* (35), 14236-40.

173. Nikaido, H.; Vaara, M., Molecular basis of bacterial outer membrane permeability. *Microbiol Rev* **1985,** *49* (1), 1-32.

174. Brandenburg, K.; Seydel, U., Investigation into the fluidity of lipopolysaccharide and free lipid A membrane systems by Fourier-transform infrared spectroscopy and differential scanning calorimetry. *Eur J Biochem* **1990,** *191* (1), 229-36.

175. Pelkmans, L.; Helenius, A., Endocytosis via caveolae. *Traffic* **2002,** *3* (5), 311-20.

176. van Duyl, B. Y.; Meeldijk, H.; Verkleij, A. J.; Rijkers, D. T.; Chupin, V.; de Kruijff, B.; Killian, J. A., A synergistic effect between cholesterol and tryptophan-flanked transmembrane helices modulates membrane curvature. *Biochemistry* **2005,** *44* (11), 4526-4532.

177. Grau-Campistany, A.; Manresa, Á.; Pujol, M.; Rabanal, F.; Cajal, Y., Tryptophan-containing lipopeptide antibiotics derived from polymyxin B with activity against Gram positive and Gram negative bacteria. *Biochimica et Biophysica Acta (BBA)-Biomembranes* **2016,** *1858* (2), 333-343.

178. Gazit, E.; Miller, I. R.; Biggin, P. C.; Sansom, M. S.; Shai, Y., Structure and orientation of the mammalian antibacterial peptide cecropin P1 within phospholipid membranes. *J Mol Biol* **1996,** *258* (5), 860-70.

179. (a) Bechinger, B.; Lohner, K., Detergent-like actions of linear amphipathic cationic antimicrobial peptides. *Biochim Biophys Acta* **2006,** *1758* (9), 1529-39; (b) Epand, R. M.; Epand, R. F., Domains in bacterial membranes and the action of antimicrobial agents. *Mol Biosyst* **2009,** *5* (6), 580-7.

180. Morrison, D. C.; Jacobs, D. M., Binding of polymyxin B to the lipid A portion of bacterial lipopolysaccharides. *Immunochemistry* **1976,** *13* (10), 813-8.

181. Nagaoka, I.; Hirota, S.; Niyonsaba, F.; Hirata, M.; Adachi, Y.; Tamura, H.; Heumann, D., Cathelicidin family of antibacterial peptides CAP18 and CAP11 inhibit the expression of TNF-alpha by blocking the binding of LPS to CD14(+) cells. *J Immunol* **2001,** *167* (6), 3329-38.

182. Pape, H.-C.; Kurtz, A.; Silbernagl, S., *Physiologie*. Georg Thieme Verlag: 2014.

183. WHO *Antimicrobial Resistance: Global report on surveillance*; 2014; p 256.

LIST OF FIGURES

List of Tables

LIST OF ABBREVIATIONS

TABLE 23. COMMON USED ABBREVIATIONS AND SPECIAL CHARACTERS

#	number of	**max**	maximum
%	percentage	**mbar**	millibar
Ø	diameter	**mβ-CD**	methyl-β-cyclodextrin
(v/v)	volume per volume	**MCR**	Maximum capacity reachable
(w/v)	weight per volume	**M-CSF**	macrophage colony-stimulating factor
°	degree	**MD2**	Myeloid differentiation 2
Å	Angstrom	**MeOH**	methanol
a.u.	arbitrary units	**mg**	milligram
AB	AB blood type, human serum	**MIC**	minimal inhibitory concentration, no culture growth
Ag/AgCl	silver/silver chloride	**MilliQ**	ultra-pure water
AMP(s)	antimicrobial peptides	**min**	minutes
arenicin-1	arenicin isoform 1	**MKK6**	Mitogen-activated protein kinase kinase 6
ATP	adenosine triphosphate	**mL**	milliliter
BFS	Bovine fetal serum	**MLV**	Multi lamellar vesicle
BMAP	bovine myeloid antimicrobial peptide	**mm**	millimeter
BODIPY	boron-dipyrromethene	**mM**	millimolar [mmol/L]
c	concentration	**MNC**	Mononuclear cell, monocyte
C_m	membrane capacitance	**mol%**	mol percent

$C_{m,s}$	specific membrane capacitance
CAP18	18 kDa cationic antimicrobial protein
CD	circular dichroism
CD14	cluster of differentiation 14
$CHCl_3$	chloroform
Chol	cholesterol
CLSM	confocal laser scanning microscopy
CO_2	carbon dioxide
cm	centimeter
cps	counts per second
CRAMP	cathelicidin-related antimicrobial peptide
DAB	L-α,γ-diaminobutyric acid
DAMP	damage-associated molecular patterns
D_{av}	average repeat distance
DMEM	Dulbecco's Modified Eagle Medium
DMF	dimethylformamide
DNA	deoxyribonucleic acid
DOPC	1,2-dioleoyl-*sn*-glycero-3-phosphatidylcholine
DRM	detergent resistant membrane
E. coli	*Escherichia coli*
ED	electron density
e.g.	*exempli gratia*, for example
ELISA	enzyme-linked immunosorbent assay
Em	emission
ER	endoplasmic reticulum
EtOH	ethanol
et seqq.	*et sequentia*, the following
Ex	excitation
F	Farad
FACS	fluorescence-activated cell sorting
FCS	fetal calf serum
MRP8	Myeloid-related protein 8
MTT	3-(4,5-dimethylthiazol-2-yl)-2,5-diphenyltetrazolium bromide
mV	millivolt
mW	milliwatt
MW	Molecular weight
MyD88	Myeloid differentiation primary-response gene 88
N	normal
NaCl	Sodium chloride
NAD(P)H	Nicotinamide adenine dinucleotide (phosphate)
NaOH	Sodium hydroxide
N_{av}	Average # of spatial correlating bilayers in the stack
NBD	*N*-7-Nitro-2,1,3-benzoxadiazole-4-yl
NF-κβ	Nuclear factor kappa beta
ng	nanogram
NHS	*N*-hydroxysuccinimide
nm	nanometer
nM	Nanomolar [nmol/L]
OCD	oriented circular dichroism
Opti-MEM	Optimized minimal essential medium
p	probability
P/L	Peptide/lipid ratio
p.a.	*pro analysi*, analytically pure
PAMP	pathogen-associated molecular patterns
PBS	phosphate buffered saline
PE	phosphatidylethanolamine
PEG	polyethylene glycol
PFA	*para*-formaldehyde
pg	picogram
PG	phosphatidylglycerol
pH	*potential hydrogenii*
PKR	Protein kinase R

FCS	fluorescence correlation spectroscopy
Fmoc	fluorenylmethyloxycarbonyl
FRAP	fluorescence recovery after photobleaching
FRET	FÖRSTER resonance energy transfer
FWHM	full width at half max
GISAXS	grazing incidence small angle X-ray scattering
GM1	
GPI	glycosylphosphatidylinositol
GUV	giant unilamellar vesicle
h	height
h	hours
hBD	Human beta-defensin
hBD-3-l	Human beta-defensin-3, linear (with cleaved disulfide bonds)
HCl	hydrochloric acid
HDP(s)	host defense peptides
HEK	human embryonic kidney
HEPES	2-[4-(2-hydroxyethyl)-piperazin-1-yl]-ethane sulfonic acid
HMGB1	high motility group box 1
hMϕ	human macrophage
HNO_3	Nitric acid
HPLC	High-performance liquid chromatography
HSS	Hanks saline solution
Hz	Hertz
Ia	Lipid A precursor
IFN	interferon
Ig	immunoglobulin
IL-1	Interleukin 1
IL-8	Interleukin 8
IL-1β	Interleukin 1β
IL-1R	Interleukin 1 receptor
IRAK	IL-1R-associated protein kinase
pm	picometer
PMB	polymyxin B
PMT	photo multiplier transmission
POPE	1-palmitoyl-2-oleoyl-*sn*-glycero-3-phosphoethanolamine
POPG	1-palmitoyl-2-oleoyl-*sn*-glycero-3-phosphoglycerole
PRR	pattern-recognition receptors
PS	phosphatidylserine
PS/Glu	Penicillin-Streptomycin/Glutamine
q.v.	*quod vide*, confer to
R	any group
R_m	membrane resistance
Rho	Rhodamine B
Rho-DHPE	*N*-(rhodamine B sulfonyl)-dihexadecanoyl-phosphatidylethanolamine
RNA	ribonucleic acid
ROI	Region of interest
rpm	revolutions per minute
(VLE) RPMI	(very low endotoxin) Roswell Park Memorial Institute
rt	room temperature
s	seconds
S100A8	Calcium-binding protein A8
SAXS	small angle X-ray scattering
SD	standard deviation
SEC	size exclusion chromatography
SM	sphingomyelin
SMH	Shai-Matsuzaki-Huang
SUV	small unilamellar vesicle
t	time point
TAK1	TGF-β-activated kinase 1
TIR	Toll/IL-1 receptor
TFA	trifluoroacetic acid
TGF-β	transforming growth factor beta

IRF	Interferon regulatory factor	**TIRAP**	Toll/interleukin-1 receptor domain-containing adaptor protein
ITO	Indium tin oxide	**TLR**	Toll like receptor
IU	International units	**TNF-α**	Tumor necrosis factor alpha
JNK	c-Jun N-terminal kinase	**TOLLIP**	Toll-interacting protein
KBr	potassium bromide	**TRAF6**	TNF-receptor associated factor 6
kDa	kilo Dalton	**TRAM**	TRIF-related adaptor molecule
KDO	2-keto-3-deoxyoctulosonate	**TRIF**	TIR-domain-containing adaptor-inducing interferon-β
KI	potassium iodide	**TX-100**	Triton X-100
L	liter	**U**	Atomic unit
LALF	*Limulus* anti-LPS factor	**UV**	Ultra violet
LBP	LPS-binding protein	**V**	Volt
LCD	liquid circular dichroism	**V**	volume
L_D	liquid-disordered	**w/**	with
LL-32	carboxy-terminal truncated fragment of LL-37	**w/o**	without
L_O	liquid-ordered	**WAXS**	wide angle X-ray scattering
LOS	lipooligosaccharide	**XRR**	X-ray reflectivity
LPS	lipopolysaccharide	**z**	net charge
LRR	leucine-rich repeat	**µg**	microgram
LY96	lymphocyte antigen 96	**µH**	hydrophobic moment
M	molar [mol/L]	**µL**	microliters
MAL	Myeloid differentiation primary-response gene 88 adaptor-like protein	**µm**	micrometer
MALDI-TOF MS	Matrix-assisted laser desorption ionization-time-of-flight mass spectrometry	**µS**	micro-Siemens
MAPK	Mitogen-activated protein kinase	**µW**	microwatt

LIST OF DEVICES & EQUIPMENT

TABLE 24. USED DEVICES AND EQUIPMENT WITH CORRESPONDING MANUFACTURING COMPANY DATA

Device	Supplier
Block heater, Stuart® test tube heater SHT1	Bibby Scientific Ltd., Staffordshire, UK
Block thermostat MBT 250	Kleinfeld Labortechnik, Gehrden, Germany
Centrifuge, Eppendorf® 5415 R	Eppendorf AG, Hamburg Germany
Centrifuge, Eppendorf® 5810 R	Eppendorf AG, Hamburg Germany
Centrifuge, Varifuge K	Heraeus-Christ, Osterode, Germany
Centrifuge, Labofuge	Heraeus-Christ, Osterode, Germany
Electroformation chamber w/ laboratory sand-bath	in-house
Eppendorf® Reference®, adjustable pipette, 10 µL	Eppendorf AG, Hamburg Germany
Eppendorf® Reference®, adjustable pipette, 100 µL	Eppendorf AG, Hamburg Germany
Eppendorf® Reference®, adjustable pipette, 1000 µL	Eppendorf AG, Hamburg Germany
Eppendorf® Reference®, adjustable pipette, 20 µL	Eppendorf AG, Hamburg Germany
Eppendorf® Reference®, adjustable pipette, 200 µL	Eppendorf AG, Hamburg Germany
Eppendorf® Reference®, adjustable pipette, 2500 µL	Eppendorf AG, Hamburg Germany
Eppendorf® Reference®2, adjustable pipette, 20 µL	Eppendorf AG, Hamburg Germany
Eppendorf® Research®, adjustable multichannel pipette, 300 µL	Eppendorf AG, Hamburg Germany
Eppendorf® Research®Pro, adjustable multichannel pipette, 1200 µL	Eppendorf AG, Hamburg Germany
EVE™ Automated Cell Counter	NanoEnTek Inc., Seoul, Korea
Hamilton GASTIGHT® Syringe, 1000 series, 1000 µL	Hamilton Robotics, Bonaduz, GR, Switzerland
Hamilton GASTIGHT® Syringe, 1700 series, 500 µL	Hamilton Robotics, Bonaduz, GR, Switzerland
HandyStep®, repeating pipette	BrandTech® Scientific, Essex, CT, USA

Hotplate stirrer, Stuart® heat-stir CB162	Bibby Scientific Ltd., Staffordshire, UK
Inverted fluorescence microscope, IX-71, manual system	Olympus, Hamburg, Germany
Inverted fluorescence microscope, IX-81, motorized system	Olympus, Hamburg, Germany
Leica TCS SP5	Leica Microsystems GmbH, Wetzlar, Germany
Microscope Wilozyt V 365	Helmut Hund GmbH, Wetzlar, Germany
Milli-Q Advantage A10	Millipore, Billerica, MA, USA
Oscilloscope, Tektronix TDS 220	Tektronix GmbH, Cologne, Germany
Patch Clamp Amplifier, Model EPC-7	List-Medical/HEKA, Darmstadt, Germany
Pipetboy acu	INTEGRA Biosciences AG, Zizers, Switzerland
Plasma Cleaner Zepto	Diener electronics GmbH & Co KG, Ebhausen, Germany
Primovert, inverted microscope	Zeiss, Oberkochen, Germany
Sonifier Cell Disruptor B15	Branson Ultrasonics Corporation, Danbury, CT, USA
Sonorex RK100 ultrasonic bath	BANDELIN electronic GmbH & Co. KG, Berlin, Germany
Spark gap, BD-10AV High Frequency Generator, 230 V	Electro-Technic Products, Chicago, IL, USA
Spex Fluorolog/ Fluorolog 3	Horiba Jobin Yvon, Edison, NJ, USA
Tecan Infinite 200P	Tecan, Crailsheim, Germany
*tetha*Pod™	SDx Tethered Membranes, Sydney, Australia
TILL Photonics microscope	FEI Munich GmbH, formerly *TILL Photonics* GmbH, Gräfelfing, Germany
Transmission microscope	Zeiss, Oberkochen, Germany
Water bath for incubation/inactivation	GFL Gesellschaft für Labortechnik mbH, Burgwedel, Germany

LIST OF SOFTWARE & PROGRAMS

TABLE 25. DEVICE SPECIFIC SOFTWARE, PROGRAMS AND ONLINE TOOLS USED

Software	Release Information	Supplier
ExPASy ProtParam	n/a	http://www.expasy.org/protparam/
Fiji	1.49g Java 1.6.0_24 (64-bit)	*National Institutes of Health*, Bethesda, MD, USA
GraphPad Prism 5	Version 5.04 (2010)	*GraphPad Software*, Inc., La Jolla, CA, USA
HeliQuest	HeliQuest V2	http://heliquest.ipmc.cnrs.fr/cgi-bin/ComputParamsV2.py
IgorPro 6.37	Version 6.3.7.2. (2015)	*WaveMetrics*, Inc., Lake Oswego, OR, USA
ImageJ	1.48v Java 1.6.0_20 (64-bit)	*National Institutes of Health*, Bethesda, MD, USA
LabVIEW	Version 2013.0.1	National Instruments, Austin, TX, USA
Live Acquisition	Version 2.2.0 (2012)	*Fei Munich* GmbH, formerly *TILL Photonics*, Graefelfing, Germany
Magellan	Version 7.1 (2011)	*Tecan*, Crailsheim, Germany
Microcal™ Origin®	Version 6.0	*Microcal Software*, Inc., Northampton, MA, USA
Microsoft® Excel	Version 16.0.6868.2062	*Microsoft*, Redmond, WA, USA
Microsoft® Office 365	Version 15.0.4745.1002	*Microsoft*, Redmond, WA, USA
Microsoft® PowerPoint®	Version 16.0.6868.2062	*Microsoft*, Redmond, WA, USA
Microsoft® Word 2016 MSO	Version 16.0.6868.2062	*Microsoft*, Redmond, WA, USA
POV-Ray	Version 3.7.0	*Persistence of Vision Raytracer* Pty. Ltd., Williamstown, VIC, Australia
Python(x,y).Ink	Version 2.7.6.1	*Python Software Foundation*, Beaverton, OR, USA
Swiss-Pdb Viewer	DeepView v4.1	*Swiss Institute for Bioinformatics* (SIB), Lausanne, Switzerland
tethaPod™ software	SDx-APP1	*eDAQ* Pty Ltd, Denistone East, NSW, Australia

LIST OF CONSUMABLES

TABLE 26. LAB CONSUMABLES

Designation	Product #	Supplier
Ag/AgCl electrodes	E255	Science Products GmbH, Hofheim, Germany
BD Microlance™ 3, sterile, 0.45x10 mm	300300	Becton, Dickinson and Company, Franklin Lakes, NJ, USA
BD Microlance™ 3, sterile, 0.5x25 mm	300400	Becton, Dickinson and Company, Franklin Lakes, NJ, USA
BD Plastipak™ syringe, 1 mL, sterile	300013	Becton, Dickinson and Company, Franklin Lakes, NJ, USA
BD Plastipak™ syringe, 3 mL, sterile	309656	Becton, Dickinson and Company, Franklin Lakes, NJ, USA
C-Chip disposable hemocytometer, non-pyrogenic, Neubauer improved	DHC-N01	NanoEnTek inc. Seoul, Korea
Cell culture flask, TC Flask T75, 75cm^2, 21 mL, sterile, pyrogen-free, non-cytotoxic, canted neck, ventilation cap	83.3911.002	Sarstedt AG & Co, Nümbrecht, Germany
Corning®, CentriStar®, 50 mL, PP, centrifuge tubes, conical bottom with plug seal cap, sterile	430291	Corning® GmbH, Wiesbaden, Germany
Costar® 96 well cell culture cluster, flat bottom with lid, sterile, non-pyrogenic, polystyrene	3596	Corning Inc., NY, USA
Costar®, serological pipette, Stripette®, single wrapped, polystyrene, sterile 10 mL, sterile	4488	Corning Inc., NY, USA
Costar®, serological pipette, Stripette®, single wrapped, polystyrene, sterile 10 mL, sterile	4489	Corning Inc., NY, USA
Cover glass Boro water-white thick. no 1, 24x24 mm, square thickness 0.13-0.17 mm	470060	AL-Labortechnik, Amstetten, Austria
Cover glass Boro water-white thick. no 1, 24x40 mm, rectangular thickness 0.13-0.17 mm	470816	AL-Labortechnik, Amstetten, Austria
Dispenser tips, classical type, 0.5 mL, sterile	613-1009	VWR International, Darmstadt, Germany
Dispenser tips, classical type, 1.25 mL, sterile	613-1010	VWR International, Darmstadt, Germany
Dispenser tips, classical type, 12.5 mL, sterile	613-1013	VWR International, Darmstadt, Germany
Dispenser tips, classical type, 2.5 mL, sterile	613-1011	VWR International, Darmstadt, Germany

Dispenser tips, classical type, 5.0 mL, sterile	613-1012	VWR International, Darmstadt, Germany
Eppendorf Protein LoBind Tubes, 0.5 mL, PCR clean	0030108094	Eppendorf AG, Hamburg, Germany
Eppendorf® GELoader®, 62 mm, 0.5-20 µL	0030001222	Eppendorf AG, Hamburg, Germany
EVE™ cell counting slides,	EVS-050	NanoEnTek inc. Seoul, Korea
Glass vial N8-1, 1.5 mL for screw cap	70213	Macherey-Nagel, Düren, Germany
Hellma® fluorescence cuvettes, Suprasil® quartz, pathlength 10x10 mm, 3.5 mL	Hellma 101-QS	Hellma Analytics, Muellheim, Germany
Ibidi cover slip for sticky-slides, unsterile, 75x25 mm	10812	Ibidi GmbH, Martinsried, Germany
Ibidi sticky-Slide 8 well, microscopy chamber, sterile	80828	Ibidi GmbH, Martinsried, Germany
ITO coated glass slides (sheet resistance of < 20 Ω)	n/a	PGO, Iserlohn, Germany
Lab-Tek® II chambered coverglass, with cover, #1.5 borosilicate, sterile, 8 well	155409	Nalge Nunc International, part of ThermoFisher Scientific Rochester, NY, USA
Lid for Nunc MaxiSorp®, sterile	263339	ThermoFisher Scientific Nunc A/S, Roskilde, Denmark
Micro tube 1,5 mL with cap, PP	72.692	Sarstedt AG & Co, Nümbrecht, Germany
Micro tube 1.5 mL, PP	72.690.001	Sarstedt AG & Co, Nümbrecht, Germany
Microscope slides, 76x26 mm (ISO Norm 8037/I), 20 mm frosted end, pre cleaned	03-0004	R. Langenbrinck, Emmendingen, Germany
Multiply®-Pro cup 0.5 mL, PP	72.735.002	Sarstedt AG & Co, Nümbrecht, Germany
Nunc® Immuno plate MaxiSorp®, sterile	442404	ThermoFisher Scientific Nunc A/S, Roskilde, Denmark
Nunc® MicroWell™ 96-Well plates with lid, black, sterile, non-treated	237105	ThermoFisher Scientific Nunc A/S, Roskilde, Denmark
PARAFILM® M, sealing film	3-1011	neoLab®, Heidelberg, Germany
Pipette Tip 200 µL, natural, 2-200 µL	70.760.002	Sarstedt AG & Co, Nümbrecht, Germany
Pipette Tip 10 µL, neutral, 0.1-20 µL	70.1115	Sarstedt AG & Co, Nümbrecht, Germany
Pipette Tip 1000 µL, natural, filling level rings, 50-1000 µL	70.762	Sarstedt AG & Co, Nümbrecht, Germany
Pipette Tip 20 µL, neutral, 0.1-20 µL	70.1116	Sarstedt AG & Co, Nümbrecht, Germany
SafeSeal micro tube 2 mL, PP	72.695.500	Sarstedt AG & Co, Nümbrecht, Germany

SAXS capillaries, quartz glass, 80x1.5 mm, wall thickness 0.01 mm	4017515	Hilgenberg GmbH, Malsfeld, Germany
Screw cap N8	70245	Macherey-Nagel, Düren, Germany
Sterican®, 0.8x120 mm, sterile	4665643	B. Braun Melsungen AG, Melsungen, Germany
Steritop-GP, 0.22 µm, polyethersulfone, 250 mL, 45 mm, radio-sterilized	SCGPT02RE	Merck Millipore, Darmstadt, Germany
Tesa® adhesive foil	n/a	Tesa®, Hamburg, Germany
Tubes with ventilation cap, sterile (13 mL, 100x16 mm, PP)	62.515.006	Sarstedt, Nümbrecht, Germany
Tubes, sterile, non-pyrogenic, red screw cap (50 mL, 114x28 mm, PP)	62.547.254	Sarstedt, Nümbrecht, Germany

LIST OF CHEMICALS & KITS

TABLE 27. CHEMICALS AND BUFFERS/MEDIA USED AND SUBSTANCES

Designation	Product #	Supplier
18:1 Biotinyl-PE	870282	Avanti® Polar Lipids, Inc., Alabaster, AL, USA
2-propanol, p.a.	33539	Sigma-Aldrich, St. Louis, MO, USA
Acetone, ACS reagent	179124	Sigma-Aldrich, St. Louis, MO, USA
Amplex® Red Cholesterol Assay Kit	A12216	Molecular Probes™, ThermoFisher Scientific Rochester, NY, USA
Atto488 carboxy, fluorophore, (MW 804 g/mol)	AD 488-2	AttoTec GmbH, Siegen, Germany
Atto633-DOPE, fluorescent phospholipids, (MW 1378 g/mol)	AD 633-161	AttoTec GmbH, Siegen, Germany
Avidin from egg white, lyophilized powder, 10-15 units/mg protein	A9275	Sigma-Aldrich, St. Louis, MO, USA
BD OptEIA™ human IL-8 ELISA Set	555244	Becton, Dickinson and Company, Franklin Lakes, NJ, USA
BD OptEIA™ human TNF-α ELISA Set	555212	Becton, Dickinson and Company, Franklin Lakes, NJ, USA
BFS (bovine fetal serum)	SBF-3111-PK	LINARIS Biologische Produkte GmbH, Dossenheim, Germany
BODIPY® FL-C_5 NHS Ester (Succinimidyl Ester)	D6184	Molecular Probes™, ThermoFisher Scientific Rochester, NY, USA
$CaCl_2$ x $2H_2O$, calcium chloride, dihydrate	208290	Merck Chemicals GmbH, Darmstadt, Germany
$CHCl_3$, chloroform, p.a., EMSURE®	1024451000	Merck Chemicals GmbH, Darmstadt, Germany

DMSO, dimethyl sulfoxide, anhydrous	276855	Sigma-Aldrich, St. Louis, MO, USA
Dulbecco's MEM, w/ 3.7 g/L $NaHCO_3$, w/ 4.5 g/L D-glucose, w/o L-glutamine and Na-pyruvate	F 0435	Biochrom GmbH part of Merck Millipore, Darmstadt, Germany
EtOH, ethanol, p.a., EMSURE®	1.00983.1000	Merck Chemicals GmbH, Darmstadt, Germany
H_2SO_4, sulfuric acid, p.a.	30743	Sigma-Aldrich, St. Louis, MO, USA
Hanks' balanced salt solution (10x), w/ $MgCl_2$, w/$CaCl_2$	H1641	Sigma-Aldrich, St. Louis, MO, USA
HCl, 1N, Titrinorm®	30024.290	VWR International, Darmstadt, Germany
HCl, 25%, EMSURE®	1.00316.1000	Merck Chemicals GmbH, Darmstadt, Germany
HEPES, 4-(2-hydroxyethyl)-1-piperazineethanesulfonic acids	391340	Merck Chemicals GmbH, Darmstadt, Germany
HNO_3, nitric acid, 100%	1.00450.1000	Merck Chemicals GmbH, Darmstadt, Germany
KCl, potassium chloride	P5405	Sigma-Aldrich, St. Louis, MO, USA
KI, potassium iodide, Suprapur®	1.05044.0050	Merck Millipore, Darmstadt, Germany
KOH, 1N, TitriPUR®, (max. $4 \cdot 10^{-5}$% Ca^{2+})	1.09107.1000	Merck Chemicals GmbH, Darmstadt, Germany
MeOH, methanol, p.a.	6009	Merck Chemicals GmbH, Darmstadt, Germany
MTT, Thiazolyl Blue Tetrazolium Bromide, BioReagent, ≥97.5% (HPLC)	M5655	Sigma-Aldrich, St. Louis, MO, USA
NaCl, sodium chloride	567440	Merck Chemicals GmbH, Darmstadt, Germany
NaOH, 1N, Titrinorm®	31627.290	VWR International, Darmstadt, Germany
$Na_2S_2O_3$, sodium thiosulfate	6512.2500	Merck Chemicals GmbH, Darmstadt, Germany
NBD-12 Cholesterol	810252	Avanti® Polar Lipids, Inc., Alabaster, AL, USA
n-Hexadecane	8.20633.0250	Merck Chemicals GmbH, Darmstadt, Germany
n-Hexane	1.04367.1000	Merck Chemicals GmbH, Darmstadt, Germany
Nonactin from *Streptomyces griseus*, ≥98% (function tested, HPLC)	N2286	Sigma-Aldrich, St. Louis, MO, USA
OptiMEM® (1x), w/ L-glutamine, w/ HEPES, w/o phenol red	11058021	Gibco™, ThermoFisher Scientific Rochester, NY, USA
PBS Dulbecco (10x) w/o Mg^{2+} and Ca^{2+}	L1835	Biochrom GmbH part of Merck Millipore, Darmstadt, Germany
PBS Dulbecco (1x) w/o Mg^{2+} and Ca^{2+}	L1825	Biochrom GmbH part of Merck Millipore, Darmstadt, Germany

Polymyxin B sulfate	21850029	Gibco™, ThermoFisher Scientific Rochester, NY, USA
Recombinant human IL-1β	200-01B	PeproTech, Rocky Hill, NJ, USA
Recombinant human TNF-α	300-01A	PeproTech, Rocky Hill, NJ, USA
Silastic® MDX4-4210 curing agent	n/a	Dow Corning Corporation, Midland, MI, USA
Silastic® MDX4-4210 Medical grade elastomer base	3097358-1004	Dow Corning Corporation, Midland, MI, USA
Sucrose	84100	Sigma-Aldrich, St. Louis, MO, USA
TFA, Trifluoroacetic acid	61030	Riedel-De Haën, Sigma-Aldrich, St. Louis, MO, USA
TMB, 3,3',5,5'-Tetramethylbenzidine	860336	Sigma-Aldrich, St. Louis, MO, USA
Triton X-100, p.a.	8603	Merck Chemicals GmbH, Darmstadt, Germany
Trypan blue	11732	Merck Chemicals GmbH, Darmstadt, Germany
Trypsin/EDTA 0.25%, 0.02% (w/v) in PBS, w/o Ca^{2+}, w/o Mg^{2+}	L2163	Biochrom GmbH part of Merck Millipore, Darmstadt, Germany
VLE RPMI 1640 w/ 2.0 g/L $NaHCO_3$, w/o L-glutamine	F1415	Biochrom GmbH part of Merck Millipore, Darmstadt, Germany
α-Hemolysin from *Staphylococcus aureus*, lyophilized powder, protein ~60%	H9395	Sigma-Aldrich, St. Louis, MO, USA
β-BODIPY® FL C_5-HPC	D3803	Molecular Probes™, ThermoFisher Scientific Rochester, NY, USA

APPENDIX II

AII. 1: HELICAL WHEEL PROJECTION OF A-HELICAL PEPTIDES

LL-37

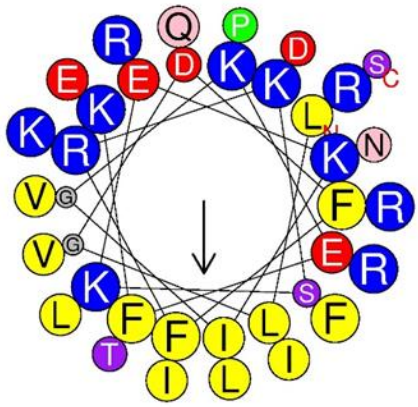

LL-32

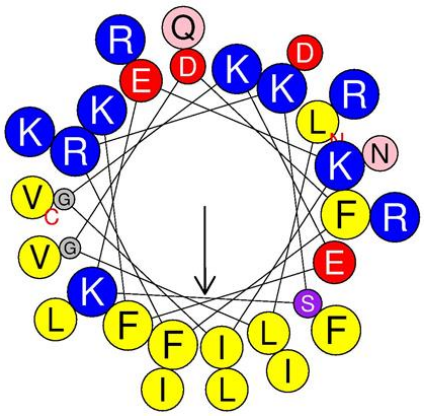

CRAMP

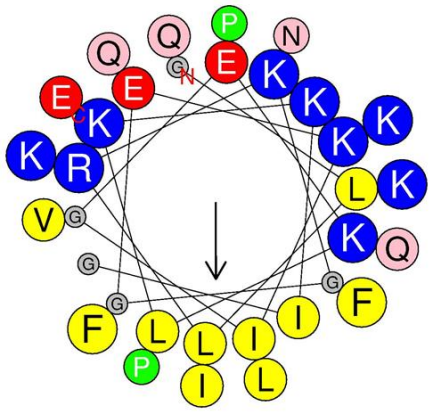

CAP18

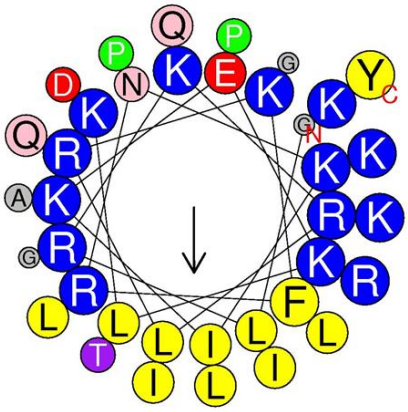

BMAP-27

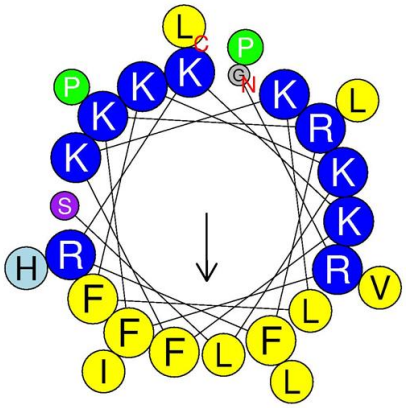

BMAP-28

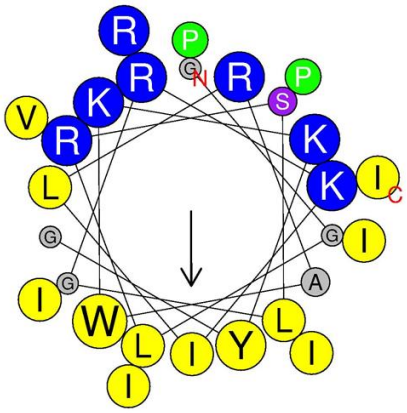

NK-2

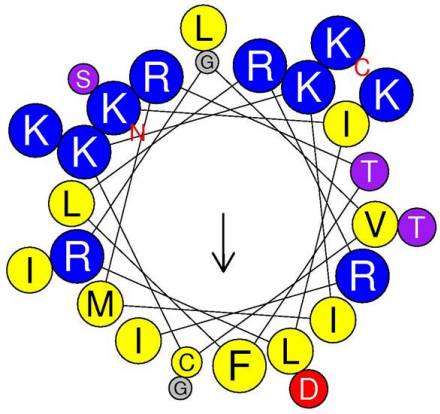

AII. 2 AMINO ACIDS

TABLE 28. SINGLE LETTER AND THREE LETTER CODE OF THE 20 CANONICAL AMINO ACIDS

A	Ala	Alanine	**M**	Met	Methionine
C	Cys	Cysteine	**N**	Asn	Asparagine
D	Asp	Aspartate	**P**	Pro	Proline
E	Glu	Glutamate	**Q**	Gln	Glutamine
F	Phe	Phenylalanine	**R**	Arg	Arginine
G	Gly	Glycine	**S**	Ser	Serine
H	His	Histidine	**T**	Thr	Threonine
I	Ile	Isoleucine	**V**	Val	Valine
K	Lys	Lysine	**W**	Trp	Tryptophan
L	Leu	Leucine	**Y**	Tyr	Tyrosine

ACKNOWLEDGMENTS

At this point, I want to thank first of all my doctoral supervisor THOMAS GUTSMANN for giving me the opportunity to write my dissertation in his workgroup. He has supported me throughout the past years and his door was always open for queries and discussions.

I also thank LARS REDECKE for his assumption of the chairperson of the examination committee and ALFRED X. TRAUTWEIN for his participation in the examination committee as second referee.

But let me express a special thanks to our technical assistants: SABRINA GROTH, IRINA VON CUBE und KERSTIN STEPHAN. Sabrina was involved in a bunch of permeabilization experiments (calcein release, KI quenching, FRET-Intercalation assay and tPod) and Irina fed and pet my cell line all over the years. Great work and support, girls – thank you! I enjoyed working with you, because you create a friendly, funny and warm working atmosphere.

Thanks to ANDRA SCHROMM for all her help and explanation around the cell and the world of immunology and signaling pathways, that would have otherwise driven me to the brink of despair with all their proteins and co-factors involved. I also thank you, Andra, for agreeing on being my BBRS mentor and the constructive food for thoughts during our semi-annual thesis committee meetings.

Thanks to RAINER BARTELS for the peptide synthesis and DOMINIK SCHWUDKE and his team for the MS-analysis of the peptides.

A further thank you goes to CHRISTIAN HÜBNER and his workgroup for giving me the opportunity to run out my FRAP experiments in his lab and for the warm welcome whenever I was around.

Thanks to JÖRG ANDRÄ for providing the NK-2 and to DOMINIK WILMS for providing the calcein release assay protocol. Also, a thank you to NADINE GEBAUER for implementing the tethaPod in our lab and her contribution to the "permeabilization paper" that is near submission.

Thanks to KLAUS BRANDENBURG for providing the LPep-peptide and always giving me a pally pat on the back.

Another thank goes to my two trainees JANA HOLM and CHEE KEONG TAN who never got discouraged and who I kept on the go with electrophysiology experiments on planar membranes. Thank you!

Thank you to SABINE DABELSTEIN for her "Back office" work, you saved me so much time by refilling tip boxes, restocking the inventory, cleaning flasks and bottles and much more. This is why all of us are able to remain focused on our experiments.

And a special thank you goes to CHRISTIAN "my roomie-lab mate-desk neighbor-Erklärbär-comedian" NEHLS and ANNIKA SAATHOFF; I have/had so much fun with you in the lab. Thank you for your support and advice!

To Julia Wernecke, the only one in the world who is allowed to call me her "measuring slave" ☺ for her patience in trying to give me an understanding of the profound X-ray physics, for the funny moments during beamtimes, night shifts, retreats and conferences. Even you were still busy with finishing your dissertation, you took time for me and helped me with the evaluation of the X-ray data; whenever I struggled with python or the data; I could bug you with questions and you always helped me! Without you, it wouldn't have been possible to evaluate the X-ray data in such a short time. Thank you so much!

Thanks to everyone else of the workgroup, I didn't mention by name in here; but all of you contributed to this work!

And last but not least, a very special thank goes to my family and any of their support, distraction and dispelling all of my doubts during the last years. Thank you for being on my side!

A THOUSAND THANKS TO ALL OF YOU – MY COMPANIONS

LIST OF PUBLICATIONS

FIRST AUTHORSHIP

In preparation	**Paulowski, L.**, Gebauer, N., Saathoff, A., Cornell, B. A., and Gutsmann, T. *A Comparative Study on Techniques for the Determination of Lipid Bilayer Permeabilization*

CO-AUTHORSHIP

In preparation	Andrä, J., **Paulowski, L.**, Kaconis, Y., Kopp, F., Koistinen, M., Brauser, A., Keese, S., Sevszik, E., Lohner, K., Brandenburg, K., Schütz, G., Sanchez-Gomez, S., Martinez de Tejada, G., Schromm, A., and Gutsmann, T. *Antimicrobial peptides provoke host-directed immunomodulation of immune cells by reorganizing membrane domains*
In preparation	Correa, W., Heinbockel, L., Brandenburg, J., Reiling, N., **Paulowski, L.**, Stephan, K., and Gutsmann, T. *Biophysical Investigations on the Interaction between Antimicrobial Peptides and Bacteria Killed by Cs-137 Irradiation*
In preparation	Hammer, M. U., Koistinen, M., **Paulowski, L.**, Winterhalter, M., and Gutsmann, T. *Polymyxin B induces adhesion and fusion of Gram-negative bacteria and lipid mimics of their membranes*

"Don't cry because it's over

Smile because it happened"

▪ *Dr. Seuss* ▪